NEUROIMAGING IN VETERINARY SCIENCE

EDITED BY: Andrea Tipold and Fintan J. McEvoy
PUBLISHED IN: Frontiers in Veterinary Science

frontiers Research Topics

ISSN 1664-8714
ISBN 978-2-88963-007-3
DOI 10.3389/978-2-88963-007-3

About Frontiers

Frontiers is more than just an open-access publisher of scholarly articles: it is a pioneering approach to the world of academia, radically improving the way scholarly research is managed. The grand vision of Frontiers is a world where all people have an equal opportunity to seek, share and generate knowledge. Frontiers provides immediate and permanent online open access to all its publications, but this alone is not enough to realize our grand goals.

Frontiers Journal Series

The Frontiers Journal Series is a multi-tier and interdisciplinary set of open-access, online journals, promising a paradigm shift from the current review, selection and dissemination processes in academic publishing. All Frontiers journals are driven by researchers for researchers; therefore, they constitute a service to the scholarly community. At the same time, the Frontiers Journal Series operates on a revolutionary invention, the tiered publishing system, initially addressing specific communities of scholars, and gradually climbing up to broader public understanding, thus serving the interests of the lay society, too.

Dedication to Quality

Each Frontiers article is a landmark of the highest quality, thanks to genuinely collaborative interactions between authors and review editors, who include some of the world's best academicians. Research must be certified by peers before entering a stream of knowledge that may eventually reach the public - and shape society; therefore, Frontiers only applies the most rigorous and unbiased reviews.
Frontiers revolutionizes research publishing by freely delivering the most outstanding research, evaluated with no bias from both the academic and social point of view. By applying the most advanced information technologies, Frontiers is catapulting scholarly publishing into a new generation.

What are Frontiers Research Topics?

Frontiers Research Topics are very popular trademarks of the Frontiers Journals Series: they are collections of at least ten articles, all centered on a particular subject. With their unique mix of varied contributions from Original Research to Review Articles, Frontiers Research Topics unify the most influential researchers, the latest key findings and historical advances in a hot research area! Find out more on how to host your own Frontiers Research Topic or contribute to one as an author by contacting the Frontiers Editorial Office: researchtopics@frontiersin.org

NEUROIMAGING IN VETERINARY SCIENCE

Topic Editors:
Andrea Tipold, University of Veterinary Medicine, Germany
Fintan J. McEvoy, University of Copenhagen, Denmark

Sophisticated imaging tools continue to provide information about the central nervous system that is novel. This has impacted the diagnosis of neurological diseases in veterinary patients by allowing non-invasive in vivo diagnosis of diseases previously not open to diagnosis or only diagnosed post mortem.

This eBook is a collection of papers submitted to the Research Topic "Neuroimaging in Veterinary Science". It contains review and research papers, case reports and an accompanying editorial. It gives insight into the contributions diagnostic imaging can make to the field of veterinary neurology.

Citation: Tipold, A., McEvoy, F. J., eds. (2019). Neuroimaging in Veterinary Science. Lausanne: Frontiers Media. doi: 10.3389/978-2-88963-007-3

Table of Contents

frontiers in Veterinary Science

EDITORIAL
published: 04 July 2019
doi: 10.3389/fvets.2019.00217

Editorial: Neuroimaging in Veterinary Science

Andrea Tipold[1]* *and Fintan J. McEvoy*[2]*

[1] Department of Small Animal Medicine and Surgery, University of Veterinary Medicine Hannover, Hanover, Germany,
[2] Department of Veterinary Clinical Sciences, University of Copenhagen, Copenhagen, Denmark

Keywords: animal models, MRI - magnetic resonance imaging, FLAIR (fluid attenuated inversion recovery), SPECT (single photon emission tomography), PET - positron emission tomography, dynamic MRI, MRI muscle imaging, dynamic susceptibility contrast (DSC)

Editorial on the Research Topic

Neuroimaging in Veterinary Science

This collection of 15 papers focuses on the developments in Neuroimaging in Veterinary Science over the last couple of years. It sheds light on aspects of current understanding and the role of imaging in important neurological diseases affecting veterinary patients and their caregivers and on areas of related research. Advances in neuroimaging have changed clinical neurology not only by contributing to improved understanding of relevant pathophysiology, but also by describing new diseases or new features of well-known diseases. This research topic places current work in veterinary neuroimaging in the context of our current understanding of clinical signs and the pathophysiology of diseases. It points a way toward future trends in the field.

There are many ways to look at the collection, depending on the specific background of the reader. The papers are mainly concerned with MRI but comparison is made with CT with regard to oncology imaging. The anatomical regions examined are as expected, brain and spinal cord including the vertebral column, but also there is consideration of the changes in para-spinal muscle groups in their response to intervertebral disc herniation. Neurological diseases are covered from the clinical diagnosis, pathophysiology and imaging protocol points of view.

With regard to spinal cord diseases, the research review contribution by Rusbridge et al. highlights research concerned with Chiari like malformation and syringomyelia, the role of syringomyelia (SM) in symptomatic disease is discussed and criteria are suggested for SM evaluation. The research paper by Kunze et al. describes the discrepancy between the grading of intervertebral disc degeneration according to the particular MRI sequence chosen. It is a reminder of the flexibility of MRI as an imaging tool, and that different sequences yield different, often non-overlapping information with respect to the anatomy and pathology imaged. In an anatomical study by Düver et al. disk to vertebral body dimension ratios are reported and breed specific differences emphasized. As a result, the understanding of breed specific diseases of the vertebral column can be improved. Again with respect to intervertebral disc disease, the paper by Trampus et al. describes alterations in MR signal from muscles in dogs with thoracolumbar disc disease; focal hyperintense T2W signals are described in muscle at sites of intervertebral disc disease.

Diseases of the brain and cranial cavity feature strongly in this research collection. The review paper by Rusbridge et al. considers MRI features suggestive of raised intracranial pressure in patients with ventriculomegaly. It identifies important anatomical abnormalities such as rostral displacement of the axis and atlas, and increased angulation of the odontoid process that should be considered in the search for causes of cerebrospinal fluid flow disruption. It also suggests novel MRI sequences to assist in the detection of adhesions and arachnoid webs in the subarachnoid

OPEN ACCESS

Edited by:
Mary M. Christopher, University of California, Davis, United States

Reviewed by:
Erik R. Wisner, University of California, Davis, United States
John Henry Rossmeisl, Virginia Tech, United States

***Correspondence:**
Andrea Tipold
Andrea.Tipold@tiho-hannover.de
Fintan J. McEvoy
fme@sund.ku.dk

Specialty section:
This article was submitted to Veterinary Imaging, a section of the journal Frontiers in Veterinary Science

Received: *24 May 2019*
Accepted: *18 June 2019*
Published: *04 July 2019*

Citation:
Tipold A and McEvoy FJ (2019) Editorial: Neuroimaging in Veterinary Science. Front. Vet. Sci. 6:217. doi: 10.3389/fvets.2019.00217

space. Anatomical malformations are also considered in the research reported by Lauda et al. In their paper the caudal fossa ratio in normal dogs is compared with the same ratio in Eurasier dogs with VLDLR (very low density lipoprotein receptor) - associated genetic cerebellar hypoplasia. They report that a sub-population of Eurasier dogs with this genetic defect show altered ratios, but not all. This suggests two phenotypes for the single genetic defect.

Physiology and pathophysiology of the brain and of intracranial diseases, detected by MRI are considered by two research papers. In the paper by Schmidt et al. perfusion magnetic resonance imaging is used to demonstrate reduced periventricular blood flow in dogs with ventriculomegaly. In the research paper by Moioli et al. changes in the intensity of the MR signal on T2 weighted fluid-attenuated inversion recovery sequences are reported to be a function of the fraction of inspired oxygen. As signal strength from CSF on these sequences is used in the evaluation of pathology, the possibility of this physiological cause of signal alteration is important.

Neoplasia, epilepsy and inflammatory brain disease also feature in the collection. In the paper by Stadler et al. a comparison is made between the accuracy of CT and MRI in determining glioma type (astrocytoma or oligodendroma), and glioma grade, high (WHO grade III or IV) or low (WHO grade II). Both modalities showed similar diagnostic performance in this clinical scenario, but the authors identified that both CT and MRI have many facets, and that the addition of techniques such as dynamic contrast—enhanced imaging in CT, or spectroscopy, or diffusion weighted imaging in MR may allow improvement in diagnostic performance.

Epilepsy is a common indication and a research focus for neuroimaging. In the review paper by Bankstahl and Bankstahl the current role of nuclear medicine in the veterinary epilepsy patient is discussed and its future role in diagnosis and research suggested. While PET and SPECT scanners are not commonly available in the wider clinical veterinary community they are not infrequently accessible in larger research settings. This paper suggests that there is value in continued use of nuclear imaging modalities in this patient group. The publication by Estey et al. identified volumetric changes in dogs with idiopathic epilepsy. With such studies it becomes evident that seizures have an impact on the brain structure or that some cases with presumed idiopathic epilepsy may have a structural cause for occurring seizures that are only detectable by advanced MR imaging and special analysis.

Inflammatory brain disease in the form of necrotizing encephalitis in dogs is reviewed in the paper by Flegel. The paper provides a helpful guide to MR imaging characteristic of necrotizing encephalitis in dogs and suggests that breed-specific imaging characteristics allow a clinical and imaging diagnosis with a relatively high degree of certainty. Flegel summarizes typical breed specific imaging features of the disease, such as lesion distribution, signal intensity, contrast enhancement, and gross changes of brain structure.

The collection also comprises papers illustrating the value of individual case reports. The paper by De Decker et al. reports imaging findings in a patient with tethered cord syndrome and highlights the potential usefulness of comparing images of the lumbosacral region obtained in neutral, flexed and extended positions to demonstrate an expected displacement of the *conus medullaris*. This so called dynamic lumbosacral MRI was of use in the patient reported and its routine application is suggested for further evaluation. The case report by Wang-Leandro et al. shows a new clinical feature of an inflammatory disease of the meninges leading to hyperacute hemorrhage. MRI features of such an early stage of hemorrhage are rarely described because of the time delay between occurrence of clinical signs and the diagnostic workup in MRI.

New ways to extract and measure data from the complicated medical imaging devices available to us is always of interest. In the research paper by Stadler et al. protocols for dynamic susceptibility contrast MRI of the canine brain are presented. These protocols (similar but with differing contrast dose per kg according to body weight) allow the creation of perfusion maps of the canine brain. These will undoubtedly have relevance for clinical veterinary neurology. Differences in size and shape amongst veterinary patients also feature in the paper by Pilegaard et al. which examines the influence of cranial shape on the ratio of the volume of the lateral ventricles to that of the cerebral cortex. It cautions that skull shape influences this index of relative volumes and so the index can be seen as breed dependent.

In setting up this Frontiers Research Topic we hoped to receive input that covered a wide range of topics in veterinary neuroimaging in the expectation that the resulting collection of work would be source of reference, information and inspiration. The collected work achieves this. It is the work of many individuals and it highlights both how much imaging has contributed and can be expected to contribute to veterinary neuroscience.

AUTHOR CONTRIBUTIONS

All authors listed have made a substantial, direct and intellectual contribution to the work, and approved it for publication.

Conflict of Interest Statement: The authors declare that the research was conducted in the absence of any commercial or financial relationships that could be construed as a potential conflict of interest.

frontiers in Veterinary Science

REVIEW
published: 28 November 2018
doi: 10.3389/fvets.2018.00280

Clinical Application of Diagnostic Imaging of Chiari-Like Malformation and Syringomyelia

Clare Rusbridge[1,2]*, *Felicity Stringer*[1] *and Susan P. Knowler*[2]

[1] *Fitzpatrick Referrals, Godalming, United Kingdom,* [2] *School of Veterinary Medicine, Faculty of Health & Medical Sciences, University of Surrey, Guildford, United Kingdom*

Chiari-like malformation (CM) and syringomyelia (SM) is a frequent diagnosis in predisposed brachycephalic toy breeds since increased availability of MRI. However, the relevance of that MRI diagnosis has been questioned as CM, defined as identification of a cerebellar herniation, is ubiquitous in some breeds and SM can be asymptomatic. This article reviews the current knowledge of neuroanatomical changes in symptomatic CM and SM and diagnostic imaging modalities used for the clinical diagnosis of CM-pain or myelopathy related to SM. Although often compared to Chiari type I malformation in humans, canine CM-pain and SM is more comparable to complex craniosynostosis syndromes (i.e., premature fusion of multiple skull sutures) characterized by a short skull (cranial) base, rostrotentorial crowding with rostral forebrain flattening, small, and ventrally orientated olfactory bulbs, displacement of the neural tissue to give increased height of the cranium and further reduction of the functional caudotentorial space with hindbrain herniation. MRI may further reveal changes suggesting raised intracranial pressure such as loss of sulci definition in conjunction with ventriculomegaly. In addition to these brachycephalic changes, dogs with SM are more likely to have craniocervical junction abnormalities including rostral displacement of the axis and atlas with increased odontoid angulation causing craniospinal junction deformation and medulla oblongata elevation. Symptomatic SM is diagnosed on the basis of signs of myelopathy and presence of a large syrinx that is consistent with the neuro-localization. The imaging protocol should establish the longitudinal and transverse extent of the spinal cord involvement by the syrinx. Phantom scratching and cervicotorticollis are associated with large mid-cervical syringes that extend to the superficial dorsal horn. If the cause of CSF channel disruption and syringomyelia is not revealed by anatomical MRI then other imaging modalities may be appropriate with radiography or CT for any associated vertebral abnormalities.

Keywords: complex craniosynostosis syndrome, basilar invagination, COMS, Chiari type I malformation, cine MRI, balanced steady-state free precession sequence, fluid signal-void sign, MRI protocol

OPEN ACCESS

Edited by:
Andrea Tipold,
University of Veterinary Medicine Hannover, Germany

Reviewed by:
Daniela Schweizer-Gorgas,
University of Bern, Switzerland
Cristian Falzone,
Diagnostica Piccoli Animali, Italy

***Correspondence:**
Clare Rusbridge
c.rusbridge@surrey.ac.uk

Specialty section:
This article was submitted to Veterinary Neurology and Neurosurgery, a section of the journal Frontiers in Veterinary Science

Received: *05 August 2018*
Accepted: *22 October 2018*
Published: *28 November 2018*

Citation:
Rusbridge C, Stringer F and Knowler SP (2018) Clinical Application of Diagnostic Imaging of Chiari-Like Malformation and Syringomyelia. Front. Vet. Sci. 5:280. doi: 10.3389/fvets.2018.00280

INTRODUCTION

Chiari-like malformation (CM) is a complex skull and craniocervical junction disorder associated with brachycephaly with skull base shortening, low volume caudal fossa and rostrotentorial, caudotentorial and craniospinal crowding. For a detailed written and visual description of the morphogenesis see the review by Knowler et al. (1). The condition has been marred in controversy since the first description, not least by what to call it (2). The eponymic term refers to the first detailed pathological description by Hans Chiari of an analogous human condition (3). The veterinary label, chosen in a round table discussion (2, 4) was considered less restrictive than an anatomical description (for example hindbrain herniation or occipital hypoplasia), which may have proved simplistic or inaccurate in the future. This prediction was true, and over the last two decades our understanding of the complex morphology has deepened and most realize that this condition is more than a cerebellar foramen magnum herniation. As a MRI description, CM should be considered an umbrella term, as the bony and parenchymal changes between and within individuals in each breed are different but have a common tendency toward pain associated with CM and the development of syringomyelia (SM). As such, and with the common feature of being associated with brachycephaly, it was recently proposed that the disorder might be better described as a brachycephalic obstructive cerebrospinal (CSF) channel syndrome (BOCCS) with similarities to brachycephalic obstructive airway syndrome (BOAS) (1).

TABLE 1 | Pathogenesis of Chiari-like malformation and syringomyelia: summary of the existing knowledge base—skull changes.

Anatomical feature	Study finding(s)	Possible implication
Brachycephaly	Brachiocephalic breeds have early closure of the spheno-occipital synchondrosis. In CKCS closure is even earlier (49, 50)	Premature closure of the spheno-occipital synchondrosis will result in a short cranial base (basicranium).
	CKCS have shorter cranium in relation to width compared to other brachycephalic dog breeds (51).	
	Griffon Bruxellois with CM have shortened basicranium and supraoccipital bone, with a compensatory lengthening of the dorsal cranial vault, especially the parietal bone (52)	Basiocranial shortening results in compensatory changes in the rostral cranial fossa which results in a head shape with rostrocaudal doming and is broad in relationship to the length (reduced cephalic index)
	Association between increased cranial height and SM in CKCS, Griffon Bruxellois and Affenpinscher (38, 40)	
	CKCS with broader and shorter skulls and increased rostro-cranial doming are at increased risk of developing SM (53)	
	Association between acute angulation at spheno-occipital synchondrosis (Sphenoid flexure) and SM (40)	May be associated with premature closure of spheno-occipital synchondrosis. This angulation occurs in rodent models where the spheno-occipital synchondrosis is damaged (1, 54)
	Rostral forebrain flattening, short basioccipital bone associated with CM pain	CM pain is associated with increased brachycephaly
	Increased risk of SM with increased proximity of dens to basioccipital bone and/or increased airorhynchy with small more ventrally rotated olfactory bulbs (39)	There are two SM phenotypes: one typified by extreme brachycephalism and one by craniospinal junction deformation
Occipital Crest	Association between reduced occipital crest and SM in CKCS, Affenpinscher and Chihuahua (40)	Suggests insufficiency of the supraoccipital bones and possibly the intraparietal bone
Frontal Sinus	Association between small frontal sinuses and SM in small breed dogs (55)	Suggests that SM may be related to rostrotentorial skull changes rather than being confined to a hind skull abnormality.
Caudal cranial fossa volume	CKCS with CM and SM have a shallower and smaller volume caudal cranial fossa compared to CKCS with CM only and other control breeds (56, 57)	Smaller caudal cranial fossa volume predisposes caudal cranial fossa overcrowding
	CKCS have a strong relationship between hindbrain volume and volume of the rostral part of the caudal cranial fossa and a weak relationship between hindbrain volume and volume of the caudal part of the caudal cranial fossa. In Labrador retrievers and other small breed dogs this relationship is reversed (56, 58)	Small breed dogs and Labrador retrievers compensate for variations in hindbrain volume by modifying growth of the occipital skull. In the CKCS, increased cerebellar size is not accommodated by increased occipital bone development and the tentorium cerebelli compensates by developing / remodeling in a rostral direction
Occipital bone volume	No difference in volume of the occipital bones between CKCS (with and without SM) and French Bulldogs (59)	Does not support theory of occipital bone hypoplasia
Jugular foramina	CKCS with CM and SM have narrowed jugular foramina in comparison with CKCS with CM only (52, 60)	Venous narrowing at the jugular foramina associated with reduced skull base can lead to elevated venous pressure and impaired CSF absorption
Venous sinus volume	CKCS with CM and SM have reduced venous sinus volume in comparison with CKCS with CM only (61)	Reduced venous sinus volume could result in intracranial hypertension and impaired CSF absorption

The analogous disease in humans was considered to be Chiari type I malformation, defined traditionally as a MRI finding of caudal displacement of the cerebellar tonsils inferior to the plane of the foramen magnum by at least 3 mm. However, like the canine disease, this description is problematic especially as there can be symptomatic disease and SM with smaller herniation (termed Chiari type 0). In an attempt to categorize the variations in humans there are now seven recognized types: 0, 1, 1.5, 2, 3, 3.5, and 4 (3–6). However, the distinction between types is challenging especially when the etiology is multifactorial and increasingly there is a call in human medicine that cerebellar tonsil herniation/Chiari malformation should be considered a radiographic sign and the focus of the diagnostic investigation should be to determine the cause of that herniation for example shallow posterior fossa (7), craniosynostosis (8), inherited disorders of connective tissue (9), spinal cord tethering (10), intracranial hypertension (11), or intracranial hypotension (12).

CM is one of the most common causes of SM in the dog which is characterized by the development of cavities in the spinal cord containing a fluid similar to CSF (13, 14) however SM can develop after any obstruction to CSF channels and has been reported in a variety of disorders ranging from acquired cerebellar herniation secondary to intracranial masses (15–18) to spinal arachnoid diverticulum (19, 20) and spinal cord tethering (21). The terminology of SM is equally confused, with some veterinary papers referring to syringohydromyelia or hydrosyringomyelia. These historical terms have been mostly discarded in human medicine (4). Equally confusing is if and when the term hydromyelia is applied. The term *syringomyelia* was first used by Charles-Prosper Ollivier d'Angers (1796–1845) deriving the term from the Greek "*syringe*" meaning tube or pipe, and "*myelio*" referring to the spinal marrow (22, 23). The term *hydroamyelus* was coined by Schüppel in 1865 to describe a dilatation of the central canal (24). In 1875, and after describing spinal cord cavities apparently separate from the central canal and surrounded by gliosis, Simon proposed that hydromyelia be used to describe central canal dilation and distension and that the term syringomyelia be reserved to describe cavities and cystic conditions independent of the central canal (25, 26). In 1876, Leyden concluded that hydromyelia and SM were identical conditions (26, 27) but Kahler and Pick made the observation that a hydromyelia is lined by ependyma whereas glial cells form the wall of SM cavities and recommended keeping a distinction between hydromyelia and SM (26, 28). However, it is difficult to distinguish between hydromyelia and SM, by radiological, clinical, or pathological means and consequently some used the combined terms syringohydromyelia or hydrosyringomyelia, to describe a cavity which is partially lined by ependymal but which also extends into the spinal cord substance (29). Thus, some clinicians argue that the term syringomyelia should only apply to a glia lined cavity separate from the central canal, that hydromyelia be reserved for central canal dilation, still lined by ependyma and that the term syringohydromyelia is correct for a cavity involving a dilated central canal that is partially lined by ependyma. However, post mortem and experimental studies have suggested that the ependyma is disrupted following only minor central canal dilatation and that all syringomyelic cavities are connected to the central canal at some level of the spinal cord (4, 30–32) therefore nowadays the simpler and original term syringomyelia is used by the majority (4). In veterinary

TABLE 2 | Pathogenesis of Chiari-like malformation and syringomyelia: summary of the existing knowledge base—craniocervical junction and cervical changes.

Anatomical feature	Study finding(s)	Possible implication
Proximity of atlas to skull (atlanto-occipital overlapping)	SM risk increases with decreased distance between atlas and occipital bones (39, 62–64)	Reduced distance between the skull and the cervical vertebrae increases risk of SM
	Greater distance between atlas and basioccipital bone is protective against SM (39)	
	CKCS with SM have shorter distance between the spheno-occipital synchondrosis and atlas (40)	
Odontoid peg impingement of ventral subarachnoid space/neural tissue	Commonly seen in association with CM (40, 56, 65)	Contributes to overcrowding and conformation change of craniospinal junction with loss of cisterna magnum
	Greater distance between atlas and odontoid peg is protective against SM (40)	
	Odontoid peg is more acutely angled, contributing to craniospinal disproportion, medullary elevation and cervical flexure (40)	
Proximity of dens to atlas	SM risk increases with decreased distance between odontoid peg and atlas in Affenpincher (40)	
Dorsal impingement subarachnoid space/spinal cord (atlantoaxial bands) at C1-C2	Commonly seen in association with CM and more prominent in extended than flexed positions (56, 62, 63, 65, 66)	Significance undetermined
Width of spinal canal	Increased width of spinal canal at C2-C3 and C3 in CKCS with SM (67)	Questionable clinical significance
Atlantoaxial subluxation	Occasional comorbidity with CM (68)	No significant association with SM
Size of C2 spinous process	Significantly smaller in CKCSs than in non-CKCS breeds (68)	
Angulation at C2-C3	No correlation (67)	

medicine a central canal dilatation is defined as a dilatation and distension of the spinal cord with a transverse diameter <2 mm (33).

Identifying a cerebellar herniation and SM on MRI is relatively straightforward and has been defined by the British Veterinary Association and UK Kennel Club with a Health Scheme for breeding dogs based on a grading system for CM, SM, and the maximum transverse diameter of the syrinx if present (33). However, the grading for CM is simplistic and only based on the degree of cerebellar herniation. The diagnosis of symptomatic CM and SM can be challenging in some breeds such as the Cavalier King Charles spaniel (CKCS) because CM, as defined by the BVA/KC Health Scheme is ubiquitous, and SM is prevalent but may be asymptomatic (34, 35). Increasingly it has become apparent that CM alone, like the analogous human condition, can have significant impact on welfare and quality of life (36, 37). Previously we used a MRI morphometric mapping approach to define CM pain and symptomatic SM in the CKCS, Griffon Bruxellois, Chihuahua, and Affenpincher (38–40) and these traits were linked to genomic regions (41, 42). However, translating this research technique to the clinic is challenging as it involves time consuming measurements and there is no objective measure of disease presence/ risk to offspring. Consequently development of a machine learning approach and computer analysis is recommended but development of this will take considerable resources (43, 44). This article serves to review the current knowledge base and provide guidelines to the clinician for the diagnostic imaging of CM-pain and symptomatic SM.

CURRENT UNDERSTANDING OF THE MORPHOLOGICAL CHANGES IN CANINE CM AND SM

Many studies, mostly in the CKCS or Griffon Bruxellois, have assessed features of skull and cervical vertebral morphology in relationship to the presence or absence of SM. Not all studies had

TABLE 3 | Pathogenesis of Chiari-like malformation and syringomyelia: summary of the existing knowledge base—neuroparenchymal changes.

Anatomical feature	Study finding(s)	Possible implication
Parenchymal (brain) volume	The absolute and relative volume of the CKCS skull is similar to other brachycephalic toy dog breeds but CKCS have a greater volume of parenchyma within the caudal cranial fossa (69) and CKCS with early onset SM have a larger volume of parenchyma within a smaller caudal cranial fossa compared to older CKCS with CM only (57, 61, 70)	Mismatch in skull and brain volume is associated with development of SM.
Cerebellar volume	CKCS have relatively increased cerebellar volume compared to other control breeds and this is associated with development of SM (71)	Caudal cranial fossa overcrowding is associated with development of SM
Cerebellar herniation	Typically present but size does not predict SM (62, 72, 73)	Obstruction of CSF channels though the foramen magnum contributes to the pathogenesis of SM but there must also be other predisposing factors.
	Positive association with the size of foramen magnum and size of cerebellar herniation (62)	Overcrowding of the caudal cranial fossa causes supraoccipital bone resorption (occipital dysplasia) and widening of the foramen magnum over time.
	The length of the cerebellar herniation increases with time. The size of the foramen magnum also increases (74, 75)	
Cerebellar pulsation	CKCS with CM and SM have significantly greater pulsation of the cerebellum compared to CKCS with CM only and other control breeds (76)	Abnormal cerebellar pulsation could lead to a mismatch in the timing of the arterial and CSF pulse waves predisposing SM (77, 78)
Position of cerebellum relative to occipital lobe	Rostrotentorial craniocerebral disproportion results in the occipital lobes being displaced caudally so that cerebellum is invaginated under the occipital lobes (40).	Overcrowding in both cranial and caudal fossa affects position of cerebellum
Medullary elevation (medullary kinking)	Higher medullary kinking index is associated with clinical signs in CKCS and Chihuahuas (47, 79)	Dogs with higher medullary elevation / kinking are more likely to have clinical signs
Caudal medulla (obex) position	Association between more caudal brainstem positions and presence of SM (79)	Caudal displacement of the obex may increase risk of SM
CSF flow	Higher peak CSF flow velocity at the foramen magnum with a lower CSF flow velocity at C2–C3 predicts SM (80)	SM is associated with alterations in the CSF velocity profile
	Turbulence at the foramen magnum and at the C2–C3 disc significantly associated with SM (80)	
	Presence CSF signal-void sign in mesencephalic aqueduct on T2W is associated with SM and increased ventricular size (81)	
Ventricle dimensions	In CKCS ventricle dimensions are positively correlated with syrinx width (57)	Evidence that SM is related to CSF channel obstruction
	Are not correlated with seizures (nor is caudal cranial fossa overcrowding) (82)	Epilepsy and CM in CKCS should be considered unrelated

good control groups, especially the earlier ones. As SM occurs secondary to CM and is more likely in older dogs (34, 35, 45, 46), it is important that the SM-clear cohort consists of dogs MRI scanned when older and typically aged 4 years or more. Equally it is important to accurately phenotype symptomatic dogs which can be challenging as the most common clinical sign is pain which is subjective and in the dog overly reliant on owner reporting (39, 47, 48).

Table 1 summarizes the existing knowledge in relationship to the skull, **Table 2** the craniocervical junction and cervical changes, **Table 3** the neuro-parenchymal changes and **Table 4** the syrinx changes.

SUMMARY OF EXISTING KNOWLEDGE OF THE MORPHOLOGICAL CHANGES IN CANINE CM AND SM

The key feature of canine CM is craniosynostosis of particularly the spheno-occipital synchondrosis. However, premature closure of the spheno-occipital and intersphenoidal synchondrosis define the canine brachycephalic skull (1, 49) and CM does not occur in all brachycephalic dogs. Therefore, CM is a more complex disorder and likely involves other premature suture closure (especially the lamboid) or other causes of insufficient cranium. The skull insufficiency results in rostrotentorial crowding which further reduces the functional caudotentorial space and causes hindbrain herniation. It is complicated by craniocervical junction deformation including change in angulation of the dens and increased proximity of the atlas to the skull and loss of the cisterna magna. Loss of the cisterna magna or other alteration in the CSF volume will affect the compliance of the CNS (90). In addition some predisposed breeds such as the CKCS have comparatively big brains (69, 71, 91). The pathogenesis of SM associated with CM is undetermined but is predisposed by two phenotypes (or combination); the first by extreme brachycephaly and the second by craniocervical junction deformation (39). This may be influenced by poor venous drainage, intracranial hypertension, changes in CNS compliance and conformational features of the spinal canal. Although CM is considered a naturally occurring model of adult Chiari type 1 malformation it is much closer to the hindbrain herniation seen with complex craniosynostosis such as Crouzon's syndrome (92).

DIAGNOSTIC IMAGING OF CM AND SM

Radiographs

Radiographs are not recommended for the investigation of CM and SM. However, if they have been obtained, for example by the general practitioner in the work-up for cervical pain, then there may be features that are suggestive of CM and SM such as flattened supraoccipital bone and close proximity of the atlas to the skull (**Figures 1**, **2**). In the instance of severe SM there may be widening of the cervical spinal canal and remodeling and scalloping of the vertebrae due to increased intraspinal pressure (93) (**Figure 2**). Dynamic (flexion and extension) atlantoaxial radiographs may be indicted to assess stability of the atlantoaxial joint especially if a foramen magnum decompression is planned (**Figure 3**).

Ultrasound

In veterinary medicine ultrasound does not feature in management of CM and SM as it does in human medicine, where 3D ultrasound it is used intraoperatively to tailor a foramen magnum decompression and optimize re-establishment of CSF flow (94, 95). Ultrasonography of the atlanto-occipital

TABLE 4 | Pathogenesis of Chiari-like malformation and syringomyelia: summary of the existing knowledge base—syrinx features.

Anatomical feature	Study finding(s)	Possible implication
Syrinx presence	If a syrinx is detected in a assymptomatic dog having MRI screening prior to breeding then there is a higher change that this dog may develop clincial signs of CMSM later in life compared to a dog without a visible syrinx (83) However dogs with no clinical signs at the age of 6 are more likely to remain asymptomatic (45)	Early development of syringomyelia is more likely to be associated with clinical signs even if the dogs is initialy assymptomatic
Site of syrinx	In CKCS, SM tends to develop first within the C2–C4, T2-T4, and T12-L2 spinal-cord segments (77, 84, 85).	SM development may be associated with subarachnoid space narrowing and/or change in the angulation of the vertebral canal
	Axial stress increases in the cranial cervical and cervico-thoracic regions where the spinal cord has most curvature (86)	Increased axial stress at the site of spinal curvature may explain the syrinx distribution in the CKCS
	In CKCS 76% of dogs with a syrinx at C1-C4 also had a syrinx in the C5-T1 and T2-L2 regions and 49% had a syrinx in the L3-L7 region (85)	In CKCS MRI imaging of the cranial cervical region only has high sensitivity for detection of SM however the extent of the disease may be underestimated
Syrinx size and symmetry	Pain is positively correlated with SM transverse width and symmetry on the vertical axis (32, 87)	Dogs with a wider asymmetrical SM more likely to experience pain
	Phantom (fictive) scratching is associated with a mid-cervical spinal cord segment syringe with extension to the superficial dorsal horn (88)	Phantom (fictive) scratching is associated with damage to the mid-cervical superficial dorsal horn
	Dogs with a wide syrinx and dorsal gray column damage are also more likely to have cervicothoracic scoliosis (87)	Gray column damage can result in an imbalance of proprioceptive information and cervical dystonia (89)

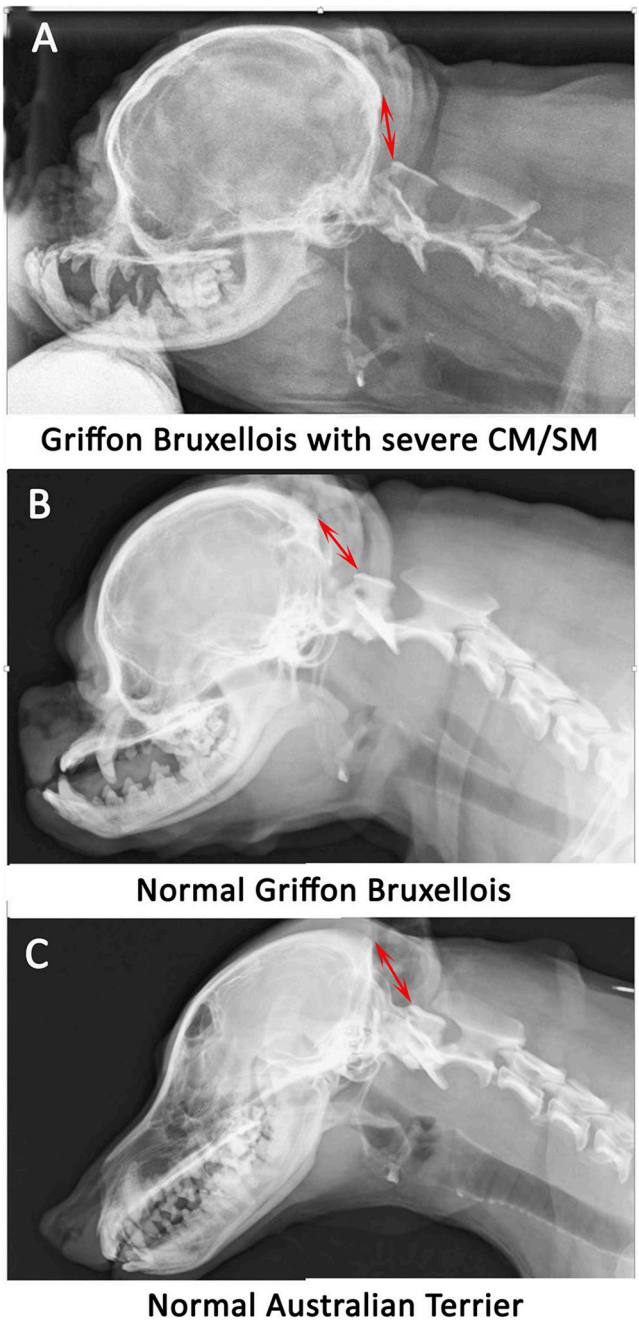

FIGURE 1 | Lateral skull and cranial cervical spinal radiographs in a Griffon Bruxellois with MRI confirmed severe CM and SM **(A)**, a normal Griffon Bruxellois **(B)**, and an Australian terrier **(C)**. The head is in extension as the space between the dorsal atlas and the occiput increases with flexion. A red arrow is placed between the occiput and the dorsal tubercle of the atlas for each dog. The atlas is considerably closer to the skull in the SM affected dog.

junction has been described, proving it is possible to discern the cerebellar herniation (96). Hypothetically, ultrasound guidance could prove a useful aid for placement of a shunt into a syrinx or ventricle via a laminectomy or craniectomy.

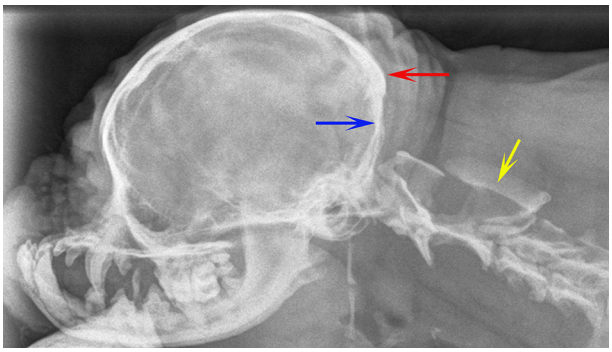

FIGURE 2 | Lateral skull and cranial cervical spinal radiographs of a 6 year old female Griffon Bruxellois presented with tetraparesis and following MRI diagnosed with symptomatic CM and SM. The skull has rostro-cranial doming and a "copper beaten" appearance due to convolutional markings relating to the gyri and presumed raised intracranial pressure. The supraoccipital bone is flattened (blue arrow) and the occipital crest is small (red arrow). A large cervical syrinx has resulting in widening of the cervical spinal canal with thinning and scalloping of the vertebrae (yellow arrow). A MRI confirmed CM, SM, and ventriculomegaly. The maximum width of the syrinx in the cervical spinal cord in a transverse section at the level of C2 was 8 mm.

Computed Tomography (CT)

CT should be performed if a vertebral malformation is suspected in association with SM especially if implanted surgical fixation is likely and to facilitate planning of this procedure (**Figure 3**). Most descriptions of CT in the investigation of CM and SM have been to answer a research hypothesis or question (51, 59, 60, 63, 97). Although CT has limited value in assessing CM and SM other than confirming a cerebellar herniation (98) and defining craniocervical junction abnormalities (63), hypothetically it could play a future role in health screening pedigree dogs assuming accurate morphometric analysis/machine learning can be translated from MRI studies and especially if risk of future disease could be predicted (99).

Myelography

Myelography and CT myelography can be used to investigate SM secondary to arachnoid diverticulae and webs/bands (100, 101) and CT myelography is the procedure of choice in the investigation of idiopathic SM if anatomical or cine MRI techniques are not available or have not revealed the cause of the CSF channel obstruction (102, 103). In veterinary medicine the most common application of CT myelography is when MRI is inappropriate because of metal implants and the owner wants to pursue further surgical management. An arachnoid web/band is indicated by a (often dorsal) flow block indicating CSF obstruction in combination with displacement or change in spinal cord caliber (**Figure 4**). An arachnoid diverticulae is a CSF containing space, lined by arachnoid mater which communicates with the subarachnoid space via a narrow "neck" enlarging via a one-way valve effect. With myelography the diverticulae will fill with contrast (101, 103, 104). Intrathecal contrast medium injections are more challenging when the spinal subarachnoid space is narrowed as a consequence of SM and should be

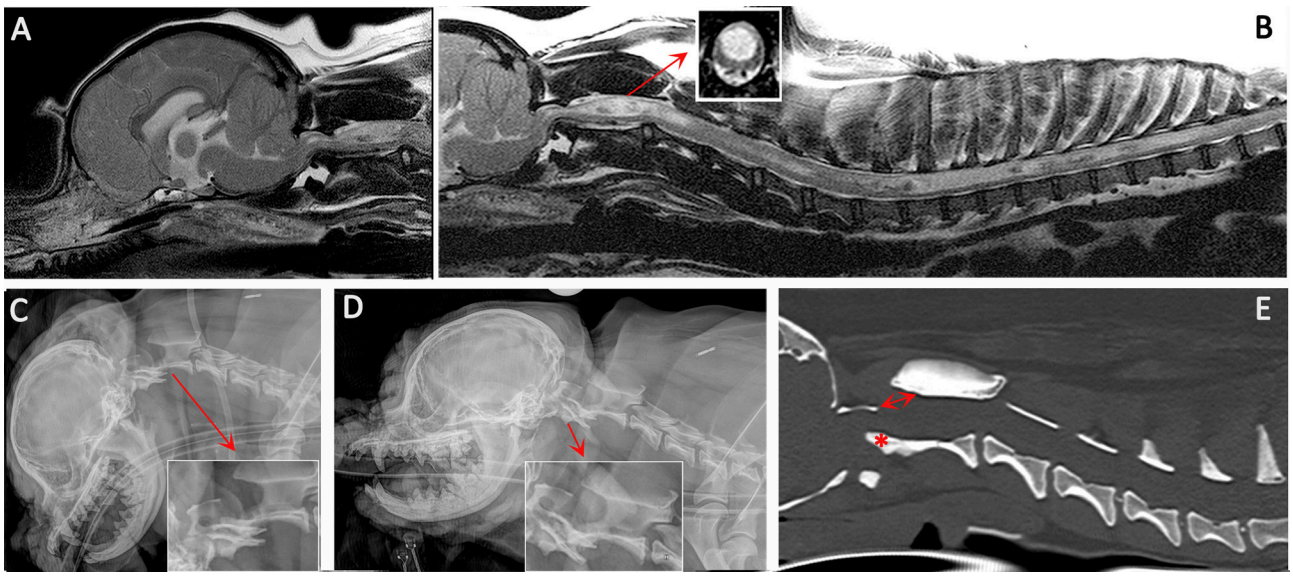

FIGURE 3 | Diagnostic imaging from a 5 year female CKCS presented with lethargy, ataxia, cervicotorticollis, and phantom scratching and following MRI diagnosed with symptomatic CM and SM. **(A)** T2-weighted mid-sagittal MRI of the brain and cranial cervical spinal cord. **(B)** T2- weighted mid sagittal MRI of the hindbrain and spine from C1 to T10. **(C)** Lateral skull and cervical spinal radiograph flexed at the atlantoaxial joint. **(D)** Lateral skull and cervical spinal radiograph extended at the atlantoaxial joint. **(E)** CT reformatted in the sagittal plane of the skull and cervical spine. MRI imaging **(A,B)** confirmed CM and SM with a large mid cervical SM involving the superficial dorsal horn thus explaining the cervicotorticollis and phantom scratching (insert). MRI also suggested atlantoaxial instability with spinal cord compression by the odontoid peg. Atlantoaxial instability was confirmed by a dynamic radiographic study **(C,D)**. The CT was obtained for pre-surgical planning. The dorsal displacement of the odontoid peg (asterisk) and dorsal opening (arrow) between the atlas and axis can be appreciated (Siemens Magnetom Symphony, A Tim System, 1.5 T, Erlangen, Germany; Toshiba Aquilion Prime 160 slice, Otawara, Japan).

undertaken by an experienced operator. CT myelography is not indicated in the investigation of SM secondary to CM.

Magnetic Resonance Imaging (MRI)

MRI is undoubtedly the modality of choice to investigate CM and/or SM. On making a diagnosis of CM/SM there are six aims for the clinician.

1) To assess and document the anatomical changes (**Figure 5**, **Supplementary Figure 1**).
2) To determine the cause of the SM. SM is an acquired disease which occurs secondary to CSF channel disruption therefore the aim of MRI is to determine the site of that obstruction. Typically disruption at the craniocervical junction due to CM results in syrinx development in the cranial cervical region (85).
3) To determine the full extent of disease, for example the caudal extent of the syrinx in the event of holocord SM (85).
4) Eliminate other potential causes of the clinical presentation and neurological localization, for example intervertebral disc disease as an alternative explanation for spinal pain.
5) Assess whether the radiological findings are consistent with the neurological localization and severity, for example forebrain signs such as seizures or cranial nerve deficits such as facial nerve paralysis cannot be explained by SM which is a spinal cord disease.
6) To determine if other diagnostic modalities are recommended, for example CT to characterize bony abnormalities that might need surgical stabilization and therefore planning.

MRI PROTOCOLS TO INVESTIGATE CM AND SM

Diagnostic MRI evaluation of CM and SM should include imaging of brain and spinal cord in at least two orientations and include protocols to produce static T1-weighted and T2-weighted sequences (102). Sagittal and transverse imaging of the brain including the craniocervical junction is essential to evaluate the rostrotentorial and caudotentorial overcrowding, CSF spaces and any compromise of the craniospinal junction. Spinal MRI establishes the presence, maximum width on transverse images, dorsal horn involvement and longitudinal extent of the syrinx/presyrinx (**Table 5** and **Supplementary Table 1**). It is recommended that at the time of scanning that the microchip or tattoo number (confirmed by the veterinary surgeon) is included on the DICOM images in addition to the Kennel Club registration number if the dog is registered. This is to permit submission to an official CMSM health scheme should the owner request it (33).

Protocols will vary between low and high field machines because of the difference in anatomical definition. T2-weighted sequences will be preferred for high field machines and T1-weighted sequences for low field machines. However, at least one region of the spinal cord, typically a sagittal sequence of

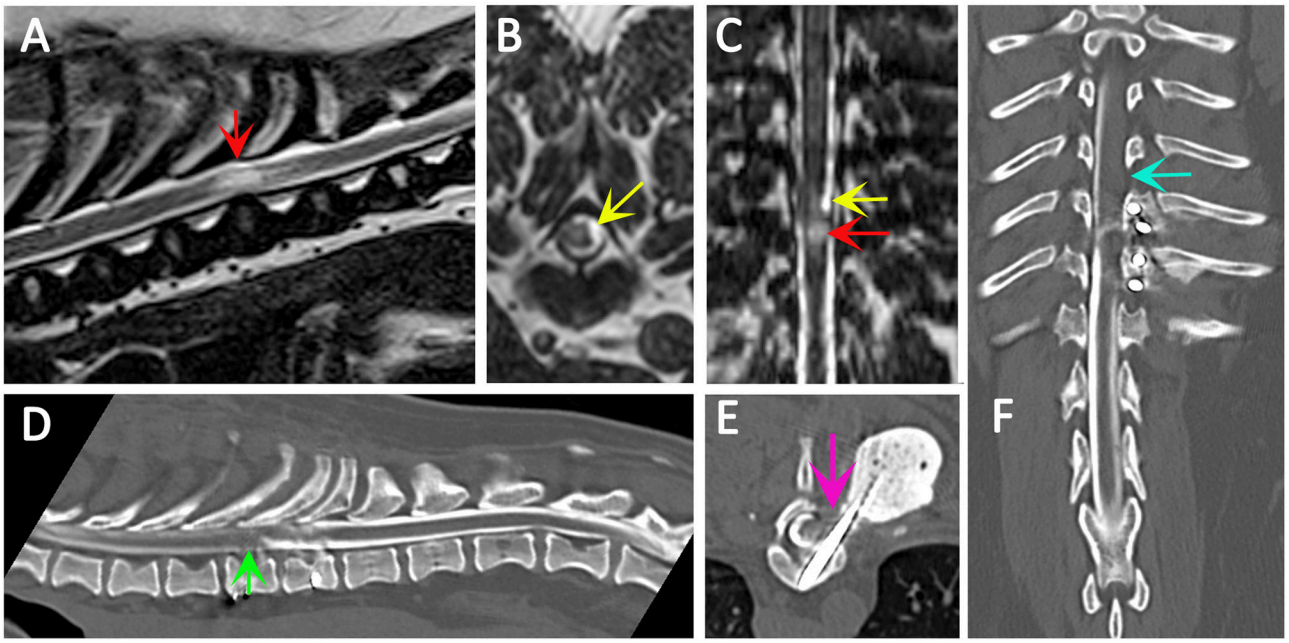

FIGURE 4 | Use of CT myelography to investigate arachnoid adhesions in in a 10 year old female Pug dog presented with signs of a thoracic myelopathy and that had previous surgical management for spinal arachnoid diverticulum and vertebral instability. Six months previous this dog had previously been managed surgically for a spinal arachnoid diverticulum (red arrow) with associated spinal cord edema/presyrinx (yellow arrow) at the level of T9/T10. She had been presented originally with a 2 year progressive history of myelopathy and the arachnoid diverticulum was considered associated with vertebral instability. Surgical management included marsupialization of the arachnoid diverticulum and spinal stabilization with Interface Pins (IMEX Veterinary Inc, Long View Texas) and Simplex-tobramycin bone cement (Howmedica, Limerick, Ireland). After an initial improvement the dog deteriorated and the metal implant precluded repeat MRI. CT myelography was performed from a lumbar injection. There is a reduced flow of contrast cranially (green arrow) and block to flow of the contrast material on the left side (blue arrow) and transverse images suggest adhesions between the spinal cord tissue and laminectomy site confirmed at surgery (pink arrow). **(A)** T2-weighted mid-sagittal MRI of the spinal cord from T6 to L1. There is a focal area of spinal cord edema (presyrinx) at the level of T9/T10 (red arrow). **(B)** Transverse 3D-CISS image at the level of T9/T10. There is a focal dilatation of the subarachnoid space at T9/T10 (yellow arrow). **(C)** Dorsal 3D-CISS image at the level of T7 to T13 demonstrating spinal cord edema (presyrinx) at the level of T9/T10 (red arrow) and suspected arachnoid diverticulum cranial to it (yellow arrow). **(D)** Midsagittal computed tomographic myelography from T6 to L2; there is reduced flow of iodinated contrast material cranial to T9 (green arrow). **(E)** transverse computed tomographic myelopathy at the level of T9. There is an adhesion between the spinal cord and laminectomy site (pink arrow). **(F)** Dorsal computed tomographic myelography from T6 to L2; there is a block of iodinated contrast material cranial to T9 (blue arrow) (Siemens Magnetom Symphony, A Tim System, 1.5 T, Erlangen, Germany; Toshiba Aquilion Prime 160 slice, Otawara, Japan). Image acknowledgment Dr Anna Tauro and Dr Colin Driver, Fitzpatrick Referrals.

the cervical region, that includes both T1 and T2-weighting is essential to determine that the signal characteristics of the fluid filled cavity is identical to CSF and to eliminate other causes of hyperintensity on T2-weighted images for example edema associated with meningoencephalomyelitis of unknown origin. As a general rule, measurements of the width of CSF spaces are considered more accurate on T1-weighted images, however T2 weighted images are more sensitive to the presence of excessive fluid within the neural tissue and in particular presyrinx (presyringomyelia) which may eventually form a syrinx (102, 105). Limited "low cost" imaging of CM or SM with a 3-sequence protocol of the hindbrain and cranial cervical spinal cord is offered by some institutions for dog breeders that wish to screen their breeding stock (33, 106), however this minimal protocol does not provide information about the brain or syrinx involvement of the thoracic and lumbar regions and is not recommended for the dog presented to a veterinarian for a diagnostic work of suspected CM or SM. Factors that influence the ability to make an accurate assessment of CM and SM are detailed in **Table 6**.

T2 Fluid-attenuated inversion recovery (FLAIR) imaging of the brain is a sequence which uses an inversion pulse and long echo time to suppress normal CSF signal on a heavily T2-weighted image. Pathology is suggested by high signal against background of normal signal from the brain and low or zero signal from the CSF (119). A FLAIR is not an essential part of CMSM protocol but is indicated in the assessment of acute hydrocephalus to demonstrate periventricular interstitial edema and to aid identification of any causative or associated lesion (120). FLAIR sequences are also indicated if meningoencephalomyelitis is suspected (121).

Paramagnetic contrast enhancement may be indicated especially if (i) there is evidence of a mass; (ii) if the cause of the CSF channel obstruction is not apparent; (iii) there is a presyrinx and need to eliminate other causes of spinal cord edema. Spinal intramedullary tumors may be cystic and it is important to distinguish these from SM (122, 123).

Anatomical Feature		Question	Rationale
Neural tissue	Olfactory bulbs	Size? Well-defined? Orientated rostrally?	Affected dogs are more likely to have small, ventrally orientated olfactory bulbs.
	Rostral forebrain	Rounded or flattened appearance rostrally?	Affected dogs, especially with CM pain, are more likely to have a flattened forebrain at the cribiform plate and frontal sinus.
	Whole brain conformation	If a close fitting box was drawn around the midsagittal brain, would it be a rectangle or closer to a square?	CM-pain is characterised by brachycephaly with a short skull base and a compensatory increase of height in the occipital region. As a result the "box" that would approximate the brain is closer to a "square cuboid".
	Cerebellar shape and position	Cerebellum rounded?	Affected dogs have a cerebellum that may be flattened / indented by the supraoccipital bones and/or occipitoatlantal ligament. Alternatively/additionally it may be tilted and invaginated under the occipital lobes.
		On a mid-sagittal view, is only the cerebellum rostral to the 4th ventricle and primary fissure under the occipital lobes?	
	Cerebellar herniation	Herniation caudal to the level of the ventral edge of the supraoccipital bone?	Ubiquitous in some breeds such as the CKCS.
	Medullary position and craniospinal junction conformation.	Herniation of medulla oblongata caudal to the level of the ventral edge of the supraoccipital bone?	More severe craniocervical conformational changes increase risk of SM.
		Craniospinal junction elevated/kinked through the craniocervical junction and over the dens?	
CSF spaces	Cranial subarachnoid space	Convolutions of gyri well defined by high contrast CSF on T2W images?	Narrowing of the sulci concurrently with ventriculomegaly suggests obstruction of the CSF pathways and raised intracranial pressure.
	Lateral ventricles	Dilated? Is the corpus callosum elevated and/or thinned?	Affected dogs often have dilatation of the entire ventricular system and associated cisterns. The corpus callosum is often thinned and elevated and the tectum may be thinner and at an abnormal angle affected by dilatation of the quadrageminal cistern. By contrast the intrathalamic adhesion appears normal.
	Third ventricle and velum interpositum	Dilated? Is intrathalamic adhesion normal size?	
	Quadrageminal cistern	Dilated? Is tectum position and thickness normal?	
	Mesencephalic aqueduct	Dilated?	Suggests reduced outflow through the lateral apertures.
	Fourth ventricle	Fourth ventricle a slit (normal) or triangular (dilated) in shape?	
	Cisterna magna and spinal subarachnoid space	Reduced?	Reduced cisterna magnum and spinal subarachnoid space will affect the ability to buffer the systolic pulse and the compliance of the central nervous system.
	Fluid flow void	Fluid flow void in ventricular system?	Suggest pulsatile or turbulent flow which may be associated with progressive disease (hydrocephalous or syrinx expansion).
Bony tissue	Stop and frontal sinus	Obvious stop? Frontal sinus evident?	Affected dogs appear to have a midface insufficiency with an absent / miniscule frontal sinus with a well-defined stop and a forehead that is a layer of skin, bone then brain.
	Cranial base (presphenoid, basisphenoid and basioccipital)	Short appearance?	Affected dogs have a short cranial base.
	Supraoccipital bone	Midline portion present? Appear curved caudal to a vertical line drawn though the inion of the occipital crest?	In affected dogs the supraoccipital bone may be rostral to a vertical line drawn though the inion of the occipital crest. It often appears flatter. The bone is thin and the midline portion may be missing (occipital dysplasia). With extensive occipital dysplasia the cerebellum may have a more rounded shape.
	Occipital crest	Reduced?	Affected dogs often have a reduced occipital crest.
	Atlas	On a midsagittal image, when the head is in extension, where is the rostral tip of the atlas in relationship to the inion of the occipital crest?	A line drawn between the inion of the occipital crest and the rostral atlas should be angled caudally.
	Odontoid peg and axis	On a midsagittal image, when the head is in extension, what is the angulation of the dens to a basioccipital bone?	In the normal dog there is a slight curvature of craniospinal juncton over the dens. In affected dogs there is increased angulation (cervical flexure).
Ligament	Occipitoatlantal ligament / membrane	On a midline sagittal image, is this ligament horizontal (normal) or is it vertical and indenting the cerebellar vermis?	This ligamentous indentation into the cerebellum is the classic feature of CM although many confuse this with the ventral supraoccipital bone because both are hypointense. The ligament is abnormally vertical because of the close proximity of the atlas to the skull and a short supraoccipital bone.
	Atlantoaxial bands	Dorsal impingement of the subarachnoid space at C1/C2?	Noted but significance not known.
Spinal cord	Presyrinx	Is there edema (presyrinx)?	The presyrinx is a potentially reversible myelopathy that may preced development of a syrinx. It is characterised by spinal cord oedema and enlargement with no cavitation.
	Syrinx	Has the outline of spinal cord expanded?	An expanded syrinx suggests active filling and therefore more risk of progressive disease. By contrast a syrinx that is circular on transverse images and elliptical on sagittal images with little or no change to outline of the spinal cord is more likely to be asymptomatic.
		Symmetrical on sagittal images ?	
		On transverse images, what is maximum diameter of the syrinx in the cervical, thoracic and thoracolumbar regions?	Symptomatic disease is more likely with a syrinx diameter of 4mm or more (CKCS).
		Does the syrinx location fit with the neurolocalisation (region of spinal cord and within spinal cord)?	Phantom scratching is associated with extension to the superficial dorsal horn in the C3-C6 spinal cord segments (corresponding to C2-C5 vertebrae). Cervicotorticollis / scoliosis are associated with extension of the syrinx into the superficial dorsal horn ipsilateral to the phantom scratching side and /or contralateral to the head tilt. Paresis and proprioceptive deficits are associated with large syringes in an appropriate region of the spinal cord.
		Is there dorsal horn involvement?	
		Is there fluid flow void?	Suggest pulsatile or turbulent flow (slosh effect) and increase risk of syrinx expansion.

Front. Vet. Sci. doi: 10.3389/fvets.2018.00280

FIGURE 5 | Suggested interpretation of MRI for diagnosis of CM pain and symptomatic SM—the authors' method. With the exception of the basic scoring by the CMSM health scheme (33), there is no objective measure for the diagnosis of CM pain. The diagnosis is made by exclusion and the weight of clinical and MRI evidence. Not all dogs will have all the features. The diagnosis of symptomatic SM is more objective reflecting the size and neuro-localization. For the supporting scientific justification see **Tables 1–4** however this method is also based on the authors own observations and interpretations of which the reader should take account.

TABLE 5 | Diagnostic imaging protocols for investigation of CM and SM.

Area	Sequence	Assessment of
ESSENTIAL PROTOCOL		
Brain and craniocervical junction	- **TW2 (high field) or T1W (low field) sagittal and transverse** - Maximum slice thickness 4 mm	- Conformation brain and craniocervical junction - CSF spaces - Other differential diagnoses
Cervical vertebral column	- **TW2 and T1W sagittal** - **TW2 (high field) or T1W (low field) transverse** with the block perpendicular to the spinal cord though the maximum width of the syrinx if SM is present, or as a block centred on C3 and extending from at least mid-point of the vertebral body of C2 - Maximum slice thickness 4 mm	- Presence of SM, central canal dilation, spinal cord edema (presyrinx) - Measurement of maximum transverse width SM - Spinal cord dorsal horn involvement by SM - CSF spaces including cisterna magna - Other differential diagnoses
Thoracic vertebral column	- **TW2 (high field) or T1W (low field) sagittal with or without transverse** with the block perpendicular to the spinal cord though the maximum width of the syrinx if SM is present. Maximum slice thickness 4 mm	- Presence of SM or central canal dilation - Measurement of maximum transverse width SM - Spinal cord dorsal horn involvement by SM - Subarachnoid space - Other differential diagnoses
ADDITIONAL OR ALTERNATIVE SEQUENCES		
Brain and craniocervical junction	- **Three-dimensional, T1-weighted, gradient-echo sequence (MPRAGE)** - **Maximum slice thickness 1mm.**	- Used by the authors as an alternative to T1W spin echo sagittal and transverse
	- **Fluid-attenuated inversion recovery (FLAIR)** - Maximum slice thickness 4 mm	- To assess potential periventricular hyperintensive lesions for example with acute hydrocephalous or inflammatory disease
Lumbar and lumbosacral vertebral column	- **TW2 (high field) or T1W (low field) sagittal with or without transverse** with the block perpendicular to the spinal cord though the maximum width of the syrinx if SM is present. Maximum slice thickness 4 mm	- If neurolocalization suggests and/or SM extends caudally to lumbar spinal cord and to investigate spinal cord tethering by the filum terminale if suspected
Area of suspected mass and /or spinal cord edema of unknown aetiology	- **Paramagnetic contrast**	- Cystic intramedullary tumours - Other differential diagnoses
Vertebral column	- **Half-Fourier acquisition single-shot turbo spin-echo (HASTE)**	- Used to some to make a more rapid assessment of the subarachnoid space
Area of suspected arachnoid web/band/dilatation	- **Balanced steady-state free precession sequences (bSSFP)**	- Recommended (high field)/essential (low field) to assess CSF space if arachnoid web suspected
	- **MRI flow studies (Cine MRI)**	- **Phase contrast cine MRI** - Identify region of flow abnormalities/obstruction - Prognostication - **Cine bSSFP** - Define the arachnoid webs or bands
	- **CT myelography**	- If bSSFP and/or Cine MRI has not identified or not possible because of metal implants and if owner/veterinarian wishes to pursue possible surgical management

T1W—T1-weighted, TW2—T2 weighted. It is recommended that at the time of scanning that the microchip or tattoo number (confirmed by the veterinary surgeon) is included on the DICOM images in addition to the Kennel Club registration number if the dog is registered. This is to permit submission to an official CMSM health scheme should the owner request (33). The parameters for a 1.5 T machine are detailed in ***Supplementary Table 1****.*

If the cause of CSF channel disruption is not apparent, then balanced steady-state free precession sequences (bSSFP) such as FIESTA (Fast Imaging Employing Steady-state Acquisition) or 3D-CISS (Three-Dimensional Constructive Interference in steady state) should be employed to improve detection of arachnoid webs and diverticulae (109, 124). These are a three dimensional gradient echo sequence that produces high contrast between the CSF and structures within the subarachnoid space. They have less flow void artifact associated with turbulent CSF and allow higher detection rates of arachnoid webs and other adhesions (102, 125) (**Figure 6**) and for low field MRI where obtaining good signal-to-noise and spatial resolution is a challenge, it is recommended that a bSSFP sequence be included in any protocol that evaluates the CSF channels (or disruption of) (109). Half-Fourier acquisition single-shot turbo spin-echo (HASTE) sequences are heavily T2W sequences that produced a myelographic effect and can be obtained in a very short time. They are also described as being useful to detect arachnoid diverticulae (126). However, the trade-off for such short imaging times is lower spatial resolution and T2 blurring artifact.

MRI flow studies are an integral part of the diagnostic work up of CM and SM in human patients (14, 102) and for review of the clinical application for SM, arachnoid webs and the subarachnoid space see Li et al. (104). Standard MRI sequences of the brain and spinal cord assume that the tissue is static with movement only occurring in blood vessels and

TABLE 6 | Factors that influence the ability of make an accurate assessment of CM and SM on MRI.

Type	Example	Notes
Protocol	Slice thickness	In the sagittal plane thinner slices (3 mm or less) are preferred to achieve 2–3 sections through the spinal canal and more chance of lesion detection. Thicker slice thickness may miss a small intramedullary lesion in an dog with a spinal cord diameter ranging between 4.1 and 10.3 mm (depending on site imaged and size of animal) (107, 108). However, MRI machines of 1 Tesla or less cannot provide thin slices with sufficient signal-to-noise ratio. Using a balanced steady state feed precession sequence (bSSFP) in addition to a conventional gradient echo and spin echo sequences may help overcome this challenge (109).
	Sequence	Protocols that achieve both T1W and T2W weighting are required to be confident in detecting a fluid filled cavity within the spinal cord and conformational changes with CM. Anatomical imaging of the entire brain is recommended and full extent of the syrinx should be determined Transverse images perpendicular to the spinal cord though the syrinx are required to assess the transverse width and extent of spinal cord involvement.
Magnetic field strength	Low field vs. high field	Signal-to-noise ratio and spatial resolution is improved when imaging with higher magnetic field-strength which allows shorter imaging times for a given resolution and/or higher resolution for a given imaging time. In addition, higher signal-to-noise ratio allows better resolution with smaller voxel size and thinner slice thickness (110).
Operator factors	Inexperience/lack of training	In veterinary medicine it is possible to operate a MRI service without any Specialist qualification. By contrast an experience MRI technician has undertaken a 3–4 year radiography degree plus additional post-graduate MRI training.
	Diligence	Out with other reasons for decreasing imaging time (economic/duration of anesthesia), operator inclination is a factor for example image quality can be improved by increasing the number of averages (NEX/NSA) which will subsequently increase the acquisition time.
Interpreter factors	Inexperience/lack of training	Failure to recognize significant lesions or over-interpretation of other features for example attributing SM to epilepsy, facial nerve paralysis, fly catching and other brain disorders or interpreting a generalized pruritus as due to SM. In humans it is reported more likely that a cervical syrinx is missed with techniques for whole spine sagittal scanning with focused lumbar spinal MRI where the physician is biased from the history for a lumbar lesion (111). Conversely, asymptomatic localized widening of the central canal may be observed in both humans and dogs (34, 112).
Patient factors	Skull and air interface	May cause susceptibility artifacts, especially on gradient echo sequences.
	Small brain and narrow spinal cord	Slice thickness should be proportional to the brain volume to achieve images with diagnostic quality i.e., animals with smaller brain volume require thinner slices. In a low field MRI this may be challenging and a bSSFP sequence is recommended.
	Positioning	Assessment for CM is normally obtained with the head in extension as reproducibility is easier and anesthesia is safer as the airway may be compromised in the flexed position (33). However, cerebellar herniation and CSF space between the cerebellum and brainstem are significantly increased in the flexed position (113).
	Microchips, orthopedic implants and shrapnel	Ferromagnetic materials cause susceptibility artifacts which may compromise interpretation especially identity microchips for studies of the cervical spine. In low field MRI a T1W turbospin echo sequence is recommended (114) and for high field MRI, spin echo sequences have smaller artifacts than gradient echo sequences (115). Titanium or oxidized zirconium implants have less susceptibly artifact than cobalt-chromium alloy implants (116)
	General anesthetic	Increased time under general anesthesia may increase risk to patient and cost thus limiting length of any MRI protocol.
Motion related artifacts	Neural tissue	Standard MRI sequences are optimized for good spatial and contrast resolution, however this results in blurring of moving structures which compromises the ability to detect fine structures such as arachnoid webs and other adhesions, septations in the syrinx or appreciate dynamic compression (104). It may also blur the edges of a syrinx cavity.
	Intrasyringeal fluid flow void	Pulsatile or turbulent motion of fluid within the syrinx produces low signal on T2W images because of an absence of activated protons in that region (117)
	Intraventricular CSF pulsation artifact	Intraventricular hyperintensity on FLAIR imaging which result in false—negative/positive interpretations of ventricular pathology and is a particular problem for FLAIR performed on low field MRI (118). The most common cause is pulsatile movement and un-inverted CSF flowing into the slice between the pulses (119). It can also occur because of inadequate inversion of CSF magnetization at the edge of the transmitted coil or because of increased CSF protein or oxygen (breathing 100% oxygen) which shortens T1 (119).

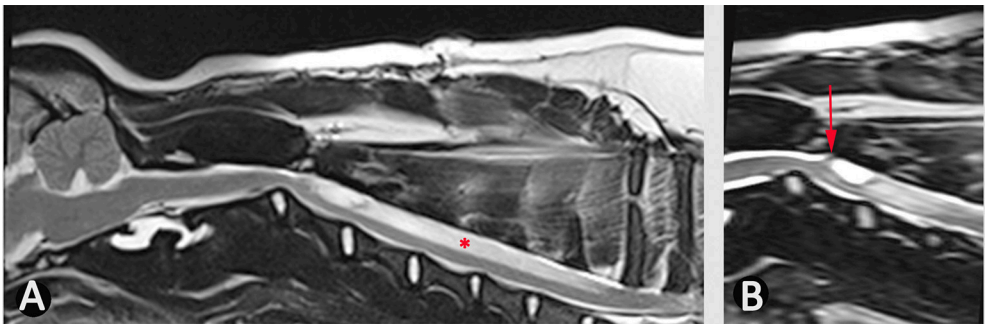

FIGURE 6 | Use of bSSFP (3D CISS) to identify a spinal cord adhesion in an 18 month old male Pug dog presented with signs of cervical myelopathy. This dog had previously been managed surgically for a spinal arachnoid diverticulum at the level of C2/C3 (age 5 months). **(A)** T2-weighted mid-sagittal MRI of the hind brain and cervical spinal cord **(B)** mid-sagittal 3D-CISS image at the level of C2–C4. There is a syrinx between C3 and C7 (asterisk). The 3D-CISS image highlights the likely cause of this syrinx as an adhesion between the spinal cord and laminectomy site (arrow) (Siemens Magnetom Symphony, A Tim System, 1.5 T, Erlangen, Germany).

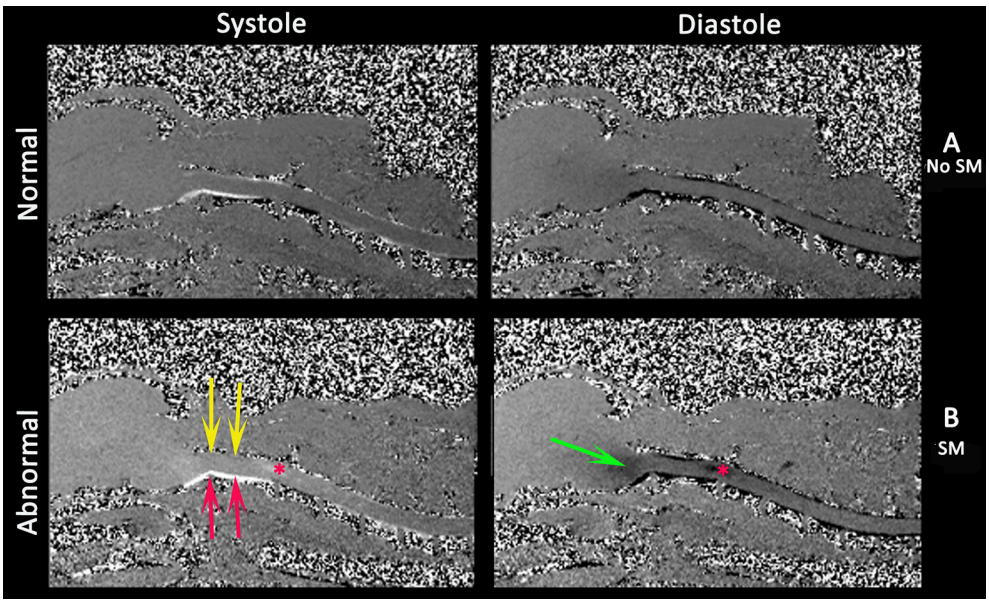

FIGURE 7 | Phase contrast cine MRI of the brain and cervical spinal cord in normal **(A)** and a CMSM affected CKCS **(B)**. Left systole, right diastole. Compared to normal **(A)**, the SM affected **(B)** has little caudal flow in the dorsal cervical subarachnoid space (yellow arrows) and by contrast high velocity flow in the ventral cervical subarachnoid space (red arrows). There is pulsatile flow in the syrinx at the level of C2/C3 (asterisk) and fluid entering the medulla parenchyma (green arrows) (Siemens Symphony Tim system, 1.5 T, Enlangen Germany).

CSF and the aim is to achieve higher spatial and contrast resolution typically at the expense of temporal resolution. This results in motion-related blurring of non-static structures (104). Cine MRI uses cardiac gating using electrocardiogram or pulse oximetry. Phase-contrast cine MRI (**Figure 7**) measures pulsatile CSF motion influenced by the cardiac cycle and can measure both CSF and syrinx fluid velocities in a defined area of interest (102, 127). By contrast cine bSSFP allows appreciation of the movement of the central nervous system and structures within the subarachnoid space. The data for a single slice is acquired multiple times over the cardiac cycle with each single image corresponding to single point in that cycle (termed a cardiac phase). All the images are then viewed sequentially as a cine loop (104). Phase contrast cine MRI is used to localize CSF channel obstruction, to demonstrate improvement (or lack thereof) post operatively and also has a role in prognostication. Syrinx fluid movement, as detected by phase contrast cine MRI, is associated with progressive neurological signs whereas lack of syrinx fluid movement is associated with no or stable neurological signs (102, 128). However, it does not allow visualization of arachnoid membranes and so in humans, and for investigation of idiopathic SM, Phase contrast cine MRI is used to localize the area of flow abnormalities/obstruction and cine bSSFP is used to define the arachnoid webs or bands (104).

In veterinary medicine, phase contrast cine MRI has been used to investigate CSF flow (80) and cine bSSFP used to investigate

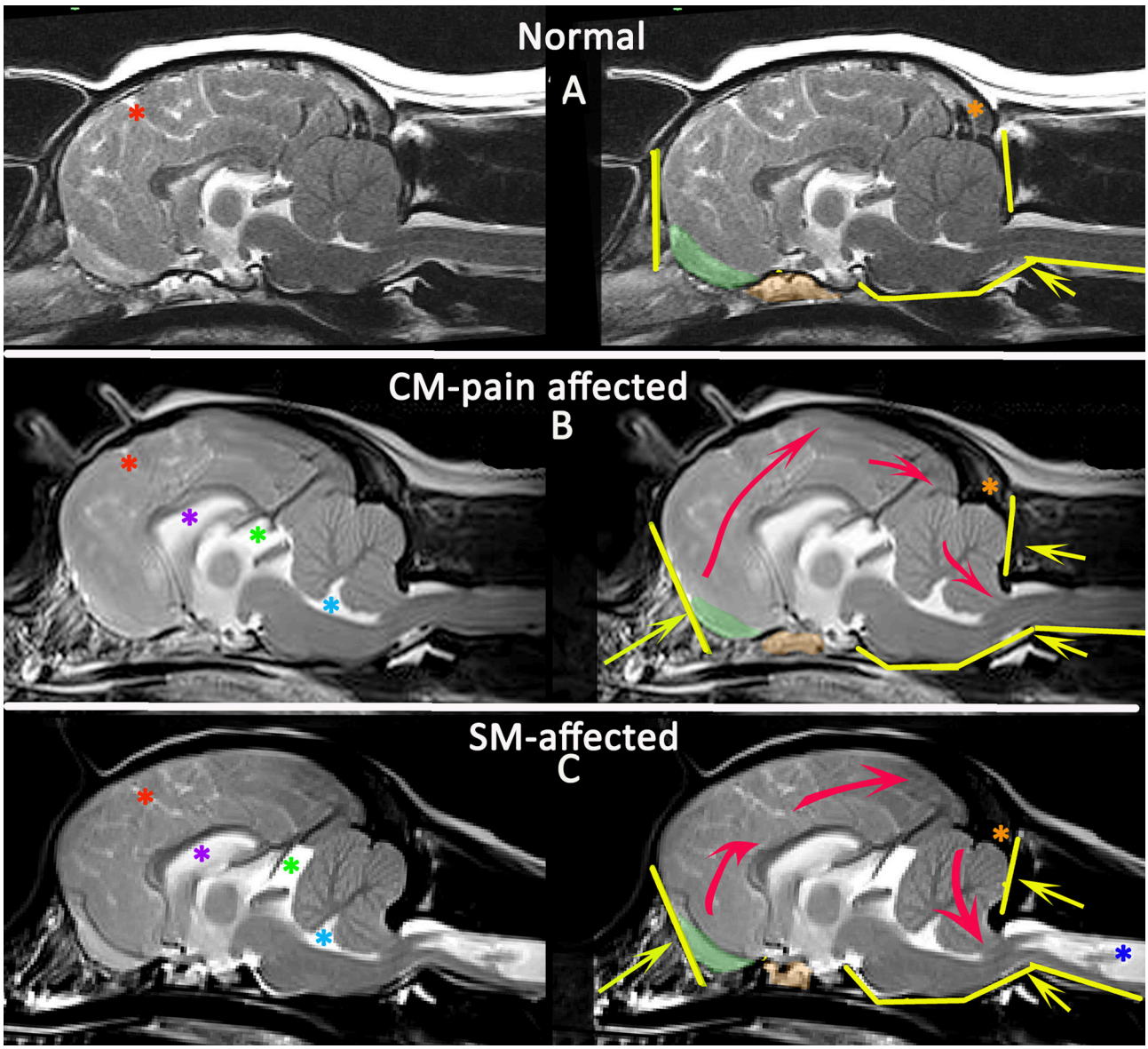

FIGURE 8 | Morphometric changes in CMSM. Mid-sagittal T2-weighted brain MRI of three CKCS: normal **(A)**, CM-pain affected **(B)**, and SM-affected **(C)**. The left column compares the CSF spaces. There is effacement of the cranial subarachnoid spaces evidenced by reduced definition of the sulci filled with high signal CSF in affected dogs **(B,C)**. A Red asterisk highlights the cruciate sulcus for comparison. In addition there is ventriculomegaly with dilatation of the lateral ventricle (purple asterisk), third ventricle and quadrigeminal cistern (green asterisk) and fourth ventricle (aqua asterisk). The right column compares the neuro-anatomical changes and also the direction in which the neuroparenchyma has been deformed and crowded by the bony restrictions. Compared to the normal CKCS **(A)**, the affected CKCS **(B,C)** are more brachycephalic with shortening of the basicranium and prephenoid bone (orange shading) with reduced and more ventrally orientated olfactory bulbs (green shading). The rostral forebrain is flattened in **(B,C)** and the rostrotentorial neuroparenchyma is displaced dorsocaudally giving increased height to the cranium particularly in **(B)**. This reduces the functional caudotentorial space contributing to the hindbrain herniation. The atlas is closer to the skull and supraoccipital bone is flattened, particularly in **(C)**, the SM-affected dog which also has a reduction of the occipital crest (orange asterisk). In addition to the brachycephaly, the SM affected dog has further compromise of the craniocervical junction by a cervical flexure and acute angulation of the odontoid peg resulting in kinking/ elevation of the craniospinal junction. The syrinx is indicated by the dark blue asterisk (Siemens Magnetom Symphony, A Tim System, 1.5 T, Erlangen, Germany).

cerebellar movement (76) (**Table 3**) but its application as a diagnostic tool has yet to be realized.

To make a diagnosis of symptomatic CM and or SM the diagnostic imaging should be related to the clinical history and examination findings.

DIAGNOSIS OF CM-PAIN

CM-pain is a difficult diagnosis because the clinical signs are non-specific and/or have alternative explanations but should be considered in a predisposed breed presenting with a signs

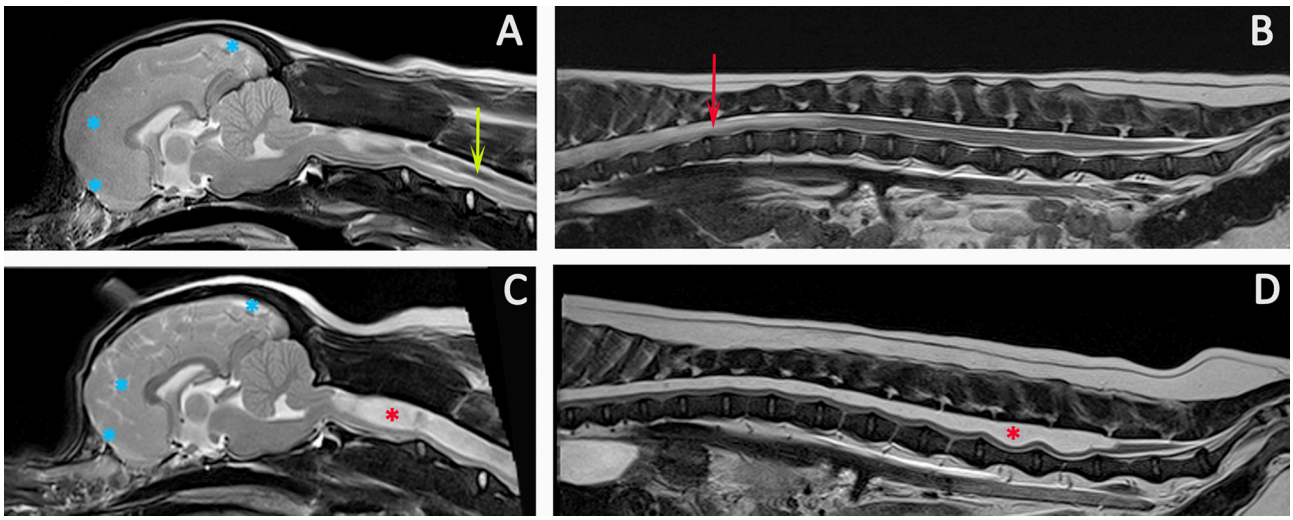

FIGURE 9 | Progression of SM. Diagnostic Imaging of a female CKCS at 8 months old **(A,B)** and 3 years old **(C,D).** The CKCS was originally presented with signs of pain. When represented at 3 years of age, the signs of pain were no longer controlled by medication and she had mild thoracic limb hypermetria, tetraparesis, and pelvic limb ataxia. T2-weighted mid-sagittal MRI of the brain and cranial cervical spinal cord in a CM and SM affected CKCS **(A)** 8 months, **(C)** 3 years old T2-weighted mid-sagittal MRI of the vertebral column from T7 to Cy1 **(B)** 8 months, **(D)** 3 years old. **(A,B)** Imaging indicated risk of progressive SM with loss of the cranial subarachnoid space and effacement of the cranial sulci (blue asterisks), fluid signal-void sign within the syrinx suggesting pulsatile or turbulent flow (green arrow) and a pre-syrinx (oedema) and central canal dilatation in the caudal thoracic spinal cord (red arrow). **(C,D)** The syrinx has progressed to holocord SM (red asterisk). Although conclusions cannot be drawn without pressure measurements, it is interesting that MRI signs that can suggest elevated intra-cranial pressure (129) and fluid surging and pulsation within the syrinx (117) are diminished with an appreciably greater cranial subarachnoid space indicated by high signal CSF within the sulci (blue asterisks) and less fluid signal-void sign within the syrinx (Siemens Magnetom Symphony, A Tim System, 1.5 T, Erlangen, Germany).

suggesting pain such as; a history of vocalization described as without obvious trigger, when shifting position when recumbent and when being lifted under the sternum to a height; spinal pain; head and ear rubbing or scratching; refusal or difficulty jumping or doing stairs; exercise intolerance/reduced activity; sleep disruption; or behavioral change described as becoming more anxious, aggressive, or withdrawn (48). Morphometric studies found CM pain was associated with increasing brachycephaly with shortening of the skull base with rostrotentorial overcrowding resulting in rostral flattening of the forebrain, reduction and ventral displacement of the olfactory bulbs and increased height of the cranium, especially in the occipital region (39). There may be changes suggesting obstruction of CSF channels including reduction in the cranial and spinal subarachnoid space in addition to ventriculomegaly of all ventricles and cisterns except the cisterna magna which is often reduced (**Figure 7**). The craniocervical changes are less pronounced than in SM affected dogs and indeed this feature is hypothesized to protect this cohort from developing SM (39). Ultimately the diagnosis must be made by ruling out other causes of pain in combination with consistent clinical and MRI findings. A guide is suggested in **Figures 5**, **8**.

DIAGNOSIS OF SYMPTOMATIC SM

The diagnosis of SM implies a fluid filled cavity related to disturbance of CSF flow, spinal cord tethering or intramedullary tumor; it is not an appropriate description for myelomalacia or cystic lesions (14). SM can be asymptomatic (34) and when interpreting MRI, an assessment should be made as to whether the location and severity of the syrinx would account for the signs. Signs of an "active" and filling syrinx include fluid signal-void sign within the syrinx cavity indicating pulsatile or turbulent flow, hypothesized to be a cause of syrinx propagation (117) (**Figure 9**).

In addition an active and filling syrinx is expansive within the spinal cord and generally has an asymmetrical shape on transverse images. By contrast a quiescent syrinx is centrally located, elliptical on sagittal images and symmetrical, usually circular on transverse images and results in little or no change to the outline of the spinal cord (87, 130). Symptomatic SM results in a myelopathy and therefore is suggested by sensory and motor signs that localize to the level of the spinal cord affected by the syrinx. However, gait disturbances may be surprisingly mild even with extensive SM. The dog in **Figure 9** was presented with a mild pelvic limb ataxia, thoracic limb hypermetria and tetraparesis and was considered by the owner to have a normal exercise tolerance. If the clinical signs are disproportionate to the extent of the syrinx, other differentials should be explored for example degenerative myelopathy related to superoxide dismutase-1 mutation as a cause of pelvic limb paresis (48, 131). The maximum width of the syrinx on transverse images should be assessed; myelopathic signs in CKCS are associated with a syrinx transverse width of 4 mm or more whereas phantom scratching and cervicotorticollis/scoliosis are associated with extension of the syrinx into the superficial dorsal horn ipsilateral to the phantom scratching side and/or

contralateral to the head tilt (48, 87). Phantom scratching is associated with extension to the superficial dorsal horn ipsilateral to the scratching side in the C3-C6 spinal cord segments (corresponding to C2-C5 vertebrae) (88). A guide is suggested in **Figures 5**, **8**.

CONCLUSION

Diagnosis of CM-pain is made by appropriate clinical signs in addition to MRI brain findings of a brachycephaly with rostrotentorial crowding including rostral flattening, olfactory bulb reduction and rotation, increased height of the cranium with reduction of the functional caudotentorial space and hindbrain herniation. There may also be changes suggesting raised intracranial pressure such as loss of sulci definition with ventriculomegaly. The cisterna magna is reduced. In addition to these brachycephalic changes, dogs with SM are more likely to have craniocervical junction abnormalities including rostral displacement of the axis and atlas with increased odontoid angulation causing craniospinal deformation and medullary oblongata elevation. Symptomatic SM is diagnosed on the basis of signs of myelopathy and presence of a large syrinx that is consistent with the neuro-localization. The imaging protocol should establish the longitudinal and transverse extent of the syrinx. If the cause of CSF channel disruption is not revealed by anatomical MRI then other imaging techniques such as bSSFP sequences may be appropriate.

AUTHOR CONTRIBUTIONS

CR: concept and original draft. FS: editing and reviewing draft. SK: graphics, editing, and reviewing draft.

ACKNOWLEDGMENTS

The authors wish to acknowledge the considerable skill and dedication of the radiography and neurology teams at Fitzpatrick Referrals.

SUPPLEMENTARY MATERIAL

The Supplementary Material for this article can be found online at: https://www.frontiersin.org/articles/10.3389/fvets.2018.00280/full#supplementary-material

Supplementary Table 1 | MRI parameters for a CM and SM specific protocol on a 1.5T machine.

Supplementary Figure 1 | Duplicate of **Figure 5** with a higher resolution.

REFERENCES

1. Knowler SP, Galea GL, Rusbridge C. Morphogenesis of canine chiari malformation and secondary syringomyelia: disorders of cerebrospinal fluid circulation. *Front Vet Sci.* (2018) 5:171. doi: 10.3389/fvets.2018.00171
2. Cappello R, Rusbridge C. Report from the Chiari-Like Malformation and Syringomyelia Working Group round table. *Vet Surg.* (2007) 36:509–12. doi: 10.1111/j.1532-950X.2007.00298.x
3. Chiari H. Ueber Veränderungen des Kleinhirns infolge von Hydrocephalie des Grosshirns. *Dtsch Med Wochenschir.* (1891) 42:1172–5. doi: 10.1055/s-0029-1206803
4. Rusbridge C, Flint G. (eds). Nomenclature. In: *Syringomyelia: A Disorder of CSF Circulation*. Berlin; Heidelberg: Springer (2014).p. 301–9. doi: 10.1007/978-3-642-13706-8_20
5. Chiari H. Ueber Veränderungen des Kleinhirns, des Pons and der medulla oblongata in Folge von genitaler Hydrocephalie des Grosshirns. *Denkschr Akad Wiss Wien* (1896) 63:71–116.
6. Azahraa Haddad F, Qaisi I, Joudeh N, Dajani H, Jumah F, Elmashala A, et al. The newer classifications of the chiari malformations with clarifications: an anatomical review. *Clin Anat.* (2018) 31:314–22. doi: 10.1002/ca.23051
7. Milhorat TH, Chou MW, Trinidad EM, Kula RW, Mandell M, Wolpert C, et al. Chiari I malformation redefined: clinical and radiographic findings for 364 symptomatic patients. *Neurosurgery* (1999) 44:1005–17. doi: 10.1097/00006123-199905000-00042
8. Cinalli G, Spennato P, Sainte-Rose C, Arnaud E, Aliberti F, Brunelle F, et al. Chiari malformation in craniosynostosis. *Childs Nerv Syst.* (2005) 21:889–901. doi: 10.1007/s00381-004-1115-z
9. Milhorat TH, Bolognese PA, Nishikawa M, Mcdonnell NB, Francomano CA. Syndrome of occipitoatlantoaxial hypermobility, cranial settling, and chiari malformation type I in patients with hereditary disorders of connective tissue. *J Neurosurg Spine* (2007) 7:601–9. doi: 10.3171/SPI-07/12/601
10. Milhorat TH, Nishikawa M, Kula RW, Dlugacz YD. Mechanisms of cerebellar tonsil herniation in patients with Chiari malformations as guide to clinical management. *Acta Neurochir.* (2010) 152:1117–27. doi: 10.1007/s00701-010-0636-3
11. Bejjani GK. Association of the Adult Chiari Malformation and Idiopathic Intracranial Hypertension: more than a coincidence. *Med Hypotheses* (2003) 60:859–63. doi: 10.1016/S0306-9877(03)00064-1
12. Richard S, Humbertjean L, Mione G, Braun M, Schmitt E, Colnat-Coulbois S. Syringomyelia caused by traumatic intracranial hypotension: case report and literature review. *World Neurosurg.* (2016) 91:674–8 e613. doi: 10.1016/j.wneu.2016.04.062
13. Brodbelt A. The Biochemistry of Syringomyelia. In: Flint G, Rusbridge C, editors. *Syringomyelia: A Disorder of CSF Circulation.* Berlin; Heidelberg: Springer (2014).p. 261–78.
14. Klekamp J. How should syringomyelia be defined and diagnosed? *World Neurosurg.* (2018) 111:e729–e745. doi: 10.1016/j.wneu.2017.12.156
15. Da Costa RC, Parent JM, Poma R, Duque MC. Cervical syringohydromyelia secondary to a brainstem tumor in a dog. *J Am Vet Med Assoc.* (2004) 225:1061–64, 1048. doi: 10.2460/javma.2004.225.1061
16. Jung DI, Park C, Kang BT, Kim JW, Kim HJ, Lim CY, et al. Acquired cervical syringomyelia secondary to a brainstem meningioma in a maltese dog. *J Vet Med Sci.* (2006) 68:1235–8. doi: 10.1292/jvms.68.1235
17. Mackillop E, Schatzberg SJ, De Lahunta A. Intracranial epidermoid cyst and syringohydromyelia in a dog. *Vet Radiol Ultrasound* (2006) 47:339–44. doi: 10.1111/j.1740-8261.2006.00150.x
18. Szabo D, Saveraid TC, Rodenas S. Cervicothoracic syringohydromyelia associated with a prosencephalic mass in a dog. *J Small Anim Pract.* (2012) 53:613–7. doi: 10.1111/j.1748-5827.2012.01266.x
19. Oxley W, Pink J. Amelioration of caudal thoracic syringohydromyelia following surgical management of an adjacent arachnoid cyst. *J Small Anim Pract.* (2012) 53:67–72. doi: 10.1111/j.1748-5827.2011.01146.x
20. Rohdin C, Nyman HT, Wohlsein P, Hultin Jaderlund K. Cervical spinal intradural arachnoid cysts in related, young pugs. *J Small Anim Pract.* (2014) 55:229–34. doi: 10.1111/jsap.12167
21. Kiviranta AM, Lappalainen AK, Hagner K, Jokinen T. Dermoid sinus and spina bifida in three dogs and a cat. *J Small Anim Pract.* (2011) 52:319–24. doi: 10.1111/j.1748-5827.2011.01062.x
22. Ollivier D'angers, C.-P. *De la Moelle Épinière et de Ses Maladies*. Paris: Crevot (1824).

23. Ollivier D'angers, C-P. *Traité des Maladies de la Moelle Épinière Contenant l'Histoire Anatomique, Physiologique et Pathologique de ce Centre Nerveux Chez l'Homme*. Paris: Crevot (1827).
24. Schuppel. Über Hydromyelus. *Arch Heilk* (1865) 6:289.
25. Simon T. Über Syringomyelia und Geshwulstbildung im Rückenmark. *Arch. Psychiat. NervenKrank* (1875) 5, 120–163.
26. Newton EJ. Syringomyelia as a manifestation of defective fourth ventricular drainage. *Ann R Coll Surg Engl.* (1969) 44:194–213.
27. Leyden E. Über Hydromyelus un Syringomyelie. *Arch Pathol Anat Physiol.* (1876) 68:1–20. doi: 10.1007/BF01879533
28. Kahler O, Pick A. Beitrag zur Lehre von der Syringo-und Hydromyelia. *Vjschr Prakt Heilkd.* (1879) 142:20–41.
29. Hogg JP, Peterson AM, El-Kadi M. Imaging of cranial and spinal cerebrospinal fluid collections. In: Kaufman HH, editor. *Cerebrospinal Fluid Collections.* San Francisco, CA: American Association of Neurological Surgeons (1998), pp. 19-56.
30. Chiari H. Ueber die Pathogenese der Sogenannten Syringomyelie. (Hierzu Tafal 13.). *Zeitschrift für Heilkunde* (1888) 9, 307.
31. Radojicic M, Nistor G, Keirstead HS. Ascending central canal dilation and progressive ependymal disruption in a contusion model of rodent chronic spinal cord injury. *BMC Neurol* (2007) 7:30. doi: 10.1186/1471-2377-7-30
32. Hu HZ, Rusbridge C, Constantino-Casas F, Jeffery N. Histopathological investigation of syringomyelia in the Cavalier King Charles Spaniel. *J Comp Pathol.* (2012) 146:192–201. doi: 10.1016/j.jcpa.2011.07.002
33. Bva T. *Chiari Malformation/Syringomyelia Scheme (CM/SM Scheme)* [Online] (2013). Available online at: http://www.bva.co.uk/canine_health_schemes/ChiariMalformationSyringomyeliaSchemeCMSMScheme.aspx: British Veterinary Assocication (Accessed July, 8 2013).
34. Parker JE, Knowler SP, Rusbridge C, Noorman E, Jeffery ND. Prevalence of asymptomatic syringomyelia in Cavalier King Charles spaniels. *Vet Rec.* (2011) 168:667. doi: 10.1136/vr.d1726
35. Wijnrocx K, Van Bruggen LWL, Eggelmeijer W, Noorman E, Jacques A, Buys N., et al. Twelve years of chiari-like malformation and syringomyelia scanning in Cavalier King Charles Spaniels in the Netherlands: towards a more precise phenotype. *PLoS ONE* (2017) 12:e0184893. doi: 10.1371/journal.pone.0184893
36. Rusbridge C. Chiari–like malformation and syringomyelia. *Eur J Compan Anim. Pract* (2013) 23:70–89. Available online at: http://www.ejcap.org/issues/ejcap-233-autumn-2013/
37. Sparks CR, Cerda-Gonzalez S, Griffith EH, Lascelles BDX, Olby NJ. Questionnaire-based analysis of owner-reported scratching and pain signs in cavalier king charles spaniels screened for chiari-like malformation and syringomyelia. *J Vet Intern Med.* (2018) 32:331–9. doi: 10.1111/jvim.14856
38. Knowler SP, Mcfadyen AK, Freeman C, Kent M, Platt SR, Kibar Z, et al. Quantitative analysis of Chiari-like malformation and syringomyelia in the griffon bruxellois dog. *PLoS ONE* (2014) 9:e88120. doi: 10.1371/journal.pone.0088120
39. Knowler SP, Cross C, Griffiths S, Mcfadyen AK, Jovanovik J, Tauro A, et al. Use of morphometric mapping to characterise symptomatic chiari-like malformation, secondary syringomyelia and associated brachycephaly in the cavalier king charles spaniel. *PLoS ONE* (2017) 12:e0170315. doi: 10.1371/journal.pone.0170315
40. Knowler SP, Kiviranta AM, Mcfadyen AK, Jokinen TS, La Ragione RM, Rusbridge C. Craniometric analysis of the hindbrain and craniocervical junction of chihuahua, affenpinscher and cavalier king charles spaniel dogs with and without syringomyelia secondary to chiari-like malformation. *PLoS ONE* (2017) 12:e0169898. doi: 10.1371/journal.pone.0169898
41. Lemay P, Knowler SP, Bouasker S, Nedelec Y, Platt S, Freeman C, et al. Quantitative Trait Loci (QTL) study identifies novel genomic regions associated to chiari-like malformation in griffon bruxellois dogs. *PLoS ONE* (2014) 9:e89816. doi: 10.1371/journal.pone.0089816
42. Ancot F, Lemay P, Knowler SP, Kennedy K, Griffiths S, Cherubini GB, et al. A genome-wide association study identifies candidate loci associated to syringomyelia secondary to Chiari-like malformation in Cavalier King Charles Spaniels. *BMC Genet* (2018) 19:16. doi: 10.1186/s12863-018-0605-z
43. Spiteri M, Knowler SP, Wells K, Rusbridge C. Mapping morphological change in cavalier king charles spaniels with syringomyelia using novel machine learning approach. In: *30th Symposium ESVN-ECVN,* Helsinki (2017).
44. Spiteri M, Knowler SP, Wells K, Rusbridge C. Mapping Morphological Change in Cavalier King Charles Spaniels With Chiari-like malformation associated pain. In: *30th Symposium ESVN-ECVN*, Helsinki (2017).
45. Thofner MS, Stougaard CL, Westrup U, Madry AA, Knudsen CS, Berg H, et al. Prevalence and heritability of symptomatic syringomyelia in Cavalier King Charles Spaniels and long-term outcome in symptomatic and asymptomatic littermates. *J Vet Intern Med.* (2015) 29:243–50. doi: 10.1111/jvim.12475
46. Schulze S, Refai M, Deutschland M, Failing K, Schmidt M. Prevalence of syringomyelia in clinically unaffected Cavalier King Charles Spaniels in Germany (2006-2016). *Tierarztl Prax Ausg K Kleintiere Heimtiere* (2018) 46:157–62. doi: 10.15654/TPK-170725
47. Kiviranta AM, Rusbridge C, Laitinen-Vapaavuori O, Hielm-Bjorkman A, Lappalainen AK, Knowler SP, et al. Syringomyelia and Craniocervical Junction Abnormalities in Chihuahuas. *J Vet Intern Med.* (2017) 31:1771–81. doi: 10.1111/jvim.14826
48. Rusbridge C. Behavioural and clinical signs of Chiari-like malformation and syringomyelia in Cavalier King Charles spaniels. In: Murphy S, editor. *BSAVA Congress 2018.* Birmingham: British Small Animal Veterinary Association (2018). p. 430.
49. Stockyard CR. The genetic and endocrinic basis for differences in form and behaviour. In: *Anatomical Memoirs* (Philadelphia, PA: Wistar Institute of Anatomy and Biology) (1941).p. 340–57.
50. Schmidt MJ, Volk H, Klingler M, Failing K, Kramer M, Ondreka N. Comparison of closure times for cranial base synchondroses in mesaticephalic, brachycephalic, and cavalier king charles spaniel dogs. *Vet Radiol Ultrasound* (2013) 54:497–503. doi: 10.1111/vru.12072
51. Schmidt MJ, Neumann AC, Amort KH, Failing K, Kramer M. Cephalometric measurements and determination of general skull type of Cavalier King Charles Spaniels. *Vet Radiol Ultrasound* (2011) 52:436–40. doi: 10.1111/j.1740-8261.2011.01825.x
52. Rusbridge C, Knowler SP, Pieterse L, Mcfadyen AK. Chiari-like malformation in the Griffon Bruxellois. *J Small Anim Pract.* (2009) 50:386–93. doi: 10.1111/j.1748-5827.2009.00744.x
53. Mitchell TJ, Knowler SP, Van Den Berg H, Sykes J, Rusbridge C. Syringomyelia: determining risk and protective factors in the conformation of the Cavalier King Charles Spaniel dog. *Canine Genet Epidemiol.* (2014) 1:9. doi: 10.1186/2052-6687-1-9
54. Dubrul EL, Laskin DM. Preadaptive potentialities of the mammalian skull: an experiment in growth and form. *Am J Anat.* (1961) 109:117–32. doi: 10.1002/aja.1001090203
55. Scrivani PV, Thompson MS, Winegardner KR, Dewey CW, Scarlett JM. Association between frontal-sinus size and syringohydromyelia in small-breed dogs. *Am J Vet Res.* (2007) 68:610–3. doi: 10.2460/ajvr.68.6.610
56. Carrera I, Dennis R, Mellor DJ, Penderis J, Sullivan M. Use of magnetic resonance imaging for morphometric analysis of the caudal cranial fossa in Cavalier King Charles Spaniels. *Am J Vet Res.* (2009) 70:340–5. doi: 10.2460/ajvr.70.3.340
57. Driver CJ, Rusbridge C, Cross HR, Mcgonnell I, Volk HA. Relationship of brain parenchyma within the caudal cranial fossa and ventricle size to syringomyelia in cavalier King Charles spaniels. *J Small Anim Pract.* (2010) 51:382–6. doi: 10.1111/j.1748-5827.2010.00952.x
58. Shaw TA, Mcgonnell IM, Driver CJ, Rusbridge C, Volk HA. Caudal cranial fossa partitioning in Cavalier King Charles spaniels. *Vet Rec.* (2013) 172:341. doi: 10.1136/vr.101082
59. Schmidt MJ, Kramer M, Ondreka N. Comparison of the relative occipital bone volume between Cavalier King Charles spaniels with and without syringohydromyelia and French bulldogs. *Vet Radiol Ultrasound* (2012) 53:540–4. doi: 10.1111/j.1740-8261.2012.01955.x
60. Schmidt MJ, Ondreka N, Rummel C, Volk H, Sauerbrey M, Kramer M. Volume reduction of the jugular foramina in Cavalier King Charles Spaniels with syringomyelia. *BMC Vet Res.* (2012) 8:158. doi: 10.1186/1746-6148-8-158
61. Fenn J, Schmidt MJ, Simpson H, Driver CJ, Volk HA. Venous sinus volume in the caudal cranial fossa in Cavalier King Charles spaniels with syringomyelia. *Vet J.* (2013) 197:896–7. doi: 10.1016/j.tvjl.2013.05.007

62. Cerda-Gonzalez S, Olby NJ, Mccullough S, Pease AP, Broadstone R, Osborne JA. Morphology of the caudal fossa in Cavalier King Charles Spaniels. *Vet Radiol Ultrasound* (2009) 50:37–46. doi: 10.1111/j.1740-8261.2008.01487.x
63. Marino DJ, Loughin CA, Dewey CW, Marino LJ, Sackman JJ, Lesser ML, et al. Morphometric features of the craniocervical junction region in dogs with suspected Chiari-like malformation determined by combined use of magnetic resonance imaging and computed tomography. *Am J Vet Res.* (2012) 73:105–11. doi: 10.2460/ajvr.73.1.105
64. Cerda-Gonzalez S, Bibi KF, Gifford AT, Mudrak EL, Scrivani PV. Magnetic resonance imaging-based measures of atlas position: Relationship to canine atlantooccipital overlapping, syringomyelia and clinical signs. *Vet J.* (2016) 209:133–8. doi: 10.1016/j.tvjl.2016.01.008
65. Cerda-Gonzalez S, Dewey CW, Scrivani PV, Kline KL. Imaging features of atlanto-occipital overlapping in dogs. *Vet Radiol Ultrasound* (2009) 50:264–8. doi: 10.1111/j.1740-8261.2009.01531.x
66. Cerda-Gonzalez S, Olby NJ, Griffith EH. Dorsal compressive atlantoaxial bands and the craniocervical junction syndrome: association with clinical signs and syringomyelia in mature cavalier king charles spaniels. *J Vet Intern Med.* (2015) 29:887–92. doi: 10.1111/jvim.12604
67. Carruthers H, Rusbridge C, Dube MP, Holmes M, Jeffery N. Association between cervical and intracranial dimensions and syringomyelia in the cavalier King Charles spaniel. *J Small Anim Pract.* (2009) 50:394–8. doi: 10.1111/j.1748-5827.2009.00768.x
68. Stalin CE, Rusbridge C, Granger N, Jeffery ND. Radiographic morphology of the cranial portion of the cervical vertebral column in Cavalier King Charles Spaniels and its relationship to syringomyelia. *Am J Vet Res.* (2008) 69:89–93. doi: 10.2460/ajvr.69.1.89
69. Cross HR, Cappello R, Rusbridge C. Comparison of cerebral cranium volumes between cavalier King Charles spaniels with Chiari-like malformation, small breed dogs and Labradors. *J Small Anim Pract.* (2009) 50:399–405. doi: 10.1111/j.1748-5827.2009.00799.x
70. Driver CJ, Rusbridge C, Cross HR, Mcgonnell I, Volk HA. Association between Chiari-like malformation and syringomyelia in cavalier King Charles spaniels. *Vet Rec.* (2010) 167:306. doi: 10.1136/vr.167.8.306-a
71. Shaw TA, Mcgonnell IM, Driver CJ, Rusbridge C, Volk HA. Increase in cerebellar volume in Cavalier King Charles Spaniels with Chiari-like malformation and its role in the development of syringomyelia. *PLoS ONE* (2012) 7:e33660. doi: 10.1371/journal.pone.0033660
72. Lu D, Lamb CR, Pfeiffer DU, Targett MP. Neurological signs and results of magnetic resonance imaging in 40 cavalier King Charles spaniels with Chiari type 1-like malformations. *Vet Rec.* (2003) 153:260–3. doi: 10.1136/vr.153.9.260
73. Harcourt-Brown TR, Campbell J, Warren-Smith C, Jeffery ND, Granger NP. Prevalence of Chiari-like malformations in clinically unaffected dogs. *J Vet Intern Med.* (2015) 29:231–7. doi: 10.1111/jvim.12477
74. Rusbridge C, Knowler SP. Coexistence of occipital dysplasia and occipital hypoplasia/syringomyelia in the cavalier King Charles spaniel. *J Small Anim Pract.* (2006) 47:603–6. doi: 10.1111/j.1748-5827.2006.00048.x
75. Driver CJ, De Risio L, Hamilton S, Rusbridge C, Dennis R, Mcgonnell IM, et al. Changes over time in craniocerebral morphology and syringomyelia in cavalier King Charles spaniels with Chiari-like malformation. *BMC Vet Res.* (2012) 8:215. doi: 10.1186/1746-6148-8-215
76. Driver CJ, Watts V, Bunck AC, Van Ham LM, Volk HA. Assessment of cerebellar pulsation in dogs with and without Chiari-like malformation and syringomyelia using cardiac-gated cine magnetic resonance imaging. *Vet J.* (2013) 198:88–91. doi: 10.1016/j.tvjl.2013.05.017
77. Clarke EC, Fletcher DF, Stoodley MA, Bilston LE. Computational fluid dynamics modelling of cerebrospinal fluid pressure in Chiari malformation and syringomyelia. *J Biomech.* (2013) 46:1801–9. doi: 10.1016/j.jbiomech.2013.05.013
78. Clarke EC, Stoodley MA, Bilston LE. Changes in temporal flow characteristics of CSF in Chiari malformation Type I with and without syringomyelia: implications for theory of syrinx development. *J Neurosurg.* (2013) 118:1135–40. doi: 10.3171/2013.2.JNS12759
79. Cerda-Gonzalez S, Olby NJ, Griffith EH. Medullary position at the craniocervical junction in mature cavalier king charles spaniels: relationship with neurologic signs and syringomyelia. *J Vet Intern Med.* (2015) 29:882–6. doi: 10.1111/jvim.12605
80. Cerda-Gonzalez S, Olby NJ, Broadstone R, Mccullough S, Osborne JA. Characteristics of cerebrospinal fluid flow in Cavalier King Charles Spaniels analyzed using phase velocity cine magnetic resonance imaging. *Vet Radiol Ultrasound* (2009) 50:467–76. doi: 10.1111/j.1740-8261.2009.01571.x
81. Scrivani PV, Freer SR, Dewey CW, Cerda-Gonzalez S. Cerebrospinal fluid signal-void sign in dogs. *Vet Radiol Ultrasound* (2009) 50:269–75. doi: 10.1111/j.1740-8261.2009.01532.x
82. Driver CJ, Chandler K, Walmsley G, Shihab N, Volk HA. The association between Chiari-like malformation, ventriculomegaly and seizures in cavalier King Charles spaniels. *Vet J.* (2012) 195:235–7. doi: 10.1016/j.tvjl.2012.05.014
83. Ives EJ, Doyle L, Holmes M, Williams TL, Vanhaesebrouck AE. Association between the findings on magnetic resonance imaging screening for syringomyelia in asymptomatic Cavalier King Charles spaniels and observation of clinical signs consistent with syringomyelia in later life. *Vet J.* (2015) 203:129–30. doi: 10.1016/j.tvjl.2014.11.010
84. Rusbridge C, Greitz D, Iskandar BJ. Syringomyelia: current concepts in pathogenesis, diagnosis, and treatment. *J Vet Intern Med.* (2006) 20:469–79. doi: 10.1111/j.1939-1676.2006.tb02884.x
85. Loderstedt S, Benigni L, Chandler K, Cardwell JM, Rusbridge C, Lamb CR, et al. Distribution of syringomyelia along the entire spinal cord in clinically affected Cavalier King Charles Spaniels. *Vet J.* (2011) 190:359–63. doi: 10.1016/j.tvjl.2010.12.002
86. Cirovic S, Lloyd R, Jovanovik J, Volk HA, Rusbridge C. Computer simulation of syringomyelia in dogs. *BMC Vet Res.* (2018) 14:82. doi: 10.1186/s12917-018-1410-7
87. Rusbridge C, Carruthers H, Dube MP, Holmes M, Jeffery ND. Syringomyelia in cavalier King Charles spaniels: the relationship between syrinx dimensions and pain. *J Small Anim Pract.* (2007) 48:432–6. doi: 10.1111/j.1748-5827.2007.00344.x
88. Nalborczyk ZR, Mcfadyen AK, Jovanovik J, Tauro A, Driver CJ, Fitzpatrick N, et al. MRI characteristics for "phantom" scratching in canine syringomyelia. *BMC Vet Res.* (2017) 13:340. doi: 10.1186/s12917-017-1258-2
89. Van Biervliet J, De Lahunta A, Ennulat D, Oglesbee M, Summers B. Acquired cervical scoliosis in six horses associated with dorsal grey column chronic myelitis. *Equine Vet J.* (2004) 36:86–92. doi: 10.2746/0425164044864624
90. Johanson CE, Duncan JA III, Klinge PM, Brinker T, Stopa EG, Silverberg GD. Multiplicity of cerebrospinal fluid functions: new challenges in health and disease. *Cerebrospinal Fluid Res.* (2008) 5:10. doi: 10.1186/1743-8454-5-10
91. Driver CJ, Rusbridge C, Mcgonnell IM, Volk HA. Morphometric assessment of cranial volumes in age-matched Cavalier King Charles spaniels with and without syringomyelia. *Vet Rec.* (2010) 167:978–9. doi: 10.1136/vr.c4109
92. Tamburrini G, Caldarelli M, Massimi L, Gasparini G, Pelo S, Di Rocco C. Complex craniosynostoses: a review of the prominent clinical features and the related management strategies. *Childs Nerv Syst.* (2012) 28:1511–23. doi: 10.1007/s00381-012-1819-4
93. Baig MN, Byrne F, Devitt A, Mccabe JP. Signs of nature in spine radiology. *Cureus* (2018) 10:e2456. doi: 10.7759/cureus.2456
94. Unsgard G, Solheim O, Lindseth F, Selbekk T. Intra-operative imaging with 3D ultrasound in neurosurgery. *Acta Neurochir Suppl.* (2011) 109:181–6. doi: 10.1007/978-3-211-99651-5_28
95. Narenthiran G, Parks C, Pettorini B. Management of Chiari I malformation in children: effectiveness of intra-operative ultrasound for tailoring foramen magnum decompression. *Childs Nerv Syst.* (2015) 31:1371–6. doi: 10.1007/s00381-015-2699-1
96. Schmidt MJ, Wigger A, Jawinski S, Golla T, Kramer M. Ultrasonographic appearance of the craniocervical junction in normal brachycephalic dogs and dogs with caudal occipital (Chiari-like) malformation. *Vet Radiol Ultrasound* (2008) 49:472–6. doi: 10.1111/j.1740-8261.2008.00411.x
97. Schmidt MJ, Biel M, Klumpp S, Schneider M, Kramer M. Evaluation of the volumes of cranial cavities in Cavalier King Charles Spaniels with Chiari-like malformation and other brachycephalic dogs as measured via computed tomography. *Am J Vet Res.* (2009) 70:508–12. doi: 10.2460/ajvr.70.4.508
98. Kromhout K, Van Bree H, Broeckx BJ, Bhatti S, Van Ham L, Polis I, et al. Low-field MRI and multislice CT for the detection of cerebellar (foramen magnum) herniation in Cavalier King Charles Spaniels. *J Vet Intern Med.* (2015) 29:238–42. doi: 10.1111/jvim.12498

99. Garcia-Real I, Kass PH, Sturges BK, Wisner ER. Morphometric analysis of the cranial cavity and caudal cranial fossa in the dog: a computerized tomographic study. *Vet Radiol Ultrasound* (2004) 45:38–45. doi: 10.1111/j.1740-8261.2004.04006.x
100. Galloway AM, Curtis NC, Sommerlad SF, Watt PR. Correlative imaging findings in seven dogs and one cat with spinal arachnoid cysts. *Vet Radiol Ultrasound* (1999) 40:445–52. doi: 10.1111/j.1740-8261.1999.tb00373.x
101. Mauler DA, De Decker S, De Risio L, Volk HA, Dennis R, Gielen I, et al. Signalment, clinical presentation, and diagnostic findings in 122 dogs with spinal arachnoid diverticula. *J Vet Intern Med.* (2014) 28:175–81. doi: 10.1111/jvim.12241
102. Heiss J. Diagnostic Investigations. In: Flint G, Rusbridge C, editors. *Syringomyelia: A Disorder of CSF Circulation.* Berlin; Heidelberg: Springer (2014).p. 125–40.
103. Sayal PP, Zafar A, Carroll TA. Syringomyelia secondary to "occult" dorsal arachnoid webs: Report of two cases with review of literature. *J Craniovertebr Junction Spine* (2016) 7:101–4. doi: 10.4103/0974-8237.181862
104. Li AE, Wilkinson MD, Mcgrillen KM, Stoodley MA, Magnussen JS. Clinical applications of cine balanced steady-state free precession MRI for the evaluation of the subarachnoid spaces. *Clin Neuroradiol.* (2015) 25:349–60. doi: 10.1007/s00062-015-0383-1
105. Goh S, Bottrell CL, Aiken AH, Dillon WP, Wu YW. Presyrinx in children with Chiari malformations. *Neurology* (2008) 71:351–6. doi: 10.1212/01.wnl.0000304087.91204.95
106. Bva. *Appendix 1 Breeding Recommendations Until Relevant EBVs are Available* [Online] (2012). Available online at: http://www.bva.co.uk/public/documents/CM-SM_breeding_recommendations.pdf: BVA, The (Accessed July, 8 2013).
107. Hecht S, Huerta MM, Reed RB. Magnetic resonance imaging (MRI) spinal cord and canal measurements in normal dogs. *Anat Histol Embryol.* (2014) 43:36–41. doi: 10.1111/ahe.12045
108. Seo E, Choi J, Choi M, Yoon J. Computed tomographic evaluation of cervical vertebral canal and spinal cord morphometry in normal dogs. *J Vet Sci.* (2014) 15:187–93. doi: 10.4142/jvs.2014.15.2.187
109. Ricciardi M. Principles and applications of the balanced steady-state free precession sequence in small animal low-field MRI. *Vet Res Commun.* (2018) 42:65–86. doi: 10.1007/s11259-017-9708-7
110. Konar M, Lang J. Pros and cons of low-field magnetic resonance imaging in veterinary practice. *Vet Radiol Ultrasound* (2011) 52:S5–14. doi: 10.1111/j.1740-8261.2010.01780.x
111. Oh CH, Kim CG, Lee JH, Yoon SH, Park HC, Park CO. Missed diagnosis of syrinx. *Asian Spine J.* (2012) 6:1–5. doi: 10.4184/asj.2012.6.1.1
112. Jinkins JR, Sener RN. Idiopathic localized hydromyelia: dilatation of the central canal of the spinal cord of probable congenital origin. *J Comput Assist Tomogr.* (1999) 23:351–3. doi: 10.1097/00004728-199905000-00004
113. Upchurch JJ, Mcgonnell IM, Driver CJ, Butler L, Volk HA. Influence of head positioning on the assessment of Chiari-like malformation in Cavalier King Charles spaniels. *Vet Rec.* (2011) 169:277. doi: 10.1136/vr.d4395
114. Piesnack S, Oechtering G, Ludewig E. [Options for the reduction of magnetic susceptibility artifacts caused by implanted microchips in 0.5 Tesla magnetic resonance imaging]. *Tierarztl Prax Ausg K Kleintiere Heimtiere* (2015) 43:83–92. doi: 10.15654/TPK-150048
115. Dengg S, Kneissl S. [Comparison of susceptibility artifacts generated by microchips with different geometry at 1.5 Tesla magnet resonance imaging. A phantom pilot study referring to the ASTM standard test method F2119-07]. *Tierarztl Prax Ausg K Kleintiere Heimtiere* (2013) 41:289–96. doi: 10.1055/s-0038-1623723
116. Ebraheim NA, Savolaine ER, Zeiss J, Jackson WT. Titanium hip implants for improved magnetic resonance and computed tomography examinations. *Clin Orthop Relat Res.* (1992) 194–8. doi: 10.1097/00003086-199202000-00028
117. Sherman JL, Barkovich AJ, Citrin CM. The MR appearance of syringomyelia: new observations. *AJR Am J Roentgenol.* (1987) 148:381–91. doi: 10.2214/ajr.148.2.381
118. Ogbole GI, Soneye MA, Okorie CN, Sammet S. Intraventricular cerebrospinal fluid pulsation artifacts on low-field magnetic resonance imaging: Potential pitfall in diagnosis? *Niger Med J.* (2016) 57:59–63. doi: 10.4103/0300-1652.180565
119. Herlihy AH, Oatridge A, Curati WL, Puri BK, Bydder GM, Hajnal JV. FLAIR imaging using nonselective inversion pulses combined with slice excitation order cycling and k-space reordering to reduce flow artifacts. *Magn Reson Med.* (2001) 46:354–64. doi: 10.1002/mrm.1198
120. Raybaud C, Greenberg G. Imaging (Normal and Abnormal). In: Mallucci C, Sgouros S, editors. *Cerebrospinal Fluid Disorders.* Boca Raton, FL: CRC Press (2010).p. 66–109.
121. Cherubini GB, Platt SR, Anderson TJ, Rusbridge C, Lorenzo V, Mantis P, et al. Characteristics of magnetic resonance images of granulomatous meningoencephalomyelitis in 11 dogs. *Vet Rec.* (2006) 159:110–5. doi: 10.1136/vr.159.4.110
122. Timpone VM, Patel SH. MRI of a syrinx: is contrast material always necessary? *AJR Am J Roentgenol.* (2015) 204:1082–5. doi: 10.2214/AJR.14.13310
123. Kobayashi K, Ando K, Kato F, Kanemura T, Imagama S, Sato K, et al. MRI characteristics of spinal ependymoma in WHO Grade II: a review of 59 cases. *Spine* (2018) 43:E525–30. doi: 10.1097/BRS.0000000000002496
124. Tauro A, Jovanovik J, Driver CJ, Rusbridge C. Clinical application of 3D-CISS MRI sequences for diagnosis and surgical planning of spinal arachnoid diverticula and adhesions in dogs. *Vet Comp Orthop Traumatol.* (2018) 31:83–94. doi: 10.3415/VCOT-16-12-0169
125. Roser F, Ebner FH, Danz S, Riether F, Ritz R, Dietz K, et al. Three-dimensional constructive interference in steady-state magnetic resonance imaging in syringomyelia: advantages over conventional imaging. *J Neurosurg Spine* (2008) 8:429–35. doi: 10.3171/SPI/2008/8/5/429
126. Seiler GS, Robertson ID, Mai W, Widmer WR, Suran J, Nemanic S, et al. Usefulness of a half-fourier acquisition single-shot turbo spin-echo pulse sequence in identifying arachnoid diverticula in dogs. *Vet Radiol Ultrasound* (2012) 53:157–61. doi: 10.1111/j.1740-8261.2011.01893.x
127. Battal B, Kocaoglu M, Bulakbasi N, Husmen G, Tuba Sanal H, Tayfun C. Cerebrospinal fluid flow imaging by using phase-contrast MR technique. *Br J Radiol.* (2011) 84:758–65. doi: 10.1259/bjr/66206791
128. Tobimatsu Y, Nihei R, Kimura T, Suyama T, Tobimatsu H. [A quantitative analysis of cerebrospinal fluid flow in posttraumatic syringomyelia]. *Nihon Seikeigeka Gakkai Zasshi* (1991) 65:505–16.
129. Bittermann S, Lang J, Henke D, Howard J, Gorgas D. Magnetic resonance imaging signs of presumed elevated intracranial pressure in dogs. *Vet J.* (2014) 201:101–8. doi: 10.1016/j.tvjl.2014.04.020
130. Marks S, Flint G. Medicolegal Aspects. In: Flint G, Rusbridge C, editors. *Syringomyelia: A Disorder of CSF Circulation.* Berlin; Heidelberg: Springer (2014).p. 289–300. doi: 10.1007/978-3-642-13706-8_19
131. Zeng R, Coates JR, Johnson GC, Hansen L, Awano T, Kolicheski A, et al. Breed distribution of SOD1 alleles previously associated with canine degenerative myelopathy. *J Vet Intern Med.* (2014) 28:515–21. doi: 10.1111/jvim.12317

Conflict of Interest Statement: The authors declare that the research was conducted in the absence of any commercial or financial relationships that could be construed as a potential conflict of interest.

frontiers in Veterinary Science

ORIGINAL RESEARCH
published: 11 March 2019
doi: 10.3389/fvets.2019.00068

Evaluation of the Canine Intervertebral Disc Structure in Turbo Spin Echo-T2 and Fast Field Echo-T1 Sequences in Magnetic Resonance Imaging

Katarina Kunze[1], *Veronika Maria Stein*[2] *and Andrea Tipold*[3]*

[1] Tierarztpraxis Dr. Dieffenbacher, Neustrelitz, Germany, [2] Vetsuisse Faculty of the University of Veterinary Medicine, Bern, Switzerland, [3] Department of Small Animal Medicine and Surgery, University of Veterinary Medicine, Hannover, Germany

In the current study the hypothesis should be proven that T1 weighted Fast Field Echo (FFE) sequence is a useful method to visualize intervertebral disc degeneration, respectively changes of the expected disc appearance. Medical records of 208 dogs were reviewed and images of 781 intervertebral discs were evaluated by two blinded examiners using a modified Pfirrmann classification system in two MRI sequences: FFE and Turbo-Spin-Echo T2-weighted sequence (T2W). The patients were allocated to three categories based on body conformation: (1) brachycephalic and chondrodystrophic breeds, (2) non-chondrodystrophic and non-brachycephalic breeds with a body weight of < 25 kg, and (3) non-chondrodystrophic and non-brachycephalic breeds with a body weight greater or equal 25 kg. In brachycephalic and chondrodystrophic dogs 340 intervertebral discs were evaluated, the majority of them presented a mild change of the normal disc structure, 53% in the FFE sequence and 41% in T2W images. High discrepancies were observed between mild and moderate degeneration: in the FFE-sequence 15% ($n = 50$) of the discs had signs of mild degeneration, whereas in T2W the same discs were graded as moderately degenerated. In non-chondrodystrophic and non-brachycephalic breeds under 25 kg body weight 320 intervertebral discs were assessed. In the FFE-sequence 52% ($n = 166$) of the intervertebral discs were judged as having a mild degeneration. In contrast, these same discs were graded as healthy discs (22%), mildly degenerated (33%), moderately degenerated (37%), and severely degenerated (8%) in T2W. In non-chondrodystrophic and non-brachycephalic breeds greater or equal 25 kg 121 intervertebral discs were assessed. The grading was equal in 43%, but differed in one grade (47%) and in two grades (10%) between the two sequences. In both sequences intervertebral disc herniations were equally well-diagnosed. The Kappa coefficient revealed a high discrepancy between the two MRI-sequences. In conclusion, FFE cannot replace the well-established T2W sequence for grading disc degeneration.

Keywords: intervertebral disc degeneration, Pfirrmann grading system, FFE-sequence, dog, MRI

OPEN ACCESS

Edited by:
Steven De Decker, Royal Veterinary College (RVC), United Kingdom

Reviewed by:
Curtis Wells Dewey, Cornell University, United States
Cristian Falzone, Independent Researcher, Zugliano, Italy

***Correspondence:**
Andrea Tipold
andrea.tipold@tiho-hannover.de

Specialty section:
This article was submitted to Veterinary Neurology and Neurosurgery, a section of the journal Frontiers in Veterinary Science

Received: *06 July 2018*
Accepted: *15 February 2019*
Published: *11 March 2019*

Citation:
Kunze K, Stein VM and Tipold A (2019) Evaluation of the Canine Intervertebral Disc Structure in Turbo Spin Echo-T2 and Fast Field Echo-T1 Sequences in Magnetic Resonance Imaging. Front. Vet. Sci. 6:68. doi: 10.3389/fvets.2019.00068

INTRODUCTION

Degeneration of the intervertebral disc occurs during physiological aging processes and pathological events (1, 2). Chondroid metaplasia leads to intervertebral disc degeneration in chondrodystrophic breeds early in life (1). In addition, in some brachycephalic breeds, such as french bulldogs, pug dogs, and boxers, morphological changes affecting the vertebral column (spondylosis deformans, thoracical vertebral malformations) are predisposing to intervertebral disc degeneration (3–5). Magnetic resonance imaging (MRI) is currently the gold standard technique to investigate intervertebral disc disease (1, 6, 7). Commonly, for the diagnostic work-up in patients with intervertebral disc herniation and spinal cord compression T2 weighted images (T2W) are evaluated in dorsal, sagittal and transversal planes (8). Currently, T2W images are additionally used to evaluate disc degeneration and can be viewed as gold standard for this evaluation. Further sequences such as pre- and post-contrast T1-weighted (T1W) images, gradient echo sequence or short tau inversion recovery (STIR) are applied to better delineate disc diseases or to rule out paraspinal soft-tissue pathology (9, 10). In T2W images different structures of healthy discs can be distinguished, such as the hyperintense nucleus pulposus surrounded by the annulus fibrosus that is isointense to adjacent muscle tissue (11). Degeneration of the intervertebral disc is a complex, multifactorial process characterized by a decreased signal intensity of the nucleus pulposus and an indistinct border between nucleus pulposus and annulus fibrosus (12, 13). Pfirrmann et al. established 2001 a five stepped grading system focusing on characteristic changes in the structure of the disc on sagittal T2 weighted images (14). Bergknut et al. evaluated and adapted this system for the canine species (15). The gradient echo sequence is another possibility to visualize the morphology of the intervertebral disc with an enhanced T1 or T2* contrast (8). In the literature different terms for gradient echo sequences are mentioned, such as Fast Field Echo (FFE) or Fast Low Angle Short (FLASH) (16). In T1 weighted FFE images, the sequence used in the current study, the intervertebral disc has a homogenous signal intensity isointense to adjacent muscle tissue. In contrast, the vertebral body displays a signal intensity, which is hypointense in comparison to cerebrospinal fluid (8, 17–19). In the present study the hypothesis should be proven that the FFE sequence is a useful method to visualize intervertebral disc degeneration or changes of the expected disc appearance and could give additional information to conventional T2W images, the proposed gold standard. Additionally, we wanted to prove, that both sequences are capable to detect disc herniation. To verify these hypotheses, more than 700 single intervertebral discs were evaluated by two blinded examiners.

MATERIALS AND METHODS

Ethics Statement

The study was conducted following the guidelines of the University of Veterinary Medicine Hannover with written consent of the dog owners and approved by the thesis committee of the University.

Case Selection

Medical records of 208 dogs presented between 2010 and 2012 at the Dept. of Small Animal Medicine and Surgery, University of Veterinary Medicine Hannover, with different neurological disorders were retrospectively reviewed. Dogs were included, when radiographs and MR images of the vertebral column were available. According to their body conformation the patients were allocated to three categories. Category 1 included brachycephalic and chondrodystrophic breeds. Category 2 comprised non-chondrodystrophic and non-brachycephalic breeds with a body weight < 25 kg and category 3 encompassed non-chondrodystrophic and non-brachycephalic breeds with a body weight equal or greater 25 kg. Breeds were classified as chondrodystrophic or brachycephalic according to the description of Parker et al. (20) and Bannasch et al. (21)

Magnetic Resonance Imaging

MRI was performed using a 3-Tesla MRI scanner (Philips Achieva, Eindhoven, The Netherlands). The intervertebral discs were evaluated in the transverse plane using a modified Pfirrmann classification system in Turbo-Spin-Echo T2-weighted sequence (T2W) (TR = 3100 ms, TE = 120 ms, flip angle = 90°) and a grading system designed by the authors in T1 weighted FFE-sequence images (FFE) (TR = 11 ms, TE = 220 ms, flip angle = 8°). MR images were reviewed by two board-certified neurologists (AT and VMS) blinded to signalement and clinical data. Five grades of disc degeneration were used to evaluate the appearance and potential degeneration of the intervertebral discs (**Figures 1**, **2**). Disc herniation was defined as "6", independent of the status of degenerative changes. In the current study "6" does not reflect the degree of disc degeneration.

Statistics

Analyses were assessed with the statistical software SAS, version 9.2 (SAS Institute, Cary, NC, USA). For comparison of the two MRI-sequences McNemar's test was used and the simple and weighted kappa coefficient established.

RESULTS

A total of 208 patients were examined. Eighty-three dogs were assigned to category 1, 86 patients to category 2, and 39 patients to category 3. In category 1, 63.9% ($n = 53$) were Dachshunds and 19.3% ($n = 16$) French bulldogs. Further breeds in category 1 included Pug dogs ($n = 4$), Boxers ($n = 3$), Shi-Tzu ($n = 3$), Havanese ($n = 2$), Sky terrier ($n = 1$) and Welsh corgi cardigan ($n = 1$). The category 2 included 27 breeds, mainly Beagles ($n = 11$), Jack Russell terriers ($n = 10$) and mixed breed dogs ($n = 23$). In category 3 a total of 17 breeds were presented, especially German Shepherd dogs ($n = 8$), Labrador Retrievers ($n = 7$), and mixed breed dogs ($n = 9$). 45 males (7 neutered) and 38 females (23 spayed) were included in category 1, 59 males (14 neutered) and 27 females (19 spayed) in category 2 and 25 males (6 neutered) and 14 females (6 spayed) in category 3. Bodyweight ranged from 3.9 to 29.8 kg (median 8.1 kg) in category 1, from 2.6 to 24 kg (median 11 kg) in category 2, and from 25 to 60 kg (median 34 kg) in category 3. The youngest patients of the study

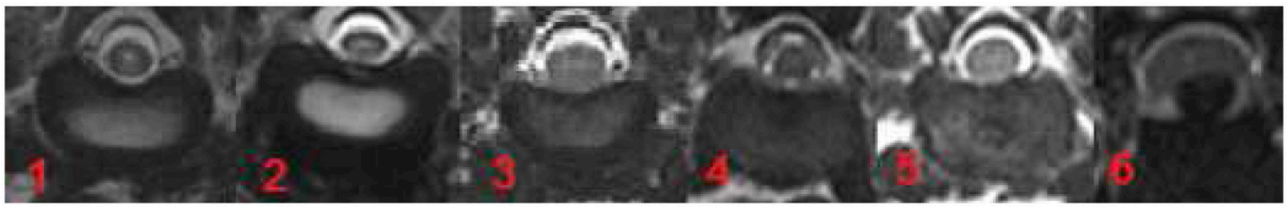

FIGURE 1 | Grading system for T2W images modified after Pfirrmann et al. (14). Grade 1 and 2 included healthy intervertebral discs in dogs younger (grade 1) or older than 12 months (grade 2). Nucleus pulposus is hyper- or isointense to cerebrospinal fluid with a clear distinction between nucleus pulposus and annulus fibrosus. Grade 3 is characterized by mild degeneration affecting at the maximum one-third of the intervertebral disc with a iso- or hypointense nucleus pulposus and a visible distinction between nucleus pulposus and annulus fibrosus. Moderate degeneration (grade 4) affected at the minimum one-third and at the maximum two-third of the intervertebral disc, the distinction between nucleus pulposus and annulus fibrosus is blurred. In severe degeneration (grade 5) more than two-third of the intervertebral disc is affected, the nucleus pulposus is hypointense, narrowing of the cerebrospinal fluid space is possible. Disc herniations are displayed under "6".

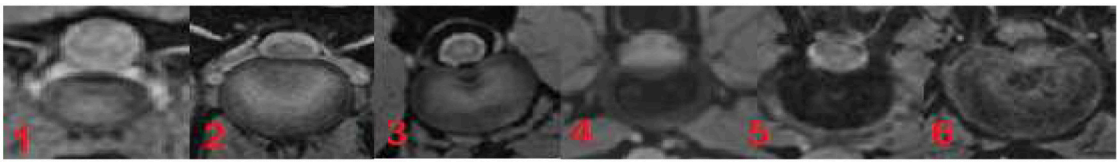

FIGURE 2 | Grading system for T1W FFE-sequence (designed by KK and AT). Grade 1 and 2 included healthy intervertebral discs in dogs younger (grade 1) or older than 12 months (grade 2). The disc displays a homogeneous structure and a signal intensity isointense to adjacent muscles (Mm trunci). Grade 3 is characterized by mild degeneration affecting at the maximum one-third of the intervertebral disc with a hypointense nucleus pulposus. Moderate degeneration (grade 4) affected at the minimum one-third and at the maximum two-third of the intervertebral disc (hypointense to surrounding tissue). In high grade degeneration (grade 5) more than two-third of the intervertebral disc is affected and hypointense to the surrounding tissue. Disc herniations are displayed under "6".

TABLE 1 | Results of kappa coefficient in three categories of dogs.

	Category 1	Category 2	Category 3
Simple Kappa coefficient	0.5703	0.3844	0.2860
Weighted Kappa coefficient	0.7779	0.6547	0.5996

were < one 1 year old and the oldest patients were 14 years old. The mean age of dogs suffering a disc extrusion was 5.73 years in category 1, 6.67 years in category 2, and 7.44 years in category 3.

A total of 781 intervertebral discs was evaluated in T2W and in T1 weighted FFE-sequence, which included 340 in category 1, 320 in category 2, and 121 in category 3 of dogs. 21 % (n = 164) of the intervertebral discs were located between C2 and T1, 44.7% (n = 349) between T1 and L1, and 34.3% (n = 268) between L1 and the sacrum. AT and VMS evaluated together the structure of the intervertebral discs using the described grading system for MR images and were blinded regarding signalement and clinical signs. Grades were ascertained after achieving a consensus between the two examiners. Evaluating the images using the described grading system statistically significant differences were found between the two MRI sequences in all three categories of dogs ($p < 0.0001$ in category 1 and 2, $p = 0.001$ in category 3). The results of the simple and weighted Kappa coefficient confirmed these results (**Table 1**).

The Kappa coefficient was chosen to demonstrate agreement between evaluation of the different grades of intervertebral disc degeneration by using the grading system for each sequence. In category 1 of dogs the highest agreement compared to the other categories was present. The higher score of the weighted Kappa coefficient reflected the finding that the evaluation of morphologic disc appearance deviated in the majority by one grade.

In both sequences the same number of intervertebral disc extrusions ("6") was assessed.

In category 1 of dogs a total of 340 intervertebral discs were evaluated. The majority of the discs were judged to have mild degeneration, 53% in the FFE-sequence and 41% in T2 weighted images. A high discrepancy was observed between evaluating mild or moderate grade degeneration. 15% (n = 50) of the discs were considered to have mild degeneration in the FFE-sequence. In T2 weighted images the same discs were assessed as moderate grade degeneration. The mean value of the grading was 3.84 in the FFE-sequence and 4.04 in T2W for category 1 of dogs. In T2 weighted images signs of disc degeneration were graded on average higher than in the FFE-sequence. In total an exact agreement between disc assessment in FFE and T2W sequences was made in 240 discs (71%). The evaluation of ninety discs (26%) differed in one grade and a partial agreement was achieved (**Figure 3**). No agreement was seen in 10 discs (3%) and the evaluation differed in more than one grade.

In category 2 of dogs the evaluation of the intervertebral discs revealed a higher grading in T2W images. On average the mean value of the grading was 3.78 in FFE-sequence and 4.09 in T2W images. The presence of mild degeneration was assessed differently between the both sequences. 52 % (n = 166) of the intervertebral discs showed signs of mild degeneration in the FFE-sequence. In T2W images only 23% (n = 75) presented these

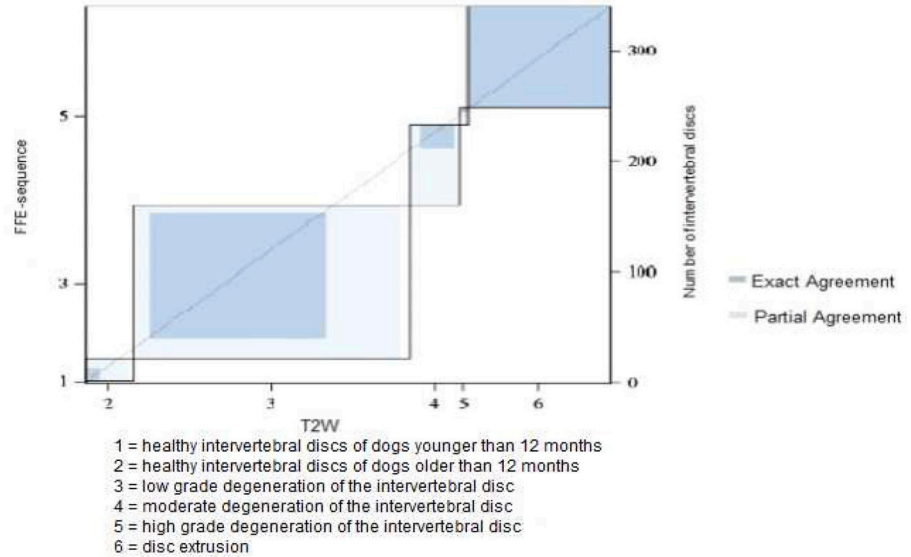

FIGURE 3 | Results of grading system agreement for intervertebral discs between T1 weighted FFE-sequence and T2 weighted images in brachycephalic and chondrodystrophic breeds (category 1).

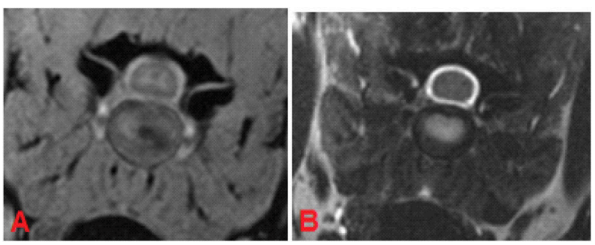

FIGURE 4 | MRI of C5-C6 intervertebral disc, transverse plane, patient 88. In the FFE-sequence a central area of decreased signal intensity in the nucleus pulposus was present accounting for less than one-third of the intervertebral disc and was evaluated as grade 3 **(A)**. In T2W the intervertebral disc was composed of a hyperintense nucleus pulposus and hypointense annulus fibrosus and was judged to be a healthy disc from an adult dog, grade 2 **(B)**.

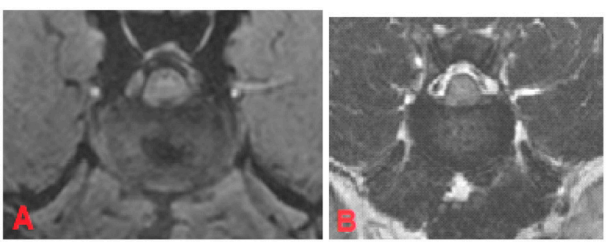

FIGURE 5 | MRI of the L1-L2 intervertebral disc, transverse plane, patient 111. In FEE-sequence the intervertebral disc had an inhomogeneous structure with a central hypointense region which takes ∼18% of the intervertebral disc and was judged as "mild degeneration" **(A)**. In T2W there was an unclear distinction between nucleus pulposus and annulus fibrosus. The signal intensity of the nucleus pulposus was hypointense to cerebrospinal fluid. The disc was assessed to have "moderate degeneration" **(B)**.

findings. Nine percent ($n = 30$) of the discs were graded "healthy" in T2W images, but showed signs of mild degeneration in the FFE-sequence (**Figures 4A,B**).

On the other hand, 19.1% ($n = 61$) of the intervertebral discs were classified as having "mild degeneration" in the FFE-sequence, whereas in T2W images signs of moderate grade degeneration were visible (**Figures 5A,B**).

The evaluation of the intervertebral discs was identical in 52.2% ($n = 168$) in both sequences, a partial agreement was achieved in 40.3% ($n = 129$) of the intervertebral discs (**Figure 6**).

In category 3 of dogs 121 intervertebral discs were evaluated. The average grade was lower than in other dog breeds: 3.48 in FFE-sequence and 3.87 in T2W. The assessement was equal in 43% ($n = 52$) of the intervertebral discs and differed in one grade in 47% ($n = 57$) and in two grades in 10% ($n = 12$) of the intervertebral discs. (**Figures 7A,B**, **8**)

In addition, the capability of the two sequences to detect disc herniation should be assessed as the second aim of the study. Intervertebral disc herniations occurred in 22 intervertebral discs in category 1, 38 intervertebral discs in category 2, and 17 intervertebral discs in category 3 of patients. In both sequences disc herniations could be equally well-diagnosed.

DISCUSSION

Intervertebral disc degeneration is a common pathological finding in dogs and can predispose dogs to disc extrusion (22). However, not every intervertebral disc degeneration lead to herniation, spinal cord compression and to neurological deficits such as ataxia or paraparesis/paraplegia (22, 23). MRI (T2W

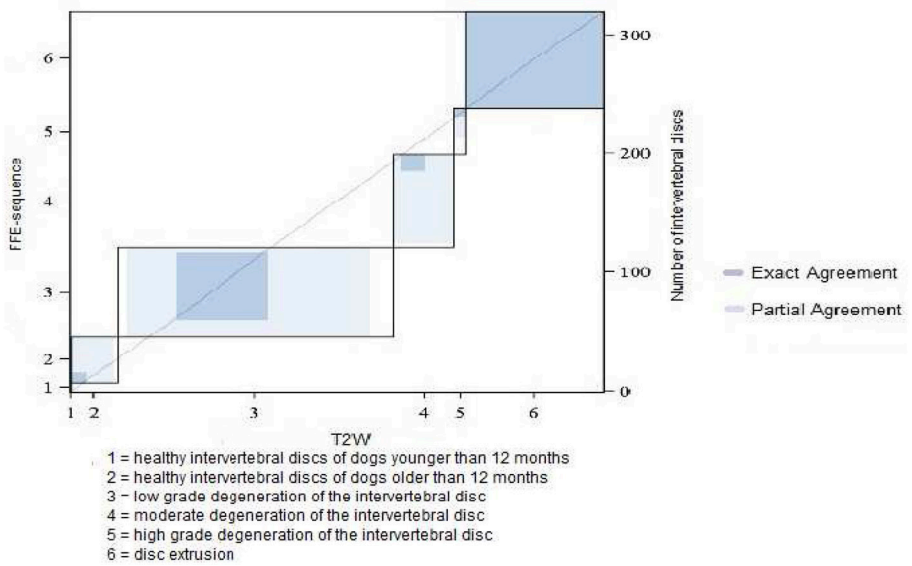

FIGURE 6 | Results of grading system agreement for intervertebral discs between T1 weighted FFE-sequence and T2 weighted images in non-chondrodystrophic and non-brachycephalic breeds with a body weight under 25 kg (category 2).

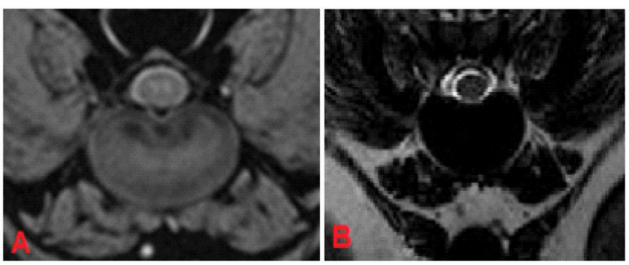

FIGURE 7 | MRI, T13-L1 intervertebral disc, transverse plane, patient 175. In FFE-sequence small hypointense areas were present leading to the assumption of a low grade degeneration **(A)**, whereas in T2W the intervertebral disc displayed a complete signal loss without any possibility to differentiate between nucleus pulposus and annulus fibrosus, grade 5 **(B)**.

sequence) is considered to be the gold standard to identify intervertebral disc degeneration *in vivo* (1, 6, 24). For the classification of the extent of intervertebral disc degeneration the Pfirrmann classification system was used and evaluated for the dog by Bergknut et al. (15) In this classification system, the intervertebral disc is evaluated in T2 weighted images and this sequence can currently be considered as gold standard. The normal nucleus pulposus appears hyperintense in comparison to surrounding tissue and correlating to proteoglycan concentrations (10, 14). Modic et al. (25) confirmed that the decrease of the signal intensity in T2W correlates with the progression of intervertebral disc degeneration. Kranenburg et al. (6) could conclude that intervertebral disc degeneration did not correlate with the severity of neurological signs. In the current study, the Pfirrmann classification system for the evaluation of intervertebral discs was used in T2 weighted images with slight modifications. For the grades 3, 4, and 5 the percentage of the extent of intervertebral disc degeneration was added. In addition, the evaluation was performed in transverse planes. This sequence was compared to a different technique, the T1W FFE-sequence in order to evaluate the suitability of this sequence in detecting structural disc changes. However, the hypothesis could not be proven that the FFE sequence is an equally useful method to visualize intervertebral disc degeneration. In the current study, it could not be evaluated, if these structural changes were indeed degenerative changes, since histopathological examinations were not performed. In comparison to T2W sequence the intervertebral disc displayed a more homogeneous structure without clear distinction between nucleus pulposus and annulus fibrosus in T1W FFE sequence as already described (18, 19). Despite this more homogenous structure grades 3, 4, and 5 could be well-defined and even the percentage of potential structural changes of the disc could be evaluated.

Statistically significant differences were found between both MRI-sequences evaluating intervertebral disc degeneration, respectively changes of the expected MRI appearance, whereas intervertebral disc extrusions and protrusions were equally diagnosed by the two sequences. The presence of mild degeneration was diagnosed differently in both sequences. In T1 weighted FFE-sequence mild degeneration was seen more frequently than in T2W images, 53% of intervertebral discs in the first category of dogs, 52% of the intervertebral discs in the second category and 49% of the intervertebral discs in the third category showed signs of mild degeneration. In contrast, in T2 weighted images only 41% of the intervertebral discs in category 1, 23% of the intervertebral discs in category 2, and only 17% of the intervertebral discs in category 3 displayed these signs. The evaluation of discs with mild degeneration in the T1 weighted FFE-sequence ranged from a healthy disc to

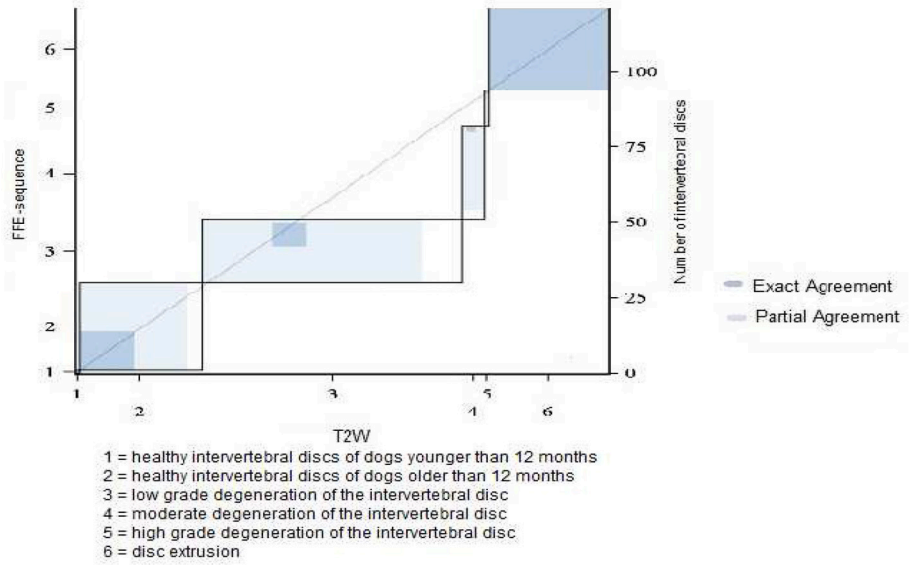

FIGURE 8 | Results of grading system agreement for intervertebral discs between T1 weighted FFE-sequence and T2 weighted images in non-chondrodystrophic and non-brachycephalic breeds with a body weight greater or equal 25 kg.

a severely degenerated disc in T2 weighted images: a healthy disc in T2 weighted images was judged in 47% in category 1 of dogs, 77% in category 2, and in 55% in category 3 signs of mild degeneration in the T1 weighted FFE-sequence, suggesting that slight changes are only visible in the T1 weighted FFE-sequence or that this sequence is more susceptible to artifacts. To prove that the described morphological changes in the T1 weighted FFE-sequence is indeed a pathological finding studies have to be performed in the future comparing MRI findings and histopathology. Interestingly, when degenerative signs were clearly visible in T2W images, signs of disc degeneration were graded on average higher than in the T1 weighted FFE-sequence. In addition, the FFE-sequence was vulnerable to susceptibility artifacts because of the absence of the 180° refocusing pulse (8). In conclusion, the present study demonstrated that T1 weighted FFE sequence is not a precise alternative to T2W images and the discrepancies between the two sequences have to be further evaluated. The superiority or inferiority of T1 weighted FFE has still to be proven to achieve an additional method to diagnose intervertebral disc degeneration. In the current study, it was not confirmed, that the described abnormal appearance of discs in T1W FFE sequence is indeed a degenerative change. A limitation of the study is, that histological examinations of the discs were not performed. All discs evaluated with the T1W FFE sequence were compared to the already well-described appearance in T2W sequence supporting the suggestion that a degeneration is highly probable. However, slight changes of the intervertebral disc structure are better visible in T1 weighted FFE images and may only represent intrinsic sequence changes. Therefore, future studies in dogs undergoing necropsy are recommended to evaluate this phenomenon.

AUTHOR CONTRIBUTIONS

KK performed the study and drafted the manuscript. VS evaluated MR images and revised the manuscript. AT designed the study, evaluated MR images and revised the manuscript.

ACKNOWLEDGMENTS

This publication was supported by Deutsche Forschungsgemeinschaft and University of Veterinary Medicine Hannover, Foundation within the funding programme Open Access Publishing.

REFERENCES

1. Brisson BA. Intervertebral disc disease in dogs. *Vet Clin North Am Small Anim Pract.* (2010) 40:829–58. doi: 10.1016/j.cvsm.2010.06.001
2. Jonathan PB, Burbidge HM. The canine intervertebral disk, part two: degenerative changes – nonchondrodystrophoid versus chondrodystrophoid disks. *J Am Anim Hospital Assoc.* (1998) 34:135–44. doi: 10.5326/15473317-34-2-135
3. Levine GJ, Levine JM, Walker MA, Pool RR, Fosgate GT. Evaluation of the association between spondylosis deformans and clinical signs of intervertebral disk disease in dogs: 172 cases (1999–2000). *J Am Vet Med Assoc.* (2006) 228:96–100. doi: 10.2460/javma.228.1.96
4. Ryan R, Gutierrez-Quintana R, Ter Haar G, De Decker S. Prevalence of thoracic vertebral malformations in French bulldogs, Pugs and English bulldogs with and without associated neurological deficits. *Vet J.* (2017) 221:259. doi: 10.1016/j.tvjl.2017.01.018
5. Kranenburg HCJ, Voorhout G, Grinwis GCM, Hazewinkel HAW, Meij BP. Diffuse idiopathic skeletal hyperostosis (DISH) and spondylosis deformans in purebred dogs: a retrospective radiographic study. *Vet J.* (2011) 190:84–90. doi: 10.1016/j.tvjl.2011.04.008

6. Kranenburg HJC, Grinwis GCM, Bergknut N, Gahrmann N, Voorhout G, Hazewinkel HAW, Meij BP. Intervertebral disc disease in dogs – Part 2: Comparison of clinical, magnetic resonance imaging, and histological findings in 74 surgically treated dogs. *Vet J.* (2013) 195:164–71. doi: 10.1016/j.tvjl.2012.06.001
7. Robertson I, Thrall DE. Imaging dogs with suspected disc herniation: Pros and Cons of myelography, computed tomography, and magnetic resonance. *Vet Radiol Ultrasound.* (2011) 52:81–4. doi: 10.1111/j.1740-8261.2010.01788.x
8. Dennis R. Optimal magnetic resonance imaging of the spine. *Vet Radiol Ultrasound.* (2011) 52:72–80. doi: 10.1111/j.1740-8261.2010.01787.x
9. Zhalniarovich Y, Adamiak Z, Pomianowski A, Jaskolska M. Most commonly used sequences and clinical protocols for brain and spine magnetic resonance imaging allowing better identification of pathological changes in dogs. *Polish J Vet Sci.* (2013) 16:157–63. doi: 10.2478/pjvs-2013-0024
10. Da Costa RC, Samii VF. Advanced imaging of the spine in small animals. *Vet Clin Small Anim.* (2010) 40:765–90. doi: 10.1016/j.cvsm.2010.05.002
11. Adams, WH, Daniel GB, Pardo AD, Selcer RR. Magnetic resonance imaging of the caudal lumbar and lumbosacral spine in 13 dogs (1990-1993). *Vet Radiol Ultrasound.* (1995) 36:3–13. doi: 10.1111/j.1740-8261.1995.tb00204.x
12. Seiler GS, Häni H, Scheidegger J, Busato A, Lang J. Staging of lumbar intervertebral disc degeneration in nonchondrodystrophic dogs using lowfield magnetic resonance imaging. *Vet Radiol Ultrasound.* (2003) 44:179–84. doi: 10.1111/j.1740-8261.2003.tb01268.x
13. Levitski, R, Lipsitz, D, Chauvet, AE. Magnetic resonance imaging of the cervical spine in 27 dogs. *Vet Radiol Ultrasound.* (1999) 40:332–41.
14. Pfirrmann CW, Metzdorf A, Zanetti M, Hodler J, Boos N. Magnetic resonance classification of lumbar intervertebral disc degeneration. *Spine.* (2001) 26:1873–78.
15. Bergknut N, Auriemma E, Wijsman S, Voorhout G, Hagman R, Lagerstedt AS, et al. Evaluation of intervertebral disk degeneration in chondrodystrophic and nonchondrodystrophic dogs by use of Pfirrmann grading of images obtained with low-field magnetic resonance imaging. *Am J Vet Res. (*2011) 72:893–8. doi: 10.2460/ajvr.72.7.893
16. Winkler, ML, Ortendahl DA, Mills TC, Crooks LE, Sheldon PE, Kaufman L, Kramer DM. Characteristics of partial flip angle and gradient reversal MR Imaging. *Radiology.* (1988) 166:17–26. doi: 10.1148/radiology.166.1.3275967
17. Schmidt S, Kappes J, Bergtholdt M, Pekar V, Dries S, Bystrov D, et al. Spine detection and labeling using a parts-based graphical model. In: KarssemeijerN, Lelieveldt B, editors. *IPMI.* Berlin, Heidelberg: Springer-Verlag (2007). p. 122–33.
18. Carrino JA, Morrison WB. Imaging of lumbar degenerative disc disease. *Spine Surg.* (2003) 15:361–83. doi: 10.1053/S1040-7383(03)00070-4
19. Kärkkäinen M, Punto LU, Tulamo RM. Magnetic resonance imaging of canine degenerative lumbar spine diseases. *Vet Radiol Ultrasound.* (1993) 34:399–404. doi: 10.1111/j.1740-8261.1993.tb02028.x
20. Parker HG, VonHoldt BM, Quignon P, Margulies EH, Shao S, Mosher DS, et al. An expressed Fgf 4 retrogene is associated with breed-defining chondrodysplasia in domestic dogs. *Science.* (2009) 325:995–8. doi: 10.1126/science.1173275
21. Bannasch D, Young A, Myers J, Truvé K, Dickinson P, Gregg J, et al. Localization of canine brachycephaly using an across breed mapping approach. *PLoS ONE.* (2010) 5:e9632. doi: 10.1371/journal.pone.0009632
22. Bergknut N, Smolders LA, Grinwis GCM, Hagman R, Lagerstedt AS, Hazewinkel HAW, et al. Intervertebral disc degeneration in the dog. Part 1: Anatomy and physiology of the intervertebral disc and characteristics of intervertebral disc degeneration. *Vet J.* (2012) 195:282–91. doi: 10.1016/j.tvjl.2012.10.024
23. Jeffery ND, Levine JM, Olby NJ, Stein VM. Intervertebral disk degeneration in dogs: consequences, diagnosis, treatment, and future directions. *J Vet Internal Med.* (2013) 27:1318–33. doi: 10.1111/jvim.12183
24. Besalti O, Pekcan Z, Sirin YS, Erbas G. Magnetic resonance imaging findings in dogs with thoracolumbar intervertebral disk disease: 69 cases (1997-2005). *J Am Vet Med Assoc.* (2006) 228:902–8. doi: 10.2460/javma.228.6.902
25. Modic MT, Masaryk TJ, Ross JS, Carter JR. Imaging of degenerative disk disease. *Radiology.* (1988) 168:177–86. doi: 10.1148/radiology.168.1.3289089

Conflict of Interest Statement: The authors declare that the research was conducted in the absence of any commercial or financial relationships that could be construed as a potential conflict of interest.

frontiers in Veterinary Science

ORIGINAL RESEARCH
published: 05 October 2018
doi: 10.3389/fvets.2018.00248

Cervical Intervertebral Disk to Vertebral Body Ratios of Different Dog Breeds Based on Sagittal Magnetic Resonance Imaging

*Pia Düver[1], Christina Precht[2], Geoffrey Fosgate[3], Franck Forterre[1] and Bianca Hettlich[1]**

[1] Division of Small Animal Surgery, Department of Clinical Veterinary Medicine, Vetsuisse Faculty, University of Bern, Bern, Switzerland, [2] Division of Clinical Radiology, Department of Clinical Veterinary Medicine, Vetsuisse Faculty, University of Bern, Bern, Switzerland, [3] Department of Production Animal Studies, Faculty of Veterinary Science, University of Pretoria, Onderstepoort, South Africa

OPEN ACCESS

Edited by:
Andrea Tipold,
University of Veterinary Medicine Hannover, Germany

Reviewed by:
Colin John Driver,
Fitzpatrick Referrals Specialist Hospital, United Kingdom
Itay Srugo,
Veterinary Neurological Center, United States

****Correspondence:***
Bianca Hettlich
bianca.hettlich@vetsuisse.unibe.ch

Specialty section:
This article was submitted to Veterinary Neurology and Neurosurgery, a section of the journal Frontiers in Veterinary Science

Received: *20 July 2018*
Accepted: *18 September 2018*
Published: *05 October 2018*

Citation:
Düver P, Precht C, Fosgate G, Forterre F and Hettlich B (2018) Cervical Intervertebral Disk to Vertebral Body Ratios of Different Dog Breeds Based on Sagittal Magnetic Resonance Imaging. Front. Vet. Sci. 5:248. doi: 10.3389/fvets.2018.00248

Objective: To establish sagittal area and length reference values and ratios between apparently normal canine cervical vertebrae and intervertebral disks using magnetic resonance imaging.

Sample: Retrospective evaluation of cervical vertebral column magnetic resonance imaging studies of 44 dogs representing 5 different breeds (Labrador Retriever, $n = 10$; French Bulldog, $n = 10$; Great Dane, $n = 9$; Chihuahua, $n = 10$; Dachshund, $n = 5$).

Procedures: Mid-sagittal measurements of vertebral body and disk areas were obtained from C3 through C7 vertebrae and C2/C3 through C6/C7 intervertebral disks. Disk to vertebra area ratios were calculated and compared among dog breeds. Additionally, sagittal vertebral body and disk length measurements were obtained and disk to vertebra length ratios calculated. Inter and intra observer variability was assessed.

Results: There were significant differences for disk to vertebral body area and length ratios between evaluated dog breeds and cervical vertebral locations ($p < 0.001$). Mean area ratio of Chihuahuas was significantly larger than all other breeds, while results from Dachshunds were only significantly different than Chihuahuas and Labrador Retrievers. Mean area ratios were statistically different between the cranial and caudal cervical vertebral locations. Regarding length ratios, results from Chihuahuas were significantly different than all breeds except Dachshunds. Mean length ratios were statistically different between all cervical locations, except C2/C3 compared to C3/C4. Intra- and interobserver variability was very good to excellent.

Conclusion and Clinical Relevance: There are significant differences in area and length ratios between dog breeds. Differences also exist in area and length ratios between the cranial and caudal cervical vertebral column. These differences may play a role in the development of vertebral column diseases including intervertebral disk disease.

Keywords: canine, cervical vertebral column, morphometry, intervertebral disk, magnetic resonance imaging, area, length, ratio

INTRODUCTION

Morphometry, a quantitative analysis of the size and shape of a form, has been used in human and animal studies to identify relationships between specific anatomic structures and diseases (1–6). The canine vertebral column has been morphometrically evaluated using anatomic specimens (macerated vertebrae) and imaging modalities, such as radiography, computed tomography (CT) and magnetic resonance imaging (MRI) (7–12).

Common disorders of the canine cervical vertebral column include intervertebral disk diseases (IVDD) and cervical spondylomyelpathy (CSM) (13–17).

IVDD often affects chondrodystrophic dogs and is characterized by degeneration of the intervertebral disk with possible spinal cord compression by disk extrusion or protrusion (14, 15). Approximately 15% of IVDD occurs in the cervical vertebral column in dogs (18). CSM is a disease mainly of large and giant breed dogs causing cervical myelopathy due to progressive spinal cord compression (17). CSM has been divided into two distinctly different types: osseous-associated and disk-associated (OA-CSM and DA-CSM, respectively). Both of these diseases have been evaluated morphometrically using various imaging modalities (13, 19–24).

MRI analysis of cervical vertebral columns of Great Danes demonstrated morphometric differences between OA-CSM affected and non-affected dogs, including smaller intervertebral disk widths, smaller vertebral canal areas and smaller spinal cord areas (21). Regarding DA-CSM, morphometric MRI comparison of affected and non-affected Doberman Pinchers showed smaller spinal cord area, smaller vertebral canal height and more square shaped vertebral bodies compared to their normal counterparts (19, 20). Disk width was evaluated as a stand-alone morphometric MRI measurement in dogs with and without DA-CSM and was found to be positively associated with age but not associated with the clinical status of the dog (22). In another morphometric study using MRI, articular process conformation was compared between Doberman Pinchers and Great Danes. Dobermans were found to have more concave caudal articular surfaces in caudal cervical locations, a morphometric difference which was proposed to explain the high incidence of DA-CSM in Dobermans (25).

There appears to only be one morphometric study evaluating area measurements of vertebral bodies in animals (26). In this study, vertebral canal and vertebral body area (among various other measurements) was calculated using CT in a rat model for human disease. We are unaware of studies reporting on the use of area measurements of disk and vertebral body of cervical vertebral columns in different dog breeds and different cervical vertebral locations. Data regarding these ratios may be useful to try to link conformation to the development of diseases, such as IVDD and CSM.

Abbreviations: CT, computed tomography; IVDD, intervertebral disk disease; IVD, intervertebral disk; MRI, magnetic resonance imaging; CSM, cervical spondylomyelpathy; OA-CSM, osseous-associated cervical spondylomyelpathy; DA-CSM, disk-associated cervical spondylomyelpathy; LR, Labrador retriever; GD, Great Dane; FB, French bulldog; CH, Chihuahua; DH, Dachshund

The purpose of this study was to determine disk to vertebral body ratios at different cervical vertebral locations and in different dog breeds using mid-sagittal MRI images. We hypothesized that (1) there would be a difference in area and length ratios based on location within the cervical vertebral column and (2) between different breeds of dogs.

MATERIALS AND METHODS

The medical record system of the Vetsuisse Faculty, University of Bern, Switzerland, was searched for canine cervical vertebral column MRI studies performed between 2009 and 2016 through the Division of Clinical Radiology. Studies had to be obtained with proper patient positioning, be of good quality and be free of artifacts impairing evaluation of vertebral bodies and intervertebral disks (IVD). Dogs had to be mature based on physeal closure. Studies had to include the vertebral column from C2 to T1 and sagittal T2 weighted images of this area had to be available. Vertebrae C3 to C7 and intervertebral disks C2/C3 through C6/C7 were evaluated but only vertebrae and disks free of diseases, which would affect their imaging appearance and shape, were measured. Disks with advanced degeneration, protrusion or extrusion, or adjacent tissue changes that influenced disk appearance were excluded. Deformed, fractured or otherwise distorted vertebral bodies (i.e., due to neoplasia) and vertebrae with new bone formation, such as spondylosis deformans were also excluded. Intervertebral disks were evaluated using Pfirrmann grades, an MRI based grading system classifying intervertebral disks and stages of degeneration (27). Briefly, Pfirrmann Grade 1 IVD is considered normal and shows the nucleus pulposus as a bright white homogeneous structure. Nucleus pulposus and annulus fibrosus can be clearly distinguished and the IVD shows a normal size. Grade 2 describes a nonhomogeneous structure of the IVD with clear distinguished nucleus pulposus and annulus fibrosus and normal disk space. The higher the Pfirrmann grade, the more IVD degeneration is present, with a black disk, no distinction between annulus fibrosus and nucleus pulposus, a hypointense signal, and a collapsed disk space representing the highest grade (grade 5). Only IVDs with a Pfirrmann grade of 2 or less were included in this study.

Measurements

Patient positioning was standardized with dogs positioned in dorsal recumbency with the head and neck extended and thoracic limbs pulled caudally. Images were obtained using a MRI with 1.0 Tesla field strength and fast spin-echo T2-weighted sequence in sagittal plane with repetition time 2,500–6,000 ms, echo time 100 ms, slice thickness 2.5–4.0 mm and gap 0.5 mm depending on the size of the patient (Philips Panorama HFO, Philips Medical Systems Nederland B.V., Best, Netherlands). All measurements were performed on midsagittal T2 weighted images of the vertebral column section evaluated. Midsagittal plane was identified by help of a concurrently displayed linked dorsal plane image using an imaging software program (IMPAX EE R20.Ink, AGFA HealthCare N.V., Belgium). Tools of the same program were used

to outline vertebral bodies and IVDs and obtain area and length measurements.

Area Measurements

Vertebral bodies (**Figure 1A**): A line was drawn along the outer vertebral cortex of each vertebral body. In areas of poorly defined cortical bone continuity, such as the mid-portion of the dorsal cortex of the vertebral body (ventral aspect of vertebral canal), a "best-fit" line was drawn to connect the two points of visible cortex. Due to the inability to distinguish between the hypointense cortical bone and annulus fibrosus along the vertebral endplates, the middle distance of the hypointense area between hyperintense medullary bone and nucleus pulposus was chosen as the border between cortical bone and annulus fibrosus.

Intervertebral disk (**Figure 1B**): A line was drawn around the outer limit of the annulus fibrosus dorsally and ventrally. Along the vertebral endplates, the previously described middle distance line was used to outline the remainder of the IVD.

The area ratio was calculated between the IVD and the vertebral body immediately caudal using the following equation:

$$area\ ratio = \frac{\textbf{disk area}}{\textbf{vertebra area}}$$

Length Measurement

Vertebral bodies (**Figure 1C**): The length of the vertebral body was measured from the midpoint of the cranial to the midpoint of the caudal vertebral endplate. To define these endplate midpoints, a line was drawn from the most prominent dorsal and to ventral bone protuberances associated with each of the cranial and caudal endplate. The midpoint of the line was determined. A connecting line through the midpoint of each of these lines was used to measure the length of the vertebral body, reaching from the most cranial to caudal cortex.

Intervertebral disk (**Figure 1D**): A height measurement line was drawn from the most dorsal to the most ventral aspect of the IVD. At the midpoint of this line, a perpendicular second line was drawn reaching from the cranial to caudal border of the IVD.

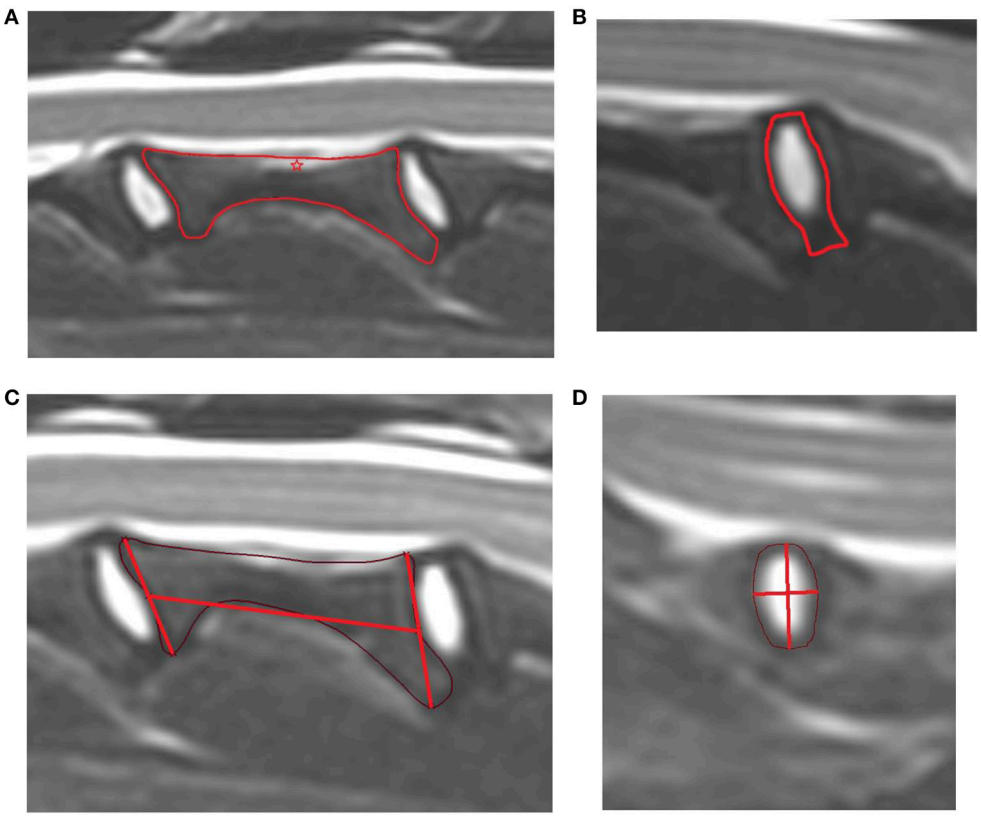

FIGURE 1 | (A) Example of the area measurement of a cervical vertebral body (red line) in a Labrador retriever. The star indicates the area in the middle of the dorsal vertebral body where the cortex cannot be followed continuously and a line of best fit was drawn. **(B)** Example of the area measurement of a cervical intervertebral disk (red line) in a Labrador Retriever. **(C)** Example of the length measurement of a cervical vertebral body in a Labrador retriever. The area outline was performed (thin purple line), then lines were drawn along the cranial and caudal endplate from the furthest dorsal and ventral aspect of the area outline (vertical red lines). The midpoints of these lines were determined and a connecting line through the midpoints was used to measure the length of the vertebral body, reaching from the most cranial to caudal cortex. **(D)** Example of the length measurement of a cervical intervertebral disk in a Chihuahua. The area outline was performed (thin red line) and a vertical line drawn from the most dorsal to ventral aspect. At the middle distance of this line, a second horizontal line was drawn at a right angle from cranial to caudal area outline. This horizontal line was used for length measurement of the disk.

This line represented the length of the IVD. The length ratio was calculated using the following equation:

$$length\ ratio = \frac{\textbf{disk length}}{\textbf{vertebra length}}$$

Intra- and Interobserver Variability

Measurements of all MRI studies were performed by one person using the same computer station and screen settings. To assess intraobserver variability, the same person repeated area and length measurements of 2 randomly selected MRI studies from each breed (except Dachshund) without access to previous measurement data. The timing between the first and the second measurement averaged 5 weeks.

To assess interobserver variability, these same 8 MRI studies used for intraobserver variability were measured by two other observers (board certified surgeon and a board certified radiologist). These observers were blinded to all previously obtained measurement data.

Statistical Analysis

Disk ratios were assessed for normality by calculating descriptive statistics, plotting histograms, and performing the Anderson-Darling test in commercial software (MINITAB Statistical Software, Release 13.32, Minitab Inc, State College, Pennsylvania, USA; NCSS 10 Statistical Software, Version 10.0.12, East Kaysville, Utah, USA). Disk ratios were described using the median and range due to the small sample size and an apparent violation of the normality assumption. Correlation between area and length ratios was assessed using Spearman's rho. The coefficient of variation was calculated to determine intra and inter observer variation among repeated measurements. The coefficient of variation is calculated as the standard deviation divided by the mean of repeated ratio measurements. Using the coefficient of variation, 0–5% was defined as "excellent," 5–10% as "very good," 10–15% as "good," and 15–20% as "acceptable." Natural logarithm transformed disk ratio data were analyzed using a mixed-effects linear regression model to determine the effects of breed and disk space. A random effect was included in the model for dog to account for the repeated measurements and fixed effect terms were included for breeds and disk space. Independent models were fit for area and length ratios and *post-hoc* pairwise comparisons were adjusted using Bonferroni correction of *p*-values. Mixed-effects models were implemented in commercially available software (IBM SPSS Statistics Version 23, International Business Machines Corp., Armonk, NY, USA) and significance was set as $p < 0.05$.

RESULTS

Between 2009 and 2016, 362 canine cervical vertebral column MRIs were performed at the Vetsuisse Faculty, University of Bern. Of the most common breeds represented, there were 50 cervical MRIs of French Bulldogs, 19 of Labrador Retrievers, 17 of Chihuahuas, 14 of Great Danes and 8 of Dachshunds. Studies of cervical MRIs of 44 dogs were ultimately included (**Table 1**) and represented five different dog breeds: Labrador retriever (LR, $n = 10$), Great Dane (GD, $n = 9$), French bulldog (FB, $n = 10$), Chihuahua (CH, $n = 10$), and Dachshund (DH, $n = 5$). Of these dogs, there were 21 females (15 spayed, 6 intact) and 23 males (15 intact, 8 neutered). The most common pathologies diagnosed were IVDD, OA-CSM, and intracranial disease (**Table 2**). In 3 MRI studies, no causative pathology was identified.

TABLE 1 | Weight and age of 44 dogs including Labrador Retriever (LR, $n = 10$), Great Dane (GD, $n = 9$), French Bulldog (FB, $n = 10$), Chihuahua (CH, $n = 10$), and Dachshund (DH, $n = 5$).

	Weight (kg)				Age (months)			
Breed	**Mean**	**SD**	**Min.**	**Max.**	**Mean**	**SD**	**Min.**	**Max.**
LR	29.7	7.5	21.0	40.0	91.3	37.4	29	149
GD	69.8	9.0	60.0	85.0	40.8	20.9	15	75
FB	12.8	2.0	8.1	16.0	62.2	17.5	35	80
CH	2.6	1.1	1.5	5.3	51.3	26.9	20	90
DH	7.7	1.8	5.1	9.9	97.0	22.5	74	130

SD, standard deviation.

Comparison of Breeds

There were significant differences for disk to vertebral body area and length ratios between evaluated dog breeds and cervical vertebral locations (**Table 3**). The mean area ratio of Chihuahuas was significantly greater than all other evaluated breeds (Labrador retrievers, Great Danes, French bulldogs, and Dachshunds). Dachshunds also had significantly greater mean area ratios compared to Labrador retrievers. The mean length ratios of Chihuahuas were significantly greater than all other breeds except Dachshunds.

Comparison of Location

Both area and length ratios were significantly different between cranial and caudal cervical locations, with smaller ratios in the cranial locations (**Table 3**).

Area Ratio Compared to Length Ratio

There was a strong correlation between area and length ratios (rho = 0.821, $p < 0.001$; **Figure 2**). However, Chihuahuas and French bulldogs tended to have higher area ratios compared to Great Danes and Labrador retrievers that tended to have lower ratios.

Repeatability

Intraobserver variability for area and length ratio was "excellent" overall (**Table 4**). When evaluating single breeds and locations, intraobserver variability was "very good" to "excellent," respectively.

Interobserver variability was "very good" for area and length ratio overall. When evaluating single breeds and locations, interobserver variability was "very good" and "excellent," respectively.

TABLE 2 | Pathologies compatible with presenting clinical signs diagnosed on MRI.

		Diseases affecting the region of interest of the study			Diseases of other locations					
	Normal	IVDD	CSM	Neoplasia	Trauma	Peripheral neuropathy	Arachnoid cyst	Syrinx	Intra-cranial	Atlantoaxial instability
	n = 3	*n* = 19	*n* = 8	*n* = 1	*n* = 1	*n* = 1	*n* = 1	*n* = 1	*n* = 7	*n* = 2
LR *n* = 10	1	5	0	1	1	1	0	0	1	0
GD *n* = 9	1	0	8	0	0	0	0	0	0	0
FB *n* = 10	1	8	0	0	0	0	0	1	0	0
CH *n* = 10	0	2	0	0	0	0	1	0	5	2
DH *n* = 5	0	4	0	0	0	0	0	0	1	0

TABLE 3 | Descriptive statistics and comparison of disk ratios based on breed and cervical disk based on a linear mixed-effects model.

Measure	Variable	Level	Disk ratio		*P*-value
			Mean	Median (IQR)	
Area ratio	Breed				<0.001
		LR	0.222[a]	0.211 (0.192, 0.250)	
		GD	0.227[a,b]	0.224 (0.201, 0.249)	
		FB	0.239[a,b]	0.252 (0.230, 0.282)	
		CH	0.349[c]	0.341 (0.313, 0.395)	
		DH	0.280[b]	0.287 (0.254, 0.310)	
	Location				<0.001
		C2/C3	0.240[a]	0.226 (0.200, 0.263)	
		C3/4	0.249[a]	0.240 (0.190, 0.307)	
		C4/5	0.273[b]	0.262 (0.206, 0.324)	
		C5/6	0.274[b]	0.260 (0.228, 0.308)	
		C6/7	0.288[b]	0.283 (0.240, 0.343)	
Length ratio	Breed				<0.001
		LR	0.216[a]	0.218 (0.182, 0.239)	
		GD	0.228[a,b]	0.222 (0.189, 0.260)	
		FB	0.214[a]	0.213 (0.175, 0.242)	
		CH	0.315[c]	0.308 (0.278, 0.358)	
		DH	0.279[b,c]	0.291 (0.228, 0.336)	
	Location				<0.001
		C2/C3	0.206[a]	0.195 (0.169, 0.229)	
		C3/4	0.222[a]	0.214 (0.175, 0.247)	
		C4/5	0.245[b]	0.233 (0.203, 0.293)	
		C5/6	0.273[c]	0.258 (0.242, 0.319)	
		C6/7	0.294[d]	0.282 (0.259, 0.329)	

IQR, interquartile range. The small letters a–d represent statistical differences—same letters indicate no difference, different letters indicate statistically significant difference.

DISCUSSION

Various imaging techniques have been used to morphometrically evaluate the canine cervical vertebral column and compare affected and non-affected dogs (19–23). To the authors' knowledge, this is the first study comparing mid-sagittal intervertebral disk to vertebral body area and length ratios of the cervical vertebral column in different dog breeds. Variations in disk to vertebral body ratio may influence local biomechanics and support development of certain degenerative diseases. Validating our hypothesis, results showed that (1) there was a statistically significant difference in area and length ratios between dog breeds and (2) between cranial and caudal cervical locations. Results of this study help to establish reference values of these ratios in various dog breeds and in different cervical locations.

The smallest breed of dog in our study (Chihuahua) had the highest disk to vertebral body area ratio, which was statistically different to all other breeds. A high area ratio means that the size of the vertebral body is relatively small compared to the intervertebral disk. Differences in this ratio could have effects on stresses placed on the intervertebral disk and vertebral structures. It is not possible to draw conclusions from this finding regarding the development of vertebral column diseases. Only 2/10 Chihuahuas were diagnosed with IVDD in contrast to 4/5 Dachshunds, 8/10 French Bulldogs and 5/10 Labradors. Therefore, the clinical significance of a high area ratio is unknown regarding the development of IVDD. Eight of nine Great Danes were diagnosed with OA-CSM; however, their area ratios—while lower compared to Chihuahuas—were not different to Dachshund, French Bulldogs and Labrador Retrievers. Since OA-CSM appears to cause changes mostly to the articular facets, it may be that this disease does not cause morphometric changes of the mid-sagittal vertebral body and disk. It would be interesting to assess these ratios in dogs affected with DA-CSM, such as the Doberman. Unfortunately, insufficient MRIs of the latter breed were available for evaluation in this study, precluding further speculation.

Regardless of overall differences in ratios between dog breeds, all dogs demonstrated smaller disk to vertebral body ratios in cranial cervical locations compared to caudal locations for both area and length. This indicates that cranial vertebrae had larger areas and lengths in relation to their respective disks than caudal vertebrae. Changes in such ratios, with larger and longer cranial vertebral bodies, may influence cervical vertebral column biomechanics. Incidence of canine cervical IVDD is highest in cranial cervical locations (18, 28). The relatively larger and longer vertebral bodies in the cranial cervical vertebral column may lead to increased lever arm stresses on the adjacent disk spaces and may contribute to the higher rate of IVDD in these locations.

In this study, dog breeds were selected to represent chondrodystrophic and non-chondrodystrophic large and small dog breeds. Dog breeds were included if acceptable MRI studies

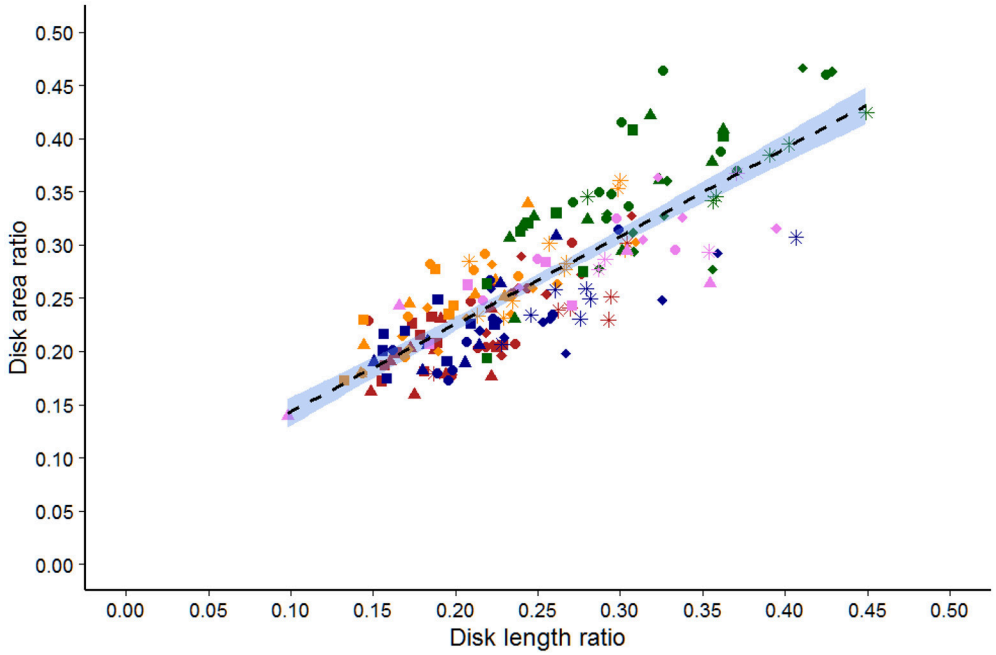

FIGURE 2 | Scatter plot of the area vs. length ratios determined by a single observer for 44 dogs of five breeds. Labrador retriever (Red), French bulldog (orange), Great Dane (blue), Chihuahua (Green), and Dachshund (violet). Squares are C2/C3, triangles are C3/C4, circles are C4/C5, diamonds are C5/C6, and stars are C6/C7 disks.

(minimum of 5 animals per breed) were available for the study period. The limited number of dogs in this study ($n = 44$) is similar to other comparable studies (11, 12).

Computed tomography and MRI are common advanced imaging modalities to evaluate the cervical vertebral column. While CT is preferred for assessment of bony structures, MRI is the modality of choice for the evaluation of intervertebral disks and spinal cord (29–31). In our study, area measurements were based on MRI, as we wanted to evaluate the intervertebral disk in addition to vertebral bone. Moreover, MRI is the first choice modality for diagnostic imaging of the head and neck at our institution and therefore provided the highest number of imaging studies per dog breed.

A canine cadaver study, comparing spinal canal and spinal cord measurements on T1 and T2 weighted images on MRI to the actual specimen, showed improved correlation of T2 weighted imaging and anatomical measurements compared to T1 weighted images (12). Consequently in our study, T2 weighted images were used to evaluate vertebrae and disks. Challenges of using T2 weighed images included the inability to clearly identify cortical bone in all areas of the outer vertebral body cortex. For example, the border of the outer cortical bone was not always clear along the dorsal vertebral body bone. In this area, cortical bone was commonly not continuously displayed in the central portion (star in **Figure 1A**). To address this, evaluators were asked to connect the visible parts of the vertebral cortical boundary with a line of best fit. Another challenge was distinction between the border of the annulus fibrosus and the vertebral endplate cortical bone, as both structures are hypointense in T2 weighted images. The middle distance of the hypointense layer combining the nucleus pulposus and endplate was defined as the border and used as the line of separation for area measurements. While these definitions and solutions helped to standardize the area outline in this study, they may not represent the true outline. Furthermore, it was not always possible to measure at the exact mid-sagittal plane because of the limited number of slices procured. Consequently, the sagittal plane closest to the center was selected for each vertebra and disk.

While patient positioning during MRI was standardized, it is still possible that disk dimensions were influenced by positioning (i.e., effects on intervertebral disk with an extended neck position in a Great Dane with a long vs. a French bulldog with a short cervical vertebral column).

Ideally, disk to vertebral body ratio measurements for reference values should be obtained from entirely normal cervical vertebral columns to exclude possible influence of disease on conformation in adjacent, normal appearing structures. Due to a high incidence of vertebral column disease in the study population, there were insufficient numbers of dogs with entirely normal cervical vertebral columns. Of dogs with clinical or incidental IVDD, measurements were limited to intervertebral disks with a Pfirrmann grade of 2 or less. While the inclusion of disks with mild degenerative changes may not be ideal, area and length measurements are not expected to be influenced. A critique on principle is the inclusion of MRI studies with any grade of disk degeneration. While disks with Pfirrmann grade 3–5 were excluded from analysis, other vertebrae and disks of the same dog were still included. It is unknown if dogs with

TABLE 4 | Repeatability assessed by calculation of the coefficient of variation (CV) for repeated measures concerning disk area and length ratios measured via MRI and stratified based on breed and disk space.

Measure	Variable	Level	Intra-observer (%)		Inter-observer (%)	
			Mean	Median (IQR)	Mean	Median (IQR)
Area ratio	Overall	All	4.59	2.95 (1.46, 5.40)	6.25	6.12 (2.55, 9.50)
	Breed	LR	5.78	3.40 (2.54, 10.96)	8.98	9.89 (4.99, 13.13)
		GD	2.21	1.14 (0.69, 5.02)	3.98	3.45 (2.24, 6.27)
		FB	2.76	1.94 (1.57, 3.23)	3.95	3.98 (1.24, 5.97)
		CH	7.23	5.17 (2.74, 10.56)	7.62	7.41 (5.96, 10.34)
	Disk	C2/C3	7.72	7.79 (2.08, 10.69)	5.28	3.62 (1.43, 9.47)
		C3/4	3.71	1.51 (0.98, 5.40)	6.31	5.95 (2.41, 8.98)
		C4/5	2.74	2.65 (1.44, 3.69)	5.67	3.98 (1.83, 9.83)
		C5/6	3.84	3.65 (1.76, 5.36)	7.01	6.68 (4.61, 9.32)
		C6/7	5.22	2.96 (1.11, 10.11)	6.85	6.32 (3.66, 10.25)
Length ratio	Overall	All	2.77	1.51 (0.88, 4.23)	5.30	5.18 (2.94, 6.62)
	Breed	LR	2.98	2.52 (0.73, 4.35)	4.80	4.34 (2.85, 7.38)
		GD	1.74	1.33 (0.87, 1.92)	4.24	3.44 (1.97, 6.40)
		FB	3.66	3.90 (1.10, 6.30)	6.97	6.47 (3.48, 8.33)
		CH	2.86	1.77 (0.83, 4.25)	5.51	5.54 (3.86, 6.44)
	Disk	C2/C3	4.98	4.96 (1.91, 6.98)	7.73	5.81 (5.27, 9.47)
		C3/4	2.58	1.39 (0.41, 3.29)	5.04	5.66 (3.36, 6.37)
		C4/5	1.88	1.09 (0.84, 3.70)	4.59	4.35 (2.46, 6.61)
		C5/6	1.83	1.42 (0.99, 3.05)	3.76	3.04 (1.84, 5.55)
		C6/7	2.83	1.87 (0.97, 5.28)	5.63	5.22 (3.02, 8.63)

disk degeneration have different disk to vertebral body ratios in general, even in areas without obvious disease. To determine this, measurements would need to be limited to MRI studies with entirely normal intervertebral disks.

Area measurements of the vertebral bodies and disks were time consuming. To provide a faster and potentially easier method, we compared disk to vertebral area ratios to length ratios. Analysis showed that area to length ratios correlated well-within a particular dog breed but deviated between different breeds. This precludes the use of length ratios when comparing data between different dog breeds. While we attempted to standardize the method for length measurement, we could not account for the inherently variable anatomic shapes of vertebral bodies. It is possible that different methods for determining length ratios may have an improved correlation to area measurements between breeds.

In conclusion, this study provides area and length ratios of intervertebral disks and vertebral bodies in the cervical vertebral column of various dog breeds. These ratios may serve as a baseline for further morphometric evaluation of cervical vertebral column diseases. Whether such ratios can be used to predict the development of specific diseases requires further investigation.

AUTHOR CONTRIBUTIONS

PD: study design, measurements, and generation of manuscript; CP: study design, interobserver control measurements, and correction of manuscript; GF: statistical analysis; FF: correction of manuscript; BH: study design, interobserver control measurements, and correction of manuscript.

REFERENCES

1. Utkualp N, Ercan I. Anthropometric measurements usage in medical sciences. *Biomed Res Int.* (2015) 2015:404261. doi: 10.1155/2015/404261
2. Shiraishi N, Katayama A, Nakashima T, Yamada S, Uwabe C, Kose K. et al. Morphology and morphometry of the human embryonic brain: a three-dimensional analysis. *Neuroimage* (2015) 115:96–103. doi: 10.1016/j.neuroimage.2015.04.044
3. Vrancken AC, Crijns SP, Ploegmakers MJ, O'Kane C, van Tienen TG, Janssen D, et al. 3D geometry analysis of the medial meniscus–a statistical shape modeling approach. *J Anat.* (2014) 225:395–402. doi: 10.1111/joa.12223
4. Pazzaglia UE, Donzelli CM, Izzi C, Baldi M, Di Gaetano G, Bondioni M. Thanatophoric dysplasia. Correlation among bone X-ray morphometry, histopathology, and gene analysis. *Skeletal Radiol.* (2014) 43:1205–15. doi: 10.1007/s00256-014-1899-1
5. Dabanoglu I. Normal morphometry of the thoracic aorta in the German shepherd dog: a computed tomographic study. *Anat Histol Embryol.* (2007) 36:163–7. doi: 10.1111/j.1439-0264.2006.00717.x
6. Ondreka N, Amort KH, Stock KF, Tellhelm B, Klumpp SW, Kramer M, et al. Skeletal morphology and morphometry of the lumbosacral junction in German shepherd dogs and an evaluation of the possible genetic basis for radiographic findings. *Vet J.* (2013) 196:64–70. doi: 10.1016/j.tvjl.2012.07.015

7. Breit S, Künzel W. Osteological features in pure-bred dogs predisposing to cervical spinal cord compression. *J Anat.* (2001) 199(Pt 5):527–37. doi: 10.1046/j.1469-7580.2001.19950527.x
8. Breit S, Künzel W. A morphometric investigation on breed-specific features affecting sagittal rotational and lateral bending mobility in the canine cervical spine (C3–C7). *Anat Histol Embryol.* (2004) 33:244–50. doi: 10.1111/j.1439-0264.2004.00546.x
9. Drost WT, Lehenbauer TW, Reeves J. Mensuration of cervical vertebral ratios in Doberman pinschers and Great Danes. *Vet Radiol Ultrasound* (2002) 43:124–31. doi: 10.1111/j.1740-8261.2002.tb01659.x
10. Fourie SL, Kirberger RM. Relationship of cervical spinal cord diameter to vertebral dimensions: a radiographic study of normal dogs. *Vet Radiol Ultrasound* (1998) 40:137–43.
11. Seo E, Choi J, Choi M, Yoon J. Computed tomographic evaluation of cervical vertebral canal and spinal cord morphometry in normal dogs. *J Vet Sci.* (2014) 15:187. doi: 10.4142/jvs.2014.15.2.187
12. Hecht S, Huerta MM, Reed RB. Magnetic resonance imaging (MRI) spinal cord and canal measurements in normal dogs. *Anat Histol Embryol.* (2014) 43:36–41. doi: 10.1111/ahe.12045
13. Murthy VD, Gaitero L, Monteith G. Clinical and magnetic resonance imaging (MRI) findings in 26 dogs with canine osseous-associated cervical spondylomyelopathy. *Can Vet J.* (2014) 55:169–74.
14. Toombs JP. Cervical intervertebral disc disease in dogs. *Compend Contin Educ Pract Vet*. (1992) 14:1477–86.
15. Hansen HJ. A pathologic-anatomical study on disk degeneration in the dog. *Acta Orthop Scand.* (1952) 11:1–117. doi: 10.3109/ort.1952.23.suppl-11.01
16. Olsson SE, Hansen HJ. Cervical disc protrusions in the dog. *J Am Vet Med Assoc.* (1952) 121:361–70.
17. da Costa RC. Cervical spondylomyelopathy (Wobbler syndrome) in dogs. *Vet Clin Small Anim Pract.* (2010) 40:881–913. doi: 10.1016/j.cvsm.2010.06.003
18. Hakozaki T, Iwata M, Kanno N, Harada Y, Yogo T, Tagawa M, et al. Cervical intervertebral disk herniation in chondrodystrophoid and nonchondrodystrophoid small-breed dogs: 187 cases (1993–2013). *J Am Vet Med Assoc.* (2015) 247:1408–11. doi: 10.2460/javma.247.12.1408
19. Decker SD, Gielen IM, Duchateau L, van Bree HJ, Waelbers T, Bavegems V, et al. Morphometric dimensions of the caudal cervical vertebral column in clinically normal Doberman Pinschers, English Foxhounds and Doberman Pinschers with clinical signs of disk-associated cervical spondylomyelopathy. *Vet J.* (2012) 191:52–7. doi: 10.1016/j.tvjl.2010.12.017
20. Decker SD, Gielen IM, Duchateau L, Saunders JH, van Bree HJ, Polis I, et al. Magnetic resonance imaging vertebral canal and body ratios in Doberman Pinschers with and without disk-associated cervical spondylomyelopathy and clinically normal English Foxhounds. *Am J Vet Res.* (2011) 72:1496–504. doi: 10.2460/ajvr.72.11.1496
21. Martin-Vaquero P, da Costa RC, Lima CG. Cervical spondylomyelopathy in Great Danes: a magnetic resonance imaging morphometric study. *Vet J.* (2014) 201:64–71. doi: 10.1016/j.tvjl.2014.04.011
22. Decker SD, Gielen IM, Duchateau L, Volk HA, Van Ham LM. Intervertebral disk width in dogs with and without clinical signs of disk associated cervical spondylomyelopathy. *BMC Vet Res.* (2012) 8:126. doi: 10.1186/1746-6148-8-126
23. Costa RC, Parent JM, Dobson H, Dobson H, Holmberg DL, Lamarre J. Morphologic and morphometric magnetic resonance imaging features of Doberman Pinschers with and without clinical signs of cervical spondylomyelopathy. *Am J Vet Res.* (2006) 67:1601–12. doi: 10.2460/ajvr.67.9.1601
24. Lim J, Yoon Y, Hwang T, Lee HC. Novel vertebral computed tomography indices in normal and spinal disorder dogs. *J Vet Sci.* (2018) 19:296–300. doi: 10.4142/jvs.2018.19.2.296
25. Bonelli MA, da Costa RC, Martin-Vaquero P, Lima CG. Comparison of angle, shape, and position of articular processes in Dobermans and Great Danes with and without cervical spondylomyelopathy. *BMC Vet Res.* (2017) 13:77. doi: 10.1186/s12917-017-0997-4
26. Laing AC, Cox R, Tetzlaff W, Oxland T. Effects of advanced age on the morphometry and degenerative state of the cervical spine in a rat model. *Anat Rec.* (2011) 294:1326–36. doi: 10.1002/ar.21436
27. Bergknut N, Auriemma E, Wijsman S, Voorhout G, Hagman R, Lagerstedt AS, et al. Evaluation of intervertebral disk degeneration in chondrodystrophic and nonchondrodystrophic dogs by use of Pfirrmann grading of images obtained with low-field magnetic resonance imaging. *Am J Vet Res.* (2011) 72:893–8. doi: 10.2460/ajvr.72.7.893
28. Cherrone KL, Dewey CW, Coates JR, Bergman RL. A retrospective comparison of cervical intervertebral disk disease in nonchondrodystrophic large dogs versus small dogs. *J Am Anim Hosp Assoc.* (2004) 40:316–20. doi: 10.5326/0400316
29. Decker SD, Gielen IM, Duchateau L, Polis I, Van Bree HJ, Van Ham LM. Agreement and repeatability of linear vertebral body and canal measurements using computed tomography (CT) and low field magnetic resonance imaging (MRI). *Vet Surg.* (2010) 39:28–34. doi: 10.1111/j.1532-950X.2009.00559.x
30. Gopal MS, Jeffery ND. Magnetic resonance imaging in the diagnosis and treatment of a canine spinal cord injury. *J Small Anim Pract.* (2001) 42:29–31. doi: 10.1111/j.1748-5827.2001.tb01981.x
31. Levitski RE, Lipsitz D, Chauvet AE. Magnetic resonance imaging of the cervical spine in 27 dogs. *Radiol Ultrasound* (1999) 40:332–41.

Conflict of Interest Statement: The authors declare that the research was conducted in the absence of any commercial or financial relationships that could be construed as a potential conflict of interest.

frontiers in Veterinary Science

ORIGINAL RESEARCH
published: 15 February 2018
doi: 10.3389/fvets.2018.00016

Magnetic Resonance Imaging Signal Alterations in Paraspinal Muscles in Dogs with Acute Thoracolumbar Intervertebral Disk Extrusion

*Peter Trampus[1], Christine Goepfert[2], Monika Welle[2], Diana Henke[3†], Franck Forterre[4] and Daniela Schweizer-Gorgas[1]**

[1] Division of Clinical Radiology, Vetsuisse-Faculty, University of Bern, Bern, Switzerland, [2] Institute of Animal Pathology, Vetsuisse-Faculty, University of Bern, Bern, Switzerland, [3] Division of Clinical Neurology, Vetsuisse-Faculty, University of Bern, Bern, Switzerland, [4] Division of Small Animal Surgery, Vetsuisse-Faculty, University of Bern, Bern, Switzerland

OPEN ACCESS

Edited by:
Andrea Tipold,
University of Veterinary Medicine Hannover, Germany

Reviewed by:
Anita Shea,
Animal Health Trust, United Kingdom
Thomas Robert Harcourt-Brown,
University of Bristol, United Kingdom

***Correspondence:**
Daniela Schweizer-Gorgas
daniela.schweizer@vetsuisse.unibe.ch

†Present address:
Diana Henke,
Tierklinik am Hasenberg,
Stuttgart, Germany

Specialty section:
This article was submitted to Veterinary Neurology and Neurosurgery, a section of the journal Frontiers in Veterinary Science

Received: 29 September 2017
Accepted: 29 January 2018
Published: 15 February 2018

Citation:
Trampus P, Goepfert C, Welle M, Henke D, Forterre F and Schweizer-Gorgas D (2018) Magnetic Resonance Imaging Signal Alterations in Paraspinal Muscles in Dogs with Acute Thoracolumbar Intervertebral Disk Extrusion. Front. Vet. Sci. 5:16. doi: 10.3389/fvets.2018.00016

Muscle signal alteration detected on MRI is seen in diverse pathologic conditions. We observed signal alterations within the paraspinal muscles in dogs with acute thoracolumbar intervertebral disk extrusion. The aim of this retrospective study was to describe MRI features of paraspinal muscle signal alteration in dogs with acute thoracolumbar intervertebral disk extrusion and to investigate an association of the signal alterations with neurological grade, type and location of intervertebral disk extrusion, degree of spinal cord compression, and presence of epidural hemorrhage. Medical records of dogs undergoing MRI because of thoracolumbar intervertebral disk extrusion between August 2014 and June 2016 were reviewed. MRI was evaluated for SI changes within the paravertebral musculature, their location, extension, affected muscles, contrast enhancement, and signal void in T2* sequences. Intervertebral disk herniation was categorized as acute non-compressive nucleus pulposus extrusion (ANNPE) or compressive intervertebral disk disease. In five patients, muscle biopsies of areas with signal intensity changes were taken during surgery. In total, 103 dogs were enrolled in the study. Paraspinal muscle signal alterations were visible in 37 dogs (36%) affecting the epaxial musculature ($n = 17$), hypaxial musculature ($n = 12$), or both ($n = 8$). All signal alterations were hyperintense on T2-weighted images and iso- or hypointense in T1-weighted images. Signal void in T2* was not observed in any dog. Postcontrast sequences were available in 30 of the 37 dogs and showed enhancement in 45%. There was neither an association with degree of compression nor epidural hemorrhage. Intervertebral disk extrusion caudal to L1 and a higher neurological grade was associated with the presence of muscle changes. Histopathology revealed mild to moderate acute muscle fiber degeneration with edema and necrosis in three of five samples. The MRI, as well as the muscle samples, show rather unspecific changes. The underlying pathomechanism might be related to ischemia or muscle spasm, but also denervation edema may explain the signal alteration.

Keywords: magnetic resonance imaging, paraspinal muscle, thoracolumbar, intervertebral disk extrusion, dog, signal alteration

INTRODUCTION

Magnetic resonance imaging (MRI) signal intensity of normal skeletal muscle is generally slightly higher than that of water and much lower than fat on T1-weighted (T1W) images and much lower than both fat and water on T2-weighted (T2W) images (1). Alterations of signal intensity of skeletal muscles due to pathologic conditions is easily identified on inversion-recovery and fat-suppressed T2W images (1, 2). The potential causes are diverse, but usually the abnormal signal intensity identified on MRI falls into one of three recognizable patterns: edematous lesions, mass lesions, or fatty infiltration (1). All three patterns have been identified within the paraspinal muscles of dogs on MRI. Edematous lesions of the paraspinal muscles have been observed in immune-mediated polymyositis of the sublumbar muscles (3), associated with meningoencephalitis of unknown origin in the cervical musculature, or due to paraspinal infection in the ventral cervical and lumbar musculature (4). In cases of paraspinal infection with abscess formation, a mass effect caused by cavitary lesions may be identified on MRI (4). Neoplastic lesions result in mass lesions within the musculature either originating from the vertebral column or the paraspinal musculature itself. A third pattern consists of fatty infiltration of paraspinal muscles and has been observed in chondrodystrophic and non-chondrodystrophic dogs, probably driven by a combination of chronicity and severity of spinal cord pathology (5).

In dogs with acute intervertebral disk herniation, we previously observed signal alterations with an edematous pattern in the paravertebral muscles. To the best of our knowledge, this finding has not been reported in the current literature. Therefore, the first aim of this retrospective study was to assess the prevalence of signal alterations within the paravertebral muscles in dogs with acute thoracolumbar intervertebral disk extrusion. Second, to describe their MRI features and investigate possible associations between the intervertebral disk herniation and neurological findings. Furthermore, we performed a histological examination of the musculature with signal alterations in five dogs to investigate the underlying pathological features.

MATERIALS AND METHODS

Patients

Medical records between August 2014 and June 2016 were reviewed and scrutinized for dogs undergoing MRI of the thoracolumbar spine as a result of acute intervertebral disk disease. Dogs were included in the study if they were presented for MRI within 7 days of the onset of clinical signs. Further inclusion criteria were a neurologic examination and that the MRI examination protocol included a fat-suppressed T2W sequence. Dogs were excluded when the medical history suggested changes in the spinal musculature may have occurred. This could be a consequence of a car accident, a fall from a great height, previous spinal surgery within a period of 1 year or previous injections in the paraspinal region. MRI examination was performed in a 1.0-T open permanent magnet (Philips HFO Panorama, Philips Medical Systems, PC Best, Netherlands).

Duration of clinical symptoms and neurological grade was noted based on clinical records. The neurological grade was classified based on neurologic examination as grade 1 (pain only), grade 2 (ambulatory paraparesis), grade 3 (non-ambulatory paraparesis), grade 4 (paraplegia with no loss of deep pain sensation), or grade 5 (paraplegia with loss of deep pain sensation) (6).

Image Analysis

Images were reviewed by a board-certified radiologist (DSG) for the presence of signal alterations within the paravertebral musculature in fat-suppressed T2W sequences, either Short-TI Inversion Recovery sequence or Spectral Presaturation with Inversion Recovery sequence. If muscle signal alterations were present, their anatomical localization was noted based on the affected muscle, the site along the vertebral column, side, laterality (uni- or bilateral), length, and signal intensity in the different sequences as well as contrast enhancement in postcontrast sequences, if available, were assessed.

Furthermore, the location and type of intervertebral disk herniation [compressive versus non-compressive intervertebral disk extrusion] was noted. Acute noncompressive nucleus pulposus extrusion (ANNPE) represents an acute extrusion of normal, non-degenerate, nucleus pulposus material, causing minimal to no spinal cord compression. The diagnosis of ANNPE have been made based on established MRI criteria consisting of (i) a focal area of intramedullary spinal cord hyperintensity on T2W images that overlies an intervertebral disk space, (ii) a reduction in volume of the T2W hyperintense nucleus pulposus signal, (iii) mild narrowing of the associated disk space, and (iv) extradural material or signal intensity change with minimal or no spinal cord compression at this level (7). The location of compressive material within the vertebral canal and degree of spinal cord compression was described, as well as establishing the presence or absence of epidural hemorrhage within the vertebral canal. Similar to a previously described grading scheme, the degree of spinal cord compression was subjectively assessed as grade 1 (less than 30% impingement), grade 2 (30–40%), grade 3 (40–50%), and grade 4 (>50%) (8).

Muscle signal alterations were compared to the location of intervertebral disk extrusion. They were described as being cranial, at the same level or caudal and compared to the location of compressive material in terms of laterality (ipsilateral, contralateral or bilateral).

To investigate possible influencing factors on the prevalence of muscle signal alterations, the association between dogs with and without muscle signal alterations and type of disk extrusion, location of intervertebral disk extrusion, degree of compression, presence of epidural hemorrhage, duration of clinical symptoms in days, and neurological grade was calculated with a Chi-Square test. For factors with low cell frequency (<5) and binary outcome (type of disk extrusion) the Fisher's exact test was performed. For low cell frequency (<5) and non-binary outcome, the number of categories was reduced to increase the counts in the remaining. Grouping was performed for the parameter "location of disk extrusion" according to the presence or absence of ribs into T3–T13 and L1–L7. The parameter "neurological grade"

was grouped into ambulatory dogs (grades 1 and 2) versus non-ambulatory dogs (grade 3, 4, and 5).

Factors which were significantly associated ($P < 0.05$) with the presence of muscle signal alterations in the univariable analysis were offered to a multivariable logistic regression model. Variables were selected by stepwise backward selection, until only significant variables and confounders (variables changing the effect of other variables by >20%) remained in the model. Model fit was assessed by deviance statistics, chi-square goodness of fit test, and visual assessment of residuals. Statistical analysis was performed in NCSS 10 Statistical Software (2015) (NCSS, LLC. Kaysville, Utah). Differences were considered statistically significant if $P < 0.05$.

Histological Examination

In five patients, biopsies of muscle parts exhibiting signal alterations were taken during decompressive surgery following MRI. Samples were fixed in 10% formalin, processed routinely, stained with hematoxylin and eosin and assessed by a board-certified pathologist.

RESULTS

Dogs

In total, 103 dogs (49 females and 54 males) met the inclusion criteria. Mean age was 6.3 years (range: 1–13 years). Affected breeds were French Bulldog ($n = 28$), Dachshund ($n = 15$), Mixed-breed dog ($n = 12$), Shih Tzu ($n = 8$), Labrador Retriever ($n = 4$), Bolonka Swetna ($n = 3$), Coton de Tuléar ($n = 2$), Cocker Spaniel ($n = 2$), Yorkshire Terrier ($n = 2$), Poodle ($n = 2$), Schnauzer ($n = 2$), Basset Hound ($n = 2$), and one of each of the following American Staffordshire Terrier, Appenzeller Sennenhund, Beagle, Border Collie, Border Terrier, Cane Corso Italiano, Chihuahua, Chinese Crested Dog, German Shepherd Dog, Entlebucher Mountain Dog, Jack Russell Terrier, Lhasa Apso, Maltese Dog, Pug, Papillon, Pekinese, Pinscher, Siberian Husky, Tibetan Spaniel, Tibetan Terrier, and West Highland White Terrier.

Muscle Signal Alterations

Signal alterations within the paraspinal muscles were noted in 37 of 103 dogs (36%). The signal intensity was hyperintense on T2W images in 29 dogs, with changes only visible on fat-suppressed sequences in eight dogs (22%) (**Figures 1** and **2**). T1W images were available in 35 dogs (95%) with hypointense signal alterations observed in six dogs (17%). For the remaining 29 dogs (83%), lesions appeared isointense on T1W images.

Contrast medium was administered in 30/37 dogs with signal alterations. Enhancement was observed on either a T1W sequence or WATS (selective water excitation pulse) in 13 dogs (43%), and no enhancement was seen in 17 dogs (57%). T2* sequences were available in all dogs, a signal void in T2* was not detected in any dog.

Anatomical Localization

In 18 dogs (49%), unilateral signal alterations were observed (nine dogs right and nine dogs left); bilateral alterations were seen in 19 dogs (51%). The observed signal alterations were seen in one muscle ($n = 13$; 35%) or in multiple paraspinal muscles ($n = 24$; 65%). Two muscles were affected in 15 dogs (41%), three muscles in four dogs (11%), four muscles in four dogs (11%) and six muscles in one dog (3%). The most commonly affected muscles were *Mm. multifidi* ($n = 15$), *M. longissimus* ($n = 14$), *M. psoas major* ($n = 11$), *M. psoas minor* ($n = 11$) and *M. iliocostalis* ($n = 2$) (**Table 1**). Signal alterations were observed in the epaxial muscles in 17 dogs (46%) (**Figure 1**), in the hypaxial muscles in 12 dogs (32%) (**Figure 2**), and in both muscle groups in 8 dogs (21%).

The most cranially observed signal alteration was at the level of the eleventh thoracic vertebra, and the most caudal located changes were observed at the level of the seventh lumbar vertebra.

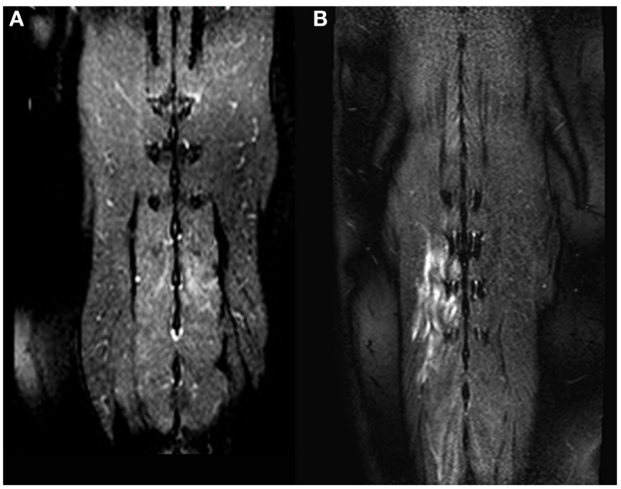

FIGURE 1 | Dorsal T2-weighted fat-suppressed images of two different dogs **(A,B)**. In **(A)**, only a mild signal alteration is visible in the *Mm. multifidi* of a French Bulldog with acute intervertebral disk herniation at the level L2/L3. More extensive signal alterations are visible in the *Mm. multifidi* of a Basset hound **(B)** with intervertebral disk extrusion at the level T12/T13. Both dogs had a neurologic grade of IV.

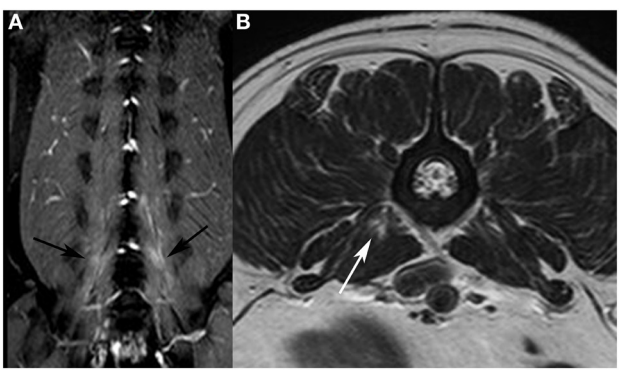

FIGURE 2 | Dorsal T2-weighted (T2W) fat-suppressed image of a French bulldog presented with intervertebral disk extrusion at the level L5/L6. **(A)** bilateral signal alterations are visible in the hypaxial muscles (black arrows). On the T2W fast spin echo transverse image **(B)**, only a focal area of increased signal intensity is visible in the *M. psoas major* on the right side (white arrow).

TABLE 1 | List of all dogs with muscle signal alteration with the duration of their clinical signs, neurologic grade, degree of compression, location of disk extrusion, level of muscle signal alteration in the vertebral column, number of adjacent vertebral bodies, affected muscles, and laterality.

Dogs with muscle signal alteration	Duration of clinical signs in days	Neurologic grade	Degree of compression	Location of disk extrusion	Level of muscle signal alteration	Number of adjacent vertebral bodies	*M. multifidus*	*M. longissimus*	*M. iliocostalis*	*M. psoas major*	*M. psoas minor*	Laterality
1	1	4	ANNPE	L1/L2	L1	1	x					Unilateral
2	1	5	3	L2/L3	T13–L3	4					x	Bilateral
3	1	4	4	T11/T12	T12–L1	3		x			x	Unilateral
4	1	4	3	L1/L2	L2	1					x	Unilateral
5	2	5	4	L4/L5	L6–L7	2					x	Bilateral
6	1	3	1	L3/L4	L2–L3	2		x				Unilateral
7	1	4	ANNPE	L2/L3	L4	1	x					Unilateral
8	1	1	3	L1/L2	L1 - L3	3	x					Unilateral
9	1	3	3	L5/L6	L5–L6	2		x			x	Bilateral
10	1	3	3	L3/L4	L3- L4	2		x		x	x	Unilateral
11	1	5	4	T12/T13	L2–L3	2				x		Bilateral
12	1	4	4	T12/T13	T12–T13	2	x					Unilateral
13	1	4	2	T12/T13	IVD L1/L2	1					x	Unilateral
14	1	4	2	L3/L4	L3–L5	3				x	x	Bilateral
15	1	5	1	T12/13	T11–L2	5	x	x				Bilateral
16	4	2	3	T12/T13	T12–T13	2	x					Bilateral
17	5	4	2	L1/L2	L3–L4	2	x	x			x	Bilateral
18	7	3	4	L4/L5	L4–L6	3	x	x				Bilateral
19	7	4	4	T12/T13	L1–L2	2	x					Bilateral
20	1	3	2	L3/L4	IVD L3/L4	1		x		x		Bilateral
21	4	4	4	L2/L3	L1–L3	3				x		Bilateral
22	7	4	4	L2/L3	L2–L3	2	x	x		x		Unilateral
23	1	4	3	L5/L6	IVD L5/L6	1				x		Unilateral
24	1	5	3	T11/T12	L1–L3	3	x					Bilateral
25	1	4	3	L1/L2	L1–L3	3				x		Bilateral
26	1	4	2	L1/L2	T12–L2	4	x					Unilateral
27	1	4	3	L1/L2	IVD L1/L2	1			x		x	Unilateral
28	3	4	2	L4/L5	IVD L2/L3	1					x	Unilateral
29	2	4	2	L2/L3	L2-4	3	x	x				Bilateral
30	1	5	1	L3/L4	L2 -L4	3		x	x			Unilateral
31	1	5	3	L2/L3	L2–L3	2		x		x		Bilateral
32	1	4	3	T12/T13	L1–L3	3	x					Bilateral
33	2	3	1	L2/L3	L2–L3	2	x					Unilateral
34	1	3	4	T13/L1	L1	1		x				Unilateral
35	2	3	2	L2/L3	L5–L7	3				x		Bilateral
36	1	3	1	L3/L4	L2–L4	3				x		Bilateral
37	1	4	1	T13/L1	L1–L3	3		x				Unilateral

The median length of signal alterations was two vertebral segments, with a range from one to five (**Table 1**).

Association with Intervertebral Disk Extrusion's Features

Intervertebral disk extrusion was most often located at T12/T13 (n = 26; 25%), followed by L2/3 (n = 17; 17%) as the second most common site. In dogs with muscle signal alterations most intervertebral disk extrusions were present at L2/L3 (n = 8; 22%), followed by L1/L2 and T12/T13 (each n = 7; 19%) (**Figure 3**). The proportion of dogs with muscle signal changes was significantly higher in dogs with an intervertebral disk extrusion between L1 and L7 compared to T3–T13 (Chi-square test, P = 0.004).

Location of muscle signal alterations in relation to location of intervertebral disk extrusion is visible in **Table 1**. Muscle signal alterations occurred most commonly at the same level as the intervertebral disk extrusion (n = 25; 68%) extending to a different degree cranial and/or caudal (**Table 1**). In two dogs (5%), the muscle signal alterations were located cranial to the affected intervertebral disk without involving the disk level, and in a further 10 dogs (27%), the signal alterations were located caudal to the affected intervertebral disk space. The muscle signal alterations were seen along one to four adjacent vertebrae with a median of two (**Table 1**).

Compressive extrusions were present in 91 dogs (88%), whereas 12 dogs (12%) had an ANNPE without compression of the spinal cord. Only one dog demonstrated ANNPE signal alterations within the paraspinal muscles and type of disk extrusion was not associated with muscle signal alterations (Fisher's exact test P = 0.20372).

Dogs presented with varying degrees of spinal cord compression; less than 30% impingement (n = 21; 20%), between 30 and 40% impingement (n = 26; 25%), between 40 and 50% (n = 29; 28%), or more than 50% (n = 27; 26%). The degree of compression was not associated with the presence of muscle signal alterations. In 13 dogs, muscle signal alterations were ipsilateral to the side of compression and in a single dog on the contralateral side. Despite unilateral compression, the muscle changes were observed bilaterally in 18 dogs. Ventral compression resulted in either unilateral or bilateral muscle signal changes.

Epidural hemorrhage was identified in 44 dogs (43%). Epidural hemorrhage was not associated with muscle signal alterations (Chi-square test, P = 0.738).

Association with Neurological Grade

In dogs with muscle signal alterations, the median neurological grade was 4, compared to a median of 3 in dogs without signal changes. The proportion of dogs with muscle signal alterations was higher in non-ambulatory dogs (neurological grades 3, 4, and 5) compared to ambulatory dogs (neurological grade 1 and 2) (Chi-square test P = 0.0017).

For both, dogs with an extrusion cranial to L1 and caudal to L1, the median neurological grade was 4.

Most dogs (n = 60; 59%) were presented within the first 24 h after the onset of clinical symptoms, the remainder within 48 h (n = 18; 18%), 3 days (n = 6; 6%), 4 days (n = 6; 6%), 5 days (n = 4; 3%), 6 days (n = 0; 0%), or 7 days (n = 9; 9%). Duration of clinical symptoms was not associated with the presence of muscle signal changes.

The two factors significantly associated with the presence of muscle signal changes in the univariable analysis were also significant in the multivariable logistic regression model. Dogs with a disk extrusion caudal to L1 had a higher risk for muscle signal changes (OR = 2.8, 95%CI = 1.1–7.0, P = 0.03) than dogs

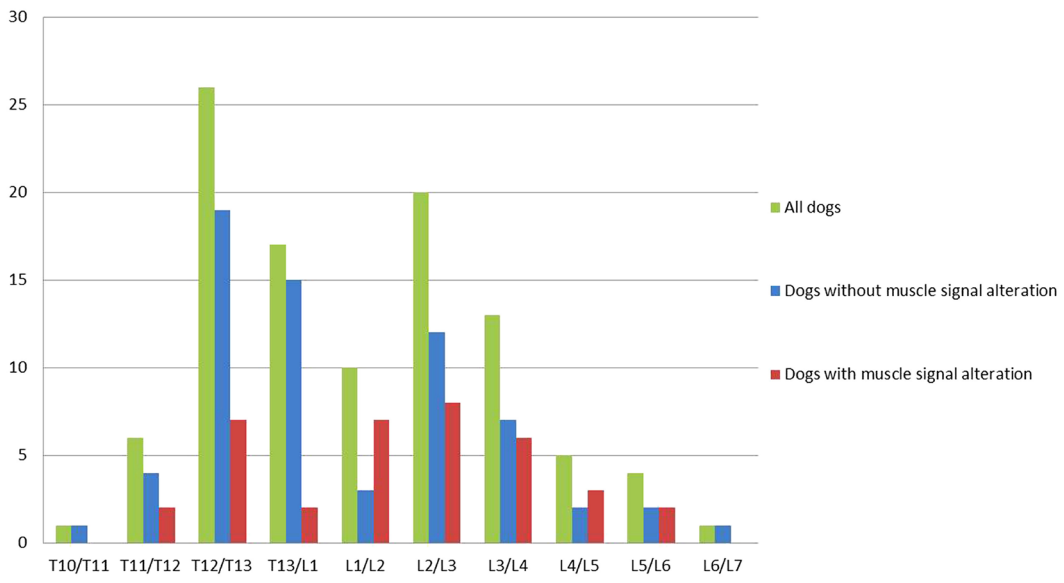

FIGURE 3 | Graph illustrating the location of the intervertebral disk extrusion of all dogs, dogs without and with muscle signal alteration. Dogs with a disk extrusion caudal to L1 had a higher risk for muscle signal changes (OR = 2.8, P = 0.03) than dogs with a disk extrusion cranial to L1.

with a disk extrusion cranial to L1. Neurological grades 1 and 2 were grouped, and used as the reference group. Grades 3, 4, and 5 were compared to the reference group, respectively. Dogs with a neurological grade of 3, 4, or 5 had a higher risk for muscle signal changes compared to dogs with a grade of 1 or 2 ($P = 0.002$). The Odds ratios for neurological grades 3, 4, and 5 were 7.3 (95%CI = 1.3–39.1), 12.1 (95% CI = 2.4–60.2) and 10.5 (95%CI = 1.7–62.7), respectively.

Histopathology

Histopathological examination revealed a focal to focally extensive, mild to moderate acute muscle fiber degeneration and necrosis in three samples, characterized by fragmentation of the sarcoplasm. The basal lamina and the endomysium were intact in most cases. Between the degenerated fibers, a mild to moderate accumulation of fibrin, neutrophilic granulocytes and edema was present. In addition, there was extensive hemorrhage in one sample and two muscle samples showed mild edema.

DISCUSSION

Paraspinal muscle signal alteration was observed in 36% of dogs with acute intervertebral disk extrusion and is, therefore, considered a common finding on MRI examination. The MRI pattern of these changes corresponds to a muscle edema. This pattern of T2-hyperintense and T1-iso- to hypointense signal abnormality is an unspecific alteration and the potential underlying causes are diverse. This finding has not been previously described in dogs or humans in association with acute intervertebral disk extrusion. The underlying cause for the signal changes is unknown; therefore muscle samples from the affected musculature were taken prospectively in five dogs to investigate the underlying pathomechanism. The results of the histopathologic examination were rather unspecific with changes including edema and focal muscle necrosis. An explanation for these changes may be trauma, ischemia or denervation, but the exact cause could not be determined by histopathology.

Penetration of extruded intervertebral disk material into the musculature may directly induce trauma and the associated signal alterations. However, this seems unlikely since the signal alterations were often observed bilaterally or even contralaterally to the extrusion. Furthermore, lesions were seen caudally or cranially to the extruded intervertebral disk without being in contact to the intervertebral disk space. Muscle signal alterations were observed in the majority of dogs within the epaxial muscles, dorsal to the level of the transverse processes of the vertebrae, but in 12 dogs, signal alterations were observed only in the hypaxial muscles, ventral to the transverse processes. These observations suggest that penetration of extruded intervertebral disk material in to the musculature is unlikely to be responsible for the signal alterations.

Both epaxial and hypaxial muscle groups are innervated by the spinal nerves from their dorsal or ventral branches, respectively (9). Damage to these nerves can lead to denervation edema within the muscle. Muscle denervation is a well-known pathologic condition in humans. The muscles of the foot, upper limb or shoulder are most commonly affected, but can be observed in any skeletal muscle (10). Causes may include trauma or entrapment of peripheral nerves, but spinal cord pathology can also result in nerve injury. The least severe form of nerve injury is neurapraxia (10). In contrast to neurotmesis and axonotmesis, this damage does not lead to structural discontinuity of axons, but instead a conduction block within the nerve causes muscle denervation (10). Denervation edema as a consequence of acute intervertebral disk extrusion has not been described in humans. In humans, where an intervertebral disk herniation at the level L3/4 or further caudal does not result in spinal cord compression, an intervertebral disk extrusion in dogs can cause spinal cord compression even at the level L6/L7 (11). Since the vertebral canal in dogs is much smaller compared to humans, intervertebral disk extrusion often results in marked compression or contusion with damage to the neurons located in the gray matter (11). We observed an association of muscle signal alterations with intervertebral disk extrusion caudal to L1, where the amount of gray matter is increasing along the lumbar spine. An association of muscle signal alterations with more severe spinal cord injury is supported by the fact that a significantly higher number of dogs with muscle signal alterations were presented with a higher neurological grade. Neurological grade or more precise, loss of deep pain perception, is a prognostic factor for neurologic recovery. At this time, it remains unclear if muscle signal alterations may be able to provide information about the neurologic recovery of the patients.

If neuronal or axonal damage occurs without inducing Wallerian degeneration of the axons, the changes in the axons are considered to be reversible (10). Otherwise, the chronic denervation results in atrophy of the muscles and fatty degeneration. A reduced cross sectional diameter and also fatty infiltration of the paraspinal musculature, especially the multifidi muscle group, has been described in humans with lower back pain as well as in experimental animal studies with induced intervertebral disk degeneration or extrusion (10, 12–17). Fatty infiltration within the paraspinal musculature has also been observed in dogs (5, 18), but no association between the degree of intervertebral disk degeneration and fatty infiltration was found and so far, the relationship of intervertebral disk disease and fatty infiltration is unclear (5). It is hypothesized that fatty infiltration in dogs is driven rather by a combination of chronicity and severity of the general spinal pathology (5). To further investigate if muscle signal alterations with an edematous pattern are reversible and if they result in degeneration with fatty infiltration, serial MRI examinations are necessary. Interesting questions to address in the future are the relationship of muscle signal alteration with pain, as well as the prevalence of muscle signal alterations in a larger cohort of dogs with ANNPE. Only one dog from all with signal alterations in the musculature was diagnosed as ANNPE based on MRI. This suggests that non-compressive spinal cord damage results less often in muscle signal alterations. This phenomenon may be explained by less severe damage of the gray matter. However, the overall lower

number of ANNPE animals compared to those with compressive intervertebral disk disease does not allow drawing this conclusion.

The muscle signal alterations were best identified in fat-suppressed T2W sequences, which are used as part of our routine protocol in dogs with acute back pain to identify changes in soft tissues (2). The sequences enable changes to be identified in a high proportion of animals, including more than one third of the dogs (36%). In some of the dogs, the lesions showed contrast enhancement, but contrast enhancement of skeletal muscles did not seem to facilitate or further characterize the lesions. This is in contrast to reported cases in humans (10). Identification of paraspinal muscle signal alterations may be helpful in clinical MRI to differentiate intervertebral disk disease from fibrocartilaginous embolism or acute versus chronic intervertebral disk herniation, but further studies are necessary to answer these questions.

In conclusion, we observed muscle signal alterations within the paraspinal muscles in more than one third of dogs with acute thoracolumbar intervertebral disk disease. The changes occur more frequently in intervertebral disk extrusions caudal to L1 and in dogs with a higher neurological grade. The rather unspecific MRI pattern of the edematous lesions as well as the histological findings obtained from five dogs hinders clarification of the underlying pathomechanism, but denervation edema may explain the signal alteration observed in dogs with acute intervertebral disk extrusion.

CONSENT

Consent procedure is not applicable, as this article is a retrospective study of clinical cases.

ETHICS STATEMENT

This study was carried out in accordance with the ethic recommendations of the veterinary Office, Kanton Bern, Switzerland.

AUTHOR CONTRIBUTIONS

Conception and design: DS-G and PT. Acquisition of data: PT, DH, MW, CG, FF, and DS-G. Analysis and interpretation of data: PT, DS-G, CG, MW. Drafting the Article: PT and DS-G. Revising article for intellectual content: DS-G, PT, and MW. Final approval of the completed article: PT, CG, MW, FF, DH, and DS-G.

ACKNOWLEDGMENTS

The authors would like to acknowledge Gertraud Schüpbach and Beatriz Vidondo for their help with the statistical analysis of the data and Lisa Thomann-Harwood for English language editing. Parts of this study were presented as oral presentation at the EVDI annual meeting, 2017, Verona, Italy.

REFERENCES

1. May DA, Disler DG, Jones EA, Balkissoon AA, Manaster BJ. Abnormal signal intensity in skeletal muscle at MR imaging: patterns, pearls, and pitfalls. *Radiographics* (2000) 20:S295–315. doi:10.1148/radiographics.20.suppl_1.g00oc18s295
2. Eminaga S, Cherubini GB, Villiers E, Targett M, Caine A. STIR muscle hyperintensity in the cervical muscles associated with inflammatory spinal cord disease of unknown origin. *J Small Anim Pract* (2013) 54(3):137–42. doi:10.1111/jsap.12035
3. Platt SR, McConnell JF, Garosi LS, Ladlow J, de Stefani A, Shelton GD. Magnetic resonance imaging in the diagnosis of canine inflammatory myopathies in three dogs. *Vet Radiol Ultrasound* (2006) 47(6):532–7. doi:10.1111/j.1740-8261.2006.00181.x
4. Holloway A, Dennis R, McConnell F, Herrtage M. Magnetic resonance imaging features of paraspinal infection in the dog and cat. *Vet Radiol Ultrasound* (2009) 50(3):285–91. doi:10.1111/j.1740-8261.2009.01535.x
5. Lerer A, Nykamp SG, Harriss AB, Gibson TWG, Koch TG, Brown SHM. MRI-based relationships between spine pathology, intervertebral disc degeneration, and muscle fatty infiltration in chondrodystrophic and non-chondrodystrophic dogs. *Spine J* (2015) 15(11):2433–9. doi:10.1016/j.spinee.2015.08.014
6. Sharp JHN, Wheeler SJ. Patient examination. In: Sharp NJH, Wheeler SJ, editors. *Small Animal Spinal Disorders, Diagnosis and Surgery*. Edinburgh, UK: Elsevier, Mosby (2005). p. 19–33.
7. Fenn J, Drees R, Volk HA, Decker SD. Inter- and intraobserver agreement for diagnosing presumptive ischemic myelopathy and acute noncompressive nucleus pulposus extrusion in dogs using magnetic resonance imaging. *Vet Radiol Ultrasound* (2016) 57(1):33–40. doi:10.1111/vru.12289
8. Noussitou FL, Gorgas D, Rohrbach H, Henke D, Howard J, Forterre F. Assessment of intramedullary spinal pressure in small breed dogs with thoracolumbar disk extrusion undergoing hemilaminectomy. *Vet Surg* (2015) 44(8):944–8. doi:10.1111/vsu.12399
9. Dyce KM, Sack WO, Wensing CJG. *Textbook of Veterinary Anatomy*. 4th ed. St. Louis, MO: Saunders/Elsevier (2010). xii, 834 p.
10. Kamath S, Venkatanarasimha N, Walsh MA, Hughes PM. MRI appearance of muscle denervation. *Skeletal Radiol* (2008) 37(5):397–404. doi:10.1007/s00256-007-0409-0
11. Bergknut N, Forterre F, Levine JM, Lasser SD, Fingeroth JM. Comparison between biped (human) and quadruped (canine/feline) intervertebral disc disease. In: Fingeroth WB, editor. *Advances in Intervertebral Disc Disease in Dogs and Cats*. Oxford, UK: Wiley Blackwell (2015). p. 14–22.
12. Altinkaya N, Cekinmez M. Lumbar multifidus muscle changes in unilateral lumbar disc herniation using magnetic resonance imaging. *Skeletal Radiol* (2016) 45(1):73–7. doi:10.1007/s00256-015-2252-z
13. Brown SHM, Gregory DE, Carr JA, Ward SR, Masuda K, Lieber RL. ISSLS prize winner: adaptations to the multifidus muscle in response to experimentally induced intervertebral disc degeneration. *Spine* (2011) 36(21):1728–36. doi:10.1097/BRS.0b013e318212b44b
14. Franke J, Hesse T, Tournier C, Schuberth W, Mawrin C, LeHuec JC, et al. Morphological changes of the multifidus muscle in patients with symptomatic lumbar disc herniation. *J Neurosurg Spine* (2009) 11(6):710–4. doi:10.3171/2009.7.SPINE08448
15. Mattila M, Hurme M, Alaranta H, Paljarvi L, Kalimo H, Falck B, et al. The multifidus muscle in patients with lumbar disc herniation. A histochemical and morphometric analysis of intraoperative biopsies. *Spine* (1986) 11(7):732–8. doi:10.1097/00007632-198609000-00013
16. Ploumis A, Michailidis N, Christodoulou P, Kalaitzoglou I, Gouvas G, Beris A. Ipsilateral atrophy of paraspinal and psoas muscle in unilateral back pain patients with monosegmental degenerative disc disease. *Br J Radiol* (2011) 84(1004):709–13. doi:10.1259/bjr/58136533
17. Hodges P, Holm AK, Hansson T, Holm S. Rapid atrophy of the lumbar multifidus follows experimental disc or nerve root injury. *Spine* (2006) 31(25):2926–33. doi:10.1097/01.brs.0000248453.51165.0b
18. Henderson AL, Hecht S, Millis DL. Lumbar paraspinal muscle transverse area and symmetry in dogs with and without degenerative lumbosacral stenosis. *J Small Animal Prac* (2015) 56(10):618–22. doi:10.1111/jsap.12385

Conflict of Interest Statement: The authors declare that the research was conducted in the absence of any commercial or financial relationships that could be construed as a potential conflict of interest.

frontiers in Veterinary Science

ORIGINAL RESEARCH
published: 22 January 2018
doi: 10.3389/fvets.2017.00241

Caudal Fossa Ratio in Normal Dogs and Eurasier Dogs with VLDLR-Associated Genetic Cerebellar Hypoplasia

*Alexander Lauda[1], Andreas Bruehschwein[2], Joanna Ficek[3], Martin J. Schmidt[4], André Klima[3], Andrea Meyer-Lindenberg[2] and Andrea Fischer[1]**

[1] Centre for Clinical Veterinary Medicine, Clinic of Small Animal Medicine, LMU Munich, Munich, Germany, [2] Centre for Clinical Veterinary Medicine, Clinic of Small Animal Surgery and Reproduction, LMU Munich, Munich, Germany, [3] Statistical Consulting Unit StaBLab, Department of Statistics, LMU Munich, Munich, Germany, [4] Department of Veterinary Clinical Science, Small Animal Clinic, Justus-Liebig-University, Giessen, Germany

Cerebellar and hindbrain malformations, such as cerebellar hypoplasia (CH), vermis hypoplasia, and Dandy–Walker malformation, occur in dogs as well as in humans. Neuroimaging is essential for a precise description of these malformations and defining translational animal models. Neuroimaging is increasingly performed in puppies, but there is a lack of data on developmental changes in the caudal fossa, which can impair assessment of caudal fossa size in this age group. The purpose of this study was to validate caudal fossa ratio (CFR) in dogs and to explore CFR in Eurasier dogs with genetic CH. CFR was calculated from midsagittal brain images of 130 dogs as caudal fossa area/total cranial cavity area. In addition, the volume of the caudal fossa was measured in 64 randomly selected dogs from this group. Repeated measurements were used to investigate inter- and intra-rater variability and influence of imaging modality. Furthermore, the influence of age, weight, and breed was explored. The CFR was a reliable parameter with negligible influence from the examiners, imaging modality, and weight of the dog. The midsagittal area of the caudal fossa and the volume of the caudal fossa correlated closely with each other. In this study, we observed a smaller CFR in puppies. The CFR in adult dogs lies within 0.255 and 0.330, while CFR is smaller in puppies up to 4 months of age. Besides age, there was also an effect of breed, which should be explored in larger data sets. Measurements of CFR in Eurasier dogs with genetic CH caused by a mutation in the very-low-density-lipoprotein-receptor gene revealed the presence of two variants, one with an enlarged caudal fossa and one with a normal to small caudal fossa. This observation indicates that there is phenotypic heterogeneity and interaction between the developing cerebellum and the surrounding mesenchyme in this animal model.

Keywords: VLDLR, genetic, Dandy–Walker malformation, cerebellar hypoplasia, posterior fossa, animal model, neuroimaging

OPEN ACCESS

Edited by:
Andrea Tipold, University of Veterinary Medicine Hannover, Germany

Reviewed by:
Clare Rusbridge, University of Surrey, United Kingdom
Gualtiero Gandini, Università di Bologna, Italy

****Correspondence:***
Andrea Fischer
andreafischer@lmu.de, andrea.fischer@med.vetmed.uni-muenchen.de

Specialty section:
This article was submitted to Veterinary Neurology and Neurosurgery, a section of the journal Frontiers in Veterinary Science

Received: *01 September 2017*
Accepted: *20 December 2017*
Published: *22 January 2018*

Citation:
Lauda A, Bruehschwein A, Ficek J, Schmidt MJ, Klima A, Meyer-Lindenberg A and Fischer A (2018) Caudal Fossa Ratio in Normal Dogs and Eurasier Dogs with VLDLR-Associated Genetic Cerebellar Hypoplasia. Front. Vet. Sci. 4:241. doi: 10.3389/fvets.2017.00241

INTRODUCTION

Animal models of human disease provide insights into pathophysiology at a molecular level, and gene discovery in dogs has become an important resource. In human medicine, neuroimaging techniques have helped to improve the definitions of hindbrain and cerebellar malformations. The classification of midbrain, cerebellar, and hindbrain malformations has evolved from several image-based

classification systems to a classification system that is based on embryonic development (1–4). This system was produced by modern neuroimaging techniques as well as increased understanding of correlations between gene mutations and certain brain imaging phenotypes. The recognition of phenotypic heterogeneity of certain gene mutations and the fact that different gene mutations may result in nearly identical neuroimaging findings has further contributed to the understanding of these mutations (4, 5). Many of these data are derived from animal studies (2).

Genetic cerebellar hypoplasia (CH) in Eurasier dogs represents the first genetically defined CH that has been described in dogs. It is caused by a fully penetrant recessive mutation in the very-low-density-lipoprotein-receptor gene (*VLDLR*) (6, 7). Genetic testing for breeders is now available (6, 7). The VLDLR is part of the Reelin signaling pathway and influences cell migration and positioning during embryonic development, especially in the cerebellum (8–10). The neuroanatomic changes are absence of the caudal aspects of the cerebellar vermis and the cerebellar hemispheres in association with large retrocerebellar fluid accumulations (11, 12). Initial observations suggested an abnormal configuration of the caudal (cranial) fossa and an enlarged caudal fossa as an additional imaging feature in some puppies with *VLDLR*-associated CH resembling a Dandy–Walker like malformation [**Figure 1**; reported in Table 3 of Ref. (7)]. The evaluation was problematic, however, because of the lack of reference data in the literature related to caudal fossa size in puppies and the different imaging modalities used.

Therefore, the aim of this study was to validate the use of the caudal fossa ratio (CFR) from area measurements of midsagittal brain images to assess caudal fossa size in dogs of various age groups, body weights, and breeds. Specifically, we aimed to explore the application of CFR to puppies with and without *VLDLR*-associated CH to define the animal model in more detail.

MATERIALS AND METHODS

Caudal fossa ratio was calculated from midsagittal brain images of 130 dogs. Study design was retrospective and observational. The data of the dogs in this study were used with the consent of their owners and the breed club. The study was approved by the institutional research review board (#09-06-2014).

Control Dogs ($n = 111$)

Magnetic resonance images from 111 control dogs (83 dogs > 6 months of age, 28 dogs ≤ 6 months of age) were derived from the MRI database of two institutions (Clinic of Small Animal Surgery and Reproduction, LMU Munich; Small Animal Clinic, Justus-Liebig-University, Giessen). Inclusion criteria were unremarkable MR images without any evidence for intracranial or skull disease. All dogs presented for neurological signs. The most common diagnosis was idiopathic epilepsy and geriatric vestibular syndrome. The adult dogs included 10 Australian Shepherds, 10 Border Collies, 13 Golden Retrievers, 14 Labrador Retrievers (large mesaticephalic breeds), 7 Boxers, 10 French Bulldogs, 7 Pugs (small and large brachycephalic breeds), and 12 Eurasier dogs without CH (**Table 1**). The breed and age of the puppies is outlined in Table S1 in Supplementary Material. The number of male and female dogs in each group is outlined in Table S2 in Supplementary Material. MRIs of the head were performed using a 1.5 T scanner (Magnetom Symphony Syngo MR, Siemens AG, Erlangen, Germany) or a 1.0 T scanner (Gyroscan Intera, Philips, Hamburg, Germany).

Comparison between MRI and CT ($n = 8$)

Eight additional dogs of various breed and age were included. Both imaging modalities, MRI and CT, were available from these dogs. These dogs suffered from various intracranial diseases. MRIs were performed using a 1.5 T scanner (Magnetom Symphony Syngo MR, Siemens AG, Erlangen, Germany). CT scans of the head were obtained using a multislice CT (Somatom Definition AS, Siemens AG, Erlangen, Germany).

Eurasier Dogs with CH ($n = 11$)

Eleven pure-breed Eurasier dogs with genetic *VLDLR*-associated CH (8 MRI, 3 CT) were included. The affected Eurasier dogs were between 2 and 7 months of age (median 2 months). One dog was an adult at the time of imaging (56 months).

Morphometric Studies

MRI measurements were conducted on T2-weighted midsagittal brain images. CT measurements were conducted on midsagittal brain images with soft tissue (window width, 300; window level,

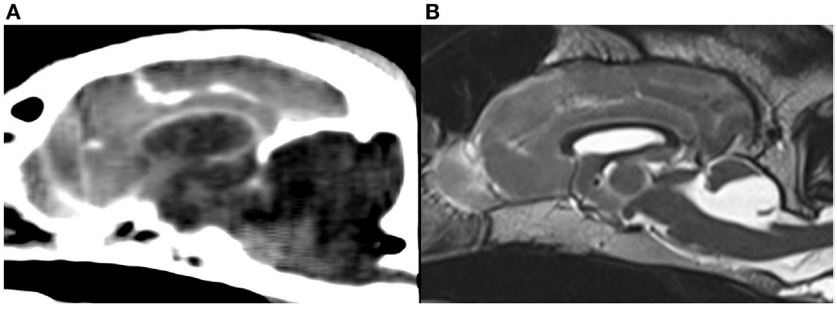

FIGURE 1 | Midsagittal brain images of Eurasier dogs with *VLDLR*-associated cerebellar hypoplasia. **(A)** CT, soft tissue window, large fluid accumulations within caudal fossa and subjectively enlarged caudal fossa, **(B)** T2-weighted MRI, retrocerebellar fluid accumulations with a cyst-like appearance and subjectively normal to small caudal fossa. Panel **(B)** was originally published under (7). Reuse is permitted by the Creative Commons Attribution CC BY license.

TABLE 1 | Caudal fossa ratio (CFR) of Eurasier dogs with *VLDLR*-associated cerebellar hypoplasia and control dogs.

Group		Age (months)		CFR		
		Median	Range	Median	Range	Mean ± SD
Eurasier (variant 1)	*n* = 3	2	2–3	0.354	0.344–0.441	0.379 ± 0.044
Eurasier (variant 2)	*n* = 8	2	2–56	0.232	0.191–0.292	0.249 ± 0.050
Control dogs > 6 months of age						
Eurasier (unaffected)	*n* = 12	52.5	13–178	0.315	0.265–0.330	0.304 ± 0.021
Mesaticephalic						
Australian Shepherd	*n* = 10	52	20–130	0.299	0.285–0.320	0.299 ± 0.011
Border Collie	*n* = 10	44.5	13–87	0.286	0.258–0.303	0.286 ± 0.012
Golden Retriever	*n* = 13	111	45–163	0.287	0.277–0.319	0.291 ± 0.012
Labrador Retriever	*n* = 14	82.5	8–176	0.299	0.274–0.324	0.299 ± 0.013
Total	*n* = 47	71	8–176	0.291	0.258–0.324	0.294 ± 0.013
Brachycephalic						
Boxer	*n* = 7	93	9–119	0.273	0.261–0.283	0.275 ± 0.010
French Bulldog	*n* = 10	48	7–74	0.308	0.284–0.315	0.304 ± 0.010
Pug	*n* = 7	30	7–107	0.285	0.255–0.304	0.282 ± 0.018
Total	*n* = 24	55.5	7–119	0.291	0.255–0.315	0.289 ± 0.018
Control dogs ≤ 6 months of age						
Different breeds (<4 months)	*n* = 20	3	1–4	0.256	0.226–0.296	0.256 ± 0.018
Different breeds (4 < 6 months)	*n* = 8	6	5–6	0.287	0.256–0.304	0.279 ± 0.016

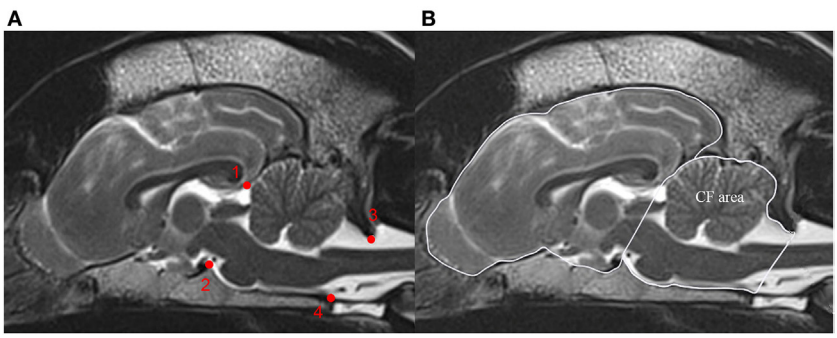

FIGURE 2 | Calculation of the caudal fossa ratio (CFR) on midsagittal brain images. The figure shows midsagittal T2-weighted magnetic resonance images of the brain of a control dog. **(A)** Bony structures used to identify the boundary of the caudal fossa. (1) Most rostral aspect of the tentorium cerebellum, (2) dorsum sella turcica, (3) caudodorsal margin of the foramen magnum, and (4) ventral margin of the foramen magnum. **(B)** Measurements on midsagittal T2-weighted MRI figure displays outline of the caudal fossa (CF area) and total cranial cavity (peripheral boundary line) for area measurements. CFR is calculated as CF area/total cranial cavity area.

+30) and bone reconstruction algorithm (window width, 2,500; window level, +500). Five image series needed to be readjusted to obtain measurements in midsagittal planes. Measurements of the midsagittal areas of the cranial cavity case and of the caudal fossa (cm^2) were based on manual delineation of the inner surface of the skull and calculations with conventional imaging software (Osirix®; v.5.6 Pixmeo Sarl). The cranial and caudal extensions of the caudal fossa were straight lines connecting the most rostral aspect of tentorium cerebellum to the dorsum sella turcica as well as the caudodorsal margin of the foramen magnum to the ventral margin of the foramen magnum (**Figure 2A**) (13). All measurements were performed twice and the mean was used for all calculations. The CFR reflected the relative size of the caudal fossa cross-sectional area and was calculated as the caudal fossa area/total cranial cavity area for all images (**Figure 2B**).

Furthermore, we made volumetric measurements of the caudal fossa from 64 randomly selected dogs from the control group with a second imaging software (3D Slicer®; v.4.4.0). The caudal fossa was defined as the space bound by the dorsal surface of the basioccipital bone, the dorsum sellae, the foramen magnum, and the apical part of the petrous part of the temporal and the basioccipital bones (14). The caudal fossa was manually delineated on each midsagittal and parasagittal T2-weighted MR image, and the caudal fossa volume was calculated by the software.

Reliability

MRI scans of eight dogs from the control group were selected in a randomized manner for assessment of intra- and inter-rater reliability of CFR. Investigators were blinded to breed, age, and the results of previous measurements. Intra-rater variability was done by repeated measurements by the first author of the

study (AL). In five dogs, CFR was measured once a day on five consecutive days (Monday to Friday) for 4 weeks; in three dogs CFR was measured once a week (Monday) for 6 weeks. Intra-rater variability was assessed by visual inspection of repeated measurements. Furthermore, the coefficient of variation was calculated to measure the dispersion of the measurements. For assessment of inter-rater variability, the same eight studies were evaluated by the first author of the study (AL) and then by a board-certified radiologist (AB) following instructions for an example case. Inter-rater variability was evaluated in linear regression. The association between caudal fossa area and caudal fossa volume was assessed in 64 dogs of the control group with linear regression analysis.

Statistical Analysis

Exploratory analysis was conducted to investigate the influence of age, weight, and breed on CFR. Based on the study of Ref. (15), we decided to compare four age groups: 1–4 months, 5–6 months, 7–12 months, and >1 year (15). A one-way ANOVA was performed to assess the overall effect of age in control dogs, preceded by the Shapiro–Wilk test for normality. The null-hypothesis could not be rejected in any of the analyzed groups. In the performed tests, the level $\alpha = 0.05$ was used to determine significance. The effect of weight was evaluated in linear regression. The difference between imaging modalities was examined in exploratory analysis and assessed in linear regression with the CT measurement ratio as the dependent variable and the MRI measurement ratio as the independent variable. In all the regression analysis in this paper, a simple regression model: $y_i = \beta_0 + \beta_1 \times x_i + \varepsilon_i$ was used, where β_0 stands for intercept and ε for the random error component. The regression coefficient β_1 represents the effect of the independent variable x on the dependent variable y. Moreover, the square root with the sign of β_1 of the R-squared is the linear correlation coefficient between x and y. In all tests, the level $\alpha = 0.05$ was used to determine significance. All the statistical analyses were performed in R software version 3.3.1.

RESULTS

Reliability

Data confirm the reliability of CFR as a robust parameter for assessment of caudal fossa size. The mean intra-rater coefficient of

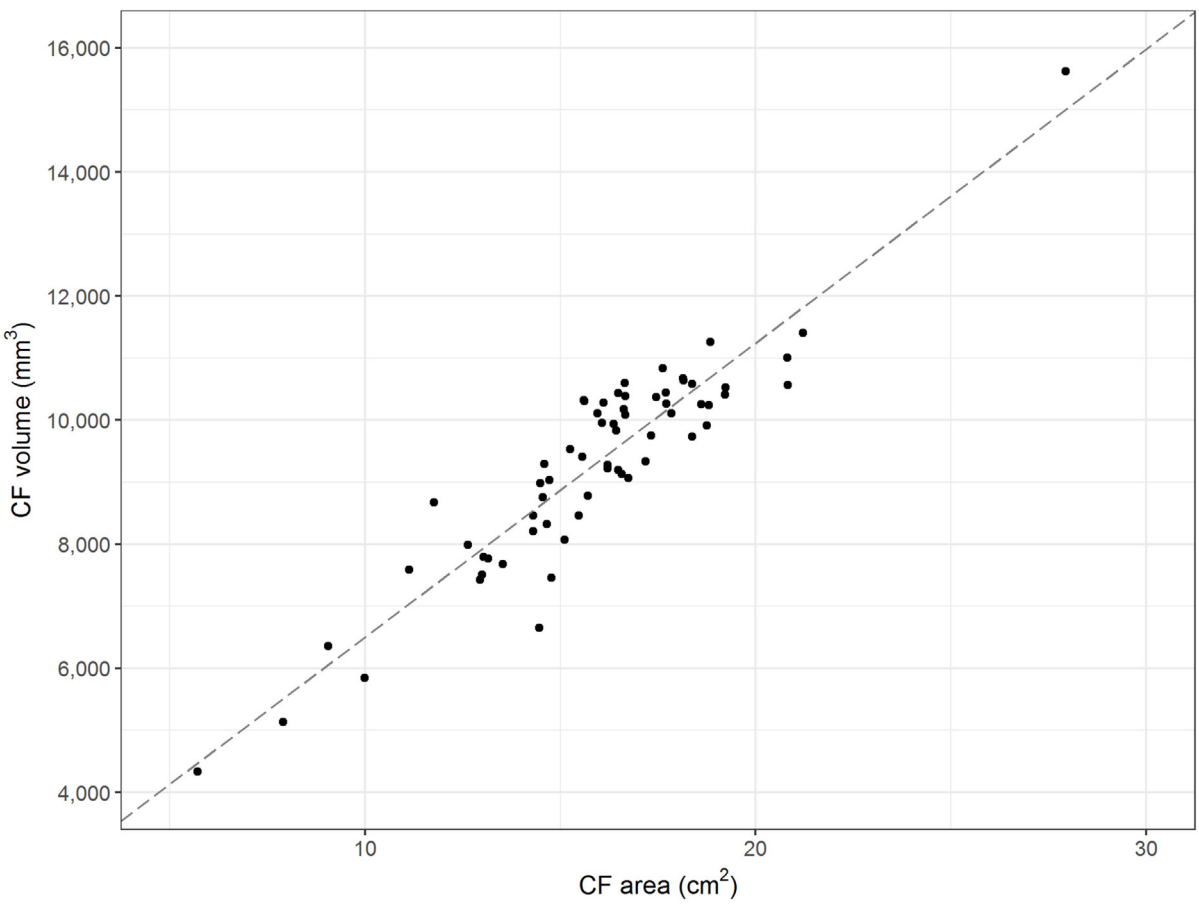

FIGURE 3 | Midsagittal area and volume of the caudal fossa. The figure displays the midsagittal area of the caudal fossa (cm^2; Osirix®) of 64 control dogs on the *x*-axis and the corresponding calculations of the volume of the caudal fossa (mm^3; 3D Slicer®) on the *y*-axis. Each dot represents the measurements of one individual dog. The line represents the regression line and shows linear correlation between midsagittal area and volume (correlation coefficient 0.93; *R*-squared 0.86).

variation equals 0.0066. Visual inspection of the repeated measurements suggests no presence of learning effects. The regression performed to assess the inter-rater reliability implies that there was a minor effect of researcher performing measurements on the CFR. The correlation coefficient equals 0.95 (*R*-squared 0.91) and the regression coefficient (β_1) is 0.91. Visual and statistical comparisons between area and volume measurements proved positive linear correlation between the midsagittal area and volume of the caudal fossa in dogs. The correlation coefficient equals 0.93 (*R*-squared 0.86) (**Figure 3**).

Influence of Age

Caudal fossa ratio was assessed in 111 control dogs of various ages. CFR was compared between four age groups: ≤4 months ($n = 20$), 5–6 months ($n = 8$), 7–12 months ($n = 7$), and >1 year ($n = 76$). All groups contained dogs with various skull morphologies. Age had a significant influence on CFR ($p < 0.001$; Table S3 in Supplementary Material). We observed a smaller CFR that was indicative of a relatively smaller size of the caudal fossa in cross-sectional images in puppies up to 4 months of age compared to adult dogs with completed skeletal growth (**Figure 4**; **Table 1**). CFR stabilized at 4 months of age and did not change after that point.

Influence of Breed and Weight

The influence of breed on CFR was assessed in 83 control dogs ≥ 6 months of age of eight different breeds. CFR ranged from 0.255 to 0.330 (0.293 ± 0.015). There were visible differences in CFR between breeds, especially between the brachycephalic breeds (**Figure 5**). However, the effect of breed on CFR was not substantial compared to the effect of age. The linear regression estimator was close to 0 ($\beta_1 < 0.001$) and therefore the effect of weight was negligible (**Figure 6**).

Imaging Modality

The differences in CFR between MRI and CT images (soft tissue window and bone window) were evaluated in eight dogs and were negligible. There was only a minor influence of the imaging modality on CFR (**Figure 7**). Measurements of the midsagittal area of the caudal fossa and the whole cranial area were smaller

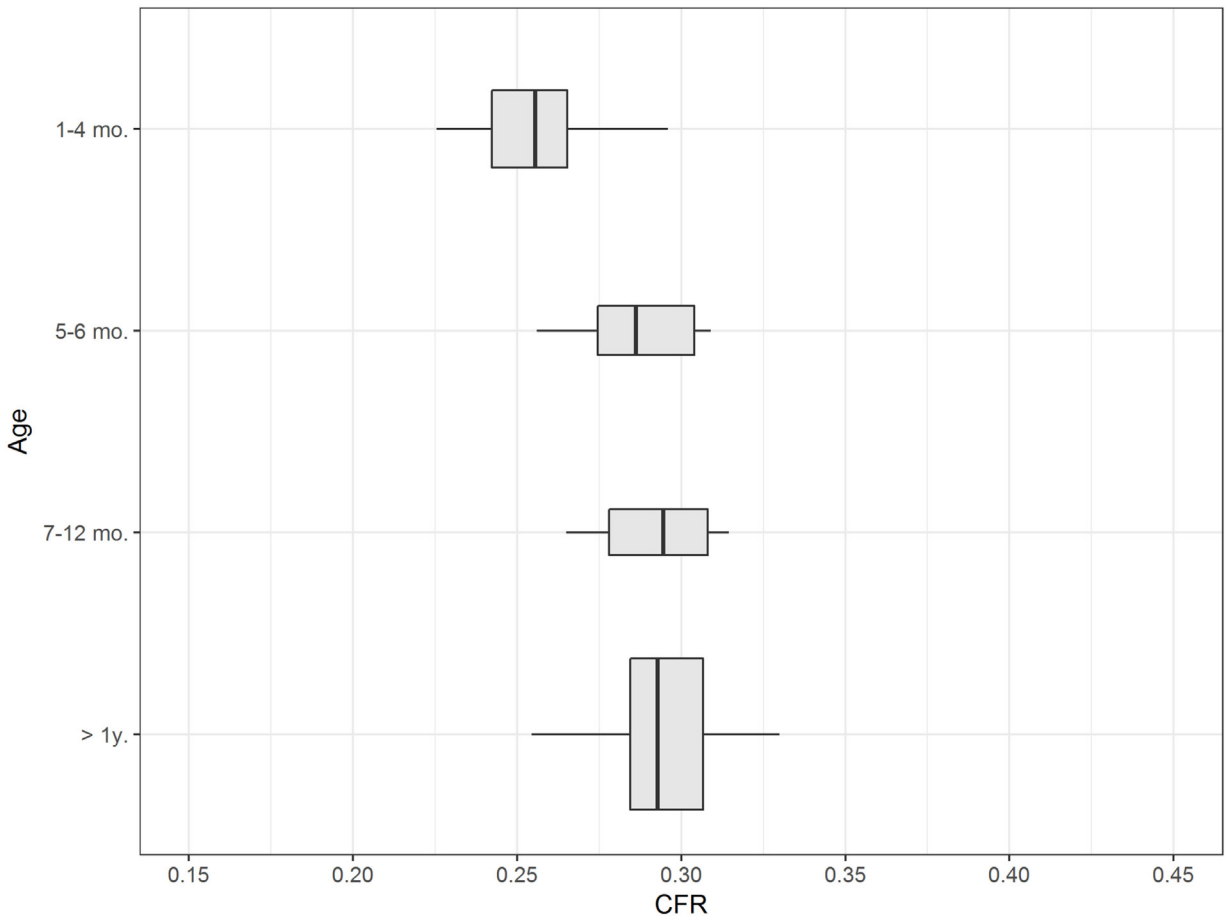

FIGURE 4 | Influence of age. The figure shows box plots of the caudal fossa ratio (CFR) of dogs from the control group. Each box plot displays CFR from dogs from one age group: ≤4 months, 5–6 months, 7–12 months, and >1 year. The width of the box plots corresponds to the number of dogs in each age group. Dogs ≤ 4months of age show a relatively smaller CFR compared to older dogs.

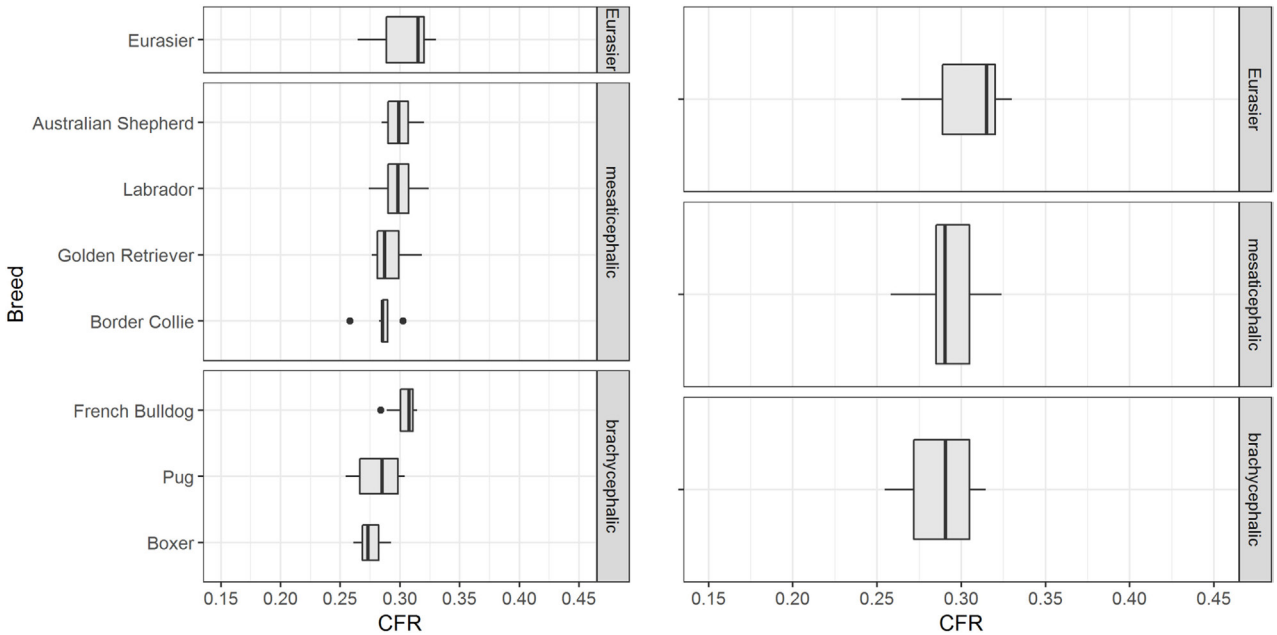

FIGURE 5 | Influence of breed. The figure shows box plots of the caudal fossa ratio (CFR) from dogs of the control group. Each box plot displays CFR of dogs from one breed. There are visible differences in CFR between breeds, especially within the brachycephalic group.

in CT than MRI, but this effect was no longer visible in the ratio. For the MRI ratio to CT ratio (soft tissue window) the correlation coefficient equals 0.95 (*R*-squared 0.90). The regression coefficient was 0.93 and thus, for one unit increase in MRI ratio, the CT ratio increases by 0.93 units. For the MRI ratio to CT ratio (bone window) the correlation coefficient equals 0.97 (*R*-squared 0.93 and regression coefficient 1.06). For the CT ratio (bone window) to CT ratio (soft tissue window) the correlation coefficient equals 0.93 (*R*-squared 0.86 and regression coefficient is 0.83).

Eurasier Dogs with *VLDLR*-Associated CH

Data confirmed a wide variation in caudal fossa size in Eurasier dogs with *VLDLR*-associated CH. Assessments were based on measurements of CFR in Eurasier dog puppies with CH and comparisons made to puppies of other breeds, adult unaffected Eurasier dogs and adult dogs of other breeds (**Figure 8**). CFR was high and above the range observed in the control dogs, which indicated the presence of an enlarged caudal fossa in three dogs with genetic CH (variant 1). In the other dogs, CFR was at the lower limit or below the range observed in control dogs (variant 2) (**Table 1**). These results were further supported by a descriptive analysis (Figure S1 in Supplementary Material).

DISCUSSION

The caudal cranial fossa henceforth in this manuscript referred to as caudal fossa for ease of reading, which is called the posterior fossa in humans, is the inner surface of the skull that surrounds the brainstem and cerebellum. Its rostral and caudal borders are the tentorium cerebelli and the foramen magnum (13, 14). A variety of brainstem and cerebellar malformations are associated with disturbed growth of the cranium (2, 3). Consequently, assessment of caudal fossa size should be part of the description and definition of animal models of brain malformations. A precise description of congenital malformations enhances comparisons with analogous diseases in humans.

Our findings establish CFR as a reliable parameter for assessment of the relative size of the caudal fossa. The measurements demonstrate excellent agreement within and between raters (intra-, inter-rater agreement). There is only a minor influence of imaging modality on the ratio and results are in the same range as reported from other authors (13, 16).

An important finding is the lack of impact of weight on CFR (**Figure 6**). This finding supports the use of CFR as a parameter that is independent of the size of the dog and can be applied to large dog breeds as well as small dog breeds and over a wide range of weights. Dog breeds also differ according to skull morphology. A review of groups of dogs from different breeds indicated an influence of breed on CFR that should be addressed in future studies. While we failed to find overall influence of a brachycephalic or a mesaticephalic skull, there were visible differences in CFR between small and large brachycephalic breeds.

We postulate that area measurements are precise parameters and reflect the basic configuration and the size of the caudal fossa in relation to the whole skull. It has been stated that three-dimensional assessments (volume measurements) are more

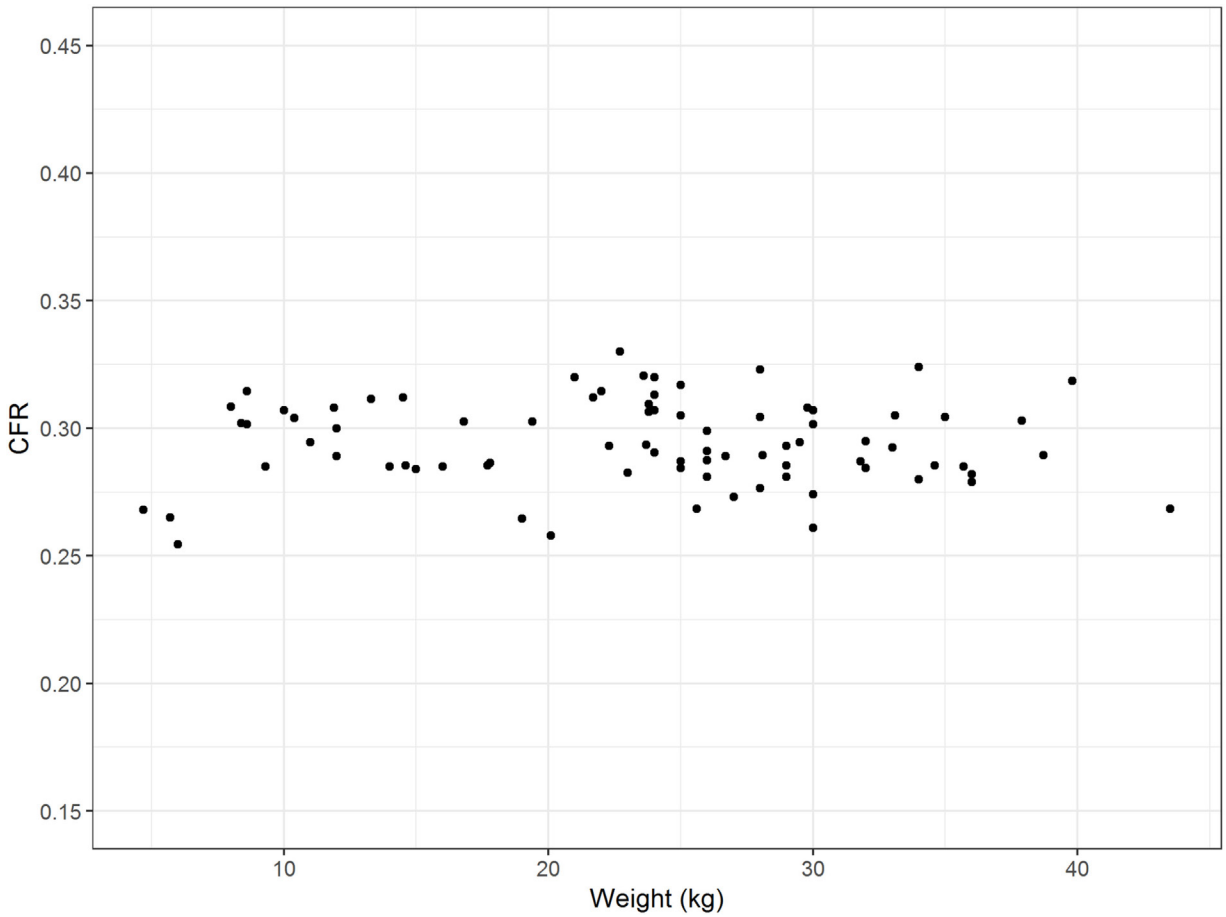

FIGURE 6 | Influence of weight. The figure displays the weight (kilograms) of the dogs on the *x*-axis and the corresponding caudal fossa ratio (CFR) on the *y*-axis. Each dot represents the measurements of one individual dog from the control group. There is no association between weight and CFR.

accurate for assessment of caudal fossa size than midsagittal area measurements in dogs (17). However, this statement occurred in the context of an investigation of pathomechanisms in Chiari malformation/syringomyelia in Cavalier King Charles Spaniels in which assessment of overcrowding requires precise measurements of the proportions of brain parenchyma and CSF space. Our investigations in 64 dogs with various skull conformations showed a close correlation between midsagittal caudal fossa area and caudal fossa volume. This result confirms the validity of CFR and provides further support for the use of CFR for the characterization of animal models. It should be noted, however, that previous studies in humans showed variable results and either weak (18) or no (17) correlation between area and volume measurements. Others have successfully applied a brainstem/cerebellar ratio for diagnosis of cerebellar atrophy and cerebellar degeneration in dogs (19). They also showed close correlation between area and volume measurements. Both brainstem/cerebellar ratio and CFR may be used for phenotyping cerebellar and hindbrain malformations in dogs.

Our data show that puppies up to 4 months (19 weeks) of age have a smaller CFR than adult dogs (**Figure 4**). This observation has not appeared in the literature to date. Some investigators excluded dogs younger than 12 months of age from measurements based on their assumption of an influence of incomplete skull growth (20, 21). Other researchers considered dogs younger than 12 months of age for their measurements (13, 22) or dogs as young as 4 months of age and assumed that there was no influence of skull growth on their results (23). Early diagnosis of brain malformations is advantageous to breeders and clients. Furthermore, neuroimaging of affected dogs and their littermates may be necessary for confirmation and precise definition of the phenotype for genetic investigations (7). A smaller CFR in puppies up to 4 months of age reflects discordant growth of the skull in puppies in which the growth of the caudal fossa is smaller. Disproportionate growth started at 50 days in German Shepherd puppies. Excessive growth of the caudodorsal cranium with development of the external sagittal crest and occipital protuberance occurred from days 70 to 107 (15).

We used CFR to validate caudal fossa size in an animal model of a genetic CH. A variant in the very-low density lipoprotein receptor gene (VLDLR:c.1713delC) is the cause of inherited CH in the Eurasier dog breed. Inheritance is recessive and genetic

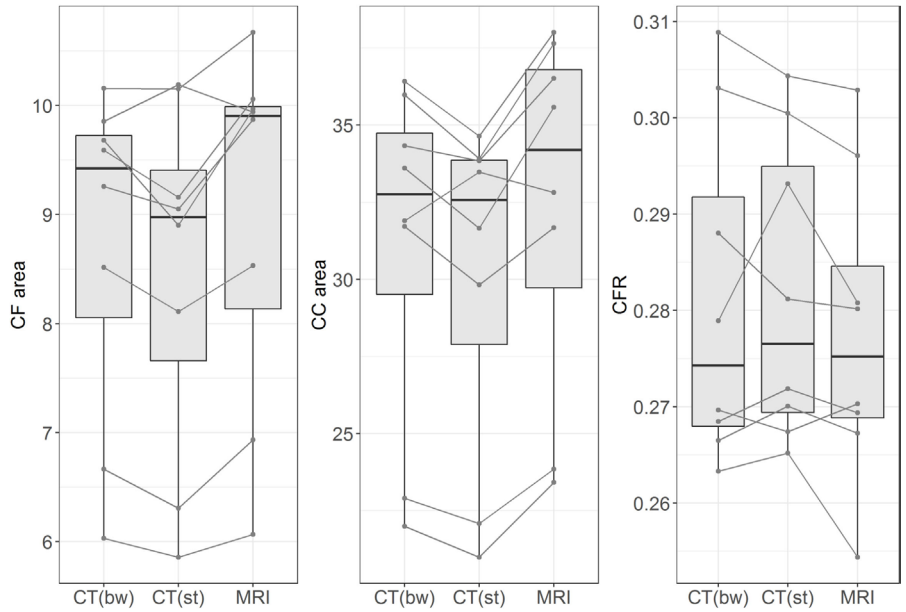

FIGURE 7 | Influence of imaging method. The figure shows box plots of measurements of midsagittal caudal fossa area (CF area, left figure), cranial case area (CC area, middle figure), and caudal fossa ratio (CFR, right figure). Each figure displays the measurements from eight dogs with different imaging methods: CT (bw), computed tomography with bone window algorithm; CT (st), computed tomography with soft tissue window algorithm; MRI, T2-weighted magnetic resonance images. The lines connect the corresponding measurements from each dog. Midsagittal CF areas and CC areas are smaller in CT (bw) and CT (st) than in MRI, but this effect is no longer seen when CFR is compared between the three imaging modalities.

testing is now available for breeders to avoid the disease (6). Clinically, homozygous dogs present with non-progressive ataxia which is first evident when the animals start to walk. VLDLR is part of the Reelin signaling pathway and involved in neuronal migration and cerebellar development (8–10). The analogous human disease has been described as disequilibrium syndrome and involves mutations in *VLDLR*. To date, there have been 12 reports from 15 families and 45 involved persons (24–30). Both humans and dogs present non-progressive cerebellar (truncal) ataxia as the main complaint. Neuroanatomic changes are strikingly similar between the two species. Caudal aspects of the cerebellar vermis and the cerebellar hemispheres are absent and replaced by large retrocerebellar fluid accumulations. Our measurements of CFR in Eurasier dogs with *VLDLR*-associated CH and appropriate controls confirm the presence of two variants: variant 1 with a grossly enlarged caudal fossa and variant 2 with a small to normal-sized caudal fossa. This observation has several implications. First, it proves phenotypic variability with regard to the size of the caudal fossa in dogs with *VLDLR*-associated CH. Wide variability in the size of the posterior fossa from normal to large is also seen in humans and mice with *FOXC1*-associated Dandy–Walker and related malformations (5). Furthermore, our observations also support an interaction between the cerebellum and the overlying mesenchyme (meninges, skull) during development. The concept that cerebellar and posterior skull development are closely linked through interactions between the rhombic lip and the overlying mesenchyme (3, 31) arose from observations in *FOXC1* mice with Dandy–Walker malformations. These mice express *FOXC1* only in the mesenchyme overlying the cerebellum and not in the cerebellum itself (5). Finally, variability in genetic background and interaction between different genes could also contribute to the conformation of the caudal fossa in this dog breed. We observed slightly more variability in caudal fossa size in unaffected Eurasier dogs compared to other dog breeds. Finally, there could be an impact of environmental or vascular factors during development. Limitations of this study are obviously the lack of MRI from breed- and age-matched controls as well as absence of measurements on T1-weighted midsagittal images and that we combined images from a 1.5 and 1.0 T MR. Furthermore, the size of the breed groups was too small to asses the influence of breed and larger cohorts with more breeds representatives of their skull type and separating large and small brachycephalic dogs (and other skull types) into different control groups need to be examined. However, CFR in some pupies with vldlr-associated CH was even larger than in adult Eurasier dogs and clearly exceeded any of our control dogs.

In summary, our data show that CFR is a reliable parameter with a negligible influence of imaging modality, examiner, and weight of the dog and a minor influence of breed. The CFR in healthy adult dogs lies within 0.255 and 0.330, but CFR is smaller in puppies. Furthermore, the midsagittal area of the caudal fossa is positively correlated with caudal fossa volume. Measurements in Eurasier dog puppies with genetic *VLDLR*-associated CH demonstrated the presence of a variant with an enlarged caudal fossa. This observation further substantiates the application of CFR for

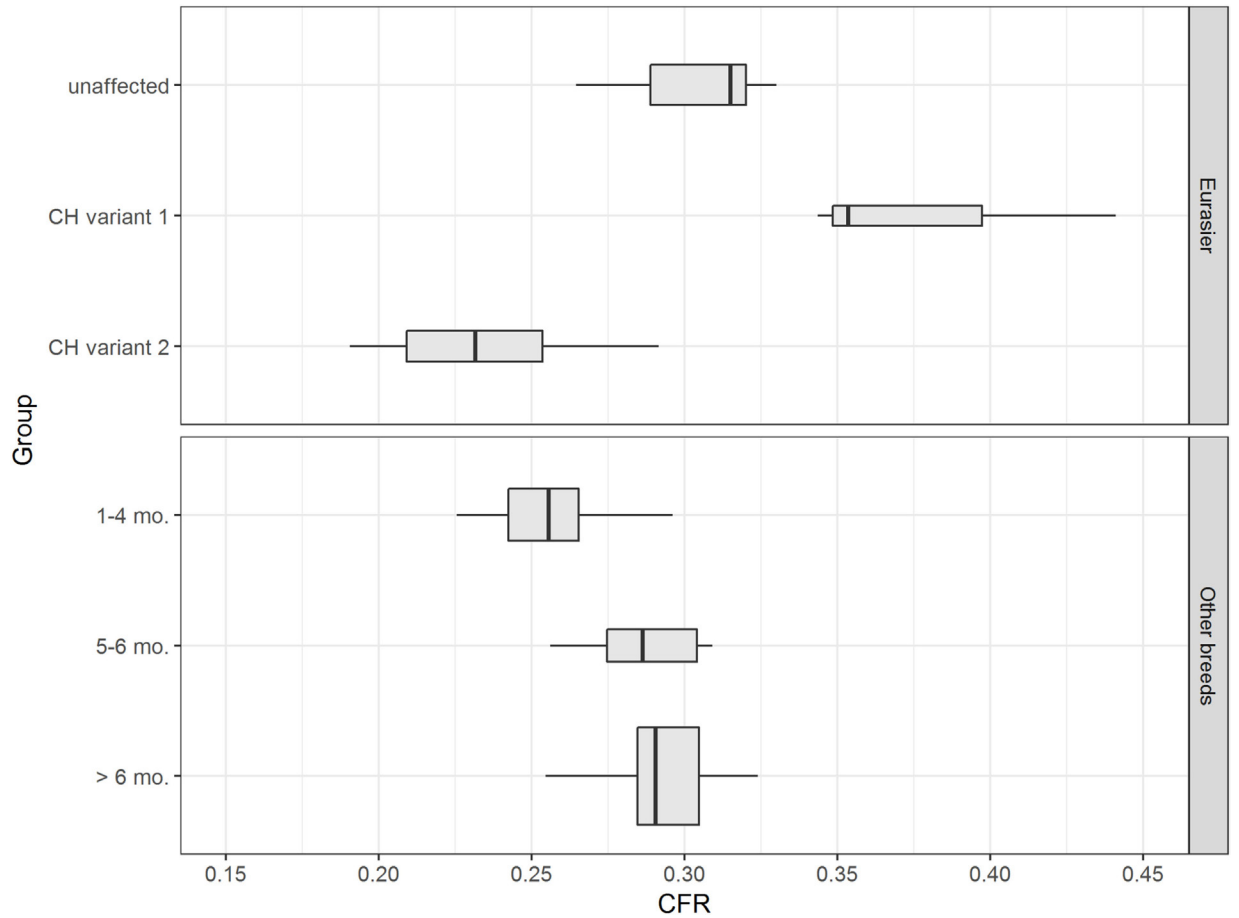

FIGURE 8 | Eurasier dogs with *VLDLR*-associated cerebellar hypoplasia (CH). The upper figure displays boxplots of caudal fossa ratio (CFR) from unaffected Eurasier dogs and Eurasier dogs with CH. The lower figure shows box plots of CFR from control dogs. Measurements of CFR in Eurasier dogs with genetic CH demonstrated the presence of two variants, including variant 1 with an enlarged caudal fossa and variant 2 with a normal-to-smaller caudal fossa.

characterization of translational animal models of cerebellar and hindbrain malformations.

ETHICS STATEMENT

The study was carried out in accordance with the German Animal Protection law. The protocol was approved by the institutional research review board of the Clinic of Small Animal Medicine; #09-06-2014. Dog owners approved use of their dogs' data for scientific purposes by signature in clinical records. Some images from diseased dogs were contributed by the breed club with the consent of the owners for research purposes.

AUTHOR CONTRIBUTIONS

AL, AF, AB, and ALM designed and coordinated the study. AL and AB determined the measurements. JF and AK performed the statistical analysis. MS contributed in acquisition of the data. AL, AF, and JF wrote the manuscript. All authors read and approved the final manuscript.

SUPPLEMENTARY MATERIAL

The Supplementary Material for this article can be found online at http://www.frontiersin.org/articles/10.3389/fvets.2017.00241/full#supplementary-material.

FIGURE S1 | Exploratory data analysis of caudal fossa ratio (CFR) in Eurasier dogs. The plots depict the distribution of CFR in unaffected Eurasier dogs and Eurasier dogs with cerebellar hypoplasia (CH). To achieve better comparability, the CFR was adjusted for age. Measurements of unaffected dogs were centered according to age group. The mean of measurements of unaffected dogs from the corresponding age group was subtracted from the measurements of dogs with CH. The plots suggest multimodal distribution of CFR in both groups and high variability among dogs with CH compared to the unaffected group.

TABLE S1 | Breed and age of control dogs ≤6 months.

TABLE S2 | Sex distribution.

TABLE S3 | Influence of age: confidence intervals.

REFERENCES

1. Barkovich AJ, Chuang SH, Norman D. MR of neuronal migration anomalies. *AJR Am J Roentgenol* (1988) 150:179–87. doi:10.2214/ajr.150.1.179
2. Barkovich AJ, Millen KJ, Dobyns WB. A developmental and genetic classification for midbrain-hindbrain malformations. *Brain* (2009) 132:3199–230. doi:10.1093/brain/awp247
3. Barkovich AJ. Developmental disorders of the midbrain and hindbrain. *Front Neuroanat* (2012) 6:7. doi:10.3389/fnana.2012.00007
4. Jissendi-Tchofo P, Severino M, Nguema-Edzang B, Toure C, Soto Ares G, Barkovich AJ. Update on neuroimaging phenotypes of mid-hindbrain malformations. *Neuroradiology* (2015) 57:113–38. doi:10.1007/s00234-014-1431-2
5. Aldinger KA, Lehmann OJ, Hudgins L, Chizhikov VV, Bassuk AG, Ades LC, et al. FOXC1 is required for normal cerebellar development and is a major contributor to chromosome 6p25.3 Dandy-Walker malformation. *Nat Genet* (2009) 41:1037–42. doi:10.1038/ng.422
6. Gerber M, Fischer A, Jagannathan V, Drogemuller M, Drogemuller C, Schmidt MJ, et al. A deletion in the VLDLR gene in Eurasier dogs with cerebellar hypoplasia resembling a Dandy-Walker-like malformation (DWLM). *PLoS One* (2015) 10:e0108917. doi:10.1371/journal.pone.0108917
7. Bernardino F, Rentmeister K, Schmidt MJ, Bruehschwein A, Matiasek K, Matiasek LA, et al. Inferior cerebellar hypoplasia resembling a Dandy-Walker-like malformation in purebred Eurasier dogs with familial non-progressive ataxia: a retrospective and prospective clinical cohort study. *PLoS One* (2015) 10:e0117670. doi:10.1371/journal.pone.0117670
8. D'Arcangelo G, Miao GG, Chen SC, Soares HD, Morgan JI, Curran T. A protein related to extracellular matrix proteins deleted in the mouse mutant reeler. *Nature* (1995) 374:719–23. doi:10.1038/374719a0
9. Lee GH, D'Arcangelo G. New insights into Reelin-mediated signaling pathways. *Front Cell Neurosci* (2016) 10:122. doi:10.3389/fncel.2016.00122
10. Ranaivoson FM, von Daake S, Comoletti D. Structural insights into Reelin function: present and future. *Front Cell Neurosci* (2016) 10:137. doi:10.3389/fncel.2016.00137
11. Adamsbaum C, Moutard ML, Andre C, Merzoug V, Ferey S, Quere MP, et al. MRI of the fetal posterior fossa. *Pediatr Radiol* (2005) 35:124–40. doi:10.1007/s00247-004-1316-3
12. Guibaud L, Larroque A, Ville D, Sanlaville D, Till M, Gaucherand P, et al. Prenatal diagnosis of 'isolated' Dandy-Walker malformation: imaging findings and prenatal counselling. *Prenat Diagn* (2012) 32:185–93. doi:10.1002/pd.3828
13. Carrera I, Dennis R, Mellor DJ, Penderis J, Sullivan M. Use of magnetic resonance imaging for morphometric analysis of the caudal cranial fossa in Cavalier King Charles Spaniels. *Am J Vet Res* (2009) 70:340–5. doi:10.2460/ajvr.70.3.340
14. Evans HE, De Lahunta A. *Miller's Anatomy of the Dog*. 4th ed. Totowa, NJ: WB Saunders (2013). 111 p.
15. Onar V, Gunes H. On the variability of skull shape in German shepherd (Alsatian) puppies. *Anat Rec A Discov Mol Cell Evol Biol* (2003) 272:460–6. doi:10.1002/ar.a.10052
16. Garcia-Real I, Kass PH, Sturges BK, Wisner ER. Morphometric analysis of the cranial cavity and caudal cranial fossa in the dog: a computerized tomographic study. *Vet Radiol Ultrasound* (2004) 45:38–45. doi:10.1111/j.1740-8261.2004.04006.x
17. Upchurch JJ, McGonnell IM, Driver CJ, Butler L, Volk HA. Influence of head positioning on the assessment of Chiari-like malformation in Cavalier King Charles Spaniels. *Vet Rec* (2011) 169:277. doi:10.1136/vr.d4395
18. Vega A, Quintana F, Berciano J. Basichondrocranium anomalies in adult Chiari type I malformation: a morphometric study. *J Neurol Sci* (1990) 99:137–45. doi:10.1016/0022-510X(90)90150-L
19. Thames RA, Robertson ID, Flegel T, Henke D, O'Brien DP, Coates JR, et al. Development of a morphometric magnetic resonance image parameter suitable for distinguishing between normal dogs and dogs with cerebellar atrophy. *Vet Radiol Ultrasound* (2010) 51:246–53. doi:10.1111/j.1740-8261.2009.01655.x
20. Schmidt MJ, Biel M, Klumpp S, Schneider M, Kramer M. Evaluation of the volumes of cranial cavities in Cavalier King Charles Spaniels with Chiari-like malformation and other brachycephalic dogs as measured via computed tomography. *Am J Vet Res* (2009) 70:508–12. doi:10.2460/ajvr.70.4.508
21. Schmidt MJ, Neumann AC, Amort KH, Failing K, Kramer M. Cephalometric measurements and determination of general skull type of Cavalier King Charles Spaniels. *Vet Radiol Ultrasound* (2011) 52:436–40. doi:10.1111/j.1740-8261.2011.01825.x
22. Carruthers H, Rusbridge C, Dube MP, Holmes M, Jeffery N. Association between cervical and intracranial dimensions and syringomyelia in the cavalier King Charles spaniel. *J Small Anim Pract* (2009) 50:394–8. doi:10.1111/j.1748-5827.2009.00768.x
23. Cross HR, Cappello R, Rusbridge C. Comparison of cerebral cranium volumes between cavalier King Charles spaniels with Chiari-like malformation, small breed dogs and Labradors. *J Small Anim Pract* (2009) 50:399–405. doi:10.1111/j.1748-5827.2009.00799.x
24. Ali BR, Silhavy JL, Gleeson MJ, Gleeson JG, Al-Gazali L. A missense founder mutation in VLDLR is associated with dysequilibrium syndrome without quadrupedal locomotion. *BMC Med Genet* (2012) 13:80. doi:10.1186/1471-2350-13-80
25. Schlotawa L, Hotz A, Zeschnigk C, Hartmann B, Gartner J, Morris-Rosendahl D. Cerebellar ataxia, mental retardation and dysequilibrium syndrome 1 (CAMRQ1) caused by an unusual constellation of VLDLR mutation. *J Neurol* (2013) 260:1678–80. doi:10.1007/s00415-013-6941-z
26. Sonmez FM, Gleeson JG, Celep F, Kul S. The very low density lipoprotein receptor-associated pontocerebellar hypoplasia and dysmorphic features in three Turkish patients. *J Child Neurol* (2013) 28:379–83. doi:10.1177/0883073812441065
27. Azmanov DN, Chamova T, Tankard R, Gelev V, Bynevelt M, Florez L, et al. Challenges of diagnostic exome sequencing in an inbred founder population. *Mol Genet Genomic Med* (2013) 1:71–6. doi:10.1002/mgg3.7
28. Kruer MC, Jepperson TN, Weimer JM, Mroch A, Davis-Keppen L, Crotwell P, et al. Mutations in VLDLR associated with ataxia with secondary vitamin E deficiency. *Mov Disord* (2013) 28:1904–5. doi:10.1002/mds.25573
29. Micalizzi A, Moroni I, Ginevrino M, Biagini T, Mazza T, Romani M, et al. Very mild features of dysequilibrium syndrome associated with a novel VLDLR missense mutation. *Neurogenetics* (2016) 17:191–5. doi:10.1007/s10048-016-0488-y
30. Valence S, Garel C, Barth M, Toutain A, Paris C, Amsallem D, et al. RELN and VLDLR mutations underlie two distinguishable clinico-radiological phenotypes. *Clin Genet* (2016) 90:545–9. doi:10.1111/cge.12779
31. Doherty D, Millen KJ, Barkovich AJ. Midbrain and hindbrain malformations: advances in clinical diagnosis, imaging, and genetics. *Lancet Neurol* (2013) 12:381–93. doi:10.1016/S1474-4422(13)70024-3

Conflict of Interest Statement: The authors declare that the research was conducted in the absence of any commercial or financial relationships that could be construed as a potential conflict of interest.

frontiers in Veterinary Science

ORIGINAL RESEARCH
published: 22 August 2017
doi: 10.3389/fvets.2017.00137

Dynamic Susceptibility Contrast Perfusion Magnetic Resonance Imaging Demonstrates Reduced Periventricular Cerebral Blood Flow in Dogs with Ventriculomegaly

Martin J. Schmidt[1], Malgorzata Kolecka[1], Robert Kirberger[2] and Antje Hartmann[3]*

[1] Department of Veterinary Clinical Sciences, Clinic for Small Animals, Justus-Liebig-University Giessen, Giessen, Germany,
[2] Companion Animal Clinical Studies, Faculty of Veterinary Science, University of Pretoria, Onderstepoort, South Africa,
[3] Hofheim Veterinary Clinic, Hofheim, Germany

OPEN ACCESS

Edited by:
Fintan John McEvoy, University of Copenhagen, Denmark

Reviewed by:
Simon Platt, University of Georgia, United States
Christopher R. Lamb, Royal Veterinary College, United Kingdom

***Correspondence:**
Martin J. Schmidt
martin.j.schmidt@vetmed.uni-giessen.de

Specialty section:
This article was submitted to Veterinary Neurology and Neurosurgery, a section of the journal Frontiers in Veterinary Science

Received: *14 June 2017*
Accepted: *09 August 2017*
Published: *22 August 2017*

Citation:
Schmidt MJ, Kolecka M, Kirberger R and Hartmann A (2017) Dynamic Susceptibility Contrast Perfusion Magnetic Resonance Imaging Demonstrates Reduced Periventricular Cerebral Blood Flow in Dogs with Ventriculomegaly. Front. Vet. Sci. 4:137. doi: 10.3389/fvets.2017.00137

The nature of ventriculomegaly in dogs is still a matter of debate. Signs of increased intraventricular pressure and atrophy of the cerebral white matter have been found in dogs with ventriculomegaly, which would imply increased intraventricular pressure and, therefore, a pathological condition, i.e., to some extent. Reduced periventricular blood flow was found in people with high elevated intraventricular pressure. The aim of this study was to compare periventricular brain perfusion in dogs with and without ventriculomegaly using perfusion weighted-magnetic-resonance-imaging to clarify as to whether ventriculomegaly might be associated with an increase in intraventricular pressure. Perfusion was measured in 32 Cavalier King Charles spaniels (CKCS) with ventriculomegaly, 10 CKCSs were examined as a control group. Cerebral blood flow (CBF) was measured using free-hand regions of interest (ROI) in five brain regions: periventricular white matter, caudate nucleus, parietal cortex, hippocampus, and thalamus. CBF was significantly lower in the periventricular white matter of the dogs with ventriculomegaly ($p = 0.0029$) but not in the other ROIs. Reduction of periventricular CBF might imply increase of intraventricular pressure in ventriculomegaly.

Keywords: normal pressure hydrocephalus, brachycephaly, magnetic resonance imaging cerebral blood flow, malformation, Cavalier King Charles spaniels

INTRODUCTION

In brachycephalic dogs, the lateral cerebral ventricles can be relatively large compared to mesaticephalic dogs (1–3). It has been widely accepted that this increase in ventricular volume is not associated with clinical signs and ventriculo-peritoneal shunting is not indicated (4–7). The finding of large lateral cerebral ventricles was referred to as ventriculomegaly in order to differentiate it from clinically relevant internal hydrocephalus (6–9). However, it was shown that signs of increased intraventricular pressure exist in both, dogs with internal hydrocephalus and neurological dysfunction, and also in clinically sound dogs with ventriculomegaly (9, 10). Furthermore, a recent morphological study (11) revealed that larger cerebral ventricles in brachycephalic dogs are associated with white matter loss as occurs in conventional internal hydrocephalus (12, 13). Based on these changes, it must be considered that canine ventriculomegaly is not a physiological variant of ventricular dimensions as previously reported (1–3, 5–7) but may be a preliminary or arrested form of internal hydrocephalus.

Many forms of hydrocephalus in humans can be associated with a reduction in periventricular cerebral blood flow (CBF) (14–16). CBF refers to the volume of blood per unit time passing through a given region of brain tissue, commonly measured in milliliter per minute per 100 g of brain tissue. This was also shown in dogs with experimentally induced internal hydrocephalus (17). The impaired perfusion is believed to be caused by increased cerebrospinal fluid (CSF) pressure and ventricular distension, which causes stretching of periventricular blood vessels and white matter fibers and consequently functional, and later to structural damage of periventricular white matter (13, 16, 18). The reversibility of hydrocephalus symptoms was associated with improved CBF in the periventricular white matter after shunting, which supports this hypothesis (19).

Magnetic resonance imaging (MRI) can be used to non-invasively measure CBF in humans and in dogs (20–23). Dynamic susceptibility contrast perfusion MRI (DSC-PMRI) allow to quantify blood volume, which passes through the vascular system of brain tissue. The technique quantifies the induced signal loss caused by paramagnetic contrast agents, which is proportional to the amount of blood in the microvasculature (24–26). DSC-PMRI was used demonstrate reduced regional CBF in the periventricular white matter in human patients with hydrocephalus (27, 28).

We hypothesize that periventricular CBF might also be decreased in dogs with ventriculomegaly just as in human patients with hydrocephalus. To investigate this hypothesis, we aim to measure brain perfusion using DSC-PMRI in dogs with ventriculomegaly and compare it to brain perfusion in normal dogs.

MATERIALS AND METHODS

Study Population

Cavalier King Charles spaniels (CKCS) were chosen for the study. From dogs that underwent MRI-scanning of the head and cervical spine for breeding selection against syringomyelia (SM), CKCSs with ventriculomegaly were selected for the study group. The presence of ventriculomegaly was based on the following criteria. Dogs with a normal ventricular system have very narrow and slit-like horns of the lateral ventricles. In the finding of ventriculomegaly, the interpreter subjectively noted a greater proportion of the intracranial volume occupied by the lateral ventricles. The closely spaced walls of the temporal horns and/or the olfactory recesses were separated by cerebrospinal fluid (**Figures 1C,D**: yellow arrows) in these brains and the lacking of a septum pellucidum created a large connection between the first and second ventricles (**Figures 1C,D**: blue arrows). CKCSs without these findings were used as a control (**Figures 1A,B**). The groups were age and weight matched. Before scanning, each dog underwent a general and neurological examination by a

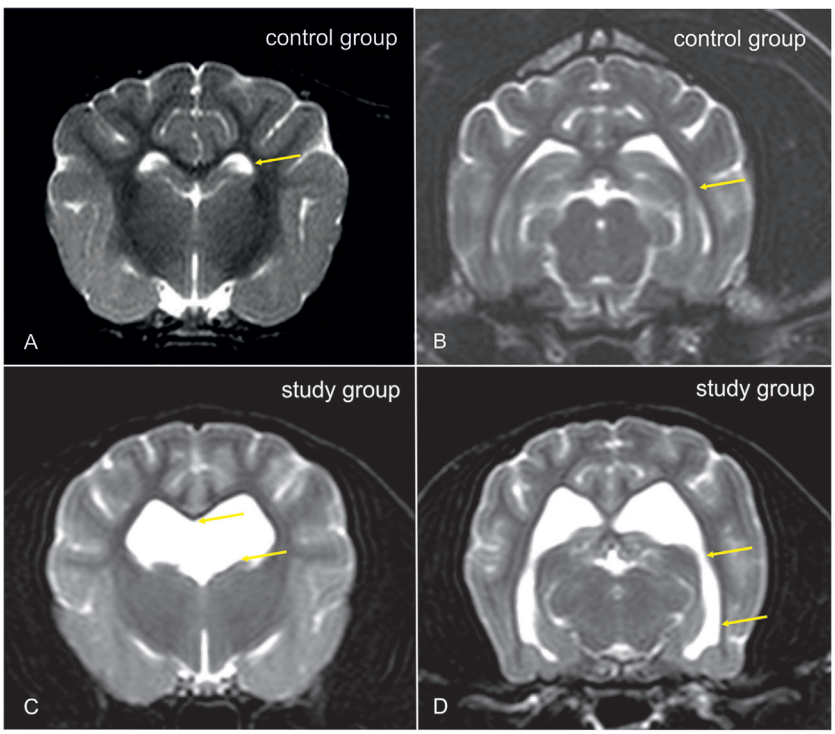

FIGURE 1 | Transverse T2-weighted images of the brain of a Cavalier King Charles spaniel (CKCS) with normal lateral cerebral ventricles [control group, **(A,B)**] and a CKCS with ventriculomegaly [study group, **(C,D)**]. In the study group, a greater proportion of the brain volume is occupied by the lateral ventricles. The closely spaced walls of the temporal horns [**(B,D)**: yellow arrows] and/or the olfactory recesses were separated by cerebrospinal fluid (CSF) in these brains, and the lacking of a septum pellucidum created a large connection between the first and second ventricles [**(C)**: yellow arrows].

board-certified neurologist. Dogs with SM or neurological signs were not included into the study. All dogs were positive for the morphological changes consistent with Chiari-like malformation. Complete blood count, biochemistry panel, and electrolytes were determined before examination.

Ethics Statement

All investigations were conducted in strict compliance with the restrictions of the German Animal Protection Law. All dogs from the study and control group were client owned and lived with their owners. The owners of the dogs gave permission for their animals to be used in this investigation. The study was approved by the Committee on the Ethics of Animal Experiments of the Justus-Liebig-University, Giessen.

Anesthesia Protocol

Standard intravenous catheters (18 gage) were placed in the right or left cephalic vein. Diazepam (0.5 mg/kg) was administered IV, and anesthesia was induced with propofol (2–4 mg/kg, IV). Dogs were endotracheally intubated and anesthesia was maintained with 1.5–2% isoflurane in oxygen. Dogs were automatically ventilated throughout the MRI examination and kept normocapnic (35–45 mmHg). CO_2 was measured using side stream capnography from the endotracheal tube.

Imaging Technique

Standard Head Examination

In order to diagnose structural changes consistent with Chiari-like malformation and SM, a standard MRI examination of the brain and spinal cord was performed prior to the perfusion studies. Imaging was performed using a 1 T MRI scanner (Gyroscan Intera, Phillips, Hamburg, Germany) and a two-part surface coil consisting of two elliptical elements, which were placed on the right and left sides of the head. Dogs were examined in sternal recumbency with their neck in extension sagittal, dorsal, and transverse images were obtained using T2-Turbospin echo sequences (TE: 120 ms, TR: 2,900 ms). Transverse FLAIR images and dorsal T1-weighted gradient echo images were acquired before and after contrast (i.e., after perfusion study) medium administration to exclude structural brain abnormalities. Field of view was 180 mm × 180 mm, matrix was 288 × 288. Slice thickness varied from 2 to 3 mm. The cervical spine was examined until the first the first thoracic vertebra. Sagittal T2-weighted images were obtained. If the presence of SM was confirmed, transverse gradient-echo images were obtained over the whole extension of the SM.

Perfusion-Weighted Imaging

Perfusion-weighted images were acquired by use of a dynamic multishot fast-field echo-echo-planar imaging sequence. Slice orientation was parallel to the base of the skull. In total, 40 dynamics/slices were acquired in a dorsal plane with a time gap of 1.6 ms. At the 10th dynamic, 0.2 mmol/kg gadoteric acid was injected at a rate of 5 ml/s using a double-headed injection pump (Accutron MR, Medtron, Saarbrücken, Germany). The injection of contrast medium was followed by a 20-ml injection of isotonic Ringer solution.

Perfusion Analysis

Image analysis was performed using a commercially available software (Stroketool, Digital Image Solutions, Frechen, Germany). The program works with established perfusion calculation algorithms (SVD-deconvolution) for quantitative perfusion imaging, which takes the arterial input function (AIF) into account (29, 30). The AIF was determined at the level of the middle cerebral artery. In this model, CBF measurements are based on time course signal changes after the infusion of a bolus of gadolinium in each voxel of the brain tissue in comparison of the same changes in the middle cerebral artery.

Regions of interest (ROIs) were manually drawn around the periventricular white matter of the frontal horn (rostral limb of the internal capsule), the caudate nucleus, the thalamus, and the cerebral cortex adjacent to the internal capsule in both hemispheres by one investigator. These ROIs were delineated on corresponding dorsal T2-weighted images linked with perfusion weighted images. CBF was measured and compared between groups as these are the most important perfusion parameters related to cerebral hemodynamic changes in human hydrocephalus (15, 31–33). The software calculated the CBF as the blood volume in the brain in a given period of time measured in ml/100 g/min. The software creates color-coded maps for the estimated parameters from gray scale MR images. In these CBF-maps, red are being highly perfused areas, dark blue indicating extremely low, and green being intermediate perfusion.

Statistical Analysis

All statistical analyses were performed by use of commercially available software (BMDP Statistical Software, Inc., Los Angeles, CA, USA). The Shapiro–Wilk test was used to assess for normality in datasets. Means and SDs were calculated for normally distributed data. The values for each region were computed as the average values of both sides. Mean values for CBF were compared by use of two-tailed independent sample *t*-tests. The level of significance was set to 0.01 for all tests. To test homogeneity of the groups, the relative frequency of male and female animals in the groups was compared using Fisher's exact test.

RESULTS

Animals

Group 1 (normal CKCSs) comprised four male and six female dogs weighing 6–9 kg (mean 7.53 ± 1.19). Group 2 (CKCSs with ventriculomegaly) included 13 male and 19 female dogs weighing 6–9 kg (mean 7.54 ± 1.05). Fisher exact test revealed no statistically difference between the number of females and males between groups ($p = 1$).

Perfusion Measurement

Mean CBF values are summarized in **Table 1**. Significantly lower CBF was found in the periventricular white matter of dogs with ventriculomegaly (**Figure 2**). Values computed from other ROIs were not significantly different between groups.

TABLE 1 | Mean ± SD quantitative estimates of CBF for the regions of interest evaluated in normal Cavalier King Charles spaniels and dogs with ventriculomegaly.

	Periventricular white matter	Caudate nucleus	Thalamus	Cerebral cortex
CBF normal dogs	100.5 ± 5.3	101.2 ± 9.97	94.44 ± 21.56	102.20 ± 4.3
CBF dogs with ventriculomegaly	42.05 ± 10.88	85.55 ± 21.33	50.56 ± 28.66	97.53 ± 6.3
p-Value	0.0029	0.077	0.367	0.0527

CBF, cerebral blood flow (milliliter per minute per 100 g of brain tissue).

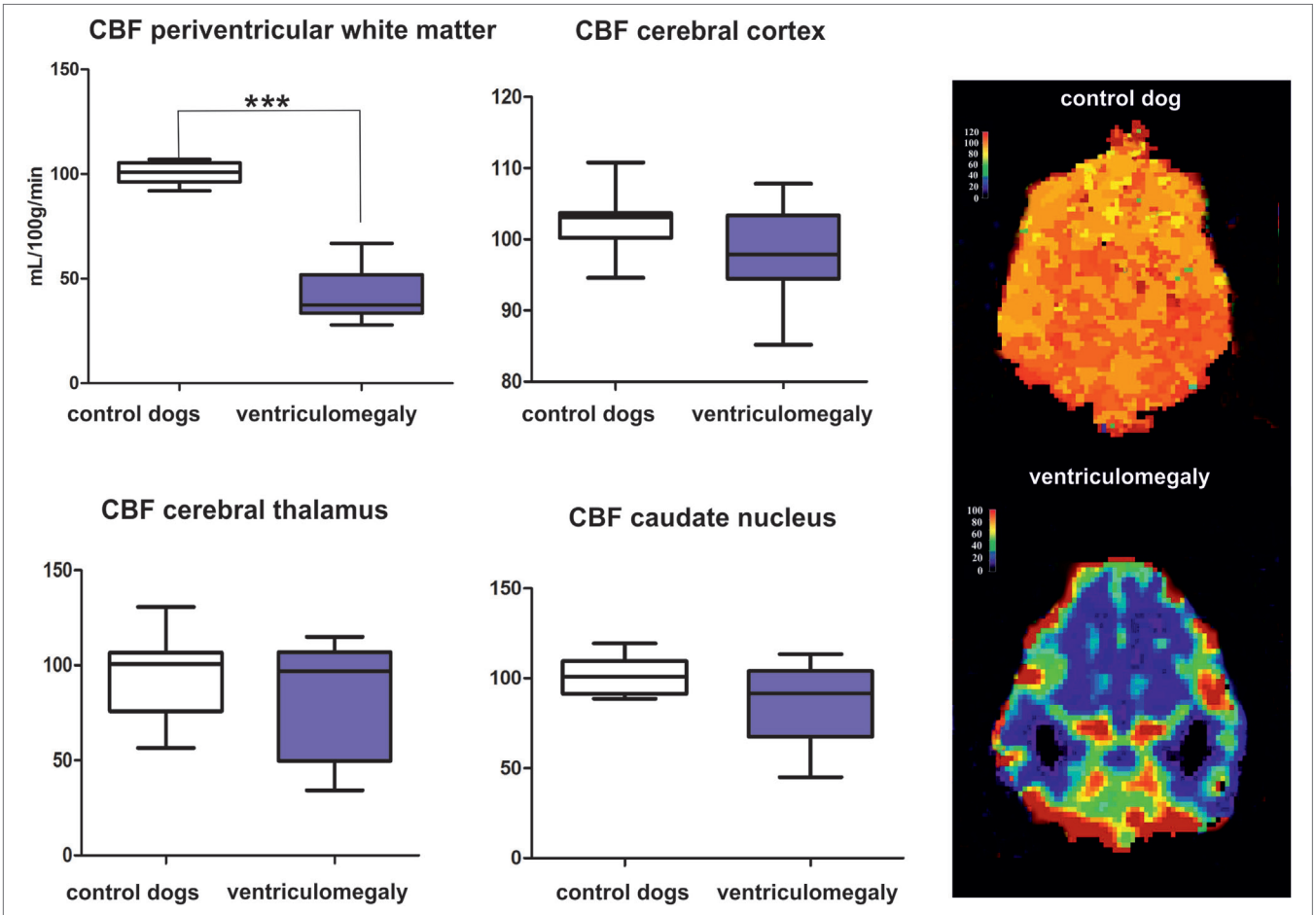

FIGURE 2 | Results of the group comparison of cerebral blood flow (CBF) between Cavalier King Charles spaniels (CKCS) with and without ventriculomegaly. Results presented as mean, range, 25, and 75 quartile in a box and whisker plot. Significantly different parameters are marked with asterisks (***$p < 0.001$). Color-coded perfusion maps are displayed for CBF values in a normal CKCS and in a Cavalier King Charles spaniel with ventriculomegaly.

DISCUSSION

The nature and origin of ventriculomegaly in dogs remain controversial and not well elucidated (11, 34, 35). Signs of increased intraventricular pressure (elevated corpus callosum, a distended third ventricle and a deformed interthalamic adhesion as well as dilated olfactory recesses) (9) and atrophy of the cerebral white matter (11) have been found in dogs with ventriculomegaly, which would imply a pathological condition to some extent. Here, we examined the regional CBF in CKCSs with ventriculomegaly compared to normal controls using DSC-PMRI with a gadolinium-based contrast agent. The results of the investigation indicate that CBF is reduced in the periventricular white matter of CKCSs with ventriculomegaly.

MR-perfusion techniques have proven to be feasible in dogs (22, 23) but accuracy and validity of the method for its standard use must be further evaluated. Positron emission tomography (PET) is considered to be the gold standard for studying cerebral hemodynamics (36). However, a PET and perfusion-based MR techniques of CBF measurements were found to be highly consistent in studies involving both humans (24, 37, 38) and dogs (39, 40). The values extracted from our study of clinically normal CKCSs come close to those measured in studies using MRI- or CT-based perfusion studies (39, 40), but differ from

others (17, 22). However, several factors limit the comparison of the present investigation with other studies. The technique is sensitive to physiological variations, which reduce measurement reproducibility. A source of potential error could originate from the use of different anesthetic drugs that can have a significant effect on cerebral blood vessels. Volatile anesthetics can cause cerebral vasodilatation and thereby an increase in CBF (41–43). Spatial resolution disparities and low signal-to-noise ratios in the perfusion-weighted images make the precise location of the ROIs difficult. The choice of arterial input can have an effect on measuring CBF (44). Missing standardization of acquisition parameters and use of variable postprocessing software constitutes another challenge for the comparison of data acquired in different studies (45). In addition, this study differs in that we have used combined and averaged measurements from the left and right forebrain in order to discount for known differences between the hemispheres (22).

The findings of ventricular enlargement that correlates with white matter atrophy as well as the reduction in periventricular CBF found here are comparable to findings in human normal pressure hydrocephalus (NPH) that predominantly affects the elderly (11, 46, 47). Visible obstructions in the ventricular system cannot be detected in both, humans with NPH and dogs with ventriculomegaly. Studies in elderly people have shown decreased CBF in the periventricular white matter in NPH patients that gradually normalized toward the subcortical white matter (48). This inadequate blood supply eventually may produce structural white matter damage and gradual atrophy (49). However, reduced CBF is also found in the frontal cerebral cortex, thalamus, and in the basal nuclei in patients with NPH (31, 32, 48, 50–52). Although we could not find significant differences between the dogs in these brain areas, the SD of averaged CBF in the dogs with ventriculomegaly was relatively high for these ROIs with some of the patients also having low measurements in the caudate nucleus and the thalamus (**Figure 1**). CBF changes in other tissue areas can, therefore, not be totally ruled out.

Based on data on this and other studies, it seems plausible that ventriculomegaly may be a preliminary stage or an arrested form of internal hydrocephalus. Ventriculomegaly has been attributed to disturbances in CSF dynamics in dogs by some authors (11, 34, 35) that may be caused by osseous obstruction of the foramen magnum, reducing the amounts of CSF expelled from the cranial cavity. Craniocervical junction anomalies that reduce the CSF outflow tract of toward the cisterna magna are often found in small brachycephalic dogs (53). The presence of a widened mesencephalic aqueduct and aqueductal CSF flow void may support the hypothesis of a hyperdynamic CSF flow through the aqueduct as a consequence of an impaired CSF outflow from the skull (9, 10, 54).

Scrivani introduced to model of a reduced intracranial compliance for dogs with disturbed CSF hemodynamics and ventricular distension (54). Following systolic expansion of the intracranial arteries, the following increase of intracranial pressure is balanced by expulsion of venous blood and CSF from the cranial cavity. If intracranial compliance is reduced, a higher CSF volume is forced from the lateral ventricles through the aqueduct with a higher velocity. The resulting signal void sign in the aqueduct was proposed to be a marker of reduced intracranial compliance in small brachycephalic dogs (54). Compared to mesaticephalic dogs, the cranial capacity, i.e., the part of the cranial cavity that is not occupied by brain tissue, is reduced in brachycephalic dogs (55), which may impair brain expansion during systole. The jugular foramen can be small in the brachycephalic CKCS (56), which may also reduce venting of venous blood from the cranial cavity. Both effects may contribute to a reduced intracranial compliance.

The influence of ventriculomegaly on brain function in dogs is unclear (4, 8, 57). Human patients with NPH show characteristic triad of neural function deficits including gait impairment, dementia, and urinary incontinence (58, 59). This could not be documented in dogs using conventional clinical evaluation. Detailed behavioral studies and breed-specific gait analyses are necessary to clarify the impact of ventriculomegaly on brain function and whether ventriculomegaly might be an indication for CSF shunting procedures in dogs.

CONCLUSION

Cerebral blood flow can be reduced in periventricular white matter in CKCSs with ventriculomegaly, which makes some increase of intraventricular pressure likely.

ETHICS STATEMENT

The study was approved by the ethics committee of the Veterinary Faculty of the Justus Liebig University.

AUTHOR CONTRIBUTIONS

Conceived and designed the experiments: AH and MS. Performed the experiments: AH, MK, and MS. Analyzed the data: MS. Contributed reagents/materials/analysis tools: AH and MS. Wrote the paper: AH, MS, and RK.

REFERENCES

1. Kii S, Uzuka Y, Taura Y, Nakaichi M, Takeuchi A, Inokuma H, et al. Magnetic resonance imaging of the lateral ventricles in beagle-type dogs. *Vet Radiol Ultrasound* (1997) 38:430–3. doi:10.1111/j.1740-8261.1997.tb00866.x
2. De Haan CE, Kraft SL, Gavin PR, Wendling LR, Griebenow ML. Normal variation in size of the lateral ventricles of the Labrador Retriever dog as assessed by magnetic resonance imaging. *Vet Radiol Ultrasound* (1994) 35:83–6. doi:10.1111/j.1740-8261.1994.tb00191.x
3. Vullo T, Korenman E, Manzo RP, Gomez DG, Deck MD, Cahill PT. Diagnosis of cerebral ventriculomegaly in normal adult beagles using quantitative MRI. *Vet Radiol Ultrasound* (1997) 38:277–81. doi:10.1111/j.1740-8261.1997.tb00855.x
4. Driver CJ, Chandler K, Walmsley G, Shihab N, Volk HA. The association between Chiari-like malformation, ventriculomegaly and seizures in cavalier King Charles spaniels. *Vet J* (2013) 195:235–7. doi:10.1016/j.tvjl.2012.05.014
5. Schwarz T, Saunders J. *Veterinary Computed Tomography*. Iowa, USA: Wiley Blackwell (2012). 185 p.

6. Gavin PR, Bagley RS. *Practical Small Animal MRI*. Iowa, USA: Wiley Blackwell (2011). 64 p.
7. Thomas B. Hydrocephalus in dogs and cats. *Vet Clin North Am Small Anim Pract* (2010) 40:143–59. doi:10.1016/j.cvsm.2009.09.008
8. Saito M, Olby NJ, Spaulding K, Muñana K, Sharp NJ. Relationship among basilar artery resistance index, degree of ventriculomegaly, and clinical signs in hydrocephalic dogs. *Vet Radiol Ultrasound* (2003) 44:687–94. doi:10.1111/j.1740-8261.2003.tb00532.x
9. Laubner S, Ondreka N, Failing K, Kramer M, Schmidt MJ. Magnetic resonance imaging signs of high intraventricular pressure – comparison of findings in dogs with clinically relevant internal hydrocephalus and asymptomatic dogs with ventriculomegaly. *BMC Vet Res* (2015) 11:181. doi:10.1186/s12917-015-0479-5
10. Ryan CT, Glass EN, Seiler G, Zwingenberger AL, Mai W. Magnetic resonance imaging findings associated with lateral cerebral ventriculomegaly in English Bulldogs. *Vet Radiol Ultrasound* (2014) 55:292–9. doi:10.1111/vru.12123
11. Schmidt MJ, Laubner S, Kolecka M, Failing K, Moritz A, Kramer M, et al. Comparison of the relationship between cerebral white matter and grey matter in normal dogs and dogs with lateral ventricular enlargement. *PLoS One* (2015) 10:e0124174. doi:10.1371/journal.pone.0124174
12. Wünschmann A, Oglesbee M. Periventricular changes associated with spontaneous canine hydrocephalus. *Vet Pathol* (2001) 38:67–73. doi:10.1354/vp.38-1-67
13. Del Bigio MR. Neuropathological changes caused by hydrocephalus. *Acta Neuropathol* (1993) 85:573–85. doi:10.1007/BF00334666
14. Mataró M, Poca MA, Salgado-Pineda P, Castell-Conesa J, Sahuquillo J, Díez-Castro MJ, et al. Postsurgical cerebral perfusion changes in idiopathic normal pressure hydrocephalus: a statistical parametric mapping study of SPECT images. *J Nucl Med* (2003) 44:1884–9.
15. Mori K, Maeda M, Asegawa S, Iwata J. Quantitative local cerebral blood flow change after cerebrospinal fluid removal in patients with normal pressure hydrocephalus measured by a double injection method with N-isopropyl-p-[123I] iodoamphetamine. *Acta Neurochir* (2002) 144:255–63. doi:10.1007/s007010200033
16. Nakada J, Oka N, Nagahori T, Endo S, Takaku A. Changes in the cerebral vascular bed in experimental hydrocephalus: an angio-architectural and histological study. *Acta Neurochir (Wien)* (1992) 114:43–50. doi:10.1007/BF01401113
17. Dombrowski SM, Schenk S, Leichliter A, Leibson Z, Fukamachi K, Luciano MG. Chronic hydrocephalus-induced changes in cerebral blood flow: mediation through cardiac effects. *J Cereb Blood Flow Metab* (2006) 26:1298–310. doi:10.1038/sj.jcbfm.9600282
18. Goh D, Minns RA. Intracranial pressure and cerebral arterial flow velocity indices in childhood hydrocephalus: current review. *Child Nerv Syst* (1995) 11:392–6. doi:10.1007/BF00717403
19. Klinge PM, Brooks DJ, Samii A, Weckesser E, van den Hoff J, Fricke H, et al. Correlates of local cerebral blood flow (CBF) in normal pressure hydrocephalus patients before and after shunting – a retrospective analysis of [(15)O]H(2)O PET-CBF studies in 65 patients. *Clin Neurol Neurosurg* (2008) 110:369–75. doi:10.1016/j.clineuro.2007.12.019
20. Petrella JR, Provenzale JM. MR perfusion imaging of the brain: techniques and applications. *Am J Roentgenol* (2000) 175:207–19. doi:10.2214/ajr.175.1.1750207
21. Tidwell AS, Robertson ID. Magnetic resonance imaging of normal and abnormal brain perfusion. *Vet Radiol Ultrasound* (2011) 52:62–71. doi:10.1111/j.1740-8261.2010.01786.x
22. Hartmann A, Driesen A, Lautenschläger IE, Scholz VB, Schmidt MJ. Quantitative analysis of brain perfusion in healthy dogs by means of magnetic resonance imaging. *Am J Vet Res* (2016) 77:1227–35. doi:10.2460/ajvr.77.11.1227
23. Stadler KL, Pease AP, Ballegeer A. Dynamic susceptibility contrast magnetic resonance imaging protocol of the normal canine brain. *Front Vet Sci* (2017) 4:41. doi:10.3389/fvets.2017.00041
24. Østergaard L, Johannsen P, Høst-Poulsen P, Gyldensted C, Rosen BR. Cerebral blood flow measurements by magnetic resonance imaging bolus tracking: comparison with [15O]H2O positron emission tomography in humans. *J Cereb Blood Flow Metab* (1998) 18:935–40. doi:10.1097/00004647-199809000-00002
25. Giesel FL, Wüstenberg T, Bongers A, Weber M, Zechmann C, Weber MA, et al. MR-based methods of the functional imaging of the central nervous system. *Röfo* (2005) 177:714–30.
26. Barbier EL, Lamalle L, Décorps M. Methodology of brain perfusion imaging. *J Magn Reson Imaging* (2001) 13:496–520. doi:10.1002/jmri.1073
27. Tanaka A, Kimura M, Nakayama Y, Yoshinaga S, Tomonaga M. Cerebral blood flow and autoregulation in normal pressure hydrocephalus. *Neurosurgery* (1997) 40:1161–7. doi:10.1097/00006123-199706000-00009
28. Walter C, Hertel F, Naumann E, Mörsdorf M. Alteration of cerebral perfusion in patients with idiopathic normal pressure hydrocephalus measured by 3D perfusion weighted magnetic resonance imaging. *J Neurol* (2005) 252:1465–71. doi:10.1007/s00415-005-0891-z
29. Østergaard L, Weisskoff RM, Chesler DA. High resolution measurement of cerebral blood flow using intravascular tracer bolus passages. Part I: mathematical approach and statistical analysis. *Magn Reson Med* (1996) 36:715–25. doi:10.1002/mrm.1910360510
30. Østergaard L, Sorensen AG, Kwong KK, Weisskoff RM, Gyldensted C, Rosen BR. High resolution measurement of cerebral blood flow using intravascular tracer bolus passages. Part II: experimental comparison and preliminary results. *Magn Reson Med* (1996) 36:726–36. doi:10.1002/mrm.1910360511
31. Ziegelitz D, Arvidsson J, Hellström P, Tullberg M, Wikkelsø C, Starck G. Pre-and postoperative cerebral blood flow changes in patients with idiopathic normal pressure hydrocephalus measured by computed tomography (CT)-perfusion. *J Cereb Blood Flow Metab* (2016) 36:1755–66. doi:10.1177/0271678X15608521
32. Virhammar J, Laurell K, Ahlgren A, Cesarini KG, Larsson EM. Idiopathic normal pressure hydrocephalus: cerebral perfusion measured with pCASL before and repeatedly after CSF removal. *J Cereb Blood Flow Metab* (2014) 34:1771–8. doi:10.1038/jcbfm.2014.138
33. Ivkovic M, Reiss-Zimmermann M, Katzen H, Preuss M, Kovanlikaya I, Heier L, et al. MRI assessment of the effects of acetazolamide and external lumbar drainage in idiopathic normal pressure hydrocephalus. *Fluids Barriers CNS* (2015) 12:9. doi:10.1186/s12987-015-0004-z
34. Driver CJ, Rusbridge C, Cross HR, McGonnell I, Volk HA. Relationship of brain parenchyma within the caudal cranial fossa and ventricle size to syringomyelia in cavalier King Charles spaniels. *J Small Anim Pract* (2010) 51:382–6. doi:10.1111/j.1748-5827.2010.00952.x
35. Rusbridge C, Greitz D, Iskandar BJ. Syringomyelia: current concepts in pathogenesis, diagnosis and treatment. *J Vet Intern Med* (2006) 20:469–79. doi:10.1111/j.1939-1676.2006.tb02884.x
36. Chen BC, Huang SC, Germano G, Kuhle W, Hawkins RA, Buxton D, et al. Noninvasive quantification of hepatic arterial blood flow with nitrogen-13-ammonia and dynamic positron emission tomography. *J Nucl Med* (1991) 32:2199–206.
37. Carroll TJ, Teneggi V, Jobin M, Squassante L, Treyer V, Hany TF, et al. Absolute quantification of cerebral blood flow with magnetic resonance, reproducibility of the method, and comparison with H215O positron emission tomography. *J Cereb Blood Flow Metab* (2002) 22:1149–56. doi:10.1097/00004647-200209000-00013
38. Lin W, Celik A, Derdeyn C. Quantitative measurements of cerebral blood flow in patients with unilateral carotid artery occlusion: a PET and MR study. *J Magn Res Imag* (2001) 14:659–67. doi:10.1002/jmri.10021
39. Gobbel GT, Cann CE, Iwamoto HS, Fike JR. Measurement of regional cerebral blood flow in the dog using ultrafast computed tomography. Experimental validation. *Stroke* (1991) 22:772–9. doi:10.1161/01.STR.22.6.772
40. Peterson KL, MacLeod AG, Wisner ER, Larson RF, Pollard RE. Quantitative assessment of blood volume, blood flow, and permeability of the brain of clinically normal dogs by use of dynamic contrast-enhanced computed tomography. *Am J Vet Res* (2008) 69:45–50. doi:10.2460/ajvr.69.1.45
41. Hansen TD, Warner DS, Todd MM, Vust LJ, Trawick DC. Distribution of cerebral blood flow during halothane versus isoflurane anesthesia in rats. *J Am Soc Anesthesiol* (1988) 69:332–7. doi:10.1097/00000542-198809000-00008
42. Farber NE, Harkin CP, Niedfeldt J, Hudetz AG, Kampine JP, Schmeling WT. Region-specific and agent-specific dilation of intracerebral microvessels by volatile anesthetics in rat brain slices. *Anesthesiology* (1997) 87:1191–8. doi:10.1097/00000542-199711000-00024

43. Matta BF, Heath KJ, Tipping K, Summors C. Direct cerebral vasodilatory effects of sevoflurane and isoflurane. *Anesthesiology* (1999) 91:677–80. doi:10.1097/00000542-199909000-00019
44. Wintermark M, Thiran JP, Maeder P, Schnyder P, Meuli R. Simultaneous measurement of regional cerebral blood flow by perfusion CT and stable xenon CT: a validation study. *AJNR Am J Neuroradiol* (2001) 22:905–14.
45. Essig M, Shiroishi MS, Nguyen TB, Saake M, Provenzale JM, Enterline D, et al. Perfusion MRI: the five most frequently asked technical questions. *AJR Am J Roentgenol* (2013) 200:24–34. doi:10.2214/AJR.12.9543
46. Hakim S, Adams RD. The special clinical problem of symptomatic hydrocephalus with normal cerebrospinal fluid pressure. Observations on cerebrospinal fluid hydrodynamics. *J Neurol Sci* (1965) 2:307–27. doi:10.1016/0022-510X(65)90016-X
47. Rekate HL. A consensus on the classification of hydrocephalus: its utility in the assessment of abnormalities of cerebrospinal fluid dynamics. *Childs Nerv Syst* (2011) 27:1535–41. doi:10.1007/s00381-011-1558-y
48. Momjian S, Owler BK, Czosnyka Z, Czosnyka M, Pena A, Pickard JD. Pattern of white matter regional cerebral blood flow and autoregulation in normal pressure hydrocephalus. *Brain* (2004) 127:965–72. doi:10.1093/brain/awh131
49. Jeppsson A, Zetterberg H, Blennow K, Wikkelsø C. Idiopathic normal-pressure hydrocephalus: pathophysiology and diagnosis by CSF biomarkers. *Neurology* (2013) 80:1385–92. doi:10.1212/WNL.0b013e31828c2fda
50. Owler BK, Momjian S, Czosnyka Z, Czosnyka M, Pena A, Harris NG, et al. Normal pressure hydrocephalus and cerebral blood flow: a PET study of baseline values. *J Cereb Blood Flow Metab* (2004) 24:17–23. doi:10.1097/01.WCB.0000093326.88757.49
51. Owler BK, Pickard JD. Normal pressure hydrocephalus and cerebral blood flow: a review. *Acta Neurol Scand* (2004) 104:325–42. doi:10.1034/j.1600-0404.2001.00092.x
52. Kristensen B, Malm J, Fagerland M, Hietala SO, Johansson B, Ekstedt J, et al. Regional cerebral blood flow, white matter abnormalities, and cerebrospinal fluid hydrodynamics in patients with idiopathic adult hydrocephalus syndrome. *J Neurol Neurosurg Psychiatry* (1996) 60:282–8. doi:10.1136/jnnp.60.3.282
53. Loughin CA, Marino DJ. Atlantooccipital overlap and other craniocervical junction abnormalities in dogs. *Vet Clin North Am Small Anim Pract* (2016) 46:243–51. doi:10.1016/j.cvsm.2015.10.008
54. Scrivani PV, Freer SR, Dewey CW, Cerda-Gonzalez S. Cerebrospinal fluid signal-void sign in dogs. *Vet Radiol Ultrasound* (2009) 50:269–75. doi:10.1111/j.1740-8261.2009.01532.x
55. Schmidt MJ, Amort KH, Failing K, Klingler M, Kramer M, Ondreka N. Comparison of the endocranial- and brain volumes in brachycephalic dogs, mesaticephalic dogs and Cavalier King Charles spaniels in relation to their body weight. *Acta Vet Scand* (2014) 13:30. doi:10.1186/1751-0147-56-30
56. Schmidt MJ, Ondreka N, Sauerbrey M, Volk HA, Rummel C, Kramer M. Volume reduction of the jugular foramina in Cavalier King Charles Spaniels with syringomyelia. *BMC Vet Res* (2012) 6:158. doi:10.1186/1746-6148-8-158
57. Lu D, Lamb CR, Pfeiffer DU, Targett MF. Neurological signs and results of magnetic resonance imaging in 40 cavalier King Charles spaniels with Chiari type 1-like malformations. *Vet Rec* (2003) 153:60–3. doi:10.1136/vr.153.9.260
58. Keong NC, Pena A, Price SJ, Czosnyka M, Czosnyka Z, Pickard JD. Imaging normal pressure hydrocephalus: theories, techniques, and challenges. *Neurosurg Focus* (2016) 41:E11. doi:10.3171/2016.7.FOCUS16194
59. Chrysikopoulos H. Idiopathic normal pressure hydrocephalus: thoughts on etiology and pathophysiology. *Med Hypotheses* (2009) 73:718–24. doi:10.1016/j.mehy.2009.04.044

Conflict of Interest Statement: The authors declare that the research was conducted in the absence of any commercial or financial relationships that could be construed as a potential conflict of interest.

frontiers in Veterinary Science

ORIGINAL RESEARCH
published: 18 December 2017
doi: 10.3389/fvets.2017.00219

Hyperintensity of Cerebrospinal Fluid on T2-Weighted Fluid-Attenuated Inversion Recovery Magnetic Resonance Imaging Caused by High Inspired Oxygen Fraction

Melania Moioli[1], Olivier Levionnois[2], Veronika M. Stein[3], Gertraud Schüpbach[4], Marta Schmidhalter[1] and Daniela Schweizer-Gorgas[1]*

[1] Clinical Radiology, Department of Clinical Veterinary Medicine, Vetsuisse-Faculty, University of Bern, Bern, Switzerland,
[2] Clinical Anesthesiology, Department of Clinical Veterinary Medicine, Vetsuisse-Faculty, University of Bern, Bern, Switzerland,
[3] Clinical Neurology, Department of Clinical Veterinary Medicine, Vetsuisse-Faculty, University of Bern, Bern, Switzerland,
[4] Department of Clinical Research and Veterinary Public Health, Veterinary Public Health Institute, Vetsuisse-Faculty, University of Bern, Bern, Switzerland

OPEN ACCESS

Edited by:
Sibylle Maria Kneissl, Veterinärmedizinische Universität Wien, Austria

Reviewed by:
Erik R. Wisner, University of California, Davis, United States
Hecht Silke, University of Tennessee, Knoxville, United States

***Correspondence:**
Melania Moioli
melania.moioli@vetsuisse.unibe.ch

Specialty section:
This article was submitted to Veterinary Imaging, a section of the journal Frontiers in Veterinary Science

Received: *20 September 2017*
Accepted: *04 December 2017*
Published: *18 December 2017*

Citation:
Moioli M, Levionnois O, Stein VM, Schüpbach G, Schmidhalter M and Schweizer-Gorgas D (2017) Hyperintensity of Cerebrospinal Fluid on T2-Weighted Fluid-Attenuated Inversion Recovery Magnetic Resonance Imaging Caused by High Inspired Oxygen Fraction. Front. Vet. Sci. 4:219. doi: 10.3389/fvets.2017.00219

In veterinary medicine, patients undergo magnetic resonance imaging (MRI) under general anesthesia to enable acquisition of artifact-free images. The fraction of inspired oxygen (FiO_2) ranges between 30 and 95%. In humans, a high FiO_2 is associated with incomplete signal suppression of peripheral cerebrospinal fluid (CSF) spaces on T2-weighted fluid-attenuated inversion recovery (T2w-FLAIR) sequences. The influence of FiO_2 on T2w-FLAIR images remains unreported in small animals. The aim of this prospective study was to investigate whether a high FiO_2 is associated with hyperintensity in peripheral CSF spaces on T2w-FLAIR images in dogs and cats. Client-owned patients undergoing brain MRI were prospectively enrolled. Animals with brain parenchymal abnormalities and/or meningeal contrast enhancement on MRI images and/or abnormal CSF analysis were excluded. Consequently, twelve patients were enrolled. Anesthesia was maintained by isoflurane 0.5–1 minimal alveolar concentration in 30% oxygen. After acquisition of transverse and dorsal T2w-FLAIR images, the FiO_2 was increased to 95%. The T2w-FLAIR sequences were then repeated after 40 min. Arterial blood gas analysis was performed in six patients at the same time as T2w-FLAIR sequence acquisition. Plot profiles of the signal intensity (SI) from CSF spaces of three cerebral sulci and adjacent gray and white matter were generated. SI ratios of CSF space and white matter were compared between the T2w-FLAIR images with 30 and 95% FiO_2. An observer blinded to the FiO_2, subjectively evaluated the SI of peripheral CSF spaces on T2w-FLAIR images as high or low. There was significant difference in the partial pressure of oxygen between the two arterial samples ($P < 0.001$). The SI ratios obtained from the T2w-FLAIR images with 95% FiO_2 were significantly higher compared with those obtained from the T2w-FLAIR images with 30% FiO_2 ($P < 0.05$). The peripheral CSF spaces were subjectively considered hyperintense in 11 of 12 cases on T2w-FLAIR images with 95% FiO_2 ($P < 0.005$). A clear difference in SI, dependent on the FiO_2 was

seen in the peripheral CSF spaces on T2w-FLAIR images. In conclusion, the influence of FiO_2 must be considered when differentiating pathological and normal CSF spaces on T2w-FLAIR images in dogs and cats.

Keywords: cerebrospinal fluid, oxygen, T2-weighted fluid-attenuated inversion recovery, magnetic resonance imaging, brain, dog, cat

INTRODUCTION

T2-weighted fluid-attenuated inversion recovery (T2w-FLAIR) sequence consists of an inversion recovery pulse to suppress the signal from cerebrospinal fluid (CSF) and a long echo time to produce a heavily T2-weighted sequence. The T2w-FLAIR sequence is an essential part of the magnetic resonance imaging (MRI) protocol of the brain for both human and veterinary medicine (1–10). Compared with conventional T2-weighted and proton density-weighted imaging, T2w-FLAIR sequence provides better detection and evaluation of lesions within or adjacent to the CSF and higher lesion conspicuity within the brain parenchyma (3, 6). The term "hyperintense cerebrospinal fluid" is used to describe failed suppression of CSF signal on T2w-FLAIR images of the brain. Incomplete suppression of the CSF signal on T2w-FLAIR images is seen with subtle variations in the composition of CSF due to pathologic conditions such as subarachnoid hemorrhage, infarction, meningitis, vascular diseases, and neoplastic conditions (6, 9, 11, 12). However, hyperintense CSF on T2w-FLAIR images can be detected without a definite CSF abnormality. Several MRI artifacts lead to incomplete suppression of CSF signal on T2w-FLAIR images such as chemical shift, truncation, cross-talk, or overlapping of imaging planes (13). Patient motion, CSF flow, inhomogeneity in the amplitude of the inversion pulse, suboptimal inversion time, or magnetic field inhomogeneity can also lead to hyperintense signal of CSF on T2w-FLAIR (13). Magnetic field inhomogeneity can be caused by paramagnetic substances (14). Oxygen is a paramagnetic substance with two unpaired electrons, it reduces T1-relaxation time and causes high signal intensity (SI) of CSF on T2w-FLAIR images in patients receiving oxygen supplementation (2, 6, 9, 11, 13–18).

The major exchange of oxygen between arterial blood and the CSF takes place at the choroid plexus of the ventricles. Arterial partial pressure of oxygen (PaO_2) is a measurement of the pressure of dissolved oxygen in the arterial blood. It is predominantly influenced by how much oxygen diffuses from the airspace of the lungs into the blood. A higher arterial partial pressure of oxygen leads to increased diffusion of the oxygen into the CSF according to the pressure gradient. Under physiological condition, the arterial partial pressure of oxygen is proportional to the inspired oxygen fraction (FiO_2). When breathing room air, the FiO_2 is approximately 21% and increases up to 100% when oxygen is supplemented. In humans, oxygen supplementation with a FiO_2 above 60% influences CSF signal on T2w-FLAIR images (11, 13, 16).

In veterinary medicine, patients undergo MRI under general anesthesia and oxygen supplementation is generally provided at various FiO_2, often up to 100% (19). However, the influence of oxygen supplementation on CSF SI has been neglected. Therefore, the aim of this prospective study was to investigate the influence of oxygen supplementation on SI of CSF on T2w-FLAIR sequences in dogs and cats.

MATERIALS AND METHODS

Client-owned dogs and cats undergoing MRI of the brain presented to the Small Animal Clinic of the Vetsuisse-Faculty, University of Bern, were prospectively enrolled between June 2016 and May 2017. The study was performed in agreement with the local ethical regulations (Veterinary Office, Canton of Bern, Switzerland—BE53/16 and No. 27510) with signed owner consent.

All dogs and cats underwent clinical and neurological examination, followed by preanesthetic bloodwork, which included hematology and biochemistry. Patients were only included if they were deemed to be cardiovascularly stable and did not require preoxygenation prior to induction of general anesthesia.

Each patient was premedicated with either a combination of acepromazine (0.005–0.02 mg/kg) and methadone (0.1–0.4 mg/kg) or methadone alone (0.1–0.4 mg/kg), administered intravenously or intramuscularly. In two patients, dexmedetomidine (0.001–0.01 mg/kg) was additionally administered to maintain cooperative sedation. Induction of general anesthesia was performed with propofol (2–4 mg/kg) administered intravenously to allow for endotracheal intubation. General anesthesia was maintained with isoflurane (0.5–1.5%) in 30% oxygen to target a PaO_2 of approximately 150 mmHg (under usual clinical conditions). The FiO_2 was continuously monitored by a calibrated gas analyzer (Datex Ohmeda S5 Anesthesia Monitor, GE Healthcare) from a side-stream sampling line at the end of the endotracheal tube. Adjustments were made manually with two flowmeters providing air and oxygen, respectively. After the first two sequences, the FiO_2 was increased to at least 95% to target a PaO_2 of approximately 600 mmHg, and maintained until the end of the MRI examination. During MRI, the patients were mechanically ventilated and the ventilation parameters adjusted in order to maintain normocapnia (Et CO_2 35–45 mmHg). Continuous monitoring of peripheral oxygen saturation (SpO_2) by tongue pulse oxymetry, respiratory spirometry, and breathing gas analysis including inspired and expired O_2, CO_2, and anesthetic inhalant were provided. Core temperature was measured *via* an esophageal probe. Plasma A-Lyte® (Baxter AG) was infused at a rate of 5 mL/kg/h. Hypotension, defined as a mean blood pressure lower than 70 mmHg, was initially treated with a crystalloid bolus (10 mL/kg infused over 10 min). Non-responsive hypotension was then treated with a colloid bolus (Voluven 2 mL/kg delivered IV over 10 min) and finally with dopamine infusion starting

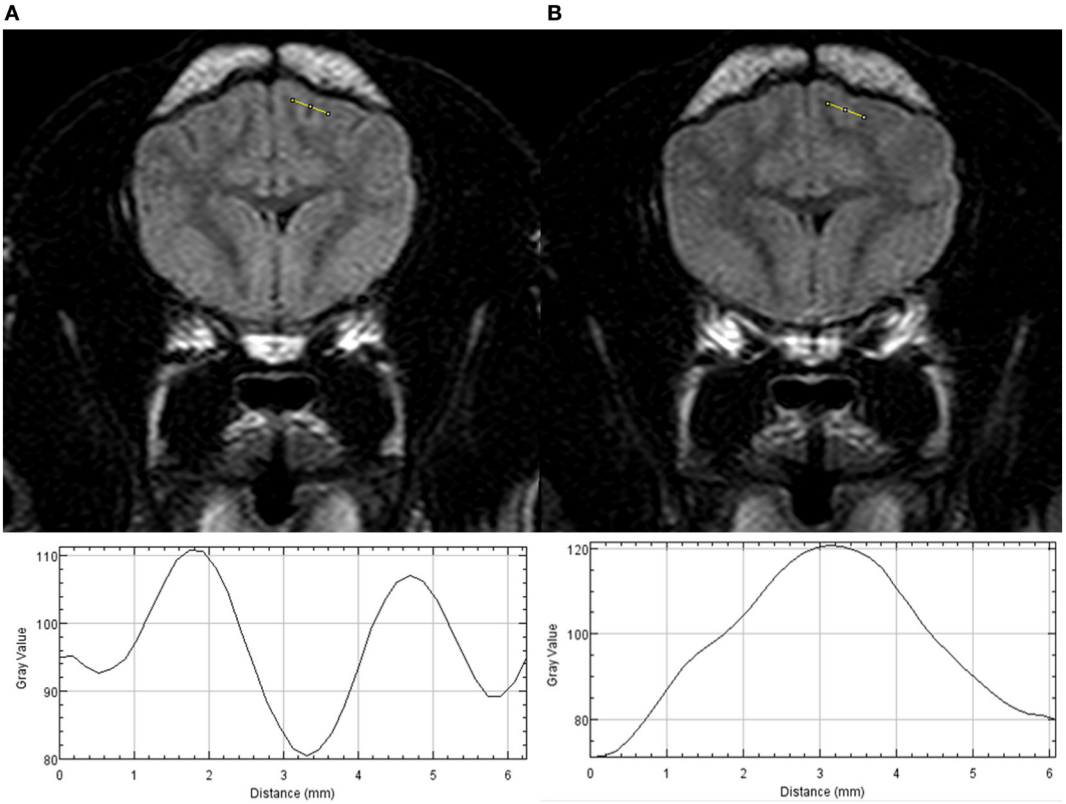

FIGURE 1 | Transverse T2w-FLAIR images at the level of the forebrain in a 6-month-old male neutered Pug acquired with 30% FiO_2 **(A)** and with 95% FiO_2 **(B)**, are presented on the top. Plot profiles of the signal intensity (SI) of the cerebrospinal fluid (CSF) space within the marginal left sulcus and of the adjacent gray and white matter have been generated from both images and are presented in the lower part of the figure. Note the different SI values of the CSF space on the y axis the CSF space has the lowest SI value on the plot profile obtained from the T2w-FLAIR acquired with 30% FiO_2 and the highest SI value on the plot profile obtained from the T2w-FLAIR acquired with 95% FiO_2.

with an infusion rate of 5 mcg/kg/min. The metatarsal artery was catheterized in a group of patients (weight >6 kg) and two arterial blood samples collected at the time of T2w-FLAIR sequence acquisition.

The animals were examined in a high-field MRI scanner [Philips Panorama HFO 1.0 T (Philips Medical Systems Nederland B.V., Best, the Netherlands)]. First, T2w-FLAIR sequences in transverse and dorsal planes were acquired (echo time 140 ms, repetition time 11,000 ms, inversion time 2,600 ms, slice thickness 3–3.5 mm, interslice gap 0.5 mm). After increasing FiO_2, T2-weighted FSE sequence in sagittal and transverse planes, T1-weighted FSE in dorsal and transverse planes, T2* in transverse plane, and DWI in transverse plane were acquired.

T2-weighted fluid-attenuated inversion recovery sequences were repeated 40 min after the FiO_2 increase. Afterward, Gadodiamide (0.5 mmol/mL, Omniscan, GE Healthcare, Germany) was administered at a dose of 0.15 mmol/kg intravenously and T1-weighted spin-echo sequence with fat suppression in the transverse plane and T1-weighted spin-echo in the dorsal plane were acquired.

After completion of the MRI examination, a CSF sample was obtained from the cerebellomedullary cistern.

Patients were excluded if MRI showed brain parenchymal abnormalities and/or abnormal meningeal contrast enhancement and/or if the CSF was abnormal on routine analysis (a normal CSF analysis consisted of CSF cells count below 5 cells/μL and/or CSF protein below 25 mg/dL).

All the measurements were performed by a second year diagnostic imaging resident (Melania Moioli).

Plot profiles of the SI from CSF spaces of three cerebral sulci (two on transverse T2w-FLAIR images and one on dorsal T2w-FLAIR images) and adjacent gray and white matter from T2w-FLAIR images acquired with a FiO_2 of 30% and 95% were generated using ImageJ[1] (**Figure 1**). If possible, profiles of the marginal sulcus, ectomarginal sulcus, and caudal suprasylvian sulcus were generated. If these sulci were not visible, the endomarginal sulcus, precruciatus sulcus, presylvian sulcus, middle ectosylvian sulcus, cruciatus sulcus, or rostral sulcus were used. On each plot profile, the SI values for the CSF space and adjacent gray and white matter were recorded.

Standardized regions of interest encompassing the same area were set over the right and left lateral ventricles and the right and

[1]https://imagej.net.

left thalamus ensuring they were in the same location on both the right and the left side and on both T2w-FLAIR images acquired with a FiO_2 of 30 and 95%.

Signal intensity ratios were calculated from T2w-FLAIR images acquired with a FiO_2 of 30 and 95%. The CSF space to white matter SI ratio and the gray matter to white matter SI ratio of three sulci and adjacent gyri were calculated. The lateral ventricle to thalamus SI ratio was calculated on the right and left side. The mean and SD of the ratios were calculated.

The ratios and the mean of the ratios from corresponding T2w-FLAIR images acquired with 30 and 95% FiO_2 were compared: the CSF space to white matter ratio of every single sulcus and adjacent white matter, the white matter to gray matter ratio of every single gyrus adjacent to the sulcus, the mean of the CSF space to white matter ratios, the mean of the white matter to gray matter ratios, and the mean of the ventricle to thalamus ratios.

Subjective assessment of the corresponding T2w-FLAIR sequences was performed using a DICOM viewer (IMPAX EE R20 XVI SU1; Agfa HealthCare Gmbh, Germany). A board certified radiologist (Marta Schmidhalter) blinded to the FiO_2 during acquisition of the T2w-FLAIR sequences evaluated whether the SI within peripheral CSF spaces showed complete or incomplete suppression. First, the observer was presented with single images in a random order at the level of forebrain, brainstem, and cervical spine from transverse T2w-FLAIR sequences obtained either with 30% FiO_2 or with 95% FiO_2, resulting in 72 evaluations. Second, the observer was presented with both transverse and dorsal images of the T2w-FLAIR sequences obtained with 30 or 95% FiO_2, and she evaluated all peripheral CSF spaces, resulting in 24 evaluations. Third, the observer was presented with the pair of T2w-FLAIR sequences acquired with 30 and 95% FiO_2 in both planes and compared the SI of the CSF spaces (12 evaluations).

The statistical analysis was performed by a second year diagnostic imaging resident (Melania Moioli) under supervision of a biostatistician (Gertraud Schüpbach). Quantitative data were assessed for normality using the Shapiro Wilk *W* test. All data were normally distributed, reported as mean ± SD and analyzed by a paired *T*-test. Subjective evaluation was analyzed using the McNemar test. All data were analyzed using a statistical software package [NCSS 10 Statistical Software (2015) NCSS, LLC., Kaysville, UT, USA[2]]. The level of significance was set to $P \leq 0.05$.

RESULTS

Twenty-three patients were enrolled in the study. Eleven patients were excluded because of brain parenchymal abnormalities on MRI or the need for preoxygenation during anesthesia induction. Twelve patients (10 dogs and 2 cats) were therefore included in the study. One each of the following dog breeds were represented: Cavalier King Charles Spaniel, Chihuahua, Maltese, Great Dane, English Springer Spaniel, English Cocker Spaniel, Dalmatian, Flat Coated Retriever, Labrador Retriever, and one mixed breed dog. The gender of the dogs was equally distributed with five female (one intact, four spayed) and five male dogs (three intact, two neutered). The mean age of the dogs was 7.8 years (SD: 2.7, range: 2.5–12 years) and the mean bodyweight was 30.8 kg (SD 13.9, range: 2.4–53 kg). Cats included a male castrated Domestic Shorthair (11 years of age, bodyweight 5.45 kg) and one female Maine Coon (5 years of age, 5.5 kg). Eight patients presented due to seizures, two for behavioral changes, one for dropped jaw, and one for acute progressive tetraparesis.

In six dogs, an arterial catheter was placed in the metatarsal artery and arterial blood samples collected. The mean PaO_2 was 140.33 mmHg (SD 35.51 mmHg, range 92.9–188.1 mmHg) with 30% FiO_2 and 492.35 mmHg (SD 54.52 mmHg, range 431.2–566.7 mmHg) with 95% FiO_2. The paired *T*-test showed a significant difference between the two means ($P < 0.001$).

Signal intensity ratios were calculated from T2w-FLAIR images acquired with 30 and 95% FiO_2 and were normally distributed. The objective measurements are presented in **Tables 1**–**3**. There was a significant difference in the CSF to adjacent white matter SI ratio of the three sulci considered separately ($P \leq 0.05$, **Table 1**) as well as in the mean of the CSF spaces to adjacent white matter ratios acquired with 30 and 95% FiO_2 ($P \leq 0.001$, **Table 1**). There was no significant difference in the gray to white matter SI ratio of the gray and white matter adjacent to the three sulci (**Table 2**) as well as no significant difference in the mean of the gray to white matter ratios acquired with 30 and 95% FiO_2 (**Table 2**). Additionally, no significant difference was found in the mean of the right and left ventricle to thalamus ratio with 30% FiO_2 and 95% FiO_2 (**Table 3**).

In the first subjective blinded evaluation on single images at the level of the forebrain as well as at the level of the brainstem, a hyperintensity of the peripheral CSF spaces was seen in 3/12

TABLE 1 | Values of the signal intensity (SI) ratios of CSF to adjacent white matter of three sulci and adjacent gyri and the mean ± SD are presented.

	1 CSF/WM		2 CSF/WM		3 CSF/WM		Mean (±SD) (1 + 2 + 3) CSF/WM	
Patient	**30% FiO_2**	**95% FiO_2**	**30% FiO_2**	**95% FiO_2**	**30% FiO_2**	**95% FiO_2**	**30% FiO_2**	**95% FiO_2**
1	1.66	1.17	1.15	1.59	1.14	1.45	1.31 (±0.3)	1.40 (±0.2)
2	1.42	1.52	0.94	1.03	1.19	1.33	1.18 (±0.2)	1.29 (±0.2)
3	0.89	1.24	1.18	1.43	1.21	1.47	1.10 (±0.2)	1.38 (±0.1)
4	1.22	1.28	1.24	1.49	1.14	1.26	1.20 (±0.1)	1.34 (±0.1)
5	0.73	1.04	0.70	1.20	0.79	1.21	0.74 (±0.1)	1.15 (±0.1)
6	1.07	1.58	1.33	1.88	1.59	1.84	1.33 (±0.3)	1.77 (±0.2)
7	1.48	1.34	1.34	1.34	1.67	1.95	1.50 (±0.2)	1.54 (±0.4)
8	1.20	1.67	1.31	1.67	1.56	1.74	1.36 (±0.2)	1.69 (±0.0)
9	1.40	1.61	1.51	1.86	1.29	1.91	1.40 (±0.1)	1.79 (±0.2)
10	1.39	1.66	1.92	1.88	1.90	1.98	1.73 (±0.3)	1.84 (±0.2)
11	1.70	1.87	1.45	1.83	1.48	1.94	1.54 (±0.2)	1.88 (±0.1)
12	1.19	1.85	1.42	2.14	1.58	2.94	1.40 (±0.2)	2.31 (±0.6)
P-value	0.03*		0.0004*		0.003*		0.001*	

*The SI ratios were calculated from T2w-FLAIR images acquired with 30 and 95% FiO_2. Significant P-values are marked with a *.*

1, first sulcus and adjacent gyrus; 2, second sulcus and adjacent gyrus; 3, third sulcus and adjacent gyrus; CSF, cerebrospinal fluid; WM, white matter; FiO_2, fraction of inspired oxygen.

[2]https://ncss.com/software/ncss.

TABLE 2 | Values of the signal intensity (SI) ratios of gray to white matter adjacent to three sulci and the mean ± SD are presented.

	1 GM/WM		2 GM/WM		3 GM/WM		Mean (±SD) (1 + 2 + 3) GM/WM	
Patient	**30% FiO_2**	**95% FiO_2**	**30% FiO_2**	**95% FiO_2**	**30% FiO_2**	**95% FiO_2**	**30% FiO_2**	**95% FiO_2**
1	1.39	1.16	1.26	1.59	1.18	1.24	1.28 (±0.1)	1.33 (±0.3)
2	1.57	1.46	1.30	1.04	1.37	1.30	1.42 (±0.1)	1.27 (±0.2)
3	1.20	1.25	1.29	1.25	1.58	1.51	1.36 (±0.2)	1.34 (±0.2)
4	1.36	1.10	1.45	1.25	1.22	1.22	1.34 (±0.1)	1.19 (±0.1)
5	1.23	1.03	1.26	1.31	1.18	1.05	1.22 (±0.0)	1.13 (±0.2)
6	1.18	1.19	1.43	1.85	1.75	1.76	1.46 (±0.3)	1.60 (±0.4)
7	1.23	1.12	1.40	1.19	1.45	1.28	1.36 (±0.1)	1.19 (±0.1)
8	1.18	1.32	1.23	1.37	1.44	1.29	1.28 (±0.1)	1.33 (±0.0)
9	1.35	1.37	1.37	1.41	1.20	1.54	1.31 (±0.1)	1.44 (±0.1)
10	1.41	1.29	1.65	1.58	1.92	1.57	1.66 (±0.3)	1.48 (±0.2)
11	1.51	1.60	1.12	1.48	1.47	1.67	1.37 (±0.2)	1.58 (±0.1)
12	1.19	1.39	1.41	1.72	1.34	1.81	1.31 (±0.1)	1.64 (±0.2)
P-value	0.32		0.31		0.87		0.79	

*The SI ratios were calculated from T2w-FLAIR images acquired with 30 and 95% FiO_2. Significant P-values are marked with a *.*

1, gyrus adjacent to the first sulcus; 2, gyrus adjacent to the second sulcus; 3, gyrus adjacent to the third sulcus; GM, gray matter; WM, white matter; FiO_2, fraction of inspired oxygen.

TABLE 3 | Values of the mean ± SD of the lateral ventricle to thalamus signal intensity (SI) ratios of the left and right side are presented.

	Mean (±SD) (R + L) LV/THA	
Patient	**30% FiO_2**	**95% FiO_2**
1	0.29 (±0.2)	0.44 (±0.1)
2	0.30 (±0.0)	0.20 (±0.0)
3	0.10 (±0.0)	0.10 (±0.0)
4	0.71 (±0.0)	0.65 (±0.1)
5	0.23 (±0.0)	0.12 (±0.0)
6	0.22 (±0.1)	0.45 (±0.2)
7	0.69 (±0.3)	0.78 (±0.1)
8	0.71 (±0.1)	0.70 (±0.1)
9	0.19 (±0.0)	0.21 (±0.1)
10	0.45 (±0.2)	0.54 (±0.4)
11	0.30 (±0.0)	0.22 (±0.0)
12	0.27 (±0.1)	0.29 (±0.0)
P-value	0.49	

*The SI ratios were calculated from T2w-FLAIR images acquired with 30 and 95% FiO_2. Significant P-values are marked with a *.*

R, right; L, left; LV, lateral ventricle; THA, thalamus; FiO_2, fraction of inspired oxygen.

T2w-FLAIR images acquired with 30% FiO_2 and in 10/12 images acquired with 95% FiO_2 ($P < 0.05$). At the level of the cervical spine, the peripheral CSF space was considered hyperintense in 5/12 T2w-FLAIR images acquired with 30% FiO_2 and in 8/12 T2w-FLAIR images acquired with 95% FiO_2. These results were not statistically significant.

In the second subjective evaluation, all transverse and dorsal images of T2w-FLAIR sequences acquired with 30 or 95% FiO_2 were taken into account. Peripheral CSF spaces were considered hyperintense in 4/12 cases acquired with 30% FiO_2 and 11/12 cases acquired with 95% FiO_2. The McNemar test showed a significant difference between these results ($P < 0.05$).

In the third evaluation, with direct comparison of the sequences acquired with 30 and 95% FiO_2, the peripheral CSF spaces were considered hyperintense in 1/12 cases on images acquired with 30% FiO_2 and in 11/12 cases on images acquired with 95% FiO_2. The McNemar test showed significant difference between these results ($P < 0.005$). Transverse T2w-FLAIR images at the level of the forebrain, brainstem, and cervical spine acquired with 30% FiO_2 and with 95% FiO_2 are shown, respectively, in **Figures 2–4**.

DISCUSSION

"Hyperintensity of CSF spaces" is a term used to describe incomplete suppression of CSF signal on T2w-FLAIR imaging (11–13). It may indicate an altered CSF composition or meningeal disease as seen in meningoencephalitis, subarachnoid hemorrhage or neoplastic conditions (5, 6, 9, 11, 12, 20). In this study, hyperintensity of the peripheral CSF spaces was evident in patients with normal CSF analysis and no brain abnormalities on MRI, but it was associated with high FiO_2 during the MRI examination. This agrees with observations in humans where CSF hyperintensity is associated with oxygen supplementation with a FiO_2 higher than 60% during the T2w-FLAIR sequence acquisition (11, 13). In veterinary medicine, during general anesthesia, high FiO_2 (up to 100%) is normally applied. This is because of its simplicity (only one gas supply) and because it is considered historically to be the safest method. However, lower FiO_2 with oxygen-enriched air (FiO_2 <50%) is sometimes preferred as it is sufficient to maintain arterial oxygenation and may reduce risk of oxygen toxicity. Indeed, lung aeration and gas exchange are improved with a FiO_2 of 40% compared to FiO_2 of 100% by reducing absorption atelectasis (19). In humans, it has been suggested, that a FiO_2 less than 50% does not induce signal changes on T2w-FLAIR images due to insufficient free oxygen (13).

Hyperintensity of CSF spaces might easily be misinterpreted as pathologic conditions of the CSF space itself or the adjacent meninges. Meningeal diseases are hard to diagnose as T2w-FLAIR images, T1-weighted post-gadolinium, and subtraction images have a limited accuracy detecting lesions (20). Fat suppressed contrast-enhanced T1-weighted images with or without fluid-attenuated inversion recovery technique increase the conspicuity of contrast enhancing meningeal lesions (21, 22) but non-enhancing lesions are still difficult to detect.

As reported in humans, the present study showed incomplete suppression of CSF on T2w-FLAIR images in the peripheral CSF spaces such as the basilar cistern and the cerebral sulci, but not in the lateral ventricles (11, 13). This phenomenon may be explained by the diffusion of oxygen from the blood to the CSF along the pia-arachnoid surface of the brain, although the major exchange of oxygen between arterial blood and the CSF takes place at the choroid plexus of the ventricles (2, 11). A significant increase in oxygen partial pressure of CSF after 100% oxygen inhalation was detected using MRI as a non-invasive method to measure pO_2 of human and fetal CSF (18). The highest oxygen concentrations were noted along the cortical surfaces, whereas lower concentrations were measured within the ventricular system (18). Furthermore,

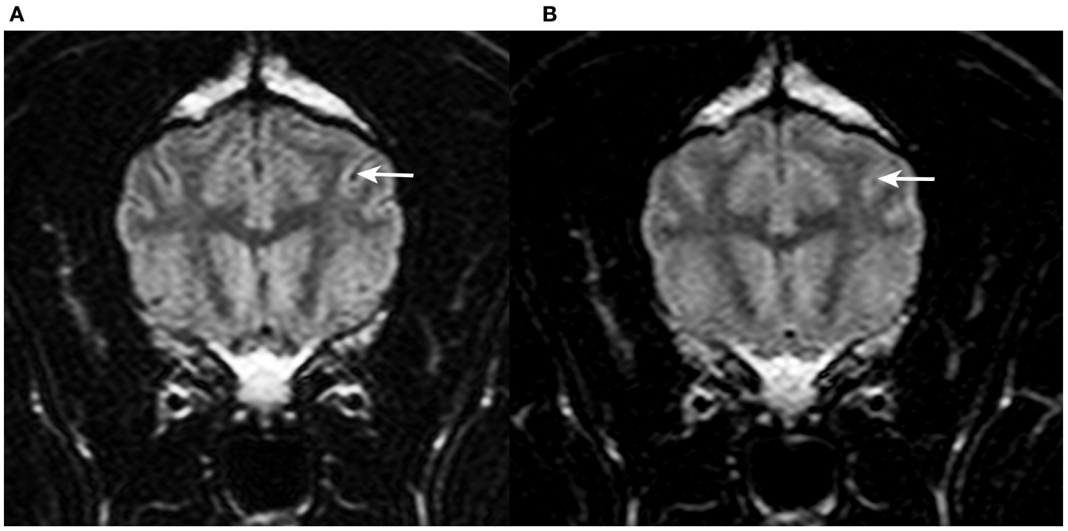

FIGURE 2 | Transverse T2w-FLAIR images at the level of the forebrain in a 9-year-old female spayed Flat Coated Retriever acquired with 30% FiO_2 **(A)** and with 95% FiO_2 **(B)**, respectively. Note low signal intensity (SI) of peripheral cerebrospinal fluid (CSF) within cerebral sulci in **(A)** (arrow) and increase in SI of CSF within the same sulcus in **(B)** (arrow).

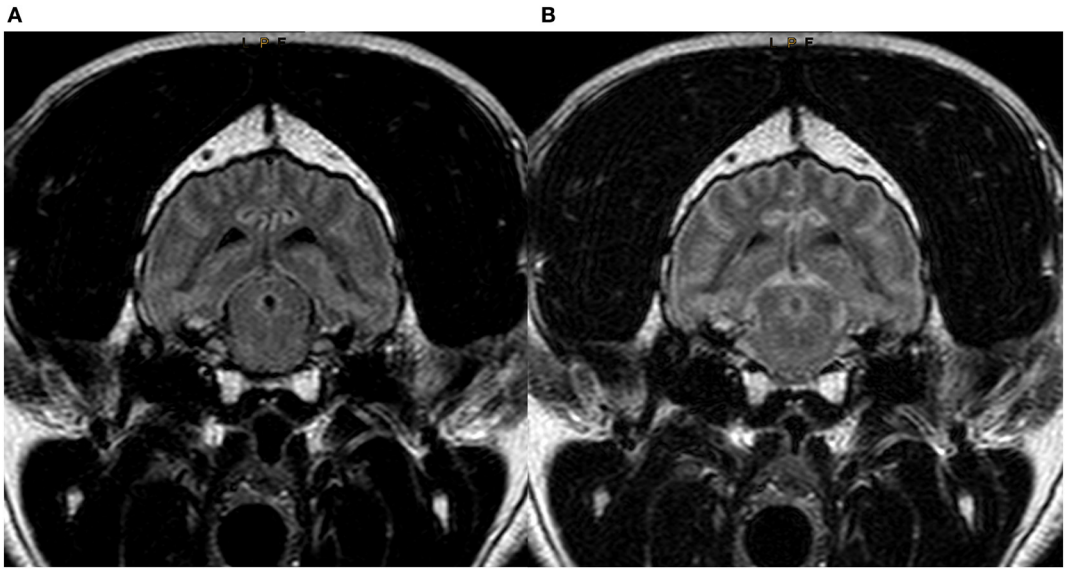

FIGURE 3 | Transverse T2w-FLAIR images at the level of the brainstem in a 7-year-old male neutered Labrador Retriever acquired with 30% FiO_2 **(A)** and with 95% FiO_2 **(B)**, respectively. Note low signal intensity (SI) of peripheral cerebrospinal fluid (CSF) around the brainstem in **(A)** and increase in SI of CSF within the same region **(B)**.

an increase in FiO_2 leads to less dilution of dissolved oxygen in the peripheral CSF spaces due to their small volume compared to the lateral ventricles, leading to a stronger local paramagnetic effect (2).

The effect of paramagnetic substances is stronger with higher magnetic field strength (23, 24). We suspect that hyperintensity of CSF on T2w-FLAIR sequences is observed less often in low-field scanners. However, all studies investigating the influence of oxygen supplementation on CSF SI on T2w-FLAIR sequences, including the present one, were performed with high field scanners ranging from 1T to 3T (1, 2, 9–11, 15, 16, 25). Therefore, the impact on images acquired with low field scanners remains unknown.

The difference in SI of CSF spaces was not only evident when comparing ratios, but also noted on subjective evaluation. Differences between the T2w-FLAIR series with low and high FiO_2 became more obvious on simultaneous comparison. Blind evaluation also revealed a significant difference. The evaluation of

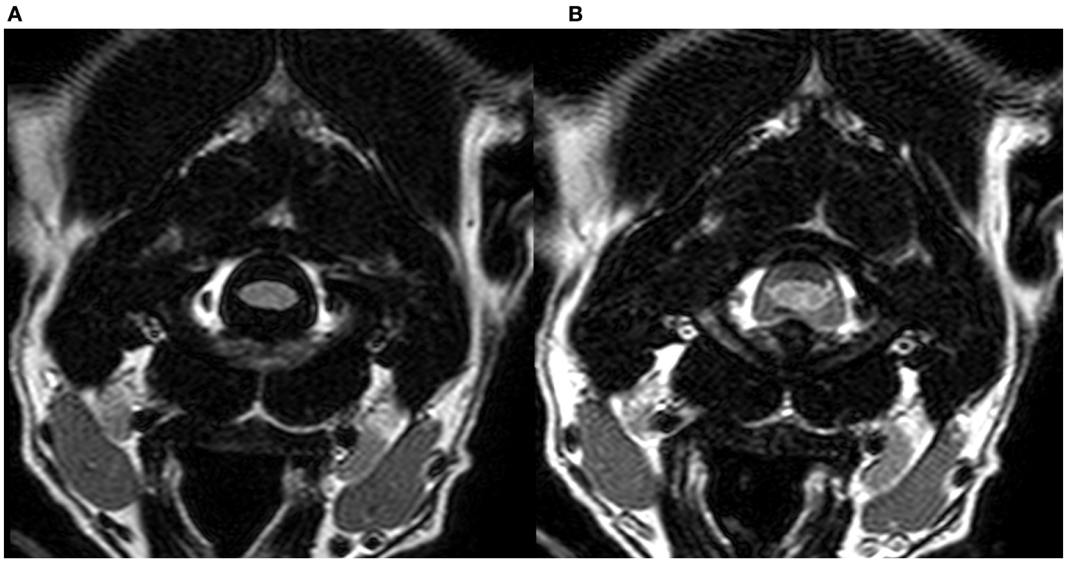

FIGURE 4 | Transverse T2w-FLAIR images at the level of the cervical spine in a 3-year-old male neutered Dalmatian acquired with 30% FiO_2 **(A)** and with 95% FiO_2 **(B)**, respectively. Note low signal intensity (SI) of peripheral cerebrospinal fluid (CSF) around the cervical spinal cord in **(A)** and increase in SI of CSF within the same region **(B)**.

CSF at different levels of the brain by subjective evaluation and SI ratios showed both a significant difference between the low and high FiO_2, while a smaller difference was found for the CSF surrounding the cervical spinal cord. CSF flow influences the SI of CSF and the high flow velocity at the level of the aqueduct and C1-C2 are possible causes for the inconsistent CSF signal. In humans, pulsation artifacts related to CSF flow are reported to occur in the basal, prepontine, and cerebellopontine angle cisterns and cause T2w-FLAIR hyperintensity in the subarachnoid space (6, 16). These artifacts are less common over the convexities of the cerebral hemispheres (6).

A limitation of this study was the heterogeneous group of animals, which included cats, small breed dogs, and even a Great Dane. They exhibited a large variety of skull shapes and brain morphology. In smaller animals, the sulci appeared smaller and distinction between the gyri and sulci as well as evaluation of CSF SI was more difficult. This meant that SI ratios could not be consistently performed at the same location. In addition to patient size, age plays a role in the appearance of sulci (26). The small sample size prohibited investigating the influence of size, body weight, skull morphology, and age on the appearance of CSF spaces (26, 27). Hyperintensity of the peripheral CSF spaces has also been reported to be associated with propofol anesthesia in one study (10). However, this is controversial as a different publication observed CSF hyperintensity with high FiO_2 both with and without propofol anesthesia (11). In our study, all patients received propofol, but hyperintensity of the peripheral CSF spaces was only associated with high FiO_2.

In conclusion, high FiO_2 during MRI examination has been shown to result in hyperintense peripheral CSF spaces on T2w-FLAIR images in dogs and cats. In veterinary medicine where patients undergo general anesthesia during MRI examinations, this finding is of major importance for the evaluation of external CSF spaces and correct identification of pathological conditions.

ETHICS STATEMENT

This prospective study was performed in agreement with the local ethical regulations (Veterinary Office, Canton of Bern, Switzerland—BE53/16 and No.27510). The animals included were patients presented to the Small Animal Clinic of the Vetsuisse-Faculty of Bern and undergoing MRI of the brain for reasons not related to the study. The patients were prospectively included if the owners provided signed informed consent. They were not designated "experimental animals."

AUTHOR CONTRIBUTIONS

All authors contributed substantially to the conception or design of the study; or the acquisition, analysis, or interpretation of data. All authors drafted the work or revised it critically for important intellectual content and gave final approval before publication. All authors investigated and resolved questions relating to the accuracy or integrity of all part of the work.

ACKNOWLEDGMENTS

We are grateful to Lisa Thomann-Harwood for language editing. Part of the results of this original research study was presented as an oral presentation at the EVDI 2017 Annual Meeting in Verona.

FUNDING

This study was self-funded from clinical income at the Clinical Radiology Division, Department of Clinical Veterinary Medicine, Vetsuisse-Faculty, University of Bern.

REFERENCES

1. Taoka T, Yuh WT, White ML, Quets JP, Maley JE, Ueda T. Sulcal hyperintensity on fluid-attenuated inversion recovery mr images in patients without apparent cerebrospinal fluid abnormality. *AJR Am J Roentgenol* (2001) 176(2):519–24. doi:10.2214/ajr.176.2.1760519
2. Anzai Y, Ishikawa M, Shaw DWW, Artru A, Yarnykh V, Maravilla KR. Paramagnetic effect of supplemental oxygen on CSF hyperintensity on fluid-attenuated inversion recovery MR images. *AJNR Am J Neuroradiol* (2004) 25(2):274–9.
3. Benigni L, Lamb CR. Comparison of fluid-attenuated inversion recovery and T2-weighted magnetic resonance images in dogs and cats with suspected brain disease. *Vet Radiol Ultrasound* (2005) 46(4):287–92. doi:10.1111/j.1740-8261.2005.00052.x
4. Cherubini GB, Mantis P, Martinez TA, Lamb CR, Cappello R. Utility of magnetic resonance imaging for distinguishing neoplastic from non-neoplastic brain lesions in dogs and cats. *Vet Radiol Ultrasound* (2005) 46(5):384–7. doi:10.1111/j.1740-8261.2005.00069.x
5. Lamb CR, Croson PJ, Cappello R, Cherubini GB. Magnetic resonance imaging findings in 25 dogs with inflammatory cerebrospinal fluid. *Vet Radiol Ultrasound* (2005) 46(1):17–22. doi:10.1111/j.1740-8261.2005.00003.x
6. Stuckey SL, Goh TD, Heffernan T, Rowan D. Hyperintensity in the subarachnoid space on FLAIR MRI. *AJR Am J Roentgenol* (2007) 189(4):913–21. doi:10.2214/AJR.07.2424
7. Falzone C, Rossi F, Calistri M, Tranquillo M, Baroni M. Contrast-enhanced fluid-attenuated inversion recovery vs. contrast-enhanced spin echo T1-weighted brain imaging. *Vet Radiol Ultrasound* (2008) 49(4):333–8. doi:10.1111/j.1740-8261.2008.00375.x
8. Young BD, Mankin JM, Griffin JF, Fosgate GT, Fowler JL, Levine JM. Comparison of two fat-suppressed magnetic resonance imaging pulse sequences to standard t2-weighted images for brain parenchymal contrast and lesion detection in dogs with inflammatory intracranial disease. *Vet Radiol Ultrasound* (2015) 56(2):204–11. doi:10.1111/vru.12220
9. Ozcan UA, Isik U, Ozpinar A, Baykan N, Dincer A. Assessment of sedated pediatric brain with 3D-FLAIR sequence at 3T MRI. *Brain Dev* (2015) 37(5):495–500. doi:10.1016/j.braindev.2014.08.008
10. Filippi CG, Ulug AM, Lin D, Heier LA, Zimmerman RD. Hyperintense signal abnormality in subarachnoid spaces and basal cisterns on MR images of children anesthetized with propofol: new fluid-attenuated inversion recovery finding. *AJNR Am J Neuroradiol* (2001) 22(2):394–9.
11. Frigon C, Jardine DS, Weinberger E, Heckbert SR, Shaw DW. Fraction of inspired oxygen in relation to cerebrospinal fluid hyperintensity on FLAIR MR imaging of the brain in children and young adults undergoing anesthesia. *AJR Am J Roentgenol* (2002) 179(3):791–6. doi:10.2214/ajr.179.3.1790791
12. Tha KK, Terae S, Kudo K, Miyasaka K. Differential diagnosis of hyperintense cerebrospinal fluid on fluid-attenuated inversion recovery images of the brain. Part I: pathological conditions. *Br J Radiol* (2009) 82(977):426–34. doi:10.1259/bjr/70065269
13. Tha KK, Terae S, Kudo K, Miyasaka K. Differential diagnosis of hyperintense cerebrospinal fluid on fluid-attenuated inversion recovery images of the brain. Part II: non-pathological conditions. *Br J Radiol* (2009) 82(979):610–4. doi:10.1259/bjr/29238647
14. Westbrook C, Kaut Roth C, Talbot J. *MRI in Practice*. 4th ed. Oxford: Wiley-Blackwell (2011). 442 p.
15. Deliganis AV, Fisher DJ, Lam AM, Maravilla KR. Cerebrospinal fluid signal intensity increase on FLAIR MR images in patients under general anesthesia: the role of supplemental O_2. *Radiology* (2001) 218(1):152–6. doi:10.1148/radiology.218.1.r01ja43152
16. Braga FT, da Rocha AJ, Hernandez Filho G, Arikawa RK, Ribeiro IM, Fonseca RB. Relationship between the concentration of supplemental oxygen and signal intensity of CSF depicted by fluid-attenuated inversion recovery imaging. *AJNR Am J Neuroradiol* (2003) 24(9):1863–8.
17. Zaharchuk G, Martin AJ, Rosenthal G, Manley GT, Dillon WP. Measurement of cerebrospinal fluid oxygen partial pressure in humans using MRI. *Magn Reson Med* (2005) 54(1):113–21. doi:10.1002/mrm.20546
18. Zaharchuk G, Busse RF, Rosenthal G, Manley GT, Glenn OA, Dillon WP. Noninvasive oxygen partial pressure measurement of human body fluids in vivo using magnetic resonance imaging. *Acad Radiol* (2006) 13(8):1016–24. doi:10.1016/j.acra.2006.04.016
19. Staffieri F, Franchini D, Carella GL, Montanaro MG, Valentini V, Driessen B, et al. Computed tomographic analysis of the effects of two inspired oxygen concentrations on pulmonary aeration in anesthetized and mechanically ventilated dogs. *Am J Vet Res* (2007) 68(9):925–31. doi:10.2460/ajvr.68.9.925
20. Keenihan EK, Summers BA, David FH, Lamb CR. Canine meningeal disease: associations between magnetic resonance imaging signs and histologic findings. *Vet Radiol Ultrasound* (2013) 54(5):504–15. doi:10.1111/vru.12055
21. D'Anjou MA, Carmel EN, Tidwell AS. Value of fat suppression in gadolinium-enhanced magnetic resonance neuroimaging. *Vet Radiol Ultrasound* (2011) 52(1 Suppl 1):S85–90. doi:10.1111/j.1740-8261.2010.01789.x
22. D'Anjou MA, Carmel EN, Blond L, Beauchamp G, Parent J. Effect of acquisition time and chemical fat suppression on meningeal enhancement on MR imaging in dogs. *Vet Radiol Ultrasound* (2012) 53(1):11–20. doi:10.1111/j.1740-8261.2011.01864.x
23. Caravan P, Farrar CT, Frullano L, Uppal R. Influence of molecular parameters and increasing magnetic field strength on relaxivity of gadolinium- and manganese-based T1 contrast agents. *Contrast Media Mol Imaging* (2009) 4(2):89–100. doi:10.1002/cmmi.267
24. Rooney WD, Johnson G, Li X, Cohen ER, Kim SG, Ugurbil K, et al. Magnetic field and tissue dependencies of human brain longitudinal $1H_2O$ relaxation in vivo. *Magn Reson Med* (2007) 57(2):308–18. doi:10.1002/mrm.21122
25. Bakshi R, Caruthers SD, Janardhan V, Wasay M. Intraventricular CSF pulsation artifact on fast fluid-attenuated inversion-recovery MR images: analysis of 100 consecutive normal studies. *AJNR Am J Neuroradiol* (2000) 21(3):503–8.
26. Scarpante E, Cherubini GB, de Stefani A, Taeymans O. Magnetic resonance imaging features of leukoaraiosis in elderly dogs. *Vet Radiol Ultrasound* (2017) 58(4):389–98. doi:10.1111/vru.12489
27. Pilegaard AM, Berendt M, Holst P, Møller A, McEvoy FJ. Effect of skull type on the relative size of cerebral cortex and lateral ventricles in dogs. *Front Vet Sci* (2017) 4:30. doi:10.3389/fvets.2017.00030

Conflict of Interest Statement: The authors declare that the research was conducted in the absence of any commercial or financial relationships that could be construed as a potential conflict of interest.

frontiers in Veterinary Science

ORIGINAL RESEARCH
published: 25 September 2017
doi: 10.3389/fvets.2017.00157

Computed Tomography and Magnetic Resonance Imaging Are Equivalent in Mensuration and Similarly Inaccurate in Grade and Type Predictability of Canine Intracranial Gliomas

Krystina L. Stadler, Jeffrey D. Ruth, Theresa E. Pancotto, Stephen R. Werre and John H. Rossmeisl*

Department of Small Animal Clinical Sciences, VA-MD College of Veterinary Medicine, Blacksburg, VA, United States

OPEN ACCESS

Edited by:
Andrea Tipold, University of Veterinary Medicine Hannover, Germany

Reviewed by:
Christopher L. Mariani, North Carolina State University, United States
Takehiko Kakizaki, Kitasato University, Japan

***Correspondence:**
Krystina L. Stadler
krystina@vt.edu

Specialty section:
This article was submitted to Veterinary Neurology and Neurosurgery, a section of the journal Frontiers in Veterinary Science

Received: *14 July 2017*
Accepted: *08 September 2017*
Published: *25 September 2017*

Citation:
Stadler KL, Ruth JD, Pancotto TE, Werre SR and Rossmeisl JH (2017) Computed Tomography and Magnetic Resonance Imaging Are Equivalent in Mensuration and Similarly Inaccurate in Grade and Type Predictability of Canine Intracranial Gliomas. Front. Vet. Sci. 4:157. doi: 10.3389/fvets.2017.00157

While magnetic resonance imaging (MRI) is the gold-standard imaging modality for diagnosis of intracranial neoplasia, computed tomography (CT) remains commonly used for diagnosis and therapeutic planning in veterinary medicine. Despite the routine use of both imaging modalities, comparison of CT and MRI has not been described in the canine patient. A retrospective study was performed to evaluate CT and MRI studies of 15 dogs with histologically confirmed glioma. Multiple lesion measurements were obtained, including two-dimensional and volumetric dimensions in pre-contrast and post-contrast images. Similar measurement techniques were compared between CT and MRI. The glioma type (astrocytoma or oligodendroglioma) and grade (high or low) were predicted on CT and MRI independently. With the exception of the comparison between CT pre-contrast volume to T2-weighted MRI volume, no other statistical differences between CT and MRI measurements were identified. Overall accuracy for tumor grade (high or low) was 46.7 and 53.3% for CT and MRI, respectively. For predicted tumor type, accuracy of CT was 53.3% and MRI and MRI 60%. Based on the results of this study, both CT and MRI contrast measurement techniques are considered equivalent options for lesion mensuration. Given the low-to-moderate predictability of CT and MRI in glioma diagnosis, histopathology remains necessary for accurate diagnosis of canine brain tumors.

Keywords: brain tumor, computed tomography, magnetic resonance imaging, canine, glioma, neuroimaging, neurooncology

INTRODUCTION

Magnetic resonance imaging (MRI) is the gold-standard imaging modality for diagnosis of intracranial neoplasia. Prior to MRI, computed tomography (CT) was considered the gold-standard imaging modality for intra-axial lesions. Following the adoption of MRI as the diagnostic modality of choice in human and veterinary medicine for intracranial disease, the comparison of diagnostic findings

Abbreviations: CT, computed tomography; MRI, magnetic resonance imaging; 2D, two-dimensional; 3D, three-dimensional; PACS, picture archiving and communication system; T1W, T1-weighted; T2W, T2-weighted; VA-MD VTH, Virginia-Maryland Veterinary Teaching Hospital; WHO, World Health Organization.

and predictability between CT and MRI has been minimally explored in the literature. To the authors' knowledge, only one study compares CT and MRI in diagnosing intra-axial gliomas (1). This study compared CT to MRI in its accuracy to detect histological tumor margins in experimentally induced gliomas in a canine model. It found that MRI was superior to CT in tumor margin detection and MRI with gadolinium contrast superior to non-contrast MRI and CT. The remaining literature available in human medicine compares CT to MRI in diagnosis of intracranial metastases, midline tumors, and meningiomas (2–4). Conclusions within these studies vary, with one concluding neither CT nor MRI was superior and the others finding MRI to be superior.

In veterinary medicine, MRI is the imaging modality of choice for diagnosis of intracranial lesions. CT, however, is more widely available than MRI in and is often used for radiation therapy planning for treatment of solitary intra-axial neoplasia (5) or stereotactic biopsy (6, 7) and remains the diagnostic modality of choice when MRI is not available. In addition, CT is often preferred for imaging of the extra-calvarial lesions of the head, in which concurrent intra-axial lesions may be detected. Given the continued use of CT as a sole or adjunct imaging modality in patients with brain tumors, the specific aims of the study were to compare lesion mensuration and predictability of tumor type and grade between CT and MRI in canine patients with histologically confirmed gliomas.

MATERIALS AND METHODS

Retrospective review of the Virginia-Maryland Veterinary Teaching Hospital's (VA-MD VTH) Picture Archiving and Communications system (PACS) and medical records were performed for client-owned canine patients with a histopathologically confirmed solitary intra-axial glioma and an MRI and CT of the brain performed within 1 month of each other. Histopathological diagnosis was performed according to World Health Organization (WHO) criteria (8, 9) by anatomic pathologists with a focus on neuropathology. Patients were not included in if the imaging studies did not include contrast administration. If beam-hardening artifact was present on the CT images at the area of interest due to the presence of stereotactic or therapeutic device, the patient was not included in the study. As convention at our institution for post-contrast CT images, patients received iopromide (370 mgI/ml, Ultravist®) at a dose of 0.45 ml/kg (814 mgI/kg). For post-contrast MRI performed at VA-MD VTH, all patients received gadopentetate dimeglumine (0.5 mmol/ml, Magnevist®) at a dose of 0.2 ml/kg.

All images were anonymized for blinded image review using a 4-digit number generated by a random number generator (http://random.org). The CT and MRI study for the same patient had a different randomized number. CT images were reviewed first, and at least 2 weeks apart from MRI images. The thinnest slice CT pre- and post-contrast and T1-weighted (T1W) pre- and post-contrast and T2-weighted (T2W) images, all transverse, were available for review. All images were reviewed on an external workstation (OsiriX v8.5.1). The images were reviewed independently by three reviewers; two radiologists (Jeffrey D. Ruth and Krystina L. Stadler) and one neurologist (Theresa E. Pancotto). The reviewers were aware that all patients had histological confirmation of glioma but were blinded to type and grade.

Based on diagnostic imaging findings previously published for predicting grade and glial tumor type in veterinary medicine (10–12), reviewers predicted the grade (high or low) and glial tumor type (astrocytoma vs. oligodendroglioma) of each lesion on CT and MRI images independent of the imaging modality. Accuracy of predicting the lesion grade and type on CT and MRI compared to histopathological diagnosis was performed using the majority agreement based on the three reviewers (Krystina L. Stadler, Theresa E. Pancotto, and Jeffrey D. Ruth, ≥2 out of 3 agreed). In addition, agreement between CT and MRI tumor grade and type independent of histopathology diagnosis was assessed.

The mensurations performed on CT and MRI on the intra-axial lesions are detailed in **Table 1** and **Figures 1** and **2**. The two-dimensional (2D) contrast enhancement measurement was obtained using the post-contrast CT and MRI transverse images by the 2D Macdonald method (13–15), involving continuous length × height dimension of contrast enhancement at the level of the greatest tumor contrast enhancement and diameter. For volumetric measurements, a free drawn region of interest was drawn on each slice surrounding the lesion and compute volume tool on OsiriX was used. T2 and T1 post-contrast volumetric measurements were performed similar to previous described methods (14–20). Volumetric measurements of T2 images included all continuous T2 hyperintensity surrounding the lesion (peritumoral edema). T1 pre-contrast volumetric measurements did not include perilesion T1 hypointesity (peritumoral edema). A zero measurement was assigned if no measurement could be performed either because the lesion was not identified or the desired measurement could not be obtained. Viewer measurements were averaged between the observers and statistical analysis of this data performed.

For statistical analysis of acquired measurements, CT pre-contrast volume was compared to CT post-contrast volume,

TABLE 1 | Summary of measurements performed on available imaging sequences.

Computed tomography (CT) pre-contrast	CT post-contrast	T1-weighted (T1W) transverse pre-contrast	T1W post-contrast	T2-weighted (T2W)
	Two-dimensional (2D) contrast dimensions		2D contrast dimensions	
Total lesion volume (cm^3)	Total lesion volume (cm^3)	Total lesion volume (cm^3)	Total lesion volume (cm^3)	Total T2W hyperintense volume (cm^3)
	Volume of contrast enhancing (CE) region only (cm^3)		Volume of CE region only (cm^3)	
	Volume of non-CE region only (cm^3)		Volume of non-CE region only (cm^3)	

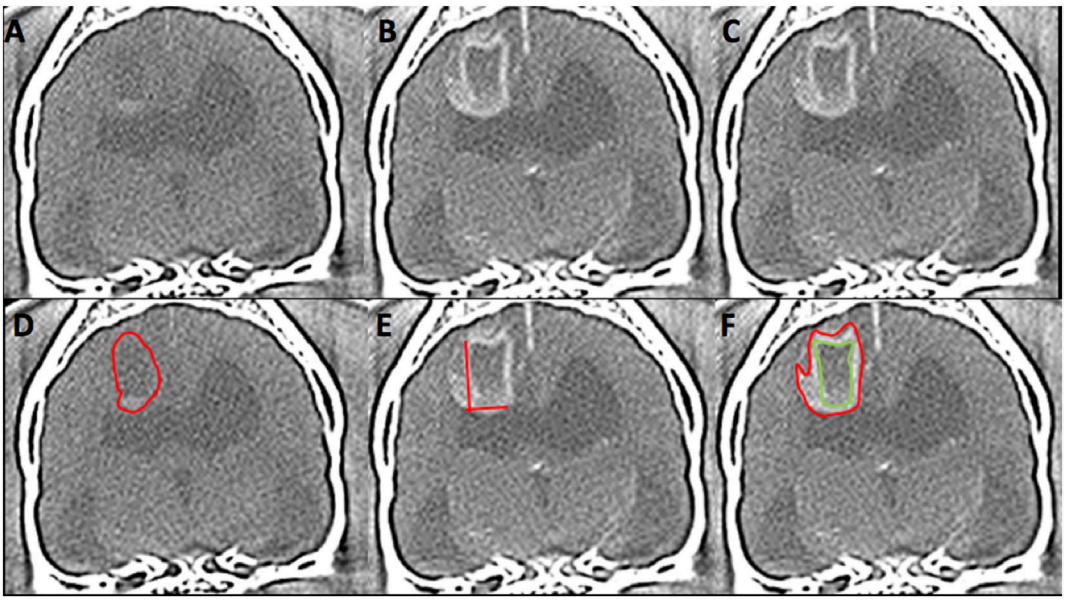

FIGURE 1 | Computed tomography (CT) images from 6 year-old female spayed French bulldog with histological high-grade astrocytoma in the dorsal cerebrum at the level of the interthalamic adhesion. This lesion was diagnosed on CT as high grade (3/3 reviewers) and an oligodendroglioma (2/3). Panels **(A,D)** represent pre-contrast images. The red outline on image **(D)** represents the hand-drawn region of interest (ROI) for volume calculation. Panels **(B,C,E,F)** are post-contrast images. The two lines on image **(E)** represent the two-dimensional McDonald method of lesion measurement. The red outline on image **(F)** represents the hand-drawn ROI for total lesion volume. The green outline represents non-contrast enhancing (CE) lesion volume and the space between the two outlines represents the ROI for CE lesion only. (Images displayed with a window width: 350, Window level: 40.)

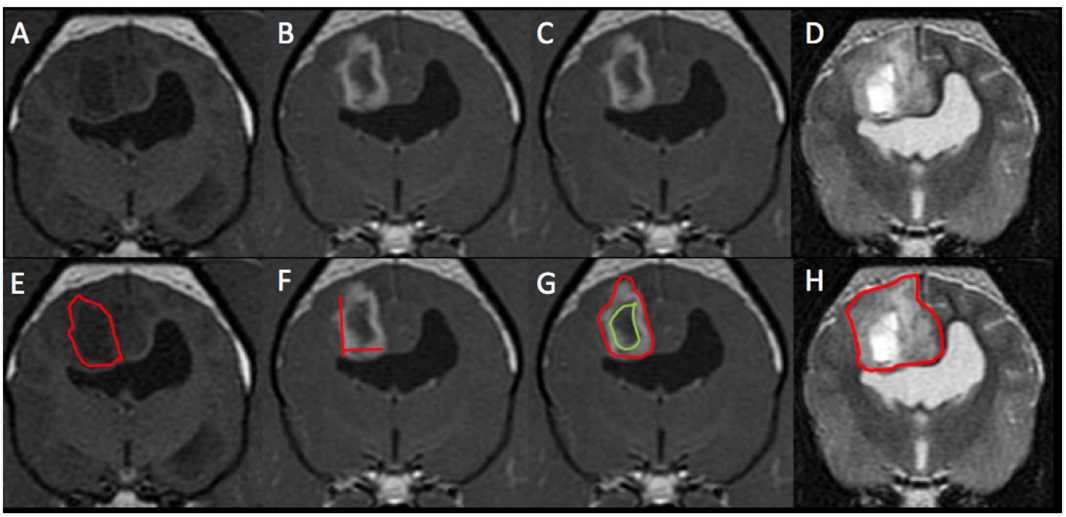

FIGURE 2 | Magnetic resonance imaging (MRI) images from the same patient from **Figure 1** with histological high-grade astrocytoma. This mass was diagnosed on MRI as high grade (3/3 reviewers) and an astrocytoma (2/3). Panels **(A,E)** represent pre-contrast T1-weighted (T1W) images. The red outline on image **(E)** represents the hand-drawn region of interest (ROI) for volume calculation. Panels **(B,C,F,G)** are T1W post-contrast images. The two lines on image **(F)** represent the two-dimensional McDonald method of lesion measurement. The red outline on image **(G)** represents the hand-drawn ROI for total lesion volume. The green outline represents non-contrast enhancing (CE) lesion volume and the space between the two outlines represents the ROI for CE lesion only. Panels **(D,H)** are T2-weighted pre-contrast images. The red outline on image **(H)** represents T2 hyperintense volume.

T1W pre-contrast volume and T2W pre-contrast volume independently. CT 2D contrast dimensions were compared to MRI 2D contrast dimensions. CT post-contrast measurements of contrast enhancing (CE) total volume, CE portion only volume, and non-CE volume were compared independently with their respective MRI T1W post-contrast measurements. Normal probability plots showed that CT contrast-enhanced total volume compared to T1W post-contrast total volume, CT pre-contrast

total volume compared to T2W post total volume, CT CE volume only compared to MRI CE volume only measurements were skewed. Accordingly, these were summarized as medians. CT pre-contrast volume compared to T1W pre-contrast volume and compared to T2W volume measurements followed a normal distribution and were summarized as least squares means (SE). Comparisons of interest between measurements were made using the Wilcoxon signed rank test (CT no contrast volume to CT with contrast volume, CT 2D to MRI 2D, CT contrast volume to T1W plus contrast volume, CT pre-contrast volume to T1W pre-contrast volume) and mixed model analysis of variance followed by Tukey's procedure for multiple comparisons (CT pre-contrast volume to T1W pre-contrast volume to T2W pre-contrast volume). Statistical significance was set at $p < 0.05$. All analyses were performed using SAS version 9.4 (Cary, NC, USA).

RESULTS

A total of 15 dogs fit the inclusion criteria. Breeds included mixed breed dog ($n = 4$), Boston terrier (3), Boxer (2), miniature Schnauzer, Golden retriever, Dachshund, English bulldog, French bulldog, and Labrador retriever (1 each). The average patient age was 8.3 years (range: 6–13 years). Ten were spayed females and five were castrated males. The average patient weight was 21.6 kg (range: 7.6–44.2 kg).

One of the 15 dogs did not have a pre-contrast CT; this dog was excluded from comparisons involving pre-contrast CT images. All CT examinations were performed at VA-MD veterinary teaching hospital using the in-house 16-slice CT scanner (Toshiba Aquillon 16, Japan). The location of the MRI scan varied with 5 patients having the MRI performed in-hospital (1.5 T Phillips Intera, USA), 10 performed at various referral institutions (1 with a 0.2-T MRI, 1 with a 1-T MRI, and 8 with a 1.5-T MRI). All CT images were evaluated at 1-mm slice thickness. MRI slice thickness varied with a range from 3.0 to 5.0 mm.

Histopathological diagnosis was achieved by stereotactic biopsy in 11 dogs and necropsy in 4 dogs. On histopathology, 10 gliomas were identified as high grade (WHO grade III or IV) and 5 were identified as low grade (WHO grade II). Eleven astrocytomas and four oligodendrogliomas were identified; of these eight astrocytomas and two oligodendrogliomas were high grade and three astrocytomas and two oligodendrogliomas were low grade. On imaging, all three observers agreed on the same grade in 9/15 (60%) of patients for CT and 8/15 (53.3%) patients for MRI. Comparing predicted tumor grade (either by 2/3 observer agreement or when all observers agreed), CT had an overall accuracy of 46.7% (7/15) and MRI had an overall accuracy of 53.3% (8/15). When comparing CT predicted grade to MRI predicted grade, agreement was seen in 9/15 cases (60%). In cases where CT and MRI diagnosis agreed, accuracy between histopathological grades was 44.4% (4/9). Sensitivity, specificity, positive predictive value (PPV), and negative predictive value (NPV) for high and low grade for both CT and MRI are detailed in **Tables 2** and **3**, respectively. Contrast enhancement volume only between CT and MRI and histopathological grade is detailed in **Table 4**.

TABLE 2 | Sensitivity, specificity, positive predictive value (PPV), and negative predictive value (NPV) for computed tomography (CT) glioma grading.

CT grade	Sensitivity (%)	Specificity (%)	PPV (%)	NPV (%)
High	60	20	60	20
Low	20	60	25	60

TABLE 3 | Sensitivity, specificity, positive predictive value (PPV), and negative predictive value (NPV) for magnetic resonance imaging (MRI) glioma grading.

MRI grade	Sensitivity (%)	Specificity (%)	PPV (%)	NPV (%)
High	60	40	67	33
Low	33	33	40	60

TABLE 4 | Contrast enhancing (CE) tumor volume for high- and low-grade gliomas on computed tomography (CT) and magnetic resonance imaging (MRI).

Tumor grade	CT-average CE volume cm^3 (range)	CT SD	MRI-average CE volume cm^3 (range)	MRI-SD
Low	1.13 (0.15–2.79)	0.35	1.44 (0.2–3.22)	1.5
High	2.4 (0–5.27)	2.49	2.13 (0.8–3.08)	2.05

TABLE 5 | Sensitivity, specificity, positive predictive value (PPV), and negative predictive value (NPV) for computed tomography (CT) glioma type prediction.

CT diagnosis	Sensitivity (%)	Specificity (%)	PPV (%)	NPV (%)
Oligodendroglioma	NA	45.5	33.3	NA
Astrocytoma	45.5	NA	NA	33.3

TABLE 6 | Sensitivity, specificity, positive predictive value (PPV), and negative predictive value (NPV) for magnetic resonance imaging (MRI) glioma type prediction.

MRI diagnosis	Sensitivity (%)	Specificity (%)	PPV (%)	NPV (%)
Oligodendroglioma	66.7	36.4	33.3	87.5
Astrocytoma	63.6	66.7	87.5	66.7

All tumors were identified as intra-axial, except for one which was identified by all three reviewers as extra-axial and was histologically confirmed to be an optic chiasm astrocytoma. For type of glioma, all three observers agreed in 6/15 (40%) patients for CT and 4/15 (26.7%) patients for MRI. Using predicted tumor type, either majority or unanimous observer agreement, CT had an accuracy of 53.3% (8/15) and MRI an accuracy of 60% (9/15). When comparing CT predicted tumor type to MRI predicted tumor type, agreement was seen in 11/15 cases (73.3%). In cases where CT and MRI tumor type agreed, accuracy (sensitivity) between histopathology was 54.5% (6/11), specificity for this group was also 54.5%. Sensitivity, specificity, PPV, and NPV for glioma type for both CT and MRI are detailed in **Tables 5** and **6**, respectively. For these analyses, the MRI diagnosed extra-axial tumor was removed from the study population. Since no tumors were misclassified as astrocytomas on CT and diagnosed as oligodendrogliomas on histopathology, the CT specificity and PPV for astrocytoma

and sensitivity and NPV for oligodendroglioma could not be calculated.

The averages, median, range, SD, and variation coefficient for CT and MRI measurements are detailed in **Tables 7** and **8**, respectively. On CT, at least one reviewer could not identify the lesion for mensuration pre- or post-contrast in the same two cases and therefore a 0 was assigned. On MRI, the lesion could not be identified on T1 pre-contrast images on two patients, both of which had lesions identified and measured on post-contrast images. Four masses were uniformly CE and thus a measurement of a non-CE volume could not be performed. In one patient with a small (0.4 cm^3 T1 + C lesion), one reviewer was unable to measure two dimensions and therefore recorded 0 and the other two had a small 2D measurement (0.5 cm^3). The comparisons acquired, the statistical test used, the statistical test SD, and *p*-value are highlighted in **Table 9**. The only statistically significant comparison was the CT pre-contrast volume compared to T2W volume.

DISCUSSION

To the author's knowledge, this is the first report detailing the application of previously described imaging characteristics of canine glioma to predict tumor types and grades. Compared to human medicine, our ability to predict glioma grade in dogs based on imaging characteristics was low. In human medicine, reports have discussed predictability of tumor grade on conventional MRI images with accuracy widely varying between studies from 65 to 94% (21–23). Law et al. (22) looked at the sensitivity, specificity, PPV, and NPV for predicting high-grade gliomas with conventional MRI and found it to be 72.5, 65, 86.1, and 44.1%, respectively. These values are greater than found with our data in dogs with high-grade gliomas on both CT and MRI. An additional human study (24) found that for low-grade astrocytomas, a 50% false positive rate was observed on MRI in predicting grade. This finding is similar to our data for high-grade gliomas, and less than what this study found with low-grade gliomas for both MRI and CT. One possible reason is the observer subjectivity with respect to the degree of contrast enhancement as it correlates to high-grade gliomas. However, subjective criteria detailed in previous veterinary literature were used for this study (12). Although objective methods of contrast enhancement quantification have been described in humans, they have not been evaluated in veterinary medicine (19). One study in dogs reported the presence of contrast enhancement as being significantly associated with high-grade compared to low-grade gliomas (10). An additional study found the absence of or mild contrast enhancement significantly correlated low-grade gliomas (11). In our study, only one tumor failed to have any contrast enhancement on CT and was diagnosed unanimously as a low-grade tumor both on CT and MRI. Interestingly, this lesion was a high-grade glioma on histopathology. When evaluating quantitative CE volumes between low- and high-grade tumors (**Table 3**), a large overlap exists between both low- and high-grade gliomas. This finding supports those of the previously reported veterinary literature (10, 11) and suggests that subjective degree and volume mensuration of contrast enhancement may not correlate with histopathological grade.

Most literature in human medicine regarding imaging predictability of gliomas is focused on glioma grade and not type. One report found that conventional MRI sequences were able to correctly differentiate 80.6–83.3% of grade II–IV astrocytomas (21). Another study, comparing primary intra-axial tumors had an accuracy of 94% (23). Results of these studies are both greater than the overall accuracy reported here using CT, MRI, or both modalities. As mentioned in previous veterinary reports (10, 11), overlap and redundancy of findings are noted between tumor

TABLE 7 | Summary of median measurement, range, SD, and variation coefficient for computed tomography (CT) measurements.

CT measurement	Median	Range	SD	Variation coefficient
Two-dimensional (2D) (cm^2)	1.62	0–6	0.79	0.63
CT pre-contrast volume (cm^3)	2.3	0–9.88	1.9	1.68
CT post-contrast volume (cm^3)	2.05	0–10.18	1	0.53
CT post-contrast contrast enhancing (CE) volume (cm^3) only	1.15	0–7.18	0.64	0.37
CT post-contrast non-CE volume only	0.53	0–6.5	0.43	0.5

TABLE 8 | Summary of median measurement, range, and SD for magnetic resonance imaging (MRI) measurements.

MRI measurement	Median	Range	SD	Variation coefficient
Two-dimensional (cm^2)	1.61	0–7.2	1.03	0.58
MRI T1-weighted (T1W) pre-contrast volume (cm^3)	3.22	0–11.3	0.3	0.3
MRI T2-weighted contrast volume (cm^3)	5.13	0.07–13.41	0.81	0.19
MRI T1W post-contrast volume (cm^3)	2.6	0.19–10.03	0.87	0.32
MRI T1W post-contrast contrast enhancing (CE) volume only (cm^3)	1.36	0–9.28	0.85	0.48
MRI T1W post-contrast non-CE volume only	1.02	0–4.05	0.42	0.5

TABLE 9 | Computed tomography (CT) to magnetic resonance imaging (MRI) comparisons, statistical test used, and *p*-value.

Comparison	Statistical test	*p*-Value
CT pre-contrast volume to CT post-contrast volume	Wilcoxon signed rank	0.86
Post-contrast: two-dimensional CT to T1-weighted (T1W) MRI	Wilcoxon signed rank	0.65
Post-contrast: CT to T1W MR contrast enhancing (CE) volume only	Wilcoxon signed rank	0.56
Post-contrast: CT to T1W non-CE volume only	Wilcoxon signed rank	0.1970
CT pre-contrast volume to T1W pre-contrast volume	Mixed model ANOVA	0.41
CT pre-contrast volume to T2-weighted (T2W) volume	Mixed model ANOVA	**0.03**
T1W pre-contrast volume to T2W volume	Mixed model ANOVA	0.35

The bold font indicates statistical significance.

types and likely the cause of low-to-moderate tumor type predictability in our study. Potentially also impacting our predictability for grade and glioma type was using a majority agreement between reviewers, in comparison to a solitary reviewer to predict diagnosis. This type of agreement is similar to what occurs in our hospital on clinical cases.

To the authors' knowledge, comparison of mensuration of gliomas using CT and MRI has not been previously described in dogs. Both contrast-enhanced 2D measurements and three-dimensional (3D) volume measurements are described in measurement techniques for clinical trial monitoring of intra-axial tumors (14). In human literature, comparison of 2D to 3D volumetric measurements in terms of therapeutic response has been found to perform similarly (20, 25). No current consensus on glioma mensuration in veterinary medicine exists; however, using the same measurement technique between serial imaging for evaluating response to therapy is recommended (15). Based on the data from this study, no statistical significance exists between CT and MRI when comparing similar measurement techniques, with the exception of comparing CT pre-contrast volume to T2W volume. This is likely due to the inclusion of perilesional edema in the T2W measurements. For better comparison of CT post-contrast and T1W post-contrast to the pre-contrast images, perilesional edema was not included in the measurement. However, it is likely that a small amount of perilesional edema was included within the pre-contrast volumetric measurement given the delineation between edema and mass was not consistently well defined. Despite the lack of perilesional edema inclusion within the T1W pre-contrast images, no statistical difference was appreciated between T1 pre-contrast and T2W volumetric measurements. To the authors' knowledge, the volumetric measurement of CT and T1W pre-contrast images has not been described. Interestingly, in multiple cases on both CT and MRI, at least one reviewer was unable to complete the measurement, either due to lack of detection, mass shape, or lack of heterogeneity (in the cause of CE vs. non-CE volume). On CT, two gliomas were not visualized on post-contrast images by at least one reviewer; however, all reviewers were able to visualize and measure the glioma volume of the glioma on T1W post-contrast images. Although not statistically significant, this finding may argue for MRI a preferred imaging modality. In addition, since the statistical findings support that CT and MRI may be used interchangeably to measure gliomas; however, from a clinical standpoint, maintaining the same imaging modality to evaluate for therapeutic response, should be performed, if possible (15).

Multiple limitations of this study exist. Since this study is retrospective in nature, the timeframe between CT and MRI could not be closely controlled, however, was specified in the inclusion criteria. Given that no significant differences in the majority of the mensuration parameters existed between the two modalities, the specified timeframe between studies likely did not affect the outcome. The majority of this study's histopathological diagnoses were achieved *via* stereotactic biopsy. Variable reliability of histological grading of stereotactic biopsy has been reported in human medicine (26, 27). Thus, it may be possible that some of the gliomas included in this study were erroneously graded and therefore contributing to the lower predictability of this study in comparison to human studies that used excisional biopsies for histopathology. An additional limitation is the relatively small sample size included in this study, largely due to overall disease prevalence, and requirements for both histopathological tumor confirmation and performance of contemporaneous CT and MRI imaging studies.

In conclusion, the results of this study suggest that both conventional CT and MRI have a low-to-moderate ability to predict types and grades of canine gliomas, and that histological evaluation is necessary for accurate diagnosis of canine brain tumors. Based on the results of this study for conventionally used contrast-enhanced measurement techniques, CT and MRI have no significant difference and thus both are considered reasonable options for tumor mensuration. Further studies are required to determine if the discriminatory abilities of CT and MRI are improved with the addition of techniques such as dynamic contrast-enhanced imaging, diffusion-weighted imaging, or MR spectroscopy and to assess if significant difference exists between the modalities for assessment of therapeutic response.

ETHICS STATEMENT

This study is retrospective in nature and not all imaging (MRI) was performed at VA-MD Veterinary Teaching Hospital. All patient imaging performed at VA-MD VTH was performed in accordance to Virginia Tech IACUC 14-235CVM and 15-122CVM. The obtaining and use of imaging studies performed outside VA-MD VTH was approved by written client consent.

AUTHOR CONTRIBUTIONS

KS: primary researcher, responsible for study development and organization, including the acquisition of patients, anonymizing and distributing cases, imaging and patient data and analyzing and organizing reviewer data. One of three image reviewers. Drafting and editing of manuscript. JRuth: assist in drafting study design. One of three image reviewers. Internal manuscript revision. TP: assist in drafting study design. One of three image reviewers. Internal manuscript revision. SW: statistician, responsible for performing data statistics and drafting the manuscript portion pertaining to. Internal manuscript revision. JRossmeisl: responsible for initial prospective clinical trial in which patients were retrospectively pulled from and assisted in getting all images needed for this study. Assist in drafting study design. Internal manuscript revision.

FUNDING

All VA-MD VTH imaging studies and one of the authors (JRossmeisl) were supported by HHS NIH/NCI R01CA139099.

REFERENCES

1. Whelan HT, Clanton JA, Wilson RE, Tulipan NB. Comparison of CT and MRI brain tumor imaging using a canine glioma model. *Pediatr Neurol* (1988) 4(5):279–83. doi:10.1016/0887-8994(88)90066-5
2. Sprung C, Baerwald R, Henkes H, Schorner W. A comparative study of CT and MRI in midline tumors of childhood and adolescence. *Childs Nerv Syst* (1989) 5(2):102–6. doi:10.1007/BF00571119
3. Schorner W, Schubeus P, Henkes H, Rottacker C, Hamm B, Felix R. Intracranial meningiomas. Comparison of plain and contrast-enhanced examinations in CT and MRI. *Neuroradiology* (1990) 32(1):12–8.
4. Schellinger PD, Meinck HM, Thron A. Diagnostic accuracy of MRI compared to CCT in patients with brain metastases. *J Neurooncol* (1999) 44(3):275–81. doi:10.1023/A:1006308808769
5. Dieterich S, Zwingenberger A, Hansen K, Pfeiffer I, Theon A, Kent MS. Inter- and intrafraction motion for stereotactic radiosurgery in dogs and cats using a modified Brainlab frameless stereotactic mask system. *Vet Radiol Ultrasound* (2015) 56(5):563–9. doi:10.1111/vru.12271
6. Moissonnier P, Blot S, Devauchelle P, Delisle F, Beuvon F, Boulha L, et al. Stereotactic CT-guided brain biopsy in the dog. *J Small Anim Pract* (2002) 43(3):115–23. doi:10.1111/j.1748-5827.2002.tb00041.x
7. Rossmeisl JH, Andriani RT, Cecere TE, Lahmers K, LeRoith T, Zimmerman KL, et al. Frame-based stereotactic biopsy of canine brain masses: technique and clinical results in 26 cases. *Front Vet Sci* (2015) 2:20. doi:10.3389/fvets.2015.00020
8. Louis DN, Ohgaki H, Wiestler OD, Cavenee WK, Burger PC, Jouvet A, et al. The 2007 WHO classification of tumours of the central nervous system. *Acta Neuropathol* (2007) 114(2):97–109. doi:10.1007/s00401-007-0243-4
9. Louis DN, Perry A, Reifenberger G, von Deimling A, Figarella-Branger D, Cavenee WK, et al. The 2016 World Health Organization classification of tumors of the central nervous system: a summary. *Acta Neuropathol* (2016) 131(6):803–20. doi:10.1007/s00401-016-1545-1
10. Young BD, Levine JM, Porter BF, Chen-Allen AV, Rossmeisl JH, Platt SR, et al. Magnetic resonance imaging features of intracranial astrocytomas and oligodendrogliomas in dogs. *Vet Radiol Ultrasound* (2011) 52(2):132–41. doi:10.1111/j.1740-8261.2010.01758.x
11. Bentley RT, Ober CP, Anderson KL, Feeney DA, Naughton JF, Ohlfest JR, et al. Canine intracranial gliomas: relationship between magnetic resonance imaging criteria and tumor type and grade. *Vet J* (2013) 198(2):463–71. doi:10.1016/j.tvjl.2013.08.015
12. Young BD, Fosgate GT, Holmes SP, Wolff CA, Chen-Allen AV, Kent M, et al. Evaluation of standard magnetic resonance characteristics used to differentiate neoplastic, inflammatory, and vascular brain lesions in dogs. *Vet Radiol Ultrasound* (2014) 55(4):399–406. doi:10.1111/vru.12137
13. Macdonald DR, Cascino TL, Schold SC Jr, Cairncross JG. Response criteria for phase II studies of supratentorial malignant glioma. *J Clin Oncol* (1990) 8(7):1277–80. doi:10.1200/JCO.1990.8.7.1277
14. Henson JW, Ulmer S, Harris GJ. Brain tumor imaging in clinical trials. *AJNR Am J Neuroradiol* (2008) 29(3):419–24. doi:10.3174/ajnr.A0963
15. Rossmeisl JH Jr, Garcia PA, Daniel GB, Bourland JD, Debinski W, Dervisis N, et al. Invited review – neuroimaging response assessment criteria for brain tumors in veterinary patients. *Vet Radiol Ultrasound* (2014) 55(2):115–32. doi:10.1111/vru.12118
16. Sorensen AG, Patel S, Harmath C, Bridges S, Synnott J, Sievers A, et al. Comparison of diameter and perimeter methods for tumor volume calculation. *J Clin Oncol* (2001) 19(2):551–7. doi:10.1200/JCO.2001.19.2.551
17. Galanis E, Buckner JC, Maurer MJ, Sykora R, Castillo R, Ballman KV, et al. Validation of neuroradiologic response assessment in gliomas: measurement by RECIST, two-dimensional, computer-assisted tumor area, and computer-assisted tumor volume methods. *Neuro Oncol* (2006) 8(2):156–65. doi:10.1215/15228517-2005-005
18. Ellingson BM, Cloughesy TF, Lai A, Nghiemphu PL, Mischel PS, Pope WB. Quantitative volumetric analysis of conventional MRI response in recurrent glioblastoma treated with bevacizumab. *Neuro Oncol* (2011) 13(4):401–9. doi:10.1093/neuonc/noq206
19. Kanaly CW, Ding D, Mehta AI, Waller AF, Crocker I, Desjardins A, et al. A novel method for volumetric MRI response assessment of enhancing brain tumors. *PLoS One* (2011) 6(1):e16031. doi:10.1371/journal.pone.0016031
20. Wang MY, Cheng JL, Han YH, Li YL, Dai JP, Shi DP. Measurement of tumor size in adult glioblastoma: classical cross-sectional criteria on 2D MRI or volumetric criteria on high resolution 3D MRI? *Eur J Radiol* (2012) 81(9):2370–4. doi:10.1016/j.ejrad.2011.05.017
21. Dean BL, Drayer BP, Bird CR, Flom RA, Hodak JA, Coons SW, et al. Gliomas: classification with MR imaging. *Radiology* (1990) 174(2):411–5. doi:10.1148/radiology.174.2.2153310
22. Law M, Yang S, Wang H, Babb JS, Johnson G, Cha S, et al. Glioma grading: sensitivity, specificity, and predictive values of perfusion MR imaging and proton MR spectroscopic imaging compared with conventional MR imaging. *AJNR Am J Neuroradiol* (2003) 24(10):1989–98.
23. Chisty IA, Rafique MZ, Hussain M, Akhtar W, Ahmed MN, Sajjad Z, et al. MRI characterization and histopathological correlation of primary intra-axial brain glioma. *J Liaquat Uni Med Health Sci* (2010) 9(2):64–9.
24. Kondziolka D, Lunsford LD, Martinez AJ. Unreliability of contemporary neurodiagnostic imaging in evaluating suspected adult supratentorial (low-grade) astrocytoma. *J Neurosurg* (1993) 79(4):533–6. doi:10.3171/jns.1993.79.4.0533
25. Wang MY, Cheng JL, Han YH, Li YL, Dou SW, Yan FS, et al. Comparison of volumetric methods for tumor measurements on two and three dimensional MRI in adult glioblastoma. *Neuroradiology* (2011) 53(8):565–9. doi:10.1007/s00234-010-0789-z
26. Mittler MA, Walters BC, Stopa EG. Observer reliability in histological grading of astrocytoma stereotactic biopsies. *J Neurosurg* (1996) 85(6):1091–4. doi:10.3171/jns.1996.85.6.1091
27. Muragaki Y, Chernov M, Maruyama T, Ochiai T, Taira T, Kubo O, et al. Low-grade glioma on stereotactic biopsy: how often is the diagnosis accurate? *Minim Invasive Neurosurg* (2008) 51(5):275–9. doi:10.1055/s-0028-1082322

Conflict of Interest Statement: The authors declare that the research was conducted in the absence of any commercial or financial relationships that could be construed as a potential conflict of interest.

frontiers in Veterinary Science

MINI REVIEW
published: 13 December 2017
doi: 10.3389/fvets.2017.00218

Recent Advances in Radiotracer Imaging Hold Potential for Future Refined Evaluation of Epilepsy in Veterinary Neurology

Marion Bankstahl[1] and Jens P. Bankstahl[2]*

[1] Department of Pharmacology, Toxicology, and Pharmacy, University of Veterinary Medicine Hannover, Center of Systems Neuroscience Hannover, Hannover, Germany, [2] Department of Nuclear Medicine, Hannover Medical School, Hannover, Germany

Non-invasive nuclear imaging by positron emission tomography and single photon emission computed tomography has significantly contributed to epileptic focus localization in human neurology for several decades now. Offering functional insight into brain alterations, it is also of particular relevance for epilepsy research. Access to these techniques for veterinary medicine is becoming more and more relevant and has already resulted in first studies in canine patients. In view of the substantial proportion of drug-refractory epileptic dogs and cats, image-guided epileptic focus localization will be a prerequisite for selection of patients for surgical focus resection. Moreover, radiotracer imaging holds potential for a better understanding of the pathophysiology of underlying epilepsy syndromes as well as to forecast disease risk after epileptogenic brain insults. Importantly, recent advances in epilepsy research demonstrate the suitability and value of several novel radiotracers for non-invasive assessment of neuroinflammation, blood–brain barrier alterations, and neurotransmitter systems. It is desirable that veterinary epilepsy patients will also benefit from these promising developments in the medium term. This paper reviews the current use of radiotracer imaging in the veterinary epilepsy patient and suggests possible future directions for the technique.

Keywords: positron emission tomography, single photon emission computed tomography, imaging, epilepsy, biomarker, positron emission tomography, single photon emission computed tomography

OPEN ACCESS

Edited by:
Fintan John McEvoy, University of Copenhagen, Denmark

Reviewed by:
Tarja Susanna Jokinen, University of Helsinki, Finland
Karin Hultin Jäderlund, Norwegian University of Life Sciences, Norway

****Correspondence:***
Marion Bankstahl
marion.bankstahl@tiho-hannover.de

Specialty section:
This article was submitted to Veterinary Neurology and Neurosurgery, a section of the journal Frontiers in Veterinary Science

Received: *27 September 2017*
Accepted: *30 November 2017*
Published: *13 December 2017*

Citation:
Bankstahl M and Bankstahl JP (2017) Recent Advances in Radiotracer Imaging Hold Potential for Future Refined Evaluation of Epilepsy in Veterinary Neurology. Front. Vet. Sci. 4:218. doi: 10.3389/fvets.2017.00218

INTRODUCTION

Molecular radiotracer imaging, including positron emission tomography (PET) and single photon emission computed tomography (SPECT), holds a tremendous potential for diagnostics of brain changes. These methods provide functional insight into the brain, which is difficult to assess by non-invasive techniques. Following injection of a radiolabeled compound, uptake and regional distribution in the brain is three-dimensionally visualized by a PET or SPECT camera based on radioactive decay detection. In addition to radioisotope imaging, up-to-date clinical scanning systems are equipped with fully functional computed tomography (CT). Very recently, integrated magnetic resonance imaging (MRI) components for anatomical co-registration are available. These advances make particularly PET/CT or PET/MRI in combination with various novel radiotracers very promising imaging techniques for evaluation of neurological diseases. Despite the use of

radiotracer imaging in human patients for some decades, this imaging modality is only rarely used in clinical veterinary neurology. This is owing to some practical limitations. Due to high cost and radiosafety requirements, PET or SPECT scanners are usually not available in veterinary practices or clinics (1). Usually, only by collaboration with nuclear medicine specialists for human patients, can these techniques be made available for veterinary patients. Clinically used radiotracers have a half-life of minutes to hours and are injected only in nano- to pico-molar concentrations making pharmacological side effects usually negligible. Still, injection of radioisotopes may require hospitalization under a radiosafety regime. Particularly some PET radiotracers with a half-life only up to about 1 h require onsite radiochemistry, often including instant isotope production using a cyclotron. These limitations have led to enormous efforts of radiochemistry research to label PET tracers with fluorine-18 with a half-life of almost 2 h, making delivery from central production sites to imaging centers possible. In spite of these restrictions, the use of radiotracer imaging in veterinary medicine, particularly in veterinary oncology, has increased during the last years. This increase is mostly driven by more individualized tumor diagnostics and treatments (2, 3). In this area, F-18-fluoro-deoxy-glucose (F-18-FDG) is, in analogy to human patients, the most successful radiotracer. F-18-FDG is a radiolabeled glucose analog which is taken up and trapped in metabolically active cells. This feature makes it very useful not only for localization of peripheral and CNS tumors and its metastases but also for measurement of epilepsy-associated altered regional brain activity. In addition to F-18-FDG, in human clinical practice, more and more radiotracers are available targeting, e.g., brain perfusion, neuroreceptor density, brain inflammation, or the burden of amyloid beta in patients with Alzheimer's disease.

ROLE OF RADIOTRACER IMAGING IN HUMAN EPILEPSY

Preliminary findings with newer radiotracers in human epilepsy patients suggest their future potential for disease evaluation and elucidation of pathophysiological mechanisms. However, the clinical application of radiotracer imaging as yet lies mainly on presurgical evaluation of pharmacoresistant patients being considered for focus resection. In these individuals, representing around one-third of epilepsy patients (4), PET and SPECT can be helpful non-invasive tools for identifying the epileptogenic zone. They are of particular value for drug-refractory patients with no structural alterations in MRI, with multifocal MRI-positive lesions which cannot all be assigned to the epileptic focus, or with inconclusive video-electroencephalogram (EEG) monitoring findings (5, 6).

Radiotracers typically used for this purpose target either brain blood perfusion [e.g., Tc-99m-hexamethyl propyleneamine oxime (Tc-99m-HMPAO) SPECT], metabolic pathways, especially glucose metabolism (F-18-FDG PET), or, occasionally, neurotransmitter receptors [e.g., C-11-flumazenil (C-11-FMZ) PET]. Hitherto, F-18-FDG is the most commonly applied tracer for detection of the epileptic focus region and is of high sensitivity particularly in patients with temporal lobe epilepsy (up to 90% sensitivity) (7–9). F-18-FDG PET is usually performed in the seizure-free interval (interictal PET) and aims at identifying brain regions with decreased glucometabolism, being considered to partially reflect, among other factors, reduced synaptic activity (10). F-18-FDG PET can also deliver information about disease severity and progression. In this regard, it has been shown in children with intractable epilepsy that the extent of the hypometabolic brain area can be indicative of the seizure burden, i.e., it grows in size with increasing seizure frequency and *vice versa* (11). Further, F-18-FDG PET can be indicative for occurrence of memory impairment (12, 13) as well as provide prognostic information on seizure freedom after surgery (14).

While most radiotracers targeting metabolic pathways or brain perfusion need an accumulation time much longer than the duration of a single seizure, Tc-99m-HMPAO SPECT, due to the high first-pass uptake of the radiotracer, can be applied during seizure activity (ictal SPECT). Furthermore, the radioactive half-life of Tc-99m of about 6 h enables a stand-by availability of the radiotracer in a video-EEG monitoring unit. To enable diagnostic success, an established setup of continuous video-EEG monitoring for immediate seizure detection of the respective patient and continuous access to the radiotracer for prompt injection immediately after seizure onset is mandatory. As Tc-99m-HMPAO accumulates in areas with high blood flow, the hyperperfused seizure focus displays a distinct increase in tracer signal. Ictal SPECT is associated with a correct focus detection in most patients with temporal lobe epilepsy (>80% sensitivity) (15, 16). In case of additionally performed interictal Tc-99m-HMPAO SPECT, the probability for detecting the seizure focus may increase by applying SISCOM analysis, i.e., subtracting interictal SPECT images from the ictal images and displaying the results on co-registered MR images (5, 17).

Diagnostic evaluation for identifying increased or decreased regional tracer uptake is usually performed by nuclear medicine physicians together with neurologists primarily by visual analysis. In principal, every brain region can be affected, directly but also as a consequence of diaschisis, i.e., secondary functional lesions in brain areas influenced by the primary affected brain region. Regions frequently affected in temporal lobe epilepsy patients include ipsilateral hippocampus, amygdala, thalamus, frontal cortex, and insula (17). Other methods of data evaluation like statistical parametric mapping analysis are not common in current clinical routine, yet can significantly increase the diagnostic sensitivity of combined ictal-interictal Tc-99m-HMPAO SPECT (17, 18).

CURRENT STATE IN VETERINARY MEDICINE

For several years now, F-18-FDG PET/CT is increasingly used also in veterinary oncology (2, 19). Initial reports indicate that F-18-FDG PET may indeed be useful for localization of brain tumors in dogs (20, 21). Brain tumors are one common MRI-positive cause of structural epilepsy in dogs (22) as well as in human patients (23). In addition, F-18-FDG brain reference data in healthy Beagles have been provided (24).

Neuro-nuclear imaging in dogs and cats may also serve to identify an epileptic focus in MRI-negative epilepsy. Currently, PET or SPECT are barely used for this purpose in veterinary medicine. Nonetheless, joint efforts in Finland have led to two recent publications supporting that F-18-FDG PET for identification of the epileptic focus region is translatable to veterinary patients. In juvenile Lagotto Romagnolo dogs with focal-onset epilepsy, Jokinen and colleagues identified regions with reduced glucose metabolism in cortical brain regions associated with EEG abnormalities (25). **Figure 1** shows an interictal F-18-FDG PET image taken from this study displaying glucose hypometabolism in the left temporal lobe. A second study performed by the same group prospectively evaluated adult Finnish Spitz dogs with focal idiopathic epilepsy by EEG and F-18-FDG and found abnormalities by visual analysis in 9/11 dogs with occipital cortex findings most consistent with the epileptic status (26). Although changes in F-18-FDG uptake were also detected by this method in part of the controls of the investigated breed, quantification on group level resulted in statistically significant lower uptake values in epileptic dogs in the hippocampus, cortical regions, and the cerebellum. Considerably, in this regard, PET imaging data have been reported to be of higher diagnostic sensitivity than visual analysis of EEG recording (26). Preferably, further prospective studies with larger group sizes will confirm these findings and evaluate whether they are representative also for other breeds. Of course, studies in epileptic cats are also desirable.

Assessment of brain perfusion by SPECT was first investigated in healthy dogs more than 15 years ago using the Tc-99m-ethyl cysteinate dimer (Tc-99m-ECD) (27). More recently, interictal Tc-99m-ECD SPECT/CT was also explored in dogs with idiopathic epilepsy, reporting hypoperfusion restricted to subcortical areas of epileptic dogs (28). Subsequently, the same group was able to further differentiate subcortical brain regions in healthy dogs, including hippocampus, thalamus, and striatum, using a high resolution SPECT scanner, but did not yet apply this technique to veterinary epilepsy patients (29). Certainly, one has to keep in mind that interictal perfusion SPECT is distinctly less sensitive for seizure focus identification compared to ictal perfusion SPECT (16, 18). Due to the logistic requirements for ictal perfusion SPECT, particularly the availability of a video-EEG monitoring unit in proximity to the scanner, however, this technique has obvious limitations for clinical routine in veterinary neurology. Nonetheless, recent progress in developing devices for non-invasive video-EEG recording (30) or seizure-alert systems based on invasive EEG recording in dogs (31, 32) might pave the way for such efforts in the close future. Ideally, future ictal perfusion SPECT studies would include the clinically more relevant perfusion tracer Tc-99m-HMPAO.

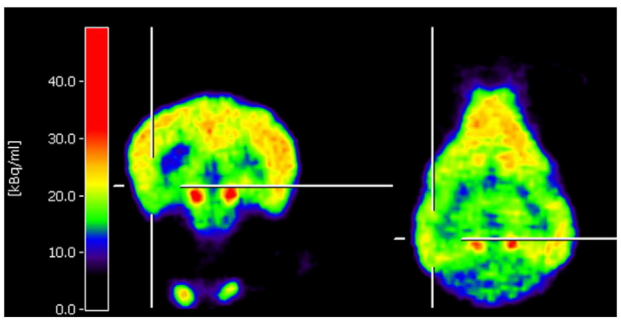

FIGURE 1 | Coronal and horizontal F-18-fluoro-deoxy-glucose positron emission tomography (PET) images from a 10.5-week-old puppy with juvenile epilepsy showing an area of hypometabolism in the left temporal lobe, indicated by the cross localizers. The hot scale represents radioactivity concentration (kBq/ml) [taken from Ref (25), permission from the copyright holder has been obtained].

In contrast to human medicine, imaging procedure in veterinary epilepsy patients requires consideration of several distinctive features. First, anesthesia necessary to achieve immobility of the subject for neuroimaging can considerably influence functional brain imaging results (33, 34). Another impact factor is the chronic anti-seizure medication in epilepsy patients. Indeed, phenobarbital, which still represents the most widely applied anti-seizure drug in dogs and cats, seems to reduce brain glucometabolism and hereby also F-18-FDG PET signal in human epilepsy patients (35). A further factor in veterinary medicine is variation in brain and skull anatomy and size of different dog and cat breeds (36, 37) hampering application of reference PET, SPECT, or MRI brain templates for image analysis. In consequence, for reliable image interpretation establishing diverse sets of reference images for different breeds will presumably be necessary.

FUTURE DIRECTIONS

Nuclear imaging is currently experiencing broad application to help filling several gaps in epilepsy research: (i) to elucidate the pathophysiological processes underlying epilepsy development and disease progression (38, 39), (ii) to identify predictive biomarkers for stratification of individuals with high risk of disease development after epileptogenic brain insults (38, 40), and (iii) to identify mechanisms of drug resistance (41).

Lasting seizure burden despite state-of-the-art anti-seizure pharmacotherapy remains a serious problem also in epileptic dogs (42, 43). Interest in establishing epilepsy surgery in pharmacoresistant cats and dogs will probably grow. As in human patients, surgical resection of the epileptic focus region may be advantageous in veterinary patients for achieving seizure freedom or control in carefully chosen refractory individuals. For selection of appropriate epilepsy surgery candidates, proper presurgical evaluation needs to be established. MRI is already widely used as a reliable technique to identify brain abnormalities in epileptic companion animals (44). However, in epilepsy cases with negative MRI, application of nuclear imaging, e.g., F-18-FDG PET or Tc-99m-HMPAO SPECT, has a significant potential to provide the necessary data for epileptic focus localization also in animals.

Besides its established benefit for presurgical patient evaluation, neuroimaging of glucose metabolism might also provide hints for ongoing epileptogenesis before clinical seizures occur. In addition, it might offer information on the brain regions involved in epilepsy development and progression. Meanwhile, a whole batch of F-18-FDG PET studies performed in several rodent models of epileptogenesis shows that glucose metabolism

decreases in brain regions associated with epilepsy development already during the latency phase, i.e., the time period between the epileptogenic insult and the first clinical seizure (45–48). In combination with other markers, F-18-FDG PET might, therefore, also serve as a prognostic biomarker for an increased risk to develop epilepsy, which is investigated in ongoing studies. An attempt to use F-18-FDG PET as a marker to predict the epileptic outcome in rats showed indeed promising preliminary results (47), but further studies in larger animal groups will be needed to confirm this approach.

An emerging field in epilepsy research is assessment of neuroinflammation as a process present during epileptogenesis as well as in chronic epilepsy (41). Particularly, radioligands of the so-called translocator protein (TSPO; also known as peripheral benzodiazepine receptor) can be utilized to visualize activated microglia, and to a lesser extent, of reactive astrocytes (49). In animal models of epileptogenesis and chronic epilepsy, various radiolabeled TSPO ligands have been evaluated. The newest-generation ligand F-18-GE180 is characterized by a favorable signal-to-noise ratio across species (50). Data gained by F-18-GE180 PET in a rat model of epileptogenesis demonstrates the suitability of TSPO PET to reveal the time course of neuroinflammation during epilepsy development and to identify brain regions involved in this process (51). Further, TSPO PET at disease onset with a different ligand (F-18-PBR111) has recently been shown to have potential of predicting the frequency of later spontaneous recurrent seizures in rats (52). In chronic epileptic rats, increased TSPO signal was found in phenobarbital-unresponsive but not in phenobarbital-responsive individuals, suggesting that TSPO PET might also serve as an indirect marker for pharmacoresistance (53). In parallel, studies in human patients support potential value of TSPO PET for localizing the seizure focus (54, 55).

In close interaction with, or even as one relevant source of neuroinflammation, increased permeability of the blood–brain barrier (BBB) leading to extravasation of blood compounds like albumin is considered to be another crucial factor for epilepsy development (56). Extravasated albumin was found also in brain tissue of human patients with chronic epilepsy (57), suggesting that BBB leakage might also play a role in epilepsy maintenance or progression. *In vivo* imaging approaches to visualize a leaky BBB are based on detection of contrast agents or radiotracers which do not cross the intact BBB. Contrast-enhanced MRI is an established technique to diagnose BBB leakage after epileptogenic insults (e.g., status epilepticus, stroke, or traumatic brain injury) in rodents and human patients (58, 59), but SPECT and PET using the radiotracers Tc-99m-diethylenetriaminepentaacetic acid and Ga-68-DTPA have also been demonstrated suitable for this purpose (58, 60, 61). While the application of gadolinium-based MRI contrast agents is related with safety risks due to compound accumulation in human brain and kidneys (62, 63), administration of nuclear imaging tracers is considered to be safe. Findings in animal models suggest that BBB leakage is highest in brain regions which are also affected by microglial activation during epileptogenesis (58, 59). The role of BBB leakage for epilepsy development in canine and feline epilepsy and the applicability of respective imaging techniques still remain to be assessed.

Nuclear imaging has also proven to be of some value for identification of human drug-refractory epilepsy patients. Drug-refractory epilepsy patients represent a large proportion of patients in both human and veterinary medicine. One mechanism attributed to drug refractoriness in epilepsy is overexpression of the efflux transporters like P-glycoprotein at the BBB, which extrudes anti-seizure drugs back into the blood, therefore resulting in sub-therapeutic drug levels at the site of the epileptic focus (64). Increased P-glycoprotein expression as mechanism of pharmacoresistance has also been suggested for canine patients (65, 66). Both human and veterinary patients affected by this mechanism might profit from alternatively being treated with anti-seizure drugs not being extruded by P-glycoprotein, or with transporter inhibitors or modulators (64, 67, 68). Prerequisite for translation of such therapeutic approaches to the clinical situation would be a diagnostic tool for identification of individuals with actual transporter overactivity. PET with the P-glycoprotein substrate tracer C-11-verapamil was shown to identify increased transporter function at the BBB in a post-status epilepticus model in rodents (69). This preclinical setup was successfully translated to drug-refractory human patients, demonstrating higher P-glycoprotein activity in pharmacoresistant individuals (70).

Besides F-18-FDG PET, the GABA-A receptor ligand 11-C-FMZ, and more recently also 18-F-FMZ, is more and more used for epileptic focus localization (41). In human patients with mesial temporal lobe epilepsy, F-18-FMZ PET can be even advantageous over F-18-FDG as it can result in more circumscribed visualization of altered temporal lobe areas like the hippocampus (71, 72). Recent generation of other radiolabeled receptor ligands like the NMDA glutamate receptor tracer F-18-GE179, will allow to further assess the role of neurotransmitter systems in epileptogenesis and chronic epilepsy (41). Various other ligands targeting neurotransmitter systems including the serotonin, dopamine, cannabinoid, opioid, or acetylcholine system have been investigated in human epilepsy patients (41). Their potential for canine and feline epilepsy patients still needs to be assessed.

CONCLUSION

Radiotracer imaging protocols for detecting abnormal glucose metabolism and brain perfusion appear prospective tools for presurgical evaluation of MRI-negative veterinary epilepsy patients in the future. Growing access to nuclear imaging modalities and recent advances in video-EEG monitoring for seizure warning will likely support this development. Evolution of diverse promising radiotracers for epilepsy research, like TSPO and neuroreceptor ligands, opens up new vistas for elucidating the pathophysiology of epileptogenesis and for predicting the risk of disease development in man, including realistic chances of being subsequently translated to veterinary medicine.

AUTHOR CONTRIBUTIONS

MB and JPB performed literature search and wrote the manuscript.

FUNDING

This publication was supported by Deutsche Forschungsgemeinschaft and University of Veterinary Medicine Hannover, Foundation within the funding programme Open Access Publishing.

REFERENCES

1. LeBlanc AK, Peremans K. PET and SPECT imaging in veterinary medicine. *Semin Nucl Med* (2014) 44(1):47–56. doi:10.1053/j.semnuclmed.2013.08.004
2. LeBlanc AK, Daniel GB. Advanced imaging for veterinary cancer patients. *Vet Clin North Am Small Anim Pract* (2007) 37(6):1059–77;v–i. doi:10.1016/j.cvsm.2007.06.004
3. Mattoon JS, Bryan JN. The future of imaging in veterinary oncology: learning from human medicine. *Vet J* (2013) 197(3):541–52. doi:10.1016/j.tvjl.2013.05.022
4. Kwan P, Brodie MJ. Early identification of refractory epilepsy. *N Engl J Med* (2000) 342(5):314–9. doi:10.1056/NEJM200002033420503
5. Kumar A, Chugani HT. The role of radionuclide imaging in epilepsy, part 1: sporadic temporal and extratemporal lobe epilepsy. *J Nucl Med Technol* (2017) 45(1):14–21. doi:10.2967/jnumed.112.114397
6. Uijl SG, Leijten FS, Arends JB, Parra J, van Huffelen AC, Moons KG. The added value of [18F]-fluoro-D-deoxyglucose positron emission tomography in screening for temporal lobe epilepsy surgery. *Epilepsia* (2007) 48(11):2121–9. doi:10.1111/j.1528-1167.2007.01197.x
7. Gok B, Jallo G, Hayeri R, Wahl R, Aygun N. The evaluation of FDG-PET imaging for epileptogenic focus localization in patients with MRI positive and MRI negative temporal lobe epilepsy. *Neuroradiology* (2013) 55(5):541–50. doi:10.1007/s00234-012-1121-x
8. Sarikaya I. PET studies in epilepsy. *Am J Nucl Med Mol Imaging* (2015) 5(5):416–30.
9. Knowlton RC, Laxer KD, Ende G, Hawkins RA, Wong ST, Matson GB, et al. Presurgical multimodality neuroimaging in electroencephalographic lateralized temporal lobe epilepsy. *Ann Neurol* (1997) 42(6):829–37. doi:10.1002/ana.410420603
10. Rocher AB, Chapon F, Blaizot X, Baron JC, Chavoix C. Resting-state brain glucose utilization as measured by PET is directly related to regional synaptophysin levels: a study in baboons. *Neuroimage* (2003) 20(3):1894–8. doi:10.1016/j.neuroimage.2003.07.002
11. Benedek K, Juhász C, Chugani DC, Muzik O, Chugani HT. Longitudinal changes in cortical glucose hypometabolism in children with intractable epilepsy. *J Child Neurol* (2006) 21(1):26–31. doi:10.1177/08830738060210011101
12. Jokeit H, Seitz RJ, Markowitsch HJ, Neumann N, Witte OW, Ebner A. Prefrontal asymmetric interictal glucose hypometabolism and cognitive impairment in patients with temporal lobe epilepsy. *Brain* (1997) 120(Pt 12):2283–94. doi:10.1093/brain/120.12.2283
13. Knopman AA, Wong CH, Stevenson RJ, Homewood J, Mohamed A, Somerville E, et al. The relationship between neuropsychological functioning and FDG-PET hypometabolism in intractable mesial temporal lobe epilepsy. *Epilepsy Behav* (2015) 44:136–42. doi:10.1016/j.yebeh.2015.01.023
14. Knowlton RC, Elgavish RA, Bartolucci A, Ojha B, Limdi N, Blount J, et al. Functional imaging: II. prediction of epilepsy surgery outcome. *Ann Neurol* (2008) 64(1):35–41. doi:10.1002/ana.21419
15. Lee Dong S, Lee Sang K, Kim Yu K, Lee Jae S, Cheon Gi J, Kang Keon W, et al. Superiority of HMPAO ictal SPECT to ECD ictal SPECT in localizing the epileptogenic zone. *Epilepsia* (2002) 43(3):263–9. doi:10.1046/j.1528-1157.2002.23001.x
16. Devous MD Sr, Thisted RA, Morgan GF, Leroy RF, Rowe CC. SPECT brain imaging in epilepsy: a meta-analysis. *J Nucl Med* (1998) 39(2):285–93.
17. Theodore WH. Presurgical focus localization in epilepsy: PET and SPECT. *Semin Nucl Med* (2017) 47(1):44–53. doi:10.1053/j.semnuclmed.2016.09.008
18. Kim S, Mountz JM. SPECT imaging of epilepsy: an overview and comparison with F-18 FDG PET. *Int J Mol Imaging* (2011) 2011:9. doi:10.1155/2011/813028
19. Lawrence J, Rohren E, Provenzale J. PET/CT today and tomorrow in veterinary cancer diagnosis and monitoring: fundamentals, early results and future perspectives. *Vet Comp Oncol* (2010) 8(3):163–87. doi:10.1111/j.1476-5829.2010.00218.x
20. Hansen AE, McEvoy F, Engelholm SA, Law I, Kristensen AT. FDG PET/CT imaging in canine cancer patients. *Vet Radiol Ultrasound* (2011) 52(2):201–6. doi:10.1111/j.1740-8261.2010.01757.x
21. Kang BT, Park C, Yoo JH, Gu SH, Jang DP, Kim YB, et al. 18F-fluorodeoxyglucose positron emission tomography and magnetic resonance imaging findings of primary intracranial histiocytic sarcoma in a dog. *J Vet Med Sci* (2009) 71(10):1397–401. doi:10.1292/jvms.001397
22. Bagley RS, Gavin PR. Seizures as a complication of brain tumors in dogs. *Clin Tech Small Anim Pract* (1998) 13(3):179–84. doi:10.1016/S1096-2867(98)80039-X
23. Politsky JM. Brain tumor-related epilepsy: a current review of the etiologic basis and diagnostic and treatment approaches. *Curr Neurol Neurosci Rep* (2017) 17(9):70. doi:10.1007/s11910-017-0777-3
24. Williams LM, Morandi F, Osborne DR, Narak J, LeBlanc AK. Kinetic analysis of 2-([(18)F]fluoro)-2-deoxy-D-glucose uptake in brains of anesthetized healthy dogs. *Am J Vet Res* (2014) 75(6):588–94. doi:10.2460/ajvr.75.6.588
25. Jokinen TS, Haaparanta-Solin M, Viitmaa R, Grönroos TJ, Johansson J, Bergamasco L, et al. FDG-PET in healthy and epileptic Lagotto Romagnolo dogs and changes in brain glucose uptake with age. *Vet Radiol Ultrasound* (2014) 55(3):331–41. doi:10.1111/vru.12129
26. Viitmaa R, Haaparanta-Solin M, Snellman M, Cizinauskas S, Orro T, Kuusela E, et al. Cerebral glucose utilization measured with high resolution positron emission tomography in epileptic Finnish Spitz dogs and healthy dogs. *Vet Radiol Ultrasound* (2014) 55(4):453–61. doi:10.1111/vru.12147
27. Peremans K, De Bondt P, Audenaert K, Van Laere K, Gielen I, Koole M, et al. Regional brain perfusion in 10 normal dogs measured using Technetium-99m ethyl cysteinate dimer spect. *Vet Radiol Ultrasound* (2001) 42(6):562–8. doi:10.1111/j.1740-8261.2001.tb00987.x
28. Martlé V, Peremans K, Audenaert K, Vermeire S, Bhatti S, Gielen I, et al. Regional brain perfusion in epileptic dogs evaluated by technetium-99m-ethyl cysteinate dimer SPECT. *Vet Radiol Ultrasound* (2009) 50(6):655–9. doi:10.1111/j.1740-8261.2009.01600.x
29. Martlé V, Peremans K, Van Ham L, Vermeire S, Waelbers T, Dobbeleir A, et al. High-resolution micro-SPECT to evaluate the regional brain perfusion in the adult Beagle dog. *Res Vet Sci* (2013) 94(3):701–6. doi:10.1016/j.rvsc.2012.11.005
30. James FMK, Cortez MA, Monteith G, Jokinen TS, Sanders S, Wielaender F, et al. Diagnostic utility of wireless video-electroencephalography in unsedated dogs. *J Vet Intern Med* (2017) 31(5):1469–76. doi:10.1111/jvim.14789
31. Coles LD, Patterson EE, Sheffield WD, Mavoori J, Higgins J, Michael B, et al. Feasibility study of a caregiver seizure alert system in canine epilepsy. *Epilepsy Res* (2013) 106(3):456–60. doi:10.1016/j.eplepsyres.2013.06.007
32. Howbert JJ, Patterson EE, Stead SM, Brinkmann B, Vasoli V, Crepeau D, et al. Forecasting seizures in dogs with naturally occurring epilepsy. *PLoS One* (2014) 9(1):e81920. doi:10.1371/journal.pone.0081920
33. Lee MS, Ko J, Lee AR, Lee IH, Jung MA, Austin B, et al. Effects of anesthetic protocol on normal canine brain uptake of 18F-FDG assessed by PET/CT. *Vet Radiol Ultrasound* (2010) 51(2):130–5. doi:10.1111/j.1740-8261.2009.01636.x
34. Waelbers T, Peremans K, Vermeire S, Duchateau L, Dobbeleir A, Audenaert K, et al. The effect of medetomidine on the regional cerebral blood flow in dogs measured using technetium-99m-ethyl cysteinate dimer SPECT. *Res Vet Sci* (2011) 91(1):138–43. doi:10.1016/j.rvsc.2010.08.003
35. Theodore WH. Antiepileptic drugs and cerebral glucose metabolism. *Epilepsia* (1988) 29(Suppl 2):S48–55. doi:10.1111/j.1528-1157.1988.tb05797.x
36. Schmidt MJ, Amort KH, Failing K, Klingler M, Kramer M, Ondreka N. Comparison of the endocranial- and brain volumes in brachycephalic dogs, mesaticephalic dogs and Cavalier King Charles spaniels in relation to their body weight. *Acta Vet Scand* (2014) 56:30. doi:10.1186/1751-0147-56-30
37. Schmidt MJ, Kampschulte M, Enderlein S, Gorgas D, Lang J, Ludewig E, et al. The relationship between brachycephalic head features in modern Persian cats and dysmorphologies of the skull and internal hydrocephalus. *J Vet Intern Med* (2017) 31(5):1487–501. doi:10.1111/jvim.14805
38. Koepp MJ, Årstad E, Bankstahl JP, Dedeurwaerdere S, Friedman A, Potschka H, et al. Neuroinflammation imaging markers for epileptogenesis. *Epilepsia* (2017) 58(Suppl 3):11–9. doi:10.1111/epi.13778
39. Bertoglio D, Verhaeghe J, Dedeurwaerdere S, Gröhn O. Neuroimaging in animal models of epilepsy. *Neuroscience* (2017) 358:277–99. doi:10.1016/j.neuroscience.2017.06.062
40. Pitkänen A, Löscher W, Vezzani A, Becker AJ, Simonato M, Lukasiuk K, et al. Advances in the development of biomarkers for epilepsy. *Lancet Neurol* (2016) 15(8):843–56. doi:10.1016/S1474-4422(16)00112-5
41. Galovic M, Koepp M. Advances of molecular imaging in epilepsy. *Curr Neurol Neurosci Rep* (2016) 16(6):58. doi:10.1007/s11910-016-0660-7
42. Lane SB, Bunch SE. Medical management of recurrent seizures in dogs and cats. *J Vet Intern Med* (1990) 4(1):26–39. doi:10.1111/j.1939-1676.1990.tb00871.x

43. Potschka H, Fischer A, Loscher W, Patterson N, Bhatti S, Berendt M, et al. International veterinary epilepsy task force consensus proposal: outcome of therapeutic interventions in canine and feline epilepsy. *BMC Vet Res* (2015) 11:177. doi:10.1186/s12917-015-0465-y
44. Hasegawa D. Diagnostic techniques to detect the epileptogenic zone: pathophysiological and presurgical analysis of epilepsy in dogs and cats. *Vet J* (2016) 215:64–75. doi:10.1016/j.tvjl.2016.03.005
45. Jupp B, Williams J, Binns D, Hicks RJ, Cardamone L, Jones N, et al. Hypometabolism precedes limbic atrophy and spontaneous recurrent seizures in a rat model of TLE. *Epilepsia* (2012) 53(7):1233–44. doi:10.1111/j.1528-1167.2012.03525.x
46. Lee EM, Park GY, Im KC, Kim ST, Woo CW, Chung JH, et al. Changes in glucose metabolism and metabolites during the epileptogenic process in the lithium-pilocarpine model of epilepsy. *Epilepsia* (2012) 53(5):860–9. doi:10.1111/j.1528-1167.2012.03432.x
47. Shultz SR, Cardamone L, Liu YR, Hogan RE, Maccotta L, Wright DK, et al. Can structural or functional changes following traumatic brain injury in the rat predict epileptic outcome? *Epilepsia* (2013) 54(7):1240–50. doi:10.1111/epi.12223
48. Zhang L, Guo Y, Hu H, Wang J, Liu Z, Gao F. FDG-PET and NeuN-GFAP immunohistochemistry of hippocampus at different phases of the pilocarpine model of temporal lobe epilepsy. *Int J Med Sci* (2015) 12(3):288–94. doi:10.7150/ijms.10527
49. Lavisse S, Guillermier M, Hérard AS, Petit F, Delahaye M, Van Camp N, et al. Reactive astrocytes overexpress TSPO and are detected by TSPO positron emission tomography imaging. *J Neurosci* (2012) 32(32):10809–18. doi:10.1523/JNEUROSCI.1487-12.2012
50. Boutin H, Murray K, Pradillo J, Maroy R, Smigova A, Gerhard A, et al. 18F-GE-180: a novel TSPO radiotracer compared to 11C-R-PK11195 in a preclinical model of stroke. *Eur J Nucl Med Mol Imaging* (2015) 42(3):503–11. doi:10.1007/s00259-014-2939-8
51. Brackhan M, Bascuñana P, Postema JM, Ross TL, Bengel FM, Bankstahl M, et al. Serial quantitative TSPO-targeted PET reveals peak microglial activation up to 2 weeks after an epileptogenic brain insult. *J Nucl Med* (2016) 57(8):1302–8. doi:10.2967/jnumed.116.172494
52. Bertoglio D, Verhaeghe J, Santermans E, Amhaoul H, Jonckers E, Wyffels L, et al. Non-invasive PET imaging of brain inflammation at disease onset predicts spontaneous recurrent seizures and reflects comorbidities. *Brain Behav Immun* (2017) 61:69–79. doi:10.1016/j.bbi.2016.12.015
53. Bogdanović RM, Syvänen S, Michler C, Russmann V, Eriksson J, Windhorst AD, et al. (R)-[11C]PK11195 brain uptake as a biomarker of inflammation and antiepileptic drug resistance: evaluation in a rat epilepsy model. *Neuropharmacology* (2014) 85:104–12. doi:10.1016/j.neuropharm.2014.05.002
54. Gershen LD, Zanotti-Fregonara P, Dustin IH, Liow JS, Hirvonen J, Kreisl WC, et al. Neuroinflammation in temporal lobe epilepsy measured using positron emission tomographic imaging of translocator protein. *JAMA Neurol* (2015) 72(8):882–8. doi:10.1001/jamaneurol.2015.0941
55. Hirvonen J, Kreisl WC, Fujita M, Dustin I, Khan O, Appel S, et al. Increased in vivo expression of an inflammatory marker in temporal lobe epilepsy. *J Nucl Med* (2012) 53(2):234–40. doi:10.2967/jnumed.111.091694
56. Friedman A, Heinemann U. Role of blood-brain barrier dysfunction in epileptogenesis. In: Noebels JL, Avoli M, Rogawski MA, Olsen RW, Delgado-Escueta AV, editors. *Jasper's Basic Mechanisms of the Epilepsies*. Bethesda MD: Oxford University Press (2012).
57. van Vliet EA, da Costa Araújo S, Redeker S, van Schaik R, Aronica E, Gorter JA. Blood-brain barrier leakage may lead to progression of temporal lobe epilepsy. *Brain* (2007) 130(Pt 2):521–34. doi:10.1093/brain/awl318
58. Breuer H, Meier M, Schneefeld S, Härtig W, Wittneben A, Märkel M, et al. Multimodality imaging of blood-brain barrier impairment during epileptogenesis. *J Cereb Blood Flow Metab* (2017) 37(6):2049–61. doi:10.1177/0271678X16659672
59. van Vliet EA, Otte WM, Gorter JA, Dijkhuizen RM, Wadman WJ. Longitudinal assessment of blood-brain barrier leakage during epileptogenesis in rats. A quantitative MRI study. *Neurobiol Dis* (2014) 63:74–84. doi:10.1016/j.nbd.2013.11.019
60. Garrigue P, Giacomino L, Bucci C, Muzio V, Filannino MA, Sabatier F, et al. Single photon emission computed tomography imaging of cerebral blood flow, blood-brain barrier disruption, and apoptosis time course after focal cerebral ischemia in rats. *Int J Stroke* (2016) 11(1):117–26. doi:10.1177/1747493015607516
61. Gilad R, Lampl Y, Eilam A, Boaz M, Loyberboim M. SPECT-DTPA as a tool for evaluating the blood-brain barrier in post-stroke seizures. *J Neurol* (2012) 259(10):2041–4. doi:10.1007/s00415-012-6445-2
62. Ranga A, Agarwal Y, Garg KJ. Gadolinium based contrast agents in current practice: risks of accumulation and toxicity in patients with normal renal function. *Indian J Radiol Imaging* (2017) 27(2):141–7. doi:10.4103/0971-3026.209212
63. Runge VM. Critical questions regarding gadolinium deposition in the brain and body after injections of the gadolinium-based contrast agents, safety, and clinical recommendations in consideration of the EMA's pharmacovigilance and risk assessment committee recommendation for suspension of the marketing authorizations for 4 linear agents. *Invest Radiol* (2017) 52(6):317–23. doi:10.1097/RLI.0000000000000374
64. Löscher W, Potschka H. Drug resistance in brain diseases and the role of drug efflux transporters. *Nat Rev Neurosci* (2005) 6(8):591–602. doi:10.1038/nrn1728
65. Jambroszyk M, Tipold A, Potschka H. Add-on treatment with verapamil in pharmacoresistant canine epilepsy. *Epilepsia* (2011) 52(2):284–91. doi:10.1111/j.1528-1167.2010.02886.x
66. Pekcec A, Unkrüer B, Stein V, Bankstahl JP, Soerensen J, Tipold A, et al. Over-expression of P-glycoprotein in the canine brain following spontaneous status epilepticus. *Epilepsy Res* (2009) 83(2–3):144–51. doi:10.1016/j.eplepsyres.2008.10.010
67. Brandt C, Bethmann K, Gastens AM, Löscher W. The multidrug transporter hypothesis of drug resistance in epilepsy: proof-of-principle in a rat model of temporal lobe epilepsy. *Neurobiol Dis* (2006) 24(1):202–11. doi:10.1016/j.nbd.2006.06.014
68. van Vliet EA, van Schaik R, Edelbroek PM, Redeker S, Aronica E, Wadman WJ, et al. Inhibition of the multidrug transporter P-glycoprotein improves seizure control in phenytoin-treated chronic epileptic rats. *Epilepsia* (2006) 47(4):672–80. doi:10.1111/j.1528-1167.2006.00496.x
69. Bankstahl JP, Bankstahl M, Kuntner C, Stanek J, Wanek T, Meier M, et al. A novel positron emission tomography imaging protocol identifies seizure-induced regional overactivity of P-glycoprotein at the blood-brain barrier. *J Neurosci* (2011) 31(24):8803–11. doi:10.1523/JNEUROSCI.6616-10.2011
70. Feldmann M, Asselin MC, Liu J, Wang S, McMahon A, Anton-Rodriguez J, et al. P-glycoprotein expression and function in patients with temporal lobe epilepsy: a case-control study. *Lancet Neurol* (2013) 12(8):777–85. doi:10.1016/S1474-4422(13)70109-1
71. Ryvlin P, Bouvard S, Le Bars D, De Lamérie G, Grégoire MC, Kahane P, et al. Clinical utility of flumazenil-PET versus [18F]fluorodeoxyglucose-PET and MRI in refractory partial epilepsy. A prospective study in 100 patients. *Brain* (1998) 121(Pt 11):2067–81. doi:10.1093/brain/121.11.2067
72. Vivash L, Gregoire MC, Lau EW, Ware RE, Binns D, Roselt P, et al. 18F-flumazenil: a gamma-aminobutyric acid A-specific PET radiotracer for the localization of drug-resistant temporal lobe epilepsy. *J Nucl Med* (2013) 54(8):1270–7. doi:10.2967/jnumed.112.107359

Conflict of Interest Statement: The authors declare that the research was conducted in the absence of any commercial or financial relationships that could be construed as a potential conflict of interest.

frontiers in Veterinary Science

ORIGINAL RESEARCH
published: 08 November 2017
doi: 10.3389/fvets.2017.00183

A Subset of Dogs with Presumptive Idiopathic Epilepsy Show Hippocampal Asymmetry: A Volumetric Comparison with Non-Epileptic Dogs Using MRI

Chelsie M. Estey[1], Curtis W. Dewey[1], Mark Rishniw[1], David M. Lin[2], Jennifer Bouma[3], Joseph Sackman[4] and Erica Burkland[1]*

[1] Department of Clinical Sciences, Cornell University Hospital for Animals, Ithaca, NY, United States, [2] Department of Biomedical Sciences, Cornell University, Ithaca, NY, United States, [3] Rochester Veterinary Specialists, Rochester, NY, United States, [4] Long Island Veterinary Specialists, Plainview, NY, United States

OPEN ACCESS

Edited by:
Steven De Decker, Royal Veterinary College, United Kingdom

Reviewed by:
Rowena Mary Anne Packer, Royal Veterinary College, United Kingdom
Daisuke Hasegawa, Nippon Veterinary and Life Science University, Japan

***Correspondence:**
Curtis W. Dewey
cwd27@cornell.edu

Specialty section:
This article was submitted to Veterinary Neurology and Neurosurgery, a section of the journal Frontiers in Veterinary Science

Received: *14 July 2017*
Accepted: *11 October 2017*
Published: *08 November 2017*

Citation:
Estey CM, Dewey CW, Rishniw M, Lin DM, Bouma J, Sackman J and Burkland E (2017) A Subset of Dogs with Presumptive Idiopathic Epilepsy Show Hippocampal Asymmetry: A Volumetric Comparison with Non-Epileptic Dogs Using MRI. Front. Vet. Sci. 4:183. doi: 10.3389/fvets.2017.00183

MRI-acquired volumetric measurements from 100 dogs with presumptive idiopathic epilepsy (IE) and 41 non-epileptic (non-IE) dogs were used to determine if hippocampal asymmetry exists in the IE as compared to the non-IE dogs. MRI databases from three institutions were searched for dogs that underwent MRI of the brain and were determined to have IE and those that were considered non-IE dogs. Volumes of the right and left hippocampi were measured using Mimics® software. Median hippocampal volumes of IE and non-IE dogs were 0.47 and 0.53 cm^3, respectively. There was no significant difference in overall hippocampal volume between IE and non-IE dogs; however, IE dogs had greater hippocampal asymmetry than non-IE dogs ($P < 0.012$). A threshold value of 1.16 from the hippocampal ratio had an 85% specificity for identifying IE-associated asymmetry. Thirty five percent of IE dogs had a hippocampal ratio >1.16. Asymmetry was not associated with any particular hemisphere ($P = 0.67$). Our study indicates that hippocampal asymmetry occurs in a subset of dogs with presumptive idiopathic/genetic epilepsy, suggesting a structural etiology to some cases of IE.

Keywords: epilepsy, hippocampus, MRI, dog, asymmetry

INTRODUCTION

Idiopathic epilepsy (IE) is the most commonly diagnosed canine neurologic disorder in veterinary medicine (1). Almost half of all dogs presenting for seizures are subsequently diagnosed with IE, and in one study IE was diagnosed in 75% of dogs with an onset of seizures before 1 year of age (2, 3). Approximately 25–30% of dogs treated for IE are refractory to treatment or are poorly controlled, often requiring multiple anticonvulsant drugs (4). Moreover, epileptic dogs that exhibit cluster seizures or status epilepticus have shorter lifespans than those that do not experience these episodes (3, 5, 6). Finally, many breeds are susceptible to IE, but how epilepsy in different breeds differs is poorly understood (4).

Our understanding of epilepsy in dogs, and how many forms of epilepsy might exist, is still rudimentary. Consequently, our inability to accurately diagnose the type of epilepsy in affected

dogs likely hampers our ability to optimally treat these patients. Ion channels, particularly calcium and sodium channels, play an important role in maintaining cellular and electrical homeostasis in the brain. Mutations in genes encoding these ion channels result in epilepsy in humans by causing ion channel dysfunction (7–9). It is suspected that similar channelopathies exist in epileptic dogs, and the majority of anticonvulsant drugs used in humans and dogs have mechanisms of action involving ion channels (4). However, despite advances in anticonvulsant medications over the years, a substantial subset of epileptic dogs (between 25 and 30%) are refractory to these drugs (4).

In humans, a population of epileptics with focal abnormalities of brain architecture has been well-documented. These patients have what is often referred to as localization-related epilepsy, the most common example of which is temporal lobe epilepsy, particularly mesial temporal lobe epilepsy (mTLE) (10, 11). mTLE is the most common type of localization-related epilepsy in people (10, 12) and is characterized by hippocampal sclerosis (HS), due to atrophy of the hippocampal gray matter (13, 14). Characteristic histopathological features of HS include neuronal loss, astrogliosis, granule cell dispersion, and mossy fiber sprouting (15, 16). Although imaging and pathological features of mTLE and HS have been described in some detail in people, the etiology of this subset of epileptics is not entirely clear and likely represents a number of different abnormalities with a similar phenotypic expression (15, 16). Overall, it has not been definitively determined if the anatomic and histopathologic abnormalities that typify mTLE/HS are a cause or a result of excessive seizure activity, or some combination thereof (15, 16). Multiple causative factors have been implicated in the development of human mTLE/HS, including febrile seizures, brain trauma, inflammatory brain conditions, as well as genetic and epigenetic factors; it is likely that many cases may be multifactorial with regard to cause (15–19). Regardless of cause, the abnormal hippocampus is structurally and functionally connected to the adjacent mesial temporal lobe, and these structures are believed to develop an epileptic circuit (20). MRI can detect focal changes in brain architecture that can provide clues regarding etiology and treatment; this is visible as a change in the volume of a given region of the brain (14). The prevalence of mTLE/HS is high enough that automated quantitative measurement techniques have been developed to detect hippocampal asymmetry (21). This identification has important treatment implications, as patients with mTLE with HS are often refractory to anticonvulsant drug therapy (10). Despite this drug refractoriness, surgical resection of the seizure focus (temporal lobe with or without hippocampal tissue) has a very high success rate in mTLE/HS people who are refractory to drug therapy (12, 22–27).

Currently, minimal information exists regarding location-dependent changes observed on MRIs from epileptic dogs (28). If a population of dogs with location-dependent epilepsy exists, surgical intervention could offer an alternative treatment for effective management of this type of epilepsy. Therefore, we sought to characterize hippocampal asymmetry in a large cohort of dogs with IE using volumetric imaging software and to compare asymmetry in this population with non-IE dogs. Furthermore, we sought to identify a subset of dogs with IE that might demonstrate substantial hippocampal asymmetry.

MATERIALS AND METHODS

MRI databases from three institutions (Cornell University Hospital for Animals, Long Island Veterinary Specialists, and Rochester Veterinary Specialists) were searched for dogs that underwent MRI of the brain and were determined to have IE and those that were considered non-IE dogs. The diagnosis of IE was based on characteristic clinical features of the disorder (i.e., recurrent seizures with normal neurological examination interictally and normal bloodwork), combined with normal MRI results. The non-IE group consisted of dogs that were imaged for ear disease, nasal disease, vestibular disease, and cranial nerve deficits. Medical records were reviewed and animals were excluded from the study if their clinical signs did not fit with a presumptive diagnosis of IE or had a multifocal neurolocalization. Animals were excluded from the non-epileptic (non-IE) group if they had centralizing neurologic signs or had any intracranial lesions on MRI.

All MRIs were performed under general anesthesia with either a 1.0 T (Siemens Magnetom Harmony, 1.0 T, Munich, Germany), 1.5 T (Philips Achieva, 3.0 T, NJ, USA), or 3.0 T unit (Toshiba Vantage Elan, 1.5 T, CA, USA). Imaging sequences were obtained in transverse (T2 fluid-attenuated inversion recovery (FLAIR), T2- and T1-weighted, and T1-weighted post-gadolinium sequences), sagittal (T2- and T1-weighted post-gadolinium sequences), and dorsal planes (T1-weighted post-gadolinium sequence). For the 1.0 and 1.5-T MRI units, measurement parameters were as follows: slice thickness, 3.5 mm; slice gap, 3.5 mm; FOV, 185 mm; matrix size of images, 480 × 480. For the 3.0-T MRI unit, measurement parameters were as follows: slice thickness, 2.0 mm; slice gap, 1.0–3.0 mm (depending on dog size); FOV, 1101 mm; matrix size of images, 400 × 400.

For each dog, three-dimensional volumes were measured using Mimics® software by one observer (Joseph Sackman) who was unaware of the status of the dogs in the study. Quantitative volumetric measurements comparing the right and left hippocampi were made for each T2-weighted slice to obtain the full anatomic boundaries these structures (**Figure 1**). The anatomic landmarks for the measurements were used from published reference information (29, 30). Each structure was measured rostral to caudal using a technique of selecting the specific pixels associated with that structure per slice. Within each slice, pixels are painted with a selection tool that distinguishes them from the rest of the image. Once all pixels are selected in each slice, the software can then render a three-dimensional representation of the structure. Volume data are then derived from this representation. We used a simple body-size-independent measure of hippocampal asymmetry by obtaining the ratio of the larger hippocampal volume to the smaller hippocampal volume. Perfect symmetry would result in a ratio of 1.0, with increasing asymmetry being represented by values increasingly greater than 1.0. Because previous investigators had used a normalization technique (absolute difference divided by the greater of the two hippocampi), we also evaluated our data using this method (28).

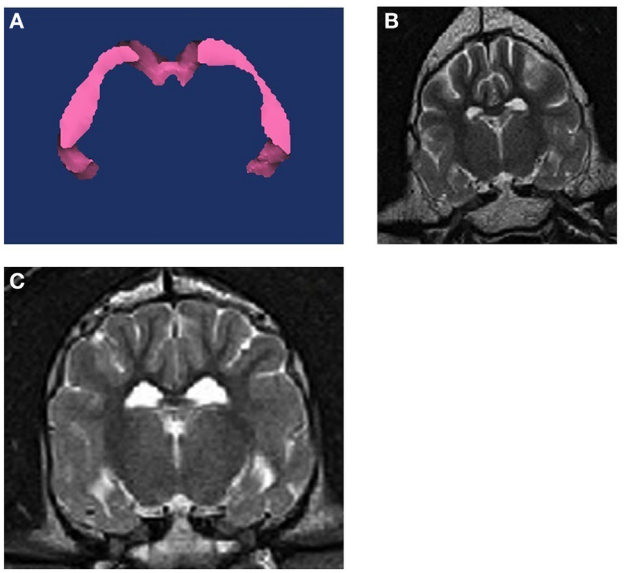

FIGURE 1 | **(A)** 3D volumetric analysis of the hippocampus. **(B)** T2W transverse MRI image at the level of the hippocampus from a non-epileptic dog. **(C)** T2W transverse MRI image at the level of the hippocampus from an epileptic dog. The right hippocampus and temporal lobe region is notably smaller on the right side of the brain.

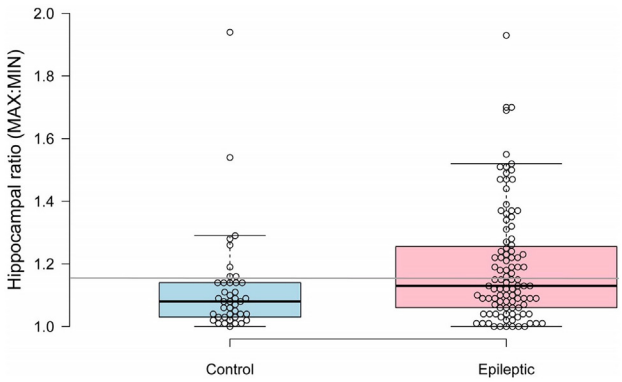

FIGURE 2 | Scatterplot comparing hippocampal ratios between non-epileptic and epileptic dogs. A threshold value of 1.16 (denoted by gray horizontal line) had an 85% sensitivity for identifying idiopathic epilepsy-associated asymmetry.

Descriptive statistics were provided for estimates of hippocampal volume differences for both IE and non-IE dogs. Data were examined for normality by a Shapiro–Wilk test for each group. Because the data were not normally distributed, comparisons of hippocampal asymmetry between groups were performed using a Mann–Whitney *U* test. To determine if asymmetry in dogs with IE was biased to one side or the other, we compared the proportion of asymmetry on the right side using a *z*-test against a nominal value of 0.5. A *P*–value <0.05 was considered significant. Receiver operating characteristic analysis was used to identify a threshold for hippocampal asymmetry that would reliably separate dogs with hippocampal asymmetry from dogs without hippocampal asymmetry. We then used this threshold value to examine the specificity of identifying epilepsy-associated asymmetry.

To examine repeatability of MRI measurements, 20 patient scans were randomly selected (using a random number generator) and all variables were re-measured by the single observer (Joseph Sackman), who was blinded to the previous measurements for the cases. Agreement between repeated measurements was examined using Limits of Agreement analysis (31).

RESULTS

We included 100 dogs with IE and 41 non-IE dogs in the study. The median age of the IE dogs was 60 months and that of the non-IE dogs was 86 months. Non-IE dogs were older than IE dogs at the time of MRI ($P = 0.01$), but had similar distributions of sex (44% male and 56% female in each group) and proportions of purebred dogs (75 vs 82%).

Median hippocampal volumes of IE and non-IE dogs were 0.47 and 0.53 cm^3, respectively. There was no significant difference in overall hippocampal volumes between the two groups ($P = 0.117$). Epileptic dogs had greater hippocampal ratios than non-IE dogs ($P = 0.012$, **Figure 1**). The ROC analysis identified a threshold hippocampal ratio of 1.14 as the optimal discriminating value. Using this threshold value, 47% of IE dogs and 20% of non-IE dogs would be considered to have asymmetry, resulting in a specificity for identifying epilepsy-associated hippocampal asymmetry of 85%. To slightly improve the specificity, we increased the threshold hippocampal ratio to 1.16. Using this higher ratio, 42% of IE dogs and 15% of non-IE dogs would be considered to have hippocampal asymmetry ($P = 0.002$), resulting in a specificity for identifying epilepsy-associated hippocampal asymmetry of 87% (**Figure 2**.). Hippocampal asymmetry was not biased to one hemisphere ($P = 0.8$).

Epileptic dogs had greater normalized hippocampal differences than non-IE dogs (median normalized difference 11.6 vs 7.1%). Using the historical threshold of 6% to denote asymmetry (15), 73% of IE dogs and 58% of non-IE dogs would be considered to have hippocampal asymmetry, resulting in 75% specificity for identifying epilepsy-associated hippocampal asymmetry. Conversely, using a normalized hippocampal difference >12.6% to denote asymmetry, 48% of IE dogs, and 20% of non-IE dogs would be considered to have hippocampal asymmetry, resulting in 86% specificity for identifying epilepsy-associated hippocampal asymmetry.

The observer performing the measurements of brain volume showed measurement repeatability for total hippocampal volumes to within approximately 40 voxels, representing a median% difference of 5.2% for the 20 randomly selected cases, without noticeable fixed or proportional bias.

DISCUSSION

Our study shows that dogs with IE have greater hippocampal asymmetry than non-IE dogs, and that a greater proportion of epileptic than non-IE dogs have hippocampal ratios indicative

of asymmetry using criteria similar to those in humans. The lack of significant difference between IE and non-IE groups with regard to overall hippocampal volume emphasizes the utility of analyzing hippocampal asymmetry using ratios vs total volumes. Whether the subset of epileptic dogs with hippocampal asymmetry (approximately 40%) has particular clinical or pathological characteristics (e.g., increased refractoriness to anticonvulsant therapy, temporal lobe epilepsy) remains to be determined. Due to the retrospective nature of this study, the authors were unable to obtain accurate clinical data regarding seizure control for the majority of IE dogs; because of this limitation, it was decided to focus the current study only on volumetric imaging and to pursue possible correlates between hippocampal asymmetry and drug refractoriness in IE dogs in a future prospective investigation.

Our findings are similar to but expand on those of previous investigators (28). Using similar methods to identify asymmetry as those investigators, our data differ in terms of the magnitude of asymmetry in IE and non-IE dogs and in terms of proportions of dogs with asymmetry in each group. Our data suggest that a threshold value of 6% for a normalized difference is likely too small to accurately identify hippocampal asymmetry and that a value of 12.6% more accurately identifies IE dogs. Similarly, we would propose a hippocampal ratio of 1.16–1.2 to define hippocampal asymmetry in epileptic dogs.

Hippocampal sclerosis is the most common neuropathological change encountered in human patients with mTLE. The causative factors of mTLE/HS have not been fully elucidated, and there are believed to be a number of subtypes of this disorder, with different etiologies (15, 16). Human patients affected by TLE/HS often present with seizures refractory to drug therapy, which are often amenable to surgical resection of the epileptogenic focus. Hippocampal asymmetry, resulting from unilateral HS, is present in 60–70% of patients with mTLE who pursue surgical treatment of refractory seizures (21). In these refractory patients, surgical treatment is associated with abolition of seizures or a significant reduction in seizure frequency in the majority of these patients (32–35) Therefore, the identification of hippocampal asymmetry in IE dogs, especially those refractory to anticonvulsant therapy, might encourage neurosurgeons to consider resection of the temporal lobe on the affected side. Because radical cerebral resection can be performed in dogs with minimal lasting effects (36), surgical intervention in these patients, if successful, could provide an alternative to life-long anticonvulsant therapy, poor seizure control, and the attendant emotional and financial impacts on the owner. As is the case with human epilepsy, poor seizure control and adverse effects of anticonvulsant medication have been shown to be significantly correlated with poor quality of life in dogs with IE, as perceived by owners (37–39). In addition, the negative impacts of IE on the daily life of epileptic dog owners have been documented (40). Whether this subset of dogs with hippocampal asymmetry would benefit from surgical intervention remains speculative at present. Additional histopathological studies of this subset of dogs, to confirm that HS is in fact present, are warranted. In addition, prospective investigation into the nature of seizure activity (i.e., refractory vs non-refractory) in dogs with hippocampal asymmetry is necessary. Further study into the nature of canine mTLE/HS may also help to elucidate causative factors of the condition. Specifically, considering that genetic and epigenetic factors have been implicated in human mTLE/HS, studying individual canine breeds that are prone to refractory epilepsy (and demonstrate hippocampal asymmetry) may lead to discovery of causative genetic disorders and/or molecular mechanisms of disease development.

Our study sets the stage for further evaluation of a subset of dogs with IE that appear to have hippocampal asymmetry. Future prospective imaging studies are planned in order to further investigate more detailed features of hippocampal and temporal lobe differences in dogs with hippocampal asymmetry, using advanced MR sequences such as tractography. If our hypothesis, that these dogs might have surgically amenable location-specific epileptogenic foci, is correct, seizure management in a sizeable proportion of epileptic dogs might take a large step forward.

AUTHOR'S NOTE

Presented in abstract form at the 2014 American College of Veterinary Radiology Annual Scientific Meeting, St. Louis, Missouri, October 2014.

AUTHOR CONTRIBUTIONS

CD—inception and supervision of project, involved in case collection, and manuscript preparation. CE—organization and collating data, writing manuscript, and literature search (resident project). MR—data analysis, statistics, manuscript review, and revision. JS—data collection, volumetric measurements, collating and organizing data. JB—evaluating MR images, manuscript preparation, and review. DL—involved in inception and supervision of project, and manuscript review. EB—assisted in data collection and organization, and manuscript review.

FUNDING

The authors received financial support from the Cornell University College of Veterinary Medicine's internal grants program for the research, authorship, and/or publication of this article.

REFERENCES

1. Podell M, Fenner WR, Powers JD. Seizure classification in dogs from a nonreferral-based population. *J Am Vet Med Assoc* (1995) 206:1721–8.
2. Zimmermann R, Hulsmeyer V, Sauter-Louis C, Fischer A. Status epilepticus and epileptic seizures in dogs. *J Vet Intern Med* (2009) 23:970–6. doi:10.1111/j.1939-1676.2009.0368.x
3. Arrol L, Penderis J, Garosi L, Cripps P, Gutierrez-Quintana R, Gonçalves R. Aetiology and long-term outcome of juvenile epilepsy in 136 dogs. *Vet Rec* (2012) 170:335. doi:10.1136/vr.100316
4. Thomas WB. Idiopathic epilepsy in dogs and cats. *Vet Clin North Am Small Anim Pract* (2010) 40:161–79. doi:10.1016/j.cvsm.2009.09.004
5. Saito M, Munana KR, Sharp NJ, Olby NJ. Risk factors for development of status epilepticus in dogs with idiopathic epilepsy and effects of status epilepticus

on outcome and survival time: 32 cases (1990-1996). *J Am Vet Med Assoc* (2001) 219:618–23. doi:10.2460/javma.2001.219.618
6. Monteiro R, Adams V, Keys D, Platt SR. Canine idiopathic epilepsy: prevalence, risk factors and outcome associated with cluster seizures and status epilepticus. *J Small Anim Pract* (2012) 53:526–30. doi:10.1111/j.1748-5827.2012.01251.x
7. Heron SE, Scheffer IE, Berkovic SF, Dibbens LM, Mulley JC. Channelopathies in idiopathic epilepsy. *Neurotherapeutics* (2007) 4:295–304. doi:10.1016/j.nurt.2007.01.009
8. Nicita F, De Liso P, Danti FR, Papetti L, Ursitti F, Castronovo A, et al. The genetics of monogenic idiopathic epilepsies and epileptic encephalopathies. *Seizure* (2012) 21:3–11. doi:10.1016/j.seizure.2011.08.007
9. Seppälä EH, Jokinen TS, Fukata M, Fukata Y, Webster MT, Karlsson EK, et al. LGI2 truncation causes a remitting focal epilepsy in dogs. *PLoS Genet* (2011) 7:e1002194. doi:10.1371/journal.pgen.1002194
10. Hammers A, Heckemann R, Koepp MJ, Duncan JS, Hajnal JV, Rueckert D, et al. Automatic detection and quantification of hippocampal atrophy on MRI in temporal lobe epilepsy: a proof-of-principle study. *Neuroimage* (2007) 36:38–47. doi:10.1016/j.neuroimage.2007.02.031
11. Velez-Ruiz NJ, Klein JP. Neuroimaging in the evaluation of epilepsy. *Semin Neurol* (2012) 32:361–73. doi:10.1055/s-0032-1331809
12. Asadi-Pooya AA, Stewart GR, Abrams DJ, Sharan A. Prevalence and incidence of drug-resistant mesial temporal lobe epilepsy in the United States. *World Neurosurg* (2017) 99:662–6. doi:10.1016/j.wneu.2016.12.074
13. Berkovic SF, Andermann F, Olivier A, Ethier R, Melanson D, Robitaille Y, et al. Hippocampal sclerosis in temporal lobe epilepsy demonstrated by magnetic resonance imaging. *Ann Neurol* (1991) 29:175–82. doi:10.1002/ana.410290210
14. Jackson GD, Berkovic SF, Tress BM, Kalnins RM, Fabinyi GC, Bladin PF. Hippocampal sclerosis can be reliably detected by magnetic resonance imaging. *Neurology* (1990) 40:1869–75. doi:10.1212/WNL.40.12.1869
15. Cendes F, Sakamoto AC, Spreafico R, Bingaman W, Becker AJ. Epilepsies associated with hippocampal sclerosis. *Acta Neuropathol* (2014) 128:21–37. doi:10.1007/s00401-014-1292-0
16. Danis B, van Rikxoort M, Kretschmann A, Zhang J, Godard P, Andonovic L, et al. Differential expression of miR-184 in temporal lobe epilepsy patients with and without hippocampal sclerosis-influence on microglial function. *Sci Rep* (2016) 6:33943. doi:10.1038/srep33943
17. Xiao Z, Peng J, Gan N, Arafat A, Yin F. Interleukin-1β plays a pivotal role via the P13K/Akt/mTOR signaling pathway in the chronicity of mesial temporal lobe epilepsy. *Neuroimmunomodulation* (2016) 23:332–44. doi:10.1159/000460254
18. Bencurova P, Baloun J, Musilova K, Radova L, Tichy B, Pail M, et al. MicroRNA and mesial temporal lobe epilepsy with hippocampal sclerosis: whole miRNome profiling of human hippocampus. *Epilepsia* (2017) 58(10):1782–93. doi:10.1111/epi.13870
19. Leal B, Chaves J, Carvalho C, Bettencourt A, Brito C, Boleixa D, et al. Immunogenetic predisposing factors for mesial temporal lobe epilepsy with hippocampal sclerosis. *Int J Neurosci* (2017):1–16. doi:10.1080/00207454.2017.1349122
20. Shih YC, Tseng CE, Lin FH, Liou HH, Tseng WY. Hippocampal atrophy is associated with altered hippocampus-posterior cingulate cortex connectivity in mesial temporal lobe epilepsy with hippocampal sclerosis. *AJNR Am J Neuroradiol* (2017) 38:626–32. doi:10.3174/ajnr.A5039
21. Farid N, Girard HM, Kemmotsu N, Smith ME, Magda SW, Lim WY, et al. Temporal lobe epilepsy: quantitative MR volumetry in detection of hippocampal atrophy. *Radiology* (2012) 264:542–50. doi:10.1148/radiol.12112638
22. Wieshmann UC, Larkin D, Varma T, Eldridge P. Predictors of outcome after temporal lobectomy for refractory temporal lobe epilepsy. *Acta Neurol Scand* (2008) 118:306–12. doi:10.1111/j.1600-0404.2008.01043.x
23. Elsharkawy AE, Alabbasi AH, Pannek H, Oppel F, Schulz R, Hoppe M, et al. Long-term outcome after temporal lobe epilepsy surgery in 434 consecutive adult patients. *J Neurosurg* (2009) 110:1135–46. doi:10.3171/2008.6.JNS17613
24. Wiebe S, Blume WT, Girvin JP, Eliasziw M. Effectiveness and efficiency of surgery for temporal lobe epilepsy study group. A randomized, controlled trial of surgery for temporal-lobe epilepsy. *N Engl J Med* (2001) 345:311–8. doi:10.1056/NEJM200108023450501
25. Engel J Jr, McDermott MP, Wiebe S, Langfitt JT, Stern JM, Dewar S, et al. Early surgical therapy for drug-resistant temporal lobe epilepsy: a randomized trial. *JAMA* (2012) 307:922–30. doi:10.1001/jama.2012.220
26. Jobst BC, Cascino GD. Resective epilepsy surgery for drug-resistant focal epilepsy: a review. *JAMA* (2015) 313:285–93. doi:10.1001/jama.2014.17426
27. Tellez-Zenteno JF, Dhar R, Wiebe S. Long-term seizure outcomes following epilepsy surgery: a systematic review and meta-analysis. *Brain* (2005) 128:1188–98. doi:10.1093/brain/awh449
28. Kuwabara T, Hasegawa D, Kobayashi M, Fujita M, Orima H. Clinical magnetic resonance volumetry of the hippocampus in 58 epileptic dogs. *Vet Radiol Ultrasound* (2010) 51:485–90. doi:10.1111/j.1740-8261.2010.01700.x
29. Leigh EJ, Mackillop E, Robertson ID, Hudson LC. Clinical anatomy of the canine brain using magnetic resonance imaging. *Vet Radiol Ultrasound* (2008) 49:113–21. doi:10.1111/j.1740-8261.2008.00336.x
30. Milne ME, Anderson GA, Chow KE, O'Brien TJ, Moffat BA, Long SN. Description of technique and lower reference limit for magnetic resonance imaging of hippocampal volumetry in dogs. *Am J Vet Res* (2013) 74:224–31. doi:10.2460/ajvr.74.2.224
31. Bland JM, Altman DG. Measuring agreement in method comparison studies. *Stat Methods Med Res* (1999) 8:136–60. doi:10.1191/096228099673819272
32. Kubova H, Lukasiuk K, Pitkanen A. New insight on the mechanisms of epileptogenesis in the developing brain. *Adv Tech Stand Neurosurg* (2012) 39:3–44. doi:10.1007/978-3-7091-1360-8_1
33. Brooks-Kayal AR, Shumate MD, Jin H, Rikhter TY, Coulter DA. Selective changes in single cell GABA(A) receptor subunit expression and function in temporal lobe epilepsy. *Nat Med* (1998) 4:1166–72. doi:10.1038/2661
34. Berkovic SF, McIntosh AM, Kalnins RM, Jackson GD, Fabinyi GC, Brazenor GA, et al. Preoperative MRI predicts outcome of temporal lobectomy: an actuarial analysis. *Neurology* (1995) 45:1358–63. doi:10.1212/WNL.45.7.1358
35. Salanova V, Markand O, Worth R. Longitudinal follow-up in 145 patients with medically refractory temporal lobe epilepsy treated surgically between 1984 and 1995. *Epilepsia* (1999) 40:1417–23. doi:10.1111/j.1528-1157.1999.tb02014.x
36. Sorjonen DC, Thomas WB, Myers LJ, Cox NR. Radical cerebral cortical resection in dogs. *Prog Vet Neurol* (1991) 2:225–36.
37. Wessman A, Volk HA, Parkin T, Ortega M, Anderson TJ. Evaluation of the quality of life in dogs with idiopathic atrophy. *J Vet Intern Med* (2014) 28:510–4. doi:10.1111/jvim.12328
38. Packer MA, Volk HA. Epilepsy beyond seizures: a review of the impact of epilepsy and its comorbidities on health-related quality of life in dogs. *Vet Rec* (2015) 177:306–15. doi:10.1136/vr.103360
39. Nettifee JA, Munana KR, Griffith EH. Evaluation of the impacts of epilepsy in dogs on their caregivers. *J Am Anim Hosp Assoc* (2017) 53:143–9. doi:10.5326/JAAHA-MS-6537
40. Chang Y, Mellor J, Anderson TJ. Idiopathic epilepsy in dogs: owners' perspectives on management with phenobarbitone and/or potassium bromide. *J Small Anim Pract* (2006) 47:574–81. doi:10.1111/j.1748-5827.2006.00203.x

Conflict of Interest Statement: The authors declared no potential conflicts of interest with respect to the research, authorship, and/or publication of this article.

The reviewer RP and handling editor declared their shared affiliation.

frontiers in Veterinary Science

REVIEW
published: 04 December 2017
doi: 10.3389/fvets.2017.00203

Breed-Specific Magnetic Resonance Imaging Characteristics of Necrotizing Encephalitis in Dogs

*Thomas Flegel**

Department of Small Animal Medicine, University of Leipzig, Leipzig, Germany

Diagnosing necrotizing encephalitis, with its subcategories of necrotizing leukoencephalitis and necrotizing meningoencephalitis, based on magnetic resonance imaging alone can be challenging. However, there are breed-specific imaging characteristics in both subcategories that allow establishing a clinical diagnosis with a relatively high degree of certainty. Typical breed specific imaging features, such as lesion distribution, signal intensity, contrast enhancement, and gross changes of brain structure (midline shift, ventriculomegaly, and brain herniation) are summarized here, using current literature, for the most commonly affected canine breeds: Yorkshire Terrier, French Bulldog, Pug, and Chihuahua.

Keywords: necrotizing encephalitis, necrotizing leucoencephalitis, necrotizing meningoencephalitis, magnetic resonance imaging, breed specific magnetic resonance imaging

OPEN ACCESS

Edited by:
Andrea Tipold,
University of Veterinary Medicine Hannover, Germany

Reviewed by:
Marcin Adam Wrzosek,
Wroclaw University of Environmental and Life Sciences, Poland
Curtis Wells Dewey,
Cornell University, United States

***Correspondence:**
Thomas Flegel
flegel@kleintierklinik.uni-leipzig.de

Specialty section:
This article was submitted to Veterinary Neurology and Neurosurgery, a section of the journal Frontiers in Veterinary Science

Received: *29 August 2017*
Accepted: *17 November 2017*
Published: *04 December 2017*

Citation:
Flegel T (2017) Breed-Specific Magnetic Resonance Imaging Characteristics of Necrotizing Encephalitis in Dogs. Front. Vet. Sci. 4:203. doi: 10.3389/fvets.2017.00203

INTRODUCTION

Necrotizing encephalitis (NE) includes several breed specific inflammatory brain diseases within the group of meningoencephalitis of unknown etiology/etiology (MUA/MUE). Several synonyms exist for MUA (non-infectious encephalitis, immune mediated encephalitis) reflecting the fact that even though these diseases have been known for decades, the underlying pathology is still not completely understood and achieving a definite diagnosis intra vitam is usually difficult. Based on histopathological features MUA can be subdivided into granulomatous meningoencephalomyelitis (GME) and NE, with the latter comprising Necrotizing Leukoencephalitis (NLE) and necrotizing meningoencephalitis (NME). These subtypes of NE are seen in specific breeds with NLE affecting Yorkshire Terriers (1–9) and French Bulldogs (10, 11), whereas NME affects Pugs (12–21), Maltese (22–24), Chihuahuas (24–33), Pekingese (25, 34), Shih Tzus (24, 25, 35), West Highland White Terriers (36), Papillons (23, 35), Coton de Tulears (35), and Brussels Griffons (35).

The often applied practice of using the rather unspecific term of MUA instead of the exact subclassification (GME, NME, or NLE) in imaging diagnostics is due to the fact, that differentiation based on imaging alone can be difficult. This situation is further complicated by the fact that magnetic resonance imaging (MRI) may generally have only moderate sensitivity in detecting inflammatory intracranial pathology. Abnormalities in brain MRI were found in 76% of dogs with inflammatory cerebrospinal fluid (CSF) (37). Therefore, imaging findings should be interpreted

Abbreviations: CSF, cerebrospinal fluid analysis; FDG-PET, fluorine-18 fluorodeoxyglucose; FLAIR, fluid-attenuated inversion recovery; GME, granulomatous meningoencephalomyelitis; MUE, meningoencephalitis of unknown etiology; NE, necrotizing encephalitis; NLE, necrotizing leucoencephalitis; NME, necrotizing meningoencephalitis; MR, magnetic resonance; MRI, magnetic resonance imaging; PET, positron emission tomography; SNE, subacute necrotizing encephalopathy.

under consideration of the CSF analysis results. However, normal CSF was found in 28.6% of dogs with histologically confirmed NLE and in 14.3% of Pugs with histologically confirmed NME (25). Similarly, a normal CSF nucleated cell count was reported in 12.5% of dogs with NE (38). Therefore, a definite diagnosis of encephalitis may often require histological confirmation based on a brain biopsy (31).

Nevertheless, common MRI features for NME and NLE that allow diagnosing these diseases with a relatively high degree of certainty are known. The typical breed specific MRI characteristics of both diseases in the most frequently affected breeds will be presented. All images provided for illustration are obtained from dogs with histologically confirmed diagnoses. The images can illustrate only some features of the specific disease in a given breed. Illustration of all possible MRI characteristics is beyond the scope of this publication.

NLE IN YORKSHIRE TERRIERS

Uni- or bilateral asymmetrical lesions are seen in the telencephalon and diencephalon. The brainstem is often less severely affected. The cerebellum and spinal cord are usually unaffected on magnetic resonance (MR) images even though in rare cases histopathological examination also shows inflammatory foci here (6, 7). Lesion distribution based on MRI has been described in 27 Yorkshire Terrier cases: forebrain ($n = 25$), thalamus ($n = 10$), midbrain ($n = 8$), and caudal brainstem ($n = 10$; 9). Additional syringohydromyelia was seen in 7/27 (26%) dogs. Lesions were multifocal in about 78% of cases. However, diagnosis in these Yorkshire Terriers was described as meningoencephalitis of unknown origin and not as NLE. Therefore, it cannot be ruled out that some of these dogs were affected by other types of encephalitis.

Telencephalic lesions usually affect the periventricular and subcortical white matter, often leaving the overlying cortical gray matter untouched (2, 5). The shape of the lesion may vary from finger-like, following the shape of subcortical white matter, to round-shaped in deep-seated lesions (**Figure 1**). Therefore, asymmetric thalamic lesions are usually round-shaped and well demarcated. They need to be differentiated from bilateral symmetric round lesions in the telencephalon (including basal nuclei), mid-thalamus and brainstem seen in subacute necrotizing encephalopathy (SNE) of Yorkshire Terriers. Signal intensity on T2-weighted and fluid-attenuated inversion recovery (FLAIR) sequences are similar in both NLE and SNE, but symmetry of lesions should clearly point toward SNE [(39, 40); **Figure 2**].

Lesions in NLE are usually hyperintense on T2-weighted and FLAIR images and hypointense to isointense on T1-weighted sequences. These signal intensity characteristics may represent multiple areas of cystic necrosis (41). The secondary white matter

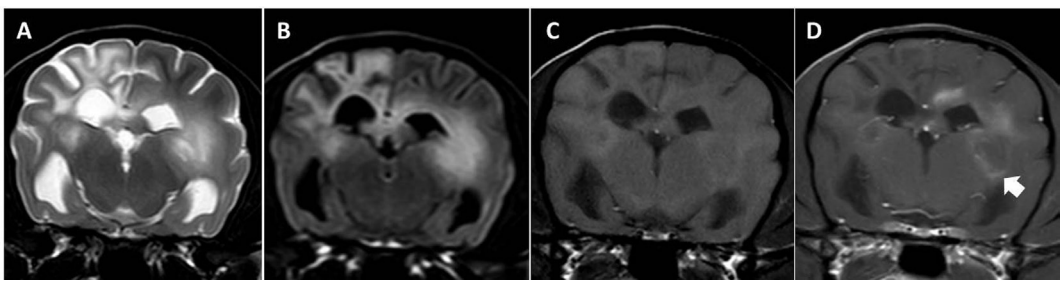

FIGURE 1 | Transverse magnetic resonance images (3 T) of a Yorkshire Terrier (2 years, female) with necrotizing leukoencephalitis. T2 **(A)** and fluid-attenuated inversion recovery **(B)** hyperintense finger-like lesions affecting the subcortical white matter, the corona radiata, and the diencephalon. Right-sided ventricular enlargement, focal widening of sulci, and mild midline shift to the right are most likely secondary to white matter loss in the right prosencephalon. Contrast enhancing lesions as on the left side [**(C)** T1-weighted native; **(D)** T1 weighted after contrast injection] and non-contrast enhancing lesions (right side) may coexist in one patient, which most likely reflects different stages of the disease. Enhancement may be patchy or it may be seen around necrotic areas (ring-like, arrow head). Meningeal contrast enhancement is deficient.

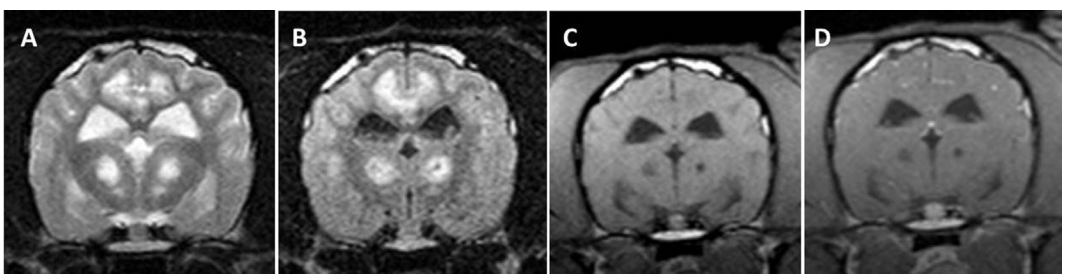

FIGURE 2 | Transverse magnetic resonance images (0.5 T) of a Yorkshire Terrier (3 years, male) with subacute necrotizing encephalopathy. Bilateral symmetric hyperintensities in the cingulate gyrus and in the thalamus on T2-weighted **(A)** and fluid-attenuated inversion recovery **(B)** images. These lesions have a hypointense center on T1-weighted **(C)** images and they do not enhance after a contrast injection **(D)**.

edema beyond the boundaries of the primary inflammatory lesions is rather mild. On positron emission tomography (PET) imaging, areas of necrosis and cavitation correspond to areas of glucose hypometabolism (30, 42).

In few cases (12%), lesions might be hyperintense on T1 and hypo- or hyperintense on T2-weighted sequences, which most likely correspond to areas of intraparenchymal hemorrhage. The latter could be verified by identification of an intralesional signal void in a T2* sequence. However, studies confirming this assumption in Yorkshire Terriers with NLE are deficient. Midline shift and ventriculomegaly are seen in 50 and 36% of dogs, respectively (25). Both are less likely to be caused by a mass effect of the inflammatory foci, but by a loss of white matter on the more severely affected hemisphere (3, 5). Brain herniation is not a feature of NLE in Yorkshire Terriers.

Lesion enhancement after a contrast injection is usually mild to moderate (5, 7, 25). It can be patchy and inhomogeneous within parenchymal lesions (87%) or ring-like in the periphery of a necrotic lesion corresponding to perinecrotic inflammation (7, 25). The degree of contrast enhancement appears to be related to the degree of lymphohistiocytic inflammation on histological examination (7). Lesions with moderate enhancement and those without enhancement may coexist in one patient (7). The first may reflect active inflammation whereas areas without enhancement may be reflecting burnt out lesions and therefore indicating a more chronic stage of the same disease (5, 7). Meningeal enhancement is lacking in NLE (25). A few Yorkshire Terriers with NLE (7%) may not show any contrast enhancement at all (6, 25).

In addition to NLE, Yorkshire Terriers can also be affected by GME. It may even be seen as a combination of NLE, NME, and GME in the same dog, as described in two cases (43). One displayed typical MRI features of NLE in the prosencephalon, whereas the other had a lesion compatible with GME. Histopathological examination, however, revealed characteristics of NLE, NME, and GME in both dogs.

NLE IN FRENCH BULLDOGS

Reports on specific MRI features of NLE in French Bulldogs are limited to three publications regarding four dogs with histologically confirmed disease, with one scan being performed post mortem (10, 11, 25). Lesions may be uni- or multifocal and can be round-shaped and clearly delineated or they may be diffuse. They are T2 and FLAIR hyperintense and can be found in the telencephalon, diencephalon and brainstem, whereas the cerebellum seems to be unaffected. These lesions are iso- to hypointense on T1-weighted images. They may represent necrotic areas in a similar way (as described earlier) for Yorkshire Terriers. However, the primary inflammatory focus is frequently masked by a secondary white matter edema and therefore it may be indistinguishable from secondary edema without a contrast injection. The primary inflammatory focus can often be identified by a mild to moderate peripheral or even ring-like enhancement on T1-weighted images after a contrast injection (**Figure 3**). More diffuse lesions may commonly show a varying degree of contrast enhancement ranging from a moderate to strong uniform pattern. However, lesions without contrast enhancement can also be seen in the same patient. Meningeal involvement is minimal and therefore it cannot be identified on MRI. Accordingly, the nucleated cell count in CSF is usually only mildly elevated (25). Midline shift is not commonly seen or is only mild. In general, lesions seem to be less severe in French Bulldogs than in Yorkshire Terriers.

One report described inflammatory changes affecting both the optic nerves and retina on histopathology (in addition to those found in the forebrain), which went unnoticed on a post mortem MR image (11).

NME IN PUGS

The majority of Pugs with NME (94%) have multifocal or diffuse, asymmetrical prosencephalic lesions with at least one lesion being located in the telencephalon (21). Lesions are more common in the middle and caudal prosencephalon, being most severe in occipital and parietal lobes, tapering off to rostral with the frontal lobes being less frequently affected (20, 21). About one-third of dogs have additional diencephalic lesions (21).

Brainstem (17%) and cerebellar (22%) involvement are much less common and lesions here are less severe than those in the prosencephalon (21, 25). However, lesion distributions may reflect the limited sensitivity of MRI to detect inflammatory lesions, especially if those are relatively mild, since it is known

FIGURE 3 | Transverse magnetic resonance images (0.5 T) of a French Bulldog (2 years, female) with necrotizing leukoencephalitis. T2 **(A)** and fluid-attenuated inversion recovery (FLAIR) **(B)** hyperintense round-shaped lesion accompanied by secondary white matter edema in the right frontal lobe. The T2 signal of the round center is partially suppressed on the FLAIR sequence indicating a liquid-like texture being consistent with necrosis. There is a ring-like contrast enhancement around the necrotic center after contrast injection [**(C)** T1-weighted native; **(D)** T1 weighted after contrast injection].

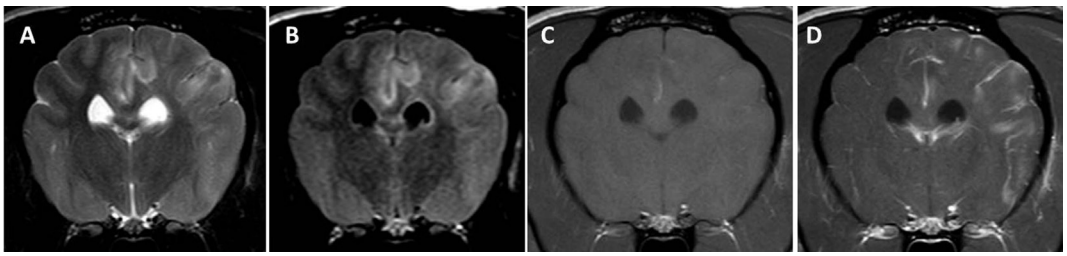

FIGURE 4 | Transverse magnetic resonance images (3 T) of a Pug (3 years, male) with necrotizing meningoencephalitis. Diffuse T2 **(A)** and fluid-attenuated inversion recovery **(B)** hyperintensities predominantly on the left in the prosencephalon resulting in the complete loss of cortical gray and white matter distinction. There is a patchy parenchymal and a leptomeningeal enhancement after a contrast injection [**(C)** T1-weighted native; **(D)** T1 weighted after contrast injection]. The midline is slightly shifted to the right side caused by the expansion of the prosencephalon on the left-hand side.

from a pathological study that 40% of Pugs with NME also have cerebellar lesions (19). In addition, one Pug with NME has been reported with a single brainstem lesion (21). In general, lesion burden in NME can be more dramatic for Pugs compared with other types of NE. However, no correlation could be demonstrated so far between MRI visible lesion severity and prognosis (21).

Lesions being hyperintense on T2-weighted and FLAIR images and mildly hypo- to isointense on T1 images may dominate in the cerebral white matter (about 30% of lesions) or they may more commonly involve gray and white matter to a similar extent. White and gray matter distinction is often missing altogether and corresponds to anatomical disruptions of those structures on histopathological examination (**Figure 4**). Focal, well-demarcated hyperintensities on T2-weighted images, which follow the white-gray matter boundaries, correlate histologically with white matter edema rather than with areas of macroscopic necrosis of brain parenchyma. Therefore, the latter is not a typical feature of NME in Pugs. Hyperintensity on T2-weighted and FLAIR images in the hippocampus and piriform lobe is mainly consistent with excitotoxic edema caused by long-lasting seizure activity, whereas similar imaging features in other forebrain regions correspond to areas of inflammation or microscopic liquefaction on histopathology (25).

Lesion enhancement after a contrast injection is varying but is usually mild to moderate with an inhomogeneous and patchy intraparenchymal pattern. Meningeal enhancement is seen in slightly more than half of the dogs involving the dura mater and more commonly the leptomeninges (21, 25). The enhancement pattern, corresponding to inflammatory infiltrates found histopathologically in sulci, explains why Pugs are more likely to experience elevated nucleated cell counts on CSF analysis than dogs with NLE (25) and why mean nucleated cell counts are higher in Pugs (250 cell/µl; SD: 172) than in Yorkshire Terriers (19 cells/µl; SD: 21) (25). Between 22 and 43% of Pugs may not show any contrast enhancement at all (21, 25). However, lack of contrast enhancement does not rule out meningitis or encephalitis (37, 44).

Midline shift away from the more severely affected brain hemisphere is seen in 25–61% of dogs (21, 25). Different types of brain herniation were detected in about one-third of cases with a caudal transtentorial herniation being most common [(20, 21, 25); **Figure 5**]. A foramen magnum herniation of the cerebellum is seen in up to 12% of dogs and may contribute to the sudden death observed in some cases (25). Uni- or bilateral ventricular dilation can be identified in about one-third of dogs, with some experiencing signs of intraventricular hypertension such as periventricular edema and dilatation of the olfactory recess. Ventricular dilatation and/or asymmetry may be attributed to the space-occupying effect of inflammatory foci and secondary edema. However, one should keep in mind that it might be just an incidental finding in some cases since ventricular asymmetry can be seen in up to 38% of normal dogs (45).

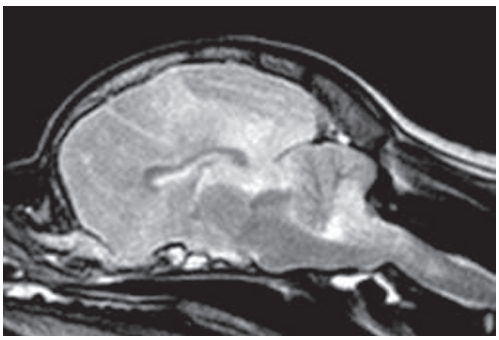

FIGURE 5 | Sagittal T2-weighted magnetic resonance image (0.5 T) of a Pug (9 months, female) with necrotizing meningoencephalitis (NME). Caudal transtentorial herniation of the occipital lobes and foramen magnum herniation of the cerebellum caused by significant swelling of the prosencephalon. This may explain the sudden death of some Pugs with NME.

NME IN CHIHUAHUAS

Magnetic resonance imaging of two dogs brains demonstrated multifocal loss of cortical gray/white matter demarcation and marked thinning and collapse of the right parietal, temporal, and occipital cortices (29). In contrast to NME in Pugs, a small rim of overlying cortical gray matter might be spared resulting in an MRI that may resemble NLE in Yorkshire Terriers (**Figure 6**). Involvement of deep white matter such as the capsula interna and diencephalon is also described [(25, 30, 32); **Figure 7**]. The lesions were hyperintense on T2-weighted images, with

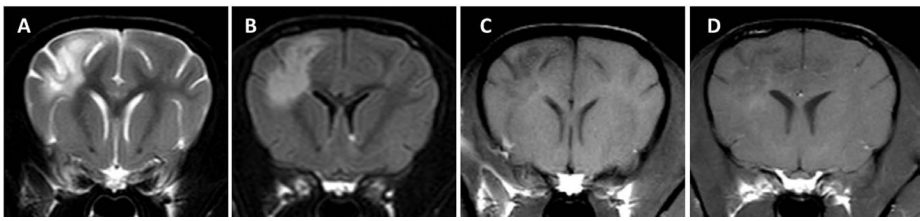

FIGURE 6 | Transverse magnetic resonance images (3 T) of a Chihuahua (11 months, female) with necrotizing meningoencephalitis. T2 **(A)** and fluid-attenuated inversion recovery **(B)** hyperintense finger-like lesions affecting the subcortical white and gray matter in the right prosencephalon. These characteristics may resemble those of Yorkshire Terriers with necrotizing leucoencephalitis since there might be a thin rim of intact cortical gray matter. However, involvement of gray matter can be visualized in most cases. The lesion is hypointense on T1-weighted images **(C)** and is only mildly enhanced in the periphery of the lesion **(D)**.

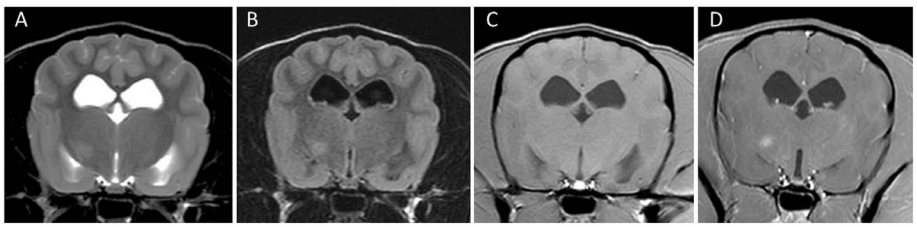

FIGURE 7 | Transverse magnetic resonance images (3 T) of a Chihuahua (5 years, female) with necrotizing meningoencephalitis. Single T2 **(A)** and fluid-attenuated inversion recovery **(B)** hyperintense round-shaped lesion in the right diencephalon. There is a small uniform contrast enhancement in the center of the lesion on the post-contrast T1-weighted image **(D)** compared to the pre-contrast T1-weighted image **(C)**.

TABLE 1 | Summary of typical imaging characteristics of necrotizing encephalitis in Yorkshire Terriers, French bulldogs, Pug dogs, and Chihuahuas.

Imaging characteristics	Yorkshire Terrier	French bulldog	Pug	Chihuahua
Type of encephalitis	NLE	NLE	NME	NME
Lesion distribution	Commonly affecting telencephalon and diencephalon, brainstem less severely affected, cerebellum and spinal cord usually spared	Commonly affecting telencephalon, diencephalon and brainstem, cerebellum usually spared	Telencephalon and diencephalon, most severe in occipital and parietal lobes, tapering off rostral with the frontal lobes being less frequently affected, brainstem and cerebellum less frequently affected	Telencephalon and diencephalon, brainstem and cerebellum usually spared
White and gray matter involvement	In subcortical white matter of telencephalon with cortical gray matter being spared	Subcortical or deep white matter	May be dominating in the cerebral white matter or more commonly involve gray and white matter to a similar extend, loss of gray and white matter distinction	Cortical gray and white matter, sometimes a small rim of overlying cortical gray matter might be spared, deep white matter
Signal intensities	Hyperintense on T2 and FLAIR, mildly hypointense to isointense on T1, sometimes mildly hyperintense on T1	Hyperintense on T2 and FLAIR, hypointense to isointense on T1	Hyperintense on T2 and FLAIR, mildly hypo- to isointense on T1	Hyperintense on T2 and FLAIR, hypointense to isointense on T1
Midline shift	Possible to the more severely affected side	Not commonly seen, only mild if present	Common	Not commonly seen
Ventriculomegaly of lateral ventricles	Possible on the more severely affected side due to white matter loss	No	Can be seen	Can be seen, difficult to differentiate from normal ventriculomegaly in this breed
Brain herniation	No	No	Can be seen	No
Contrast enhancement	Mild to moderate, inhomogeneous or ring-like around a necrotic center, lesions with and without contrast enhancement may coexist in one patient, no meningeal enhancement	Varying, reaching from moderate to strong uniform, sometimes ring-like in the periphery of the lesion, no meningeal enhancement	Mild to moderate, inhomogeneous and patchy intraparenchymal pattern, meningeal enhancement is common, usually leptomeningeal enhancement	Mild intraparenchymal enhancement, meningeal enhancement not described

NME, necrotizing meningoencephalitis; NLE, necrotizing leukoencephalitis; FLAIR, fluid-attenuated inversion recovery.

T2-weighted hypointensity and slight post-contrast enhancement (29). Brainstem and cerebellum seem to be largely unaffected (29). Lesions correspond to intensely cellular, non-suppurative meningoencephalitis, often with cystic necrosis in subcortical white matter (29). On fluorine-18 fluorodeoxyglucose-PET scans the lesions correspond to areas of hypometabolism (30). CSF analysis can be normal in some dogs and hinders establishing a definite intra vitam diagnosis (29).

In the case of Chihuahuas, the situation is further complicated by the fact that GME can also be seen in this breed and therefore has to be differentiated from NME (25, 46).

NE IN OTHER CANINE BREEDS

Imaging characteristics of the four breeds described here are summarized in **Table 1**. For the other breeds, having been reported to be affected by either NLE or NME, none or only single case reports of MRI characteristics are available and therefore generalizations do not seem feasible.

FUTURE DEVELOPMENTS

Despite the fact that imaging characteristics of NME and NLE have been outlined earlier, diagnosis is usually presumptive if based on imaging alone. Often, histological confirmation based on a brain biopsy is required to establish a definite diagnosis (20). However, performing brain biopsies is invasive and it is associated with certain morbidity. Therefore, non-invasive methods of imaging immunology are being investigated in human medicine. Inflammatory cells can be labeled with intravenously injected paramagnetic or superparamagnetic compounds (47, 48). Alternatively, cellular labeling can be achieved using other dipoles that are less common in normal tissue than hydrogen such as ^{19}F, ^{13}C, or ^{15}N (47). Cells labeled this way may potentially be tracked by MRI in inflammatory and ischemic intracranial lesions allowing cellular characterization of encephalitis without the need for a histological examination.

AUTHOR CONTRIBUTIONS

TF has gathered all information and wrote the manuscript.

ACKNOWLEDGMENTS

The authors acknowledge support from the German Research Foundation (DFG) and Leipzig University within the program of Open Access Publishing.

FUNDING

The funding does apply to the publication fee only.

REFERENCES

1. Tipold A, Fatzer R, Jaggy A. Necrotizing encephalitis in Yorkshire terriers. *J Small Anim Pract* (1993) 34:623–8. doi:10.1111/j.1748-5827.1993.tb02598.x
2. Sawashima Y, Sawashima K, Taura Y, Shimada A, Umemura T. Clinical and pathological findings of a Yorkshire terrier affected with necrotizing encephalitis. *J Vet Med Sci* (1996) 58:659–61. doi:10.1292/jvms.58.659
3. Jull BA, Merryman JI, Thomas WB, McArthur A. Necrotizing encephalitis in a Yorkshire terrier. *J Am Vet Med Assoc* (1997) 211:1005–7.
4. Ducote JM, Johnson KE, Dewey CW, Walker MA, Coates JR, Berridge BR. Computed tomography of necrotizing meningoencephalitis in 3 Yorkshire terriers. *Vet Radiol Ultrasound* (1999) 40:617–21. doi:10.1111/j.1740-8261.1999.tb00888.x
5. Lotti D, Capucchio MT, Gaidolfi E, Merlo M. Necrotizing encephalitis in a Yorkshire terrier: clinical, imaging, and pathologic findings. *Vet Radiol Ultrasound* (1999) 40:622–6. doi:10.1111/j.1740-8261.1999.tb00889.x
6. Kuwamura M, Adachi T, Yamate J, Kotani T, Ohashi F, Summers BA. Necrotizing encephalitis in the Yorkshire terrier: a case report and literature review. *J Small Anim Pract* (2002) 43:459–63. doi:10.1111/j.1748-5827.2002.tb00014.x
7. Von Praun F, Matiasek K, Grevel V, Alef M, Flegel T. Magnetic resonance imaging and pathologic findings associated with necrotizing encephalitis in two Yorkshire terriers. *Vet Radiol Ultrasound* (2006) 47:260–4. doi:10.1111/j.1740-8261.2006.00137.x
8. Higginbotham MJ, Kent M, Glass EN. Noninfectious inflammatory central nervous system diseases in dogs. *Compend Contin Educ Vet* (2007) 29:488–97.
9. Wrozek M, Nicopon J, Giza E, Niedzwiedz A, Sotysiak Z. Meningoencephalitis of unknown origin in a cohort of 27 Yorkshire terriers in Poland: clinical manifestation, topographic magnetic resonance imaging characteristics, clinical outcome. 24th Symposium ESVN-ECVN, Trier, Germany. *J Vet Intern Med* (2012) 26:842.
10. Timmann D, Konar M, Howard J, Vandevelde M. Necrotising encephalitis in a French bulldog. *J Small Anim Pract* (2007) 48:339–42. doi:10.1111/j.1748-5827.2006.00239.x
11. Spitzbarth I, Schenk HC, Tipold A, Beinecke A. Immunohistochemical characterization of inflammatory and glial responses in a case of necrotizing leucoencephalitis in a French bulldog. *J Comp Pathol* (2010) 142:235–41. doi:10.1016/j.jcpa.2009.08.158
12. Cordy DR, Holliday TA. A necrotizing meningoencephalitis of pug dogs. *Vet Pathol* (1989) 26:191–4. doi:10.1177/030098588902600301
13. Kobayashi Y, Ochiai K, Umemura T, Goto N, Ishida T, Itakura C. Necrotizing meningoencephalitis in pug dogs in Japan. *J Comp Pathol* (1994) 110:129–36. doi:10.1016/S0021-9975(08)80184-3
14. Tipold A. Diagnosis of inflammatory and infectious diseases of the central nervous system in dogs: a retrospective study. *J Vet Intern Med* (1995) 9:304–14. doi:10.1111/j.1939-1676.1995.tb01089.x
15. Hinrichs U, Tobias R, Baumgärtner W. Ein Fall von nekrotisierender Menigoenzephalitis beim Mops (pug dog encephalitis–PDE). *Tierärztl Prax* (1996) 24:489–92.
16. Kuwabara M, Tanaka S, Fujiwara K. Magnetic resonance imaging and histopathology of encephalitis in a pug. *J Vet Med Sci* (1998) 60:1353–5. doi:10.1292/jvms.60.1353
17. Uchida K, Hasegawa T, Ikeda M, Yamaguchi R, Tateyama S. Detection of an autoantibody from pug dogs with necrotizing encephalitis (pug dog encephalitis). *Vet Pathol* (1999) 36:301–7. doi:10.1354/vp.36-4-301
18. Hasegawa T, Uchida K, Sugimoto M. Long-term management of necrotizing meningoencephalitis in a pug dog. *Canine Pract* (2000) 25:20–2.
19. Levine JM, Fosgate GT, Porter B, Schatzberg SJ, Greer K. Epidemiology of necrotizing meningoencephalitis in pug dogs. *J Vet Intern Med* (2008) 22:961–8. doi:10.1111/j.1939-1676.2008.0137.x
20. Flegel T, Henke D, Boettcher IC, Aupperle H, Oechtering G, Matiasek K. Magnetic resonance imaging finding in histologically confirmed pug dog encephalitis. *Vet Radiol Ultrasound* (2008) 49:419–24. doi:10.1111/j.1740-8261.2008.00400.x
21. Young BD, Levine JM, Fosgate GT, de Lahunta A, Flegel T, Matiasek K, et al. Magnetic resonance imaging characteristics of necrotizing meningoencephalitis in pug dogs. *J Vet Intern Med* (2009) 23:527–37. doi:10.1111/j.1939-1676.2009.0306.x
22. Stalis IH, Chadwick B, Dayrell-Hart B, Summers BA, Van Winkle TJ. Necrotizing meningoencephalitis of Maltese dogs. *Vet Pathol* (1995) 32:230–5. doi:10.1177/030098589503200303

23. Suzuki M, Uchida K, Morozumi M, Hasegawa T, Yanai T, Nakayama H, et al. A comparative pathological study on canine necrotizing meningoencephalitis and granulomatous meningoencephalomyelitis. *J Vet Med Sci* (2003) 65:1233–9. doi:10.1292/jvms.65.1319
24. Jung DI, Kang BT, Park C, Yoo JH, Gu SH, Jeon HW, et al. A comparison of combination therapy (cyclosporine plus prednisolone) with sole prednisolone therapy in 7 dogs with necrotizing meningoencephalitis. *J Vet Med Sci* (2007) 69:1303–6. doi:10.1292/jvms.69.1303
25. Flegel T. *Diagnostics and Therapy of Granulomatous and Necrotizing Encephalitis in Dogs. Habilitation Theses*. Leipzig: University of Leipzig (2010).
26. Matsuki N, Fujiwara K, Tamahara S, Uchida K, Matsunaga S, Nakayama H, et al. Prevalence of autoantibody in cerebrospinal fluids from dogs with various CNS diseases. *J Vet Med Sci* (2004) 66:295–7. doi:10.1292/jvms.66.295
27. Kube SA, Dickinson PJ, Affolter TW, Higgins RJ. Necrotizing meningoencephalitis in Chihuahua dogs. *J Vet Intern Med* (2005) 19:461. doi:10.1111/j.1939-1676.2005.tb02714.x
28. Zarfoss M, Schatzberg S, Venator K, Cutter-Schatzberg K, Cuddon P, Pintar J, et al. Combined cytosine arabinoside and prednisone therapy for meningoencephalitis of unknown aetiology in 10 dogs. *J Small Anim Pract* (2006) 47:588–95. doi:10.1111/j.1748-5827.2006.00172.x
29. Higgins RJ, Dickinson PJ, Kube SA, Moore PF, Couto SS, Vernau KM, et al. Necrotizing meningoencephalitis in five Chihuahua dogs. *Vet Pathol* (2008) 45:336–46. doi:10.1354/vp.45-3-336
30. Eom KD, Lim CY, Gu SH, Kang BT, Kim YB, Jang DP, et al. Positron emission tomography features of canine necrotizing meningoencephalitis. *Vet Radiol Ultrasound* (2008) 49:595–9. doi:10.1111/j.1740-8261.2008.00437.x
31. Flegel T, Oevermann A, Oechtering G, Matiasek K. Diagnostic yield and adverse effects of MRI-guided free-hand brain biopsies through a mini-burr hole in dogs with encephalitis. *J Vet Intern Med* (2012) 26:969–76. doi:10.1111/j.1939-1676.2012.00961.x
32. de Lahunta A, Glass E. Visual system. In: de Lahunta A, Glass E, editors. *Veterinary Neuroanatomy and Clinical Neurology*. St Louis, MO: Saunders Elsevier (2009). p. 411–2.
33. Vernau KM, Liu H, Higgins RJ, Dickinson PJ, Sturges BK, Vernau W, et al. Dog leucocyte antigen class II association in Chihuahuas with necrotizing meningoencephalitis. 2010 ACVIM Forum, Anaheim, USA. *J Vet Intern Med* (2010) 24:736. doi:10.1111/j.1939-1676.2010.0521.x
34. Cantile C, Chianini F, Arispici M, Fatzer R. Necrotizing meningoencephalitis associated with cortical hippocampal hamartia in a Pekingese dog. *Vet Pathol* (2001) 38:119–22. doi:10.1354/vp.38-1-119
35. Cooper JJ, Schatzberg SJ, Vernau KM, Summers BA, Porter BF, Siso S, et al. Necrotizing encephalomyelitis in atypical dog breeds: a case series and literature review. *J Vet Intern Med* (2014) 28:198–203. doi:10.1111/jvim.12233
36. Aresu L, D'Angelo A, Zannatta R, Valenza F, Capuchio MT. Canine necrotizing encephalitis associated with anti-glomerular basement membrane glomerulonephritis. *J Comp Pathol* (2007) 136:279–82. doi:10.1016/j.jcpa.2007.02.008
37. Lamb CR, Croson PJ, Capello R, Cherubini GB. Magnetic resonance imaging findings in 25 dogs with inflammatory cerebrospinal fluid. *Vet Radiol Ultrasound* (2005) 46:17–22. doi:10.1111/j.1740-8261.2005.00003.x
38. Granger N, Smith PM, Jeffery ND. Clinical findings and treatment of non-infectious meningoencephalomyelitis in dogs: a systematic review of 457 published cases from 1962 to 2008. *Vet J* (2010) 184:290–7. doi:10.1016/j.tvjl.2009.03.031
39. Fischer A, Baiker K, Hofmann S, Medl S, Schmahl W, Bauer MF, et al. Subacute necrotizing encephalopathy in Yorkshire terriers is associated with combined respiratory chain complex I and IV defect. *J Vet Intern Med* (2008) 22:770. doi:10.1111/j.1939-1676.2008.0103.x
40. Baiker K, Hofmann S, Fischer A, Gödde T, Medl S, Schmahl W, et al. Leigh-like subacute necrotizing encephalopathy in Yorkshire terriers: neuropathological characterisation, respiratory chain activities and mitochondrial DNA. *Acta Neuropathol* (2009) 118:697–709. doi:10.1007/s00401-009-0548-6
41. Talarico LR, Schatzberg SJ. Idiopathic granulomatous and necrotising inflammatory disorders of the canine central nervous system: a review and future perspectives. *J Small Anim Pract* (2010) 51:138–49. doi:10.1111/j.1748-5827.2009.00823.x
42. Kang B-T, Kim S-G, Lim C-Y, Gu S-H, Jang D-P, Kim Y-B, et al. Correlation between fluorodeoxyglucose positron emission tomography and magnetic resonance imaging findings of non-suppurative meningoencephalitis in 5 dogs. *Can Vet J* (2010) 51:986–92.
43. Hoffmann MV, Iseringhausen M, Spitzbarth I, Gerhauser I, Hunkeler D, Oevermann A, et al. Concomitant granulomatous, necrotizing meningoencephalitis and necrotizing leukoencephalitis in two Yorkshire terriers. 24th Symposium ESVN-ECVN, Trier, Germany. *J Vet Intern Med* (2012) 26:842.
44. Keenihan EK, Summers BA, David FH, Lamb CR. Canine meningeal disease: associations between magnetic resonance imaging signs and histological findings. *Vet Radiol Ultrasound* (2013) 54:504–15. doi:10.1111/vru.12055
45. Pivetta M, De Risio L, Newton R, Dennis R. Prevalence of lateral ventricle asymmetry in brain MRI studies of neurologically normal dogs and dogs with idiopathic epilepsy. *Vet Radiol Ultrasound* (2013) 54:516–21. doi:10.1111/vru.12063
46. Luján Feliu-Pascal A, Matiasek L, de Stefani A, Beltrán E, De Risio L. Efficacy of mycophenolate mofetil for the treatment of presumptive granulomatous meningoencephalomyelitis: preliminary results. Abstract 20th Symposium ESVN-ECVN, Bern, Switzerland. *J Vet Intern Med* (2008) 22:508. doi:10.1111/j.1939-1676.2008.0047.x
47. Stoll G, Bendszus M. New approaches to neuroimaging of central nervous system inflammation. *Curr Opin Neurol* (2010) 23:282–6. doi:10.1097/WCO.0b013e328337f4b5
48. Inturi S, Wang G, Chen F, Banda NK, Holers VM, Wu L, et al. Modulatory role of surface coating of superparamagnetic iron oxide nanoworms in complement opsonization and leukocyte uptake. *ACS Nano* (2015) 9:10758–68. doi:10.1021/acsnano.5b05061

Conflict of Interest Statement: The author declares that the research was conducted in the absence of any commercial or financial relationships that could be construed as a potential conflict of interest.

frontiers in Veterinary Science

CASE REPORT
published: 18 August 2017
doi: 10.3389/fvets.2017.00134

Dynamic Lumbosacral Magnetic Resonance Imaging in a Dog with Tethered Cord Syndrome with a Tight Filum Terminale

Steven De Decker, Vicky Watts and David M. Neilson*

Department of Clinical Science and Services, Royal Veterinary College, University of London, Hatfield, United Kingdom

A 1-year and 11-month- old English Cocker Spaniel was evaluated for clinical signs of progressive right pelvic limb lameness and urinary incontinence. Neurological examination was suggestive of a lesion localized to the L4–S3 spinal cord segments. No abnormalities were seen on magnetic resonance imaging (MRI) performed in the dog in dorsal recumbency and the hips in a neutral position and the conus medullaris ended halfway the vertebral body of L7. An MRI of the hips in extended and flexed positions demonstrated minimal displacement of the conus medullaris in the cranial and caudal directions, respectively. Similar to the images in neutral position, the conus medullaris ended halfway the vertebral body of L7 in both the extended and flexed positions. In comparison, an MRI of the hips in neutral, extended, and flexed positions performed in another English Cocker Spaniel revealed obvious cranial displacement of the conus medullaris with the hips in extension and caudal displacement with hips in flexion. A standard dorsal lumbosacral laminectomy was performed. Visual inspection of the vertebral canal revealed excessive caudal traction on the conus medullaris. After sectioning the distal aspect of the filum terminale, the conus medullaris regained a more cranial position. A neurological examination 4 weeks after surgery revealed clinical improvement. Neurological examinations at 2, 4, 7, and 12 months after surgery did not reveal any abnormalities, and the dog was considered to be clinically normal. Tethered cord syndrome with a tight filum terminale is a very rare congenital anomaly and is characterized by an abnormally short and inelastic filum terminale. Therefore, this disorder is associated with abnormal caudal traction on the spinal cord and decreased physiological craniocaudal movements of the neural structures within the vertebral canal. Although further studies are necessary to evaluate and quantify physiological craniocaudal movement of the spinal cord and conus medullaris in neurologically normal dogs, the results of this report suggest further exploration of dynamic MRI to demonstrate decreased craniocaudal displacement of the conus medullaris in dogs with tethered cord syndrome with a tight filum terminale.

Keywords: spinal dysraphism, spinal malformation, magnetic resonance imaging, cauda equina, conus medullaris

OPEN ACCESS

Edited by:
Andrea Tipold, University of Veterinary Medicine Hannover, Germany

Reviewed by:
Sonia Añor, Universitat Autònoma de Barcelona, Spain
Simon Platt, University of Georgia, United States

****Correspondence:***
Steven De Decker
sdedecker@rvc.ac.uk

Specialty section:
This article was submitted to Veterinary Neurology and Neurosurgery, a section of the journal Frontiers in Veterinary Science

Received: *18 June 2017*
Accepted: *03 August 2017*
Published: *18 August 2017*

Citation:
De Decker S, Watts V and Neilson DM (2017) Dynamic Lumbosacral Magnetic Resonance Imaging in a Dog with Tethered Cord Syndrome with a Tight Filum Terminale. Front. Vet. Sci. 4:134. doi: 10.3389/fvets.2017.00134

CASE PRESENTATION

A 1-year and 11-months-old, female neutered English Cocker Spaniel was evaluated for clinical signs of progressive right pelvic limb lameness of 16 months duration and intermittent urinary incontinence of 2 weeks duration. Orthopedic and neurological examinations; radiographs of the hips, pelvis, and right stifle; and spinal magnetic resonance imaging (MRI) performed at 10 months before

referral had not revealed the underlying cause of the dog's clinical signs. No clinical improvement was seen after medical treatment with carprofen and meloxicam. General physical examination did not reveal any abnormalities. Neurological examination revealed mild paraparesis, right pelvic limb lameness, a low-tail carriage, decreased tail tone, a decreased withdrawal reflex in the right pelvic limb, and proprioceptive deficits in the right pelvic limb expressed by delayed hopping, but intact paw placement. Pain could be elicited on lumbosacral palpation, dorsal extension of the tail, and extension of both hips. No other neurological deficits were identified. Her neurological lesion was localized to the L4–S3 spinal cord segments. A complete blood count, biochemistry panel, and urinalysis, including bacterial culture, did not reveal any abnormalities. After premedication with methadone (0.2 mg/kg IM) and acepromazine (0.01 mg/kg IM), anesthesia was induced with propofol (4–6 mg/kg, IV) and maintained with sevoflurane in 100% oxygen. An MRI (1.5 T, Intera, Philips Medical Systems, Eindhoven, the Netherlands) of the lumbar and lumbosacral vertebral column was performed with the dog supported in dorsal recumbency by a high-density foam trough with flexed limbs in a neutral position (i.e., frog-leg position). The imaging protocol included sagittal, transverse, and dorsal plane T2-weighted [repetition time (ms) (TR), echo time (ms) (TE), 3,000/120], sagittal and dorsal plane T2-weighted short tau inversion recovery (STIR) (TR/TE, 3,612/80), and transverse plane T2-weighted BAL TGRAD (TR/TE, 7.9/3.9) sequences. Sagittal and transverse plane T1-weighted (T1W TSE) (TR/TE, 400/8) images were acquired before and after IV injection with gadolinium contrast (0.1 ml/kg gadoterate meglumine, Dotarem, Guerbet, Milton Keynes, England). No abnormalities were seen on MRI, and the conus medullaris ended halfway the vertebral body of L7 (**Figure 1**). Sagittal T2-weighted images were subsequently acquired with the hips in extended and flexed positions. Extended views were obtained by extending the pelvic limbs caudally and securing them in maximal extension of the coxofemoral joints with velcro straps secured to the MRI table. Flexed views were obtained by pulling the pelvic limbs cranially and restraining them beside the thorax with extended stifles. An MRI with the hips in extended and flexed positions demonstrated minimal displacement of the conus medullaris in the cranial and caudal directions, respectively. Similar to the images in neutral position, the conus medullaris ended halfway the vertebral body of L7 in both the extended and flexed positions (**Figure 1**). However, the dog demonstrated an increase in heart rate, from 60 to 90 beats per minute, when images were acquired with the lumbosacral joint in flexed position. The heart rate returned to normal level after administration of an IV bolus of 0.05 mg/kg methadone. Differential diagnoses included tethered cord syndrome with tight filum terminale and dynamic lumbosacral vertebral canal stenosis. Recovery from general anesthesia was uneventful, and a neurological examination before discharge from hospitalization did not reveal any deterioration of clinical signs or neurological deficits.

For comparative purposes, an MRI of the hips in neutral, extended, and flexed positions was performed on the same day in a 6-year and 4-month-old, male neutered, English Cocker Spaniel

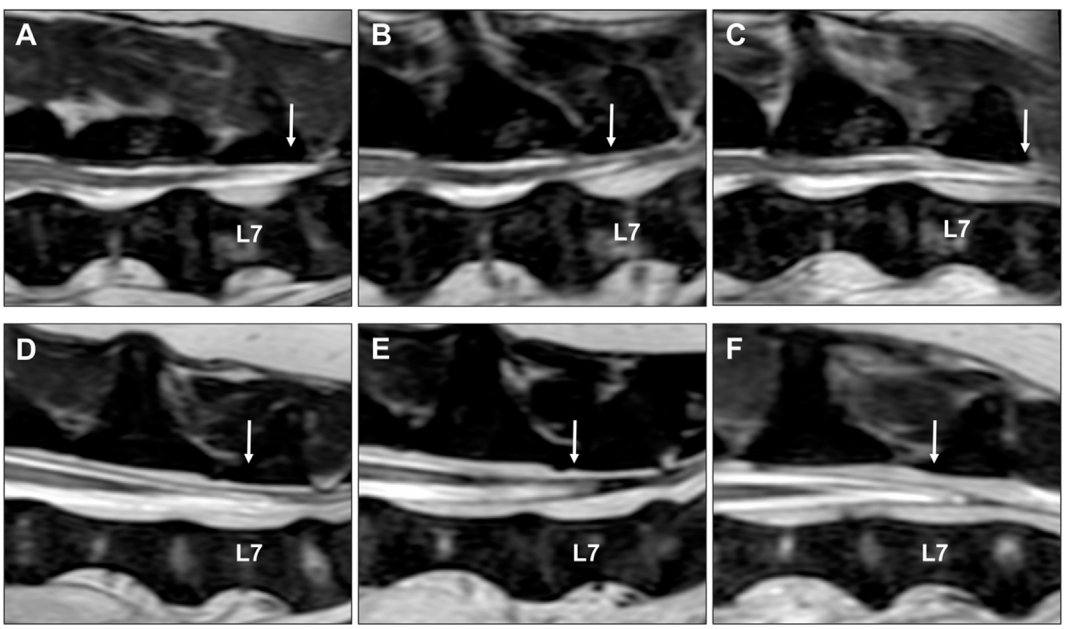

FIGURE 1 | Sagittal T2-weighted images of an English Cocker spaniel with thoracolumbar intervertebral disk extrusion with the hips in neutral **(A)**, extended **(B)**, and flexed **(C)** positions. **(A)** The conus medullaris (arrow) terminates at the caudal aspect of the L7 vertebral body. **(B)** The conus medullaris (arrow) is displaced in a cranial direction when the hips are extended and terminates now halfway the L7 vertebral body. **(C)** The conus medullaris (arrow) is displaced in a caudal direction when the hips are flexed and terminates now at the level of the L7–S1 intervertebral disk space. Sagittal T2-weighted images of an English Cocker spaniel with tethered cord syndrome with a tight filum terminale with the hips in neutral **(D)**, extended **(E)**, and flexed **(F)** positions. The conus medullaris (arrow) terminates halfway the L7 vertebral body in all three positions, and only minimal displacement is seen between different positions.

with non-ambulatory paraparesis caused by a lesion affecting the T3–L3 spinal cord segments. An MRI revealed generalized intervertebral disk degeneration and an L1–L2 intervertebral disk extrusion as the cause of the dog's clinical signs. With the hips in neutral position, the conus medullaris ended at the caudal aspect of the L7 vertebral body (**Figure 1**). The conus medullaris moved cranially until halfway the vertebral body of L7 in the extended position and moved caudally overlying the L7–S1 intervertebral disk space when an MRI was performed with the hips in a flexed position (**Figure 1**).

Medical management was started with gabapentin (10 mg/kg, q8h, PO) and restricted exercise. A re-examination 2 weeks later demonstrated progression of her clinical signs characterized by more severe urinary incontinence. General anesthesia was induced and maintained with the aforementioned protocol. A standard dorsal lumbosacral laminectomy, from L7 to S1 was performed. Subjective visual inspection of the vertebral canal revealed excessive caudal traction of the conus medullaris. The conus medullaris was also not as freely moveable in the vertebral canal as normally expected. No other abnormalities were detected. After sectioning the distal aspect of the filum terminale from the cranial aspect of the lamina of S2, the conus medullaris regained a more cranial position (**Figure 2**). The wound was closed routinely. Intraoperative analgesia was provided with ketamine (loading dose of 0.5 mg/kg IV followed by infusion at a rate of 10 μg/kg/min IV) and methadone (0.1 mg/kg q4h, IV). Postoperative analgesia consisted of a combination of methadone (0.2 mg/kg, q4h, IV), carprofen (2 mg/kg, q12h, PO), and gabapentin (10 mg/kg, q8h, PO). The dog was discharged from the hospital 2 days after surgery. The owner was advised to ensure strict rest for 4 weeks in combination with gabapentin and carprofen for 2 more weeks. The surgical findings were considered diagnostic for tethered cord syndrome with a tight filum terminale. The results of a neurological examination 4 weeks after surgery revealed improvement of the dog's signs. At this time, the dog demonstrated mild lameness and proprioceptive deficits in the right pelvic limb. The urinary incontinence had resolved. Neurological examinations at 2, 4, 7, and 12 months after surgery did not reveal any abnormalities, and the dog was considered clinically normal.

BACKGROUND

Tethered cord syndrome is a rare congenital anomaly in which progressive neurological signs are caused by abnormal caudal traction on the conus medullaris and caudal spinal cord segments (1, 2). This anomaly can be seen in association with a variety of spinal malformations and has been considered a form of occult spinal dysraphism (3). However, in the majority of human patients, tethered cord syndrome is associated with an abnormal short, thickened, and inelastic filum terminale without other spinal malformations (3). This is also referred to as tethered cord syndrome with a tight filum terminale (1, 4) and has been reported only once previously in the veterinary literature (5). As a consequence of excessive caudal traction, tethered cord syndrome is classically associated with an abnormal caudodorsal position of the conus medullaris (1–4). In people, the tip of the conus medullaris terminates at the level of L1, and termination caudal at the L2 vertebral level in patients with suggestive clinical signs is considered diagnostic for tethered cord syndrome with a tight filum terminale (1–3). However, making a diagnosis of tethered cord syndrome in dogs is challenging because of variation in termination of the conus medullaris (6) and filum terminale

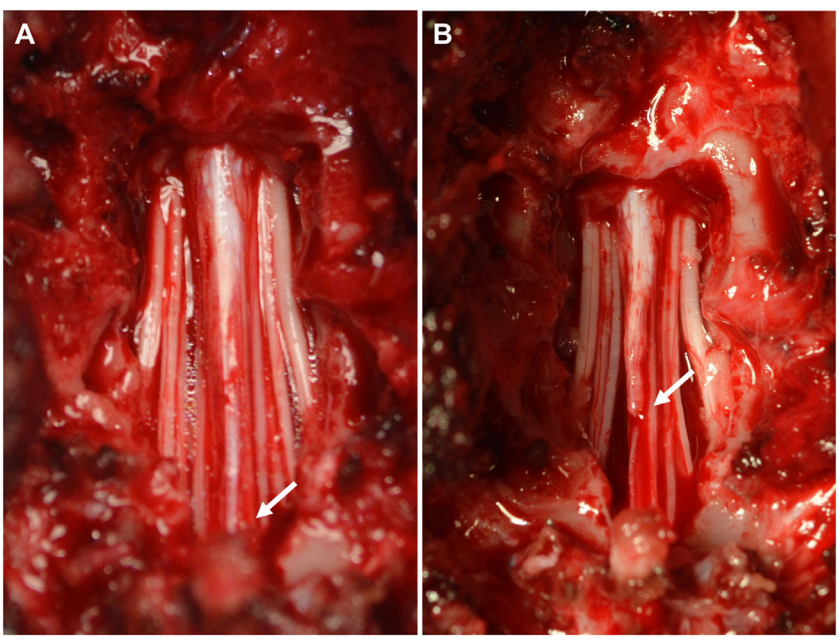

FIGURE 2 | Intraoperative pictures before **(A)** and after **(B)** sectioning the filum terminale. **(A)** Visual inspection of the vertebral canal reveals excessive caudal traction on the conus medullaris (arrow). **(B)** The conus medullaris regains a more cranial position after sectioning the distal aspect of the filum terminale.

(7) between, and possibly also within, dog breeds. Obtaining a diagnosis is further complicated by the fact that a proportion of people with tethered cord syndrome presents with the conus medullaris in an anatomical normal position without evidence of caudal displacement. This is referred to as occult tethered cord syndrome, and development of clinical signs has been attributed to decreased elasticity of the filum terminale and hence increased traction on the conus medullaris (8, 9). Decreased elasticity of the filum terminale has been suggested to limit the normal physiologic movements of the spinal cord and conus medullaris in response to everyday movements of the body and vertebral canal (10). Performing MRI in different body positions (i.e., the prone and supine position) has therefore been considered with the aim to demonstrate decreased conus medullaris motion in people with occult tethered cord syndrome (9).

DISCUSSION

Obtaining a diagnosis of tethered cord syndrome with a tight filum terminale is challenging in dogs for several reasons (5). The anatomical variation in conus medullaris termination and the theoretical possibility of occult tethered cord syndrome make it difficult to consider an abnormal caudal position of the conus medullaris as a reliable diagnostic criterion in dogs (5). Therefore, this case report explored the possibility of dynamic MRI with the hips in neutral, extended, and flexed positions to facilitate diagnosing this rare congenital anomaly. Although the results of single-case reports should be interpreted with caution, our findings suggest that dynamic MRI might be useful in evaluating the degree of craniocaudal displacement of the conus medullaris and thereby indirectly assessing the elasticity of the filum terminale. Compared to a dog of the same breed and imaged under identical conditions, the dog with tethered cord syndrome demonstrated only minimal craniocaudal displacement of the conus medullaris after an MRI was performed with the hips in extension and flexion (**Figure 1**). This finding in combination with suggestive clinical signs and exclusion of other structural abnormalities were considered suggestive for tethered cord syndrome with a tight filum terminale. Excessive caudal traction on the conus medullaris was confirmed during surgery, and the dog recovered completely after sectioning of the filum terminale. Although sectioning of the filum terminale is considered a technically easy and relative safe surgical procedure, reported complications in humans include cerebrospinal fluid leakage, headaches, infection, pseudomeningocele, and retethering (11). Ideally, a second MRI scan would have been performed to evaluate a potential increase in craniocaudal conus medullaris displacement after sectioning of the filum terminale. However, this was not performed because there was no clinical indication to justify the costs and requirement of general anesthesia in this clinical case.

Craniocaudal displacement of the conus medullaris in response to physiological movements of the vertebral canal and extremities has been well documented in humans (12–14). It has been suggested that the sliding or craniocaudal movement of the neural structures within the vertebral canal should be considered a protective mechanism, which represents transmission of tensile forces through the neural structures, thereby preserving the spinal cord and nerve roots from excessive strain (14). Therefore, maintaining free sliding of the neural structures and meninges has been considered an essential condition for maintaining a healthy and normal functioning spinal cord (13, 14).

The conus medullaris is the most caudal tapered ending of the spinal cord. This is continued by a filamentous structure, the filum terminale, which extends caudally and attaches to a sacral or caudal vertebra (7). The normal filum terminale has elastic properties and has therefore the capability of protecting the spinal cord by buffering linear stress to the spinal cord during physiological flexion and extension of the vertebral canal (15). Tight filum terminale is characterized by shortening and loss of elastic properties, which is associated with decreased transmission of tensile forces and restricted spinal cord movement (15, 16). This decreased elasticity will result in repetitive, excessive, and progressive traction on the conus medullaris and caudal spinal cord segments. The cumulative effects of hypoxia, decreased oxidative metabolism, and anatomic deformation will then ultimately result in progressive signs of pain and dysfunction of the caudal lumbar and lumbosacral spinal cord segments (17, 18).

In human medicine, several physical tests have been described to facilitate the clinical diagnosis of radiculopathies and spinal cord disorders (19). One of these physical tests is the straight leg raise test in which the patient is placed in dorsal recumbency and asked to flex the hips, while keeping the knees in an extended position (12, 19). This position is similar to the position of the dog, described in this report, when lumbosacral MR images were obtained with flexed hips and extended stifle joints. In agreement with the findings in the "control" dog, a caudal displacement of the conus medullaris is observed in asymptomatic people after performing the straight leg raise test (12–14). The importance of extending the stifle joint while flexing the hips is demonstrated by a lack of caudal conus medullaris displacement when both the hips and knees are flexed. This latter position is referred to as the sham straight leg raise test (14).

Although the findings of this report suggest that dynamic MRI can be considered to evaluate the presence or absence of physiologic craniocaudal conus medullaris displacement, it is difficult to draw firm conclusions from single-case reports. The variation of conus medullaris termination between and possibly within breeds makes it difficult to objectively quantify the normal degree of conus medullaris displacement in unaffected dogs. In humans, the degree of hip flexion has also been associated with differences in magnitude of conus medullaris displacement, and therefore, variations can be seen between and within individual patients (13). Although a diagnosis of tethered cord syndrome with a tight filum terminale was suspected based on the subjective observation of decreased to absent conus medullaris displacement between extended and flexed positions, further studies are necessary to evaluate if this finding can be used as a reliable diagnostic criterion for this rare congenital disorder. It is further unclear which MRI sequence would be most useful to evaluate termination of the conus medullaris. The presence of a large quantity of epidural fat in the lumbosacral vertebral canal can complicate recognizing the most caudal tip of the conus medullaris on conventional T2-weighted and T1-weighted images. Applying fat suppression techniques, such as fat saturation techniques,

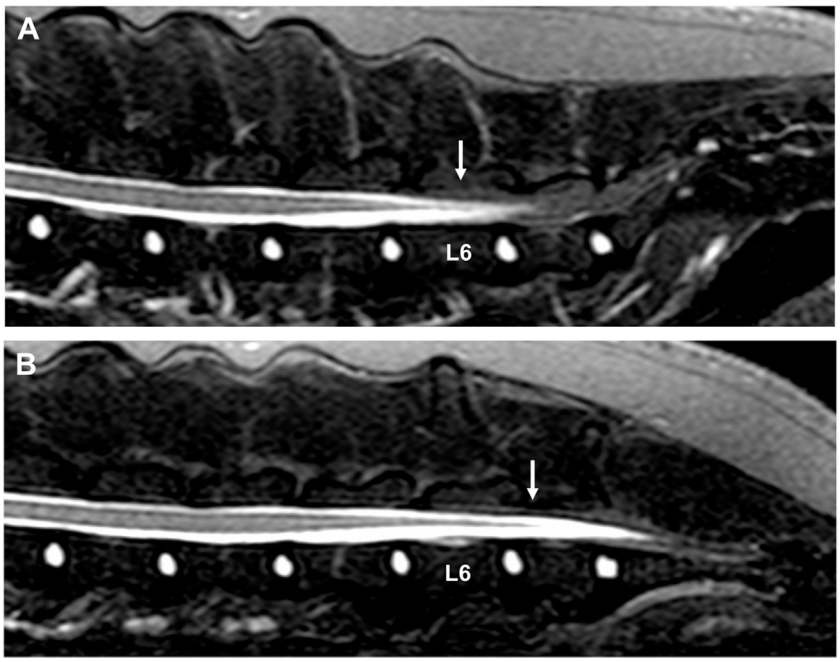

FIGURE 3 | Sagittal short tau inversion recovery images of a 3-year-old Bullmastiff with caudal lumbar spinal hyperesthesia. **(A)** The conus medullaris terminates at the caudal aspect of the L6 vertebral body with the hips in a neutral position (arrow). **(B)** The conus medullaris is displaced caudally and terminates now at the cranial aspect of the L7 vertebral body when the hips are flexed (arrow). The MRI study did not reveal the cause of the dog's clinical signs.

STIR, spectral attenuated inversion recovery (SPIR), or spectral attenuated inversion recovery sequences (SPAIR) can therefore be considered when trying to evaluate termination of the conus medullaris (**Figure 3**).

CONCLUDING REMARKS

This case report explored the possibility of dynamic MRI with the hips in neutral, extended, and flexed positions to evaluate the degree of craniocaudal displacement and indirectly the elastic properties of the filum terminale. Decreased to absent displacement of the conus medullaris was considered suggestive for decreased elasticity of the filum terminale, and hence, a diagnosis of tethered cord syndrome with a tight filum terminale was suspected. Although this diagnosis was confirmed during surgery, further studies are necessary to evaluate craniocaudal conus medullaris displacement in neurologically affected and unaffected dogs before this finding can be considered a reliable diagnostic criterion for tethered cord syndrome with a tight filum terminale in dogs.

ETHICS STATEMENT

The owners of clinical cases described in this study gave informed consent for the diagnostic procedures, treatment, and use of clinical data, such as medical history, imaging studies, and intraoperative pictures for research and publication purposes. All owners were informed that dynamic MRI with the hips in neutral, extended, and flexed positions would be performed. Because all diagnostic studies and initiated treatments were part of daily clinical activities, this project did not reach the threshold for submission to the local ethical and welfare committee.

AUTHOR CONTRIBUTIONS

SD, VW, and DN were involved in the care of this patient and were involved in planning this case report. SD was responsible for conception of this case report and preparation of the first draft. VW and DN provided feedback and were involved in revising the manuscript. All authors have read and approved the final version of the manuscript.

REFERENCES

1. Lew SM, Kothbauer KF. Tethered cord syndrome: an updated review. *Pediatr Neurosurg* (2007) 43:236–48. doi:10.1159/000098836
2. Hertzler DA, Depowell JJ, Stevenson CB, Mangano FT. Tethered cord syndrome: a review of the literature from embryology to adult presentation. *Neurosurg Focus* (2010) 29:E1. doi:10.3171/2010.3.FOCUS1079
3. Michelson DJ, Ashwal S. Tethered cord syndrome in childhood: diagnostic features and relationship to congenital anomalies. *Neurol Res* (2004) 26:745–53. doi:10.1179/016164104225017974
4. Yamada S, Won DJ. What is the true tethered cord syndrome? *Childs Nerv Syst* (2007) 23:371–5. doi:10.1007/s00381-006-0276-3
5. De Decker S, Gregori T, Kenny PJ, Hoy C, Erles K, Volk HA. Tethered cord syndrome associated with a thickened filum terminale in a dog. *J Vet Intern Med* (2015) 29:405–9. doi:10.1111/jvim.12522
6. De Lahunta A, Glass E, editors. Lower motor neuron: spinal nerve, general somatic efferent system. In: *Veterinary Neuroanatomy and Clinical Neurology*. 3rd ed. St Louis, Missouri: Elsevier Saunders (2009). p. 77–133.
7. Fletcher TF. Spinal cord and meninges. In: Evans HE, de Lahunta A, editors. *Miller's and Evans Anatomy of the Dog*. 4th ed. St Louis, Missouri: Elsevier Saunders (2013). p. 589–610.

8. Tu A, Steinbok P. Occult tethered cord syndrome: a review. *Childs Nerv Syst* (2013) 29:1635–40. doi:10.1007/s00381-013-2129-1
9. Nakanishi K, Tanaka N, Kamei N, Nakamae T, Izumi B, Ohta R, et al. Use of prone position magnetic resonance imaging for detecting the terminal filum in patients with occult tethered cord syndrome. *J Neurosurg Spine* (2013) 18:76–84. doi:10.3171/2012.10.SPINE12321
10. Hendson G, Dunham C, Steinbok P. Histopathology of the filum terminale in children with and without tethered cord syndrome with attention to the elastic tissue within the filum. *Childs Nerv Syst* (2016) 32:1683–93. doi:10.1007/s00381-016-3123-1
11. Ostling LR, Bierbrauer KS, Kuntz C IV. Outcome, reoperation, and complications in 99 consecutive children operated for tight or fatty filum. *World Neurosurg* (2012) 77:187–91. doi:10.1016/j.wneu.2011.05.017
12. Rade M, Könönen M, Vanninen R, Marttila J, Shacklock M, Kankaanpää M, et al. Young investigator award winner: in vivo magnetic resonance imaging measurement of spinal cord displacement in the thoracolumbar region of asymptomatic subjects. Part 1: straight leg raise test. *Spine* (2014) 39:1288–93. doi:10.1097/BRS.0000000000000263
13. Rade M, Shacklock M, Könönen M, Marttila J, Vanninen R, Kankaanpää M, et al. Part 3; developing methods of in vivo measurement of spinal cord displacement in the region of the thoracolumbar region of asymptomatic subjects with unilateral and bilateral straight leg raise tests. *Spine* (2015) 40:935–41. doi:10.1097/BRS.0000000000000914
14. Rade M, Könönen M, Marttila J, Shacklock M, Vanninen R, Kankaanpää M, et al. In vivo MRI measurement of spinal cord displacement in the thoracolumbar region of asymptomatic subjects with unilateral and sham straight leg raise test. *PLoS One* (2016) 11. doi:10.1371/journal.pone.0155927
15. De Vloo P, Monea AG, Sciot R, van Loon J, Van Calenbergh F. The filum terminale: a cadaveric study of anatomy, histology, and elastic properties. *World Neurosurg* (2016) 90:565–73. doi:10.1016/j.wneu.2015.12.103
16. Saker E, Henry BM, Tomaszewski KA, Loukas M, Iwanaga J, Oskouian RJ, et al. The filum terminale internum and externum: a comprehensive review. *J Clin Neurosci* (2017) 40:6–13. doi:10.1016/j.jocn.2016.12.020
17. Yamada S, Iacono RP, Andrade T, Mandybur G, Yamada BS. Pathophysiology of tethered cord syndrome. *Neurosurg Clin N Am* (1995) 6:311–23.
18. Filipiddis AS, Kalani Y, Theodore N, Rekate HL. Spinal cord traction, vascular compromise, hypoxia, and metabolic derangements in the pathophysiology of tethered cord syndrome. *Neurosurg Focus* (2010) 29:E1. doi:10.3171/2010.3.FOCUS1085
19. Johnson B, Stromqvist B. The straight leg raising test and the severity of symptoms in lumbar disc herniation: a preoperative and postoperative evaluation. *Spine* (1995) 29:27–30. doi:10.1097/00007632-199501000-00006

Conflict of Interest Statement: The authors declare that the research was conducted in the absence of any commercial or financial relationships that could be construed as a potential conflict of interest.

frontiers in Veterinary Science

CASE REPORT
published: 27 September 2017
doi: 10.3389/fvets.2017.00161

MRI Findings of Early-Stage Hyperacute Hemorrhage Causing Extramedullary Compression of the Cervical Spinal Cord in a Dog with Suspected Steroid-Responsive Meningitis-Arteritis

Adriano Wang-Leandro, Enrice-Ina Huenerfauth, Katharina Heissl and Andrea Tipold*

Department of Small Animal Medicine and Surgery, University of Veterinary Medicine Hannover, Foundation, Hannover, Germany

OPEN ACCESS

Edited by:
John Henry Rossmeisl, Virginia Tech, United States

Reviewed by:
Elsa Beltran, Royal Veterinary College, United Kingdom
Theresa Elizabeth Pancotto, Virginia Tech, United States

***Correspondence:**
Adriano Wang-Leandro
adriano.wang@tiho-hannover.de

Specialty section:
This article was submitted to Veterinary Neurology and Neurosurgery, a section of the journal Frontiers in Veterinary Science

Received: *14 August 2017*
Accepted: *13 September 2017*
Published: *27 September 2017*

Citation:
Wang-Leandro A, Huenerfauth E-I, Heissl K and Tipold A (2017) MRI Findings of Early-Stage Hyperacute Hemorrhage Causing Extramedullary Compression of the Cervical Spinal Cord in a Dog with Suspected Steroid-Responsive Meningitis-Arteritis. Front. Vet. Sci. 4:161. doi: 10.3389/fvets.2017.00161

A 9-month-old female Weimaraner was presented to the emergency service due to episodes of fever and neck pain. Physical examination revealed a stiff neck posture and elevated body temperature. Shortly after clinical examination was performed, the dog developed peracute onset of non-ambulatory tetraparesis compatible with a C1–C5 spinal cord (SC) lesion. Immediately thereafter (<1 h), MRI of the cervical SC was performed with a 3-T scanner. A left ventrolateral intradural-extramedullary SC compression caused by a round-shaped structure at the level of C3—C4 was evidenced. The structure was iso- to slightly hyperintense in T1-weighted (T1W) sequences compared to SC parenchyma and hyperintense in T2-weighted, gradient echo, and fluid-attenuated inversion recovery. Moreover, the structure showed a strong homogeneous contrast uptake in T1W sequences. Cerebrospinal fluid (CSF) analysis revealed a mixed pleocytosis, as well as elevated protein and erythrocyte count. Early-stage hyperacute extramedullary hemorrhage was suspected due to immune mediated vasculitis. The dog was maintained under general anesthesia and artificial ventilation for 24 h and long-term therapy with corticosteroids and physiotherapy was initiated. Eight weeks after initial presentation, the dog was ambulatory, slightly tetraparetic. Follow-up MRI showed a regression of the round-shaped structure and pleocytosis was not evident in CSF analysis. This report describes an early-stage hyperacute extramedullary hemorrhage, a condition rarely recorded in dogs even in experimental settings.

Keywords: magnetic resonance imaging, steroid-responsive meningitis-arteritis, canine, tetraparesis, signal intensity, subarachnoid hematoma, bleeding, immune-mediated vasculitis

CASE DESCRIPTION

A 9-month-old female Weimaraner (32.2 kg) was referred to the Department of Small Animal Medicine and Surgery of the University of Veterinary Medicine Hannover because of acute presentation of cervical pain and fever. The dog had no previous history of illness.

The symptoms were first noted by the owners 2 days before presentation when the dog was obtunded, inappetent, unwilling to stand up, and showed a stiff gait. The primary care veterinarian administered Metamizol (50 mg/kg TID, rectally) to reduce the fever.

At admission to the clinic, physical examination revealed a kyphotic posture with stiffness of the neck and head, body temperature of 39.3°C and a marked cervical hyperesthesia. The complete blood count (CBC) showed a leukocytosis of 35.12×10^3 cells/μl [reference interval (RI) $6–12 \times 10^3$ cells/μl] with a neutrophilia of 25.29 cells/μl (RI $3–10 \times 10^3$ cells/μl). Serum biochemistry revealed a mild elevation of the alkaline phosphatase and lactate values. Furthermore, prothrombin and partial thromboplastin time were elevated (laboratory findings are available in the Table S1 in Supplementary Material).

Approximately 45 min after the general physical examination was performed, the dog's clinical status worsened acutely. At this time point, besides the cervical hyperesthesia, neurological examination revealed a non-ambulatory tetraparesis with less voluntary movement present on the left limbs. Moreover, all limbs were spastic, spinal reflexes were normal and evaluation of cranial nerves was unremarkable. Therefore, the neuroanatomical localization of the lesion was set within C1–C5 spinal cord (SC) segments.

Immediately thereafter, general anesthesia was induced and MRI of the cervical SC was performed. For image acquisition, the dog was positioned in dorsal recumbency and a 15-channel sensitivity-encoding (SENSE) spine coil was used. Sagittal T1- and T2-weighted (T2W) sequences were performed (TR 11.3, TE 5.2; TR 3,100, TE 120, respectively), as well as transversal T1-weighted (T1W) (TR 11.3, TE 5.2) and T2W (TR 8,000, TE 120), T2*gradient echo (GRE; TR 660, TE 6.9), spectral attenuated inversion recovery (SPAIR; TR 5237, TE 100), and fluid-attenuated inversion recovery (FLAIR; TR 10,000, TE 140) sequences were acquired with a 3-T MRI scanner (Philips Achieva, Eindhoven, The Netherlands). Gadolinium was administered as contrast medium (Dotarem® 0.2 mmol/kg; i.v.) and sagittal and transversal T1W images were acquired post-contrast. Images were analyzed with commercially available software (RadiAnt DICOM Viewer, Version 4.0.3, Poznan, Poland).

MRI revealed an intradural-extramedullary compression of the SC at the level of C3–C4. The compression was caused by a round-shaped structure which showed a high intensity signal in T2W, GRE, SPAIR, and FLAIR sequences and an inhomogeneous iso- to slightly hyperintense signal in T1W sequences (**Figure 1**). A homogeneous strong contrast enhancement was noticed in T1W sequences after contrast medium administration. Additionally, a well-defined horizontal line dividing the mass into two different signal intensities was evidenced in both acquired planes of T2W sequences.

Furthermore, subarachnoidal space depicted ventral and dorsal to the SC in sagittal views did not display a strong hyperintense signal in T2W images, as characteristic in normal conditions. Instead, an inhomogeneous, mostly hypointense (T2W, T1W, and GRE) signal was present.

After performing a lumbar tap, cerebrospinal fluid (CSF) had a xanthochromic macroscopic appearance and the analysis evidenced a neutrophilic–monocytic mixed pleocytosis (value: 300 cells/μl; RI < 5 cells/μl) with elevated protein content (value: 851.82 mg/dl; RI < 40 mg/dl) and erythrocytes (value: 5,120 cells/μl). IgA levels in serum and CSF were within the upper reference value or elevated, respectively (IgA value for serum: 97.6 μg/ml; RI in serum: <100 μg/ml; IgA value in CSF: 16.4 μg/ml; RI in CSF: <0.2 μg/ml).

Due to the signalement, history, clinical presentation, and findings collected from diagnostic tests, an early-stage hyperacute, intradural-extramedullary compressive hemorrhage of the cervical SC secondary to an immune mediated vasculitis was suspected. A long-term protocol starting with high dose glucocorticosteroids was applied as previously reported (1), and artificial ventilation was administered for the first 24 h. During hospitalization, the dog developed a urinary tract infection which was treated with antibiotics according to antibiogram results and received daily physiotherapy sessions. The patient showed clinical improvement and was discharged from the clinic 16 days after initial presentation.

Eight weeks after initial presentation, follow-up general and neurological examinations, CBC and serum biochemistry, CSF analysis, and MRI of the cervical SC were performed. Same MRI protocols as used during the first examination were applied in the follow-up. At this time point, the dog was ambulatory showing a mild spastic tetraparesis, having the left limbs more affected and did not show any signs of pain during paravertebral palpation of the cervical region. Neuroanatomical localization during follow-up was consistent with a C1–C5 SC lesion. CBC and serum biochemistry were unremarkable and CSF taken from the cerebellomedullary cistern revealed a mild elevation of total protein content (value: 37.11 mg/dl; RI < 25 mg/dl). MRI revealed a focal intramedullary T2W hyperintensity at the level of C3–C4 with a presence of a left lateral T2W, GRE hypointense, and T1W hypo- to isointense structure, in comparison to unaffected SC segments, compatible with chronic hemorrhage, most probably residually lying within the subarachnoid space. Same signal pattern was noted within the SC parenchyma, suggesting focal intramedullary bleedings in the chronic stage (**Figure 2**). At this time point, subarachnoidal space dorsal and ventral to the SC in sagittal images appeared continuously T2W hyperintense. Additionally, a focal ventral intramedullary hyperintensity was noticed at the level of C2 (**Figure 2**; green arrowheads).

BACKGROUND

MRI represents a fundamental clinical tool for the understanding of the severity, extend, and localization of hemorrhages affecting the central nervous system (2). Temporal characterization of hemorrhage using MRI is challenging, as signal intensity in the different sequences varies depending on hemoglobin degradation product stages (3). Evolvement of signal intensity of canine blood has been recently described during *in vitro* and *in vivo* experimental studies (4, 5); however, the earliest time point in which signal intensity was recorded in such studies was 12 h after the hemorrhage was induced. Moreover, as hemorrhagic lesions are often associated with mass effect compressing the SC, further characterization of each temporal stage of bleedings

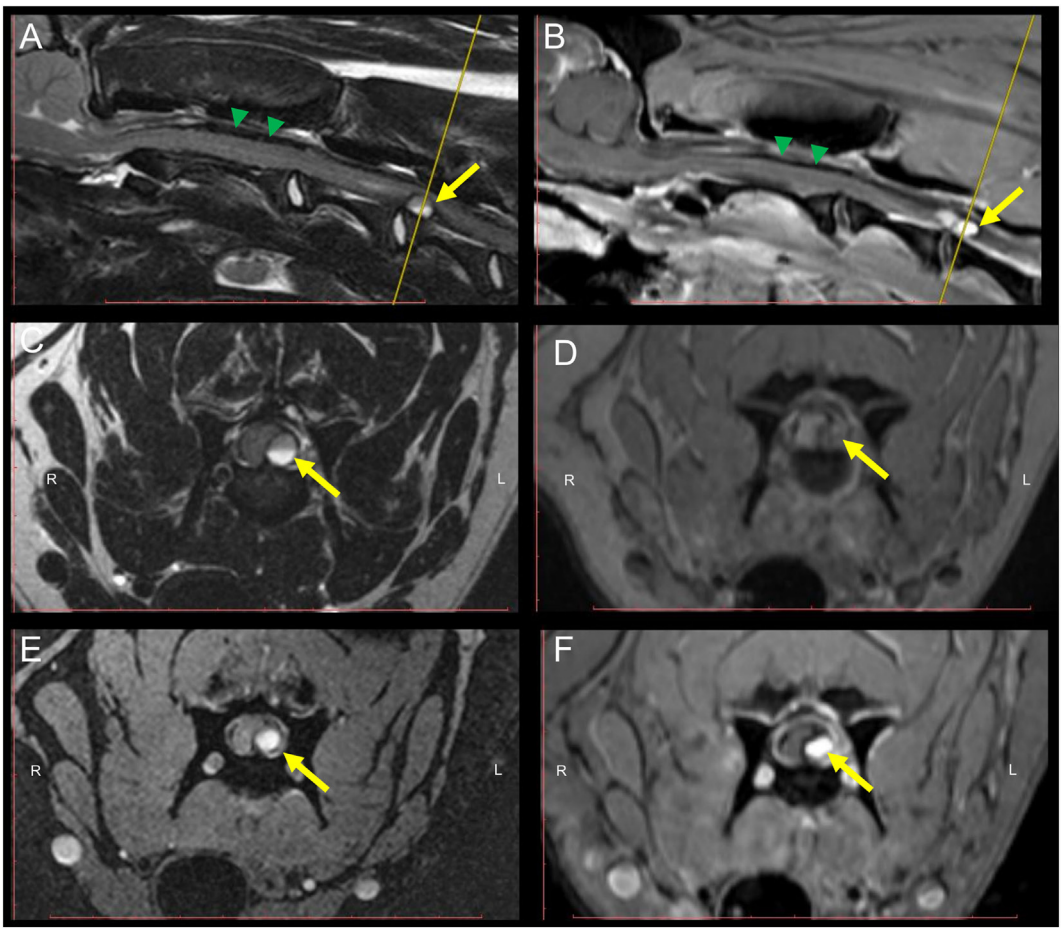

FIGURE 1 | MRI of the cervical spinal cord (SC) of a 9-month-old Weimaraner with peracute onset of non-ambulatory tetraparesis. Sagittal T2W **(A)** and post-contrast T1W **(B)** sequences depict an intradural-extramedullary left sided ventrolateral compression of the SC at the level of C3–C4. The yellow arrow points at the round-shaped structure causing the SC compression. Green arrowheads point to the T2W and T1W inhomogeneous, mostly hypointense material present within the subarachnoidal space dorsal to the SC. Transversal T2W **(C)**, pre-contrast T1W **(D)**, GRE **(E)**, and post-contrast T1W **(F)** sequences. A hyperintense signal of the core of the mass lesion compressing the SC can be evidenced in all sequences. A horizontal fluid-fluid level is noticed within the core of the round-shaped lesion in T2W sequences **(A,C)**. The yellow line in the sagittal T2W and post-contrast T1W **(A,B)** indicates the level at which transversal sequences are depicted. Abbreviations: T2W, T2-weighted; T1W, T1-weighted; GRE, T2*, gradient echo.

may be fundamental for ruling out neoplastic and inflammatory processes and subsequently for clinical decision making (6).

MRI signal characteristics of early-stage hyperacute subarachnoid hemorrhage have been previously reported in humans (7). Nonetheless, An and colleagues (5) recently demonstrated different signal intensity patterns in the subacute stage of hemorrhages between canines and humans, suggesting that direct extrapolation of human data for interpretation of MRI blood signal intensity in dogs may not be completely accurate.

This case report describes the MRI findings of an early-stage hyperacute cervical intradural, extramedullary hemorrhage causing compression of the SC.

DISCUSSION

Subarachnoid bleedings within the vertebral canal represent an unusual condition in dogs and humans (6, 8, 9). Immune-mediated diseases causing vasculitis and consequently rupture of blood vessels within the subarachnoid space have been previously described in humans (2, 10, 11). Steroid-responsive meningitis-arteritis (SRMA) is a common inflammatory disease causing meningitis in young dogs (1). In SRMA, a necrotizing fibrinoid arteritis occurs within the leptomeninges (12). Moreover, neutrophilic leukocytosis with presence of left shift is a common finding in dogs with SRMA (1). Although coagulation time alterations are not commonly described in SRMA, increased prothrombine and partial thromboplastin time values could be affected during systemic inflammatory diseases and could be an early indicator of disseminated intravascular coagulation (13).

Albeit performing a CSF tap in a dog with subarachnoid hemorrhage due to vasculitis represents a risk that could lead to further bleeding within the leptomeninges, CSF analysis and characterization are considered to be pivotal for the diagnosis

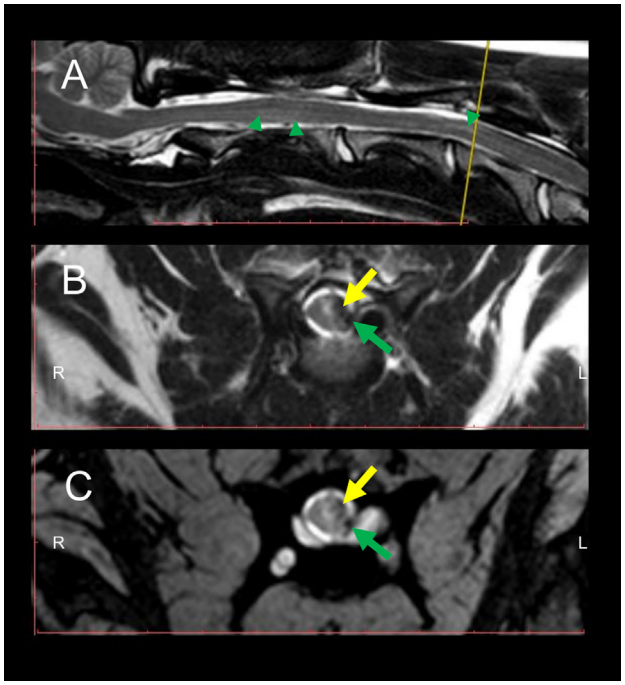

FIGURE 2 | Follow-up MRI of the cervical spinal cord (SC) 8 weeks after initial presentation at the clinic. Intramedullary hyperintensities are present in the sagittal T2W sequence **(A)** dorsally to the vertebral body of C2 and at the level of C3–C4 (green arrowheads) in comparison to signal intensity of non-affected SC segments. Transversal T2W **(B)** and GRE **(C)** sequences depict intramedullary hyperintensities and concomitant presence of hypointense intramedullary lesions at the level of the left dorsal horn and left lateral white matter tracts (yellow arrows) as well as in the subarachnoid space (green arrows). The yellow line in the sagittal T2W sequence **(A)** indicates the level at which transversal sequences are depicted. Abbreviations: T2W, T2-weighted; GRE, T2*, gradient echo.

and subsequently prompt treatment initiation of dogs with SRMA (1, 12). Increased levels of IgA in both, serum and CSF, have been shown to be a sensitive diagnostic tool for the diagnosis of SRMA; however, around 10% of the patients may be classified as false negatives (14). In this case, elevation of IgA levels in CSF could be explained due to complete disruption of the blood–SC barrier causing free entrance of this protein into the subarachnoidal space.

Signal intensity within the core of the round-shaped lesion was increased in all performed sequences and suggests presence of peracute arterial bleeding, which is typically characterized by high concentration of oxyhemoglobin within the erythrocytes (3, 7). Oxyhemoglobin displays diamagnetic properties, contrary to later stages of hemoglobin degradation such as deoxy-, methemoglobin, or hemosiderin with paramagnetic behavior (7). Therefore, an absence of lesional signal voidance in GRE sequences, an otherwise characteristic sign for hemorrhage, is to be expected at this stage.

Moreover, additional to the round-shaped structure compressing the SC in the described dog, a later stage of hyperacute hemorrhage is suspected to be present and distributed along the subarachnoid space visualized dorsal and ventral to the SC in sagittal T2W images, as signal intensity is depicted mildly inhomogeneous and hypointense in T2W, T1W, and GRE sequences, probably due to an increase in deoxyhemoglobin at these localizations (7). Nevertheless, rupture of small venous vessels could cause flow of deoxyhemoglobin rich erythrocytes into the subarachnoid space as well. Due to the larger magnetic moment of impaired electrons, paramagnetic substances cause magnetic field inhomogeneities and subsequently susceptibility effects in GRE sequences (3). Additionally, strong contrast enhancement of the lesion in T1W sequences suggests still an active bleeding process or a continuously disrupted blood–SC barrier.

Interestingly, in sagittal and transversal T2W sequences, signal intensity within the structure compressing the SC varies in the dorso-ventral axis, showing a clearly defined division. This finding suggests a separation and sedimentation of the cellular components of blood during first stages of bleeding (3). Since the dog was positioned in dorsal recumbency for image acquisition, the segment showing lower signal intensity is seen dorsally and it represents cellular accumulation before clot retraction occurs; conversely, the supernatant, which is presumably mostly composed of blood plasma is the most T2W hyperintense portion of the lesion (3).

Surgical decompression of the SC is the gold standard for treatment of subarachnoid hemorrhages causing SC compression in humans; nevertheless, a complete recovery of neurological deficits is achieved in approximately 40% of the cases (15). In dogs, surgical treatment seems to have a positive impact in the outcome of dogs with extramedullary hematomas as well (6). Medical treatment with corticosteroids was preferred in this case, as an immune mediated vasculitis was the highly likely underlying disease and the coagulation profile of the patient suggested a high risk of intraoperative bleeding. Moreover, artificial ventilation during the first 24 h was chosen as a supportive measure due to peracute worsening of clinical signs before performing MRI scan and suspected active hemorrhage that could eventually further compress the SC.

In follow-up MRI, regression of the round-shaped structure compressing the SC was evidenced. Moreover, T2W and GRE hypointense areas located in the subarachnoidal space and intramedullary are compatible with chronic stage of hemorrhage (5). During this stage, remaining extracellular hemoglobin is oxidized to ferritin and hemosiderin, which is phagocytized by macrophages and accumulated within the lysosomes (3). Hemosiderin and ferritin are highly paramagnetic, causing therefore susceptibility effects in GRE sequences (3, 7).

As conclusion, early-stage hyperacute hemorrhages in dogs display similar MRI characteristics as in humans, where hyperintensities in T2W, GRE, SPAIR, and FLAIR sequences and strong contrast enhancement in T1W may be evidenced.

ETHICS STATEMENT

As this manuscript does not describe any experimental procedure or clinical trial, but it represents a report of a single clinical case presented to a referral teaching veterinary hospital, no ethical approval was needed. The owner signed a consent form that the dog's data can be used for scientific studies.

AUTHOR CONTRIBUTIONS

AW-L was involved in the clinical approach of the case, interpreted MRI images, and wrote the manuscript. E-IH was involved in the clinical approach of the case. KH was involved in the clinical approach of the case. AT supervised the clinical approach of the case, interpreted MRI images, and discussed and critically revised the manuscript. All authors participated in revising and correcting the final version of the manuscript.

ACKNOWLEDGMENTS

Part of the information contained in this manuscript was accepted as a poster in the 30th Symposium of the European College of Veterinary Neurology, 21st–23rd September 2017, in Helsinki.

FUNDING

This publication was supported by the Deutsche Forschungsgemeinschaft and University of Veterinary Medicine Hannover within the funding programme Open Access Publishing.

SUPPLEMENTARY MATERIAL

The Supplementary Material for this article can be found online at http://journal.frontiersin.org/article/10.3389/fvets.2017.00161/full#supplementary-material.

REFERENCES

1. Tipold A, Schatzberg SJ. An update on steroid responsive meningitis-arteritis. *J Small Anim Pract* (2010) 51(3):150–4. doi:10.1111/j.1748-5827.2009.00848.x
2. Heit JJ, Iv M, Wintermark M. Imaging of intracranial hemorrhage. *J Stroke* (2017) 19(1):11–27. doi:10.5853/jos.2016.00563
3. Parizel PM, Makkat S, Van Miert E, Van Goethem JW, van den Hauwe L, De Schepper AM. Intracranial hemorrhage: principles of CT and MRI interpretation. *Eur Radiol* (2001) 11(9):1770–83. doi:10.1007/s003300000800
4. Jeong J, Park S, Jeong E, Kim N, Kim M, Jung Y, et al. Time-dependent low-field MRI characteristics of canine blood: an in vitro study. *J Vet Sci* (2016) 17(1):103–9. doi:10.4142/jvs.2016.17.1.103
5. An D, Park J, Shin JI, Kim HJ, Jung DI, Kang JH, et al. Temporal evolution of MRI characteristics in dogs with collagenase-induced intracerebral hemorrhage. *Comp Med* (2015) 65(6):517–25.
6. Hague DW, Joslyn S, Bush WW, Glass EN, Durham AC. Clinical, magnetic resonance imaging, and histopathologic findings in 6 dogs with surgically resected extraparenchymal spinal cord hematomas. *J Vet Intern Med* (2015) 29(1):225–30. doi:10.1111/jvim.12481
7. Schellinger PD, Fiebach JB. Intracranial hemorrhage: the role of magnetic resonance imaging. *Neurocrit Care* (2004) 1(1):31–45. doi:10.1385/NCC:1:1:31
8. Domenicucci M, Ramieri A, Paolini S, Russo N, Occhiogrosso G, Di Biasi C, et al. Spinal subarachnoid hematomas: our experience and literature review. *Acta Neurochir* (2005) 147(7):741–50; discussion 50. doi:10.1007/s00701-004-0458-2
9. Zhang HM, Zhang YX, Zhang Q, Song SJ, Liu ZR. Subarachnoid hemorrhage due to spinal cord schwannoma presenting findings mimicking meningitis. *J Stroke Cerebrovasc Dis* (2016) 25(8):e123–5. doi:10.1016/j.jstrokecerebrovasdis.2016.04.024
10. Lee JY, Kim YS, Kim HY, Park DW, Bae SC, Lee YJ. Non-aneurysmal subarachnoid hemorrhage in two patients with systemic lupus erythematosus: case reports and literature review. *Int J Rheum Dis* (2016). doi:10.1111/1756-185x.12867
11. Marder CP, Narla V, Fink JR, Tozer Fink KR. Subarachnoid hemorrhage: beyond aneurysms. *AJR Am J Roentgenol* (2014) 202(1):25–37. doi:10.2214/AJR.12.9749
12. Tipold A, Stein VM. Inflammatory diseases of the spine in small animals. *The Vet Clin North Am Small Anim Pract* (2010) 40(5):871–9. doi:10.1016/j.cvsm.2010.05.008
13. Herring J, McMichael M. Diagnostic approach to small animal bleeding disorders. *Top Companion Anim Med* (2012) 27(2):73–80. doi:10.1053/j.tcam.2012.07.004
14. Maiolini A, Carlson R, Schwartz M, Gandini G, Tipold A. Determination of immunoglobulin A concentrations in the serum and cerebrospinal fluid of dogs: an estimation of its diagnostic value in canine steroid-responsive meningitis-arteritis. *Vet J* (2012) 191(2):219–24. doi:10.1016/j.tvjl.2010.12.018
15. Kreppel D, Antoniadis G, Seeling W. Spinal hematoma: a literature survey with meta-analysis of 613 patients. *Neurosurg Rev* (2003) 26(1):1–49. doi:10.1007/s10143-002-0224-y

Conflict of Interest Statement: The authors declare that the research was conducted in the absence of any commercial or financial relationships that could be construed as a potential conflict of interest.

The reviewer TP and handling editor declared their shared affiliation.

frontiers in Veterinary Science

ORIGINAL RESEARCH
published: 16 March 2017
doi: 10.3389/fvets.2017.00030

Effect of Skull Type on the Relative Size of Cerebral Cortex and Lateral Ventricles in Dogs

*Anders M. Pilegaard[1], Mette Berendt[1], Pernille Holst[1], Arne Møller[2] and Fintan J. McEvoy[1]**

[1] Department of Veterinary Clinical and Animal Sciences, University of Copenhagen, Frederiksberg, Denmark,
[2] Center of Functionally Integrative Neuroscience, Department of Clinical Medicine, Aarhus University, Aarhus, Denmark

Volume measurements of the brain are of interest in the diagnosis of brain pathology. This is particularly so in the investigation hydrocephalus and canine cognitive dysfunction (CCD), both of which result in thinning of the cerebral cortex and enlarged ventricles. Volume assessment can be made using computed tomography or more usually magnetic resonance imaging (MRI). There is, however, some uncertainty in the interpretation of such volume data due to the great variation in skull size and shape seen in dog. In this retrospective study, we examined normal MRI images from 63 dogs <6 years of age. We used a continuous variable, the cranial index (CrI) to indicate skull shape and compared it with MRI volume measurements derived using Cavalieri's principle. We found a negative correlation between CrI and the ratio of cortical to ventricular volume. Breeds with a high CrI (large laterolateral compared to rostrocaudal cranial cavity dimension) had a smaller ratio of cortical to ventricular volume (low C:V ratio) than breeds with lower CrI skull types. It is important to consider this effect of skull shape on the relative volume estimates of the cerebral cortex and ventricles when trying to establish if pathology is present.

Keywords: canine cognitive dysfunction, hydrocephalus, skull type, lateral ventricles, cerebrum, cavalieri's principle

OPEN ACCESS

Edited by:
Susanne M. Stieger-Vanegas, Oregon State University, USA

Reviewed by:
Takehiko Kakizaki, Kitasato University, Japan
Derek Cissell, University of California Davis, USA

****Correspondence:***
Fintan J. McEvoy
fme@sund.ku.dk

Specialty section:
This article was submitted to Veterinary Imaging, a section of the journal Frontiers in Veterinary Science

Received: *12 October 2016*
Accepted: *17 February 2017*
Published: *16 March 2017*

Citation:
Pilegaard AM, Berendt M, Holst P, Møller A and McEvoy FJ (2017) Effect of Skull Type on the Relative Size of Cerebral Cortex and Lateral Ventricles in Dogs. Front. Vet. Sci. 4:30. doi: 10.3389/fvets.2017.00030

1. INTRODUCTION

Measurements of cerebral cortical and ventricular volumes are of diagnostic interest in the dog. This is especially so in dogs suspected of canine cognitive dysfunction (CCD). This is a disease of elderly dogs (≥8 years) resembling human Alzheimer's disease (1, 2). CCD is macroscopically characterized by cortical atrophy and widening of the ventricles and immunohistochemically by, e.g., deposition of the peptide, amyloid beta ($A\beta$) (3–10). Parameters that describes cerebral and ventricular volumes, such as the ratio of the volume of cerebral cortex to that of the lateral ventricles (C:V ratio) are of interest when trying to establish an antemortem diagnosis of CCD. Volume data alone cannot make such a diagnosis, but these data can be combined with clinical examination findings, including cognitive tests to help diagnostic accuracy. Various methods have been used to estimate the volume of brain structures on MRI scans in dogs. Each method has its own advantages and disadvantages. Visual rating scales are open to bias and subjectivity and yield a categorical variable but have been used for evaluating brain atrophy in aging dogs (7). Others have used the interthalamic adhesion thickness (5), which is a simple measurement to perform but may not accurately reflect three-dimensional structures. In the diagnosis of CCD, Cavalieri's principle was used to demonstrate a significantly smaller cortex/ventricle ratio when comparing a group of dogs with CCD (mean age, 12.6 years) with

a healthy control group (mean age, 8.8 years) (11). It is uncertain to what extent differences in the C:V ratio relate to pathology or to breed differences in skull size and shape. It is these differences in dogs without CCD or other disease known to influence brain volume that this study addresses.

Skull shape in dogs is commonly classified as dolichocephalic, mesaticephalic, or brachycephalic (12). An alternative approach to this categorical variable for classification is to use a continuous variable. Such a variable can be constructed as an index derived from various skull dimensions. One such index has been designated the cranial index (CrI) (12). This index can be used not only in analysis as a continuous variable but also to categorize dogs as brachycephalic (high CrI), mesaticephalic (intermediate CrI), or dolichocephalic (low CrI). Studies on the influence of skull shape on the regions of the brain, e.g., the olfactory bulb (13) and ventricles (14, 15), indicate that the size of the cerebral ventricles might be correlated to skull shape. The classification of skull shape is not uniform across studies.

In this retrospective study, we use Cavalieri's principle to determine ventricular and cerebral volumes in dogs of different breeds and size. Cavalieri's principle is an established methodology in volumetric stereological measurement. It is particularly easily applied to MRI, computer tomography, and Positron emission tomography images of brain structures (16–20). The measurements obtained are used to calculate the C:V ratio. We examine the relationship between this ratio and an index of skull shape to address the hypothesis that skull shape has and effect on C:V ratio in dogs. We further examined the reproducibility of our measurements to give an indication of clinical applicability.

2. MATERIALS AND METHODS

2.1. Study Population

Records for dogs ≤6 years old that had MRI scans performed as part of a clinical investigation for neurological disease at the Copenhagen University Hospital for Companion Animals, Denmark, between 2008 and 2012 were reviewed. Inclusion criteria required that the images were evaluated by a board-certified radiologist and were found to be without imaging evidence of pathology.

2.2. Imaging and Randomization

Images were obtained using a low-field MRI scanner [Esaote Vetscan 0.2 Tesla (Esaote Group, Genova, Italy)]. All dogs were placed under general anesthesia for imaging. MRI images were viewed and measured in a DICOM viewer (RemotEye, NeoLogica s.r.l., Cairo Montenotte, Italy). Only T1-weighted images (TE in the range 16.00–18.00 ms and TR 600–800) in transverse and dorsal planes were used for evaluation of cortical and lateral ventricular size in this study. MRI scan measurements were made by the first author (AP) after training from a board-certified specialist in veterinary radiology (FM) and a medical neurologist (AM) in the use of the medical viewer, recognition of relevant brain anatomy, assessment of the cranial index (CrI), and the application of Cavalieri's principle. Patients were randomized for MRI measurements.

2.3. Cranial Index

The cranial index (CrI) was used as a descriptor of skull shape (12). It describes the width of the skull in relation to its length. CrI was calculated as follows:

$$CrI = \frac{Cranial\ width}{Cranial\ length} \cdot 100. \quad (1)$$

The cranial length is defined as being the maximum distance from the cranial to the caudal aspect of the cranial cavity. The cranial width was defined as the maximum distance (lateral to lateral) across the cranial cavity. These distances were measured from sagittal (cranial length) and transverse (cranial width) plane MRI images.

2.4. Cavalieri's Principle

Volumetric estimation of cortex size and the lateral ventricle size was achieved using Cavalieri's principle. This stereological method allows estimation of volume as follows:

$$V_{Total} = d \cdot a_p \cdot \sum p, \quad (2)$$

where V_{Total} is the total volume of the object to be measured, d is the distance between the sections that are being analyzed (i.e., slice thickness plus slice interval), a_p is the area associated with one counting point (see below), and $\sum p$ is the sum of all such points counted for the given object, in this case either the cortex or ventricle. Because of contrast resolution limitations imposed by the magnetic field strength, cortex was defined as both white and gray substance. Structures not included as cortex included the olfactory bulb, hippocampus, pons, brain stem, thalamus, cerebellum, and structures associated with these. To ensure unbiased estimations, Cavalieri's principle requires that the object to be measured is placed randomly with respect to the grid and that the entire object is included in the image stack. In MRI scanning, the former is easily achieved since the first section (slice) of a sequence is randomly positioned within the patient. There is no specific alignment of any anatomical feature on the z-axis of the scanner, so that the start point is essentially random.

2.4.1. Counting Procedure

The first author (AP) performed the counting procedure. Two image planes were used in the counting procedure: the sagittal plane images to assist the orientation of brain structures and transverse plane images for actual counting. The cortex and ventricles were measured separately. The counting procedure starts at the most rostral slice that includes the structure (cortex or ventricle) to be measured. Counting continues caudally to the most caudal slice that includes the structure to be measured. Counting requires the use of a grid, with regularly spaced crosses, which is superimposed on the image. This can be generated digitally and superimposed on the image if the viewing software permits or, as was done for this study, can be printed on a transparent sheet of plastic (A4 size) and placed directly on the viewing monitor, superimposed on the sections to be measured. Once placed on the monitor, the grid is left *in situ*

for the entire counting procedure. Slice thickness was set in this study in the range 4.5–5 mm. By scrolling through the stack of transverse images, a check was made to ensure that images were zoomed to allow satisfactory evaluation of each structure to be measured (ventricle or cortex) but not so enlarged that any part of the structure extend beyond the limits of point counting grid. Once a suitable level of zoom was established for the particular region (ventricle or cortex), it was maintained for evaluation of that region in the entire stack in that patient. The image distance represented by the distance between the counting points on the grid for that particular image stack and zoom setting was then measured using the viewer software. The square of this distance gives the area associated with each counting point, a_p for the variable in equation (2). The degree of zooming was unchanged within any region, ventricle or cortex in a particular individual, but it can be and typically was altered between regions and individuals. Thus, values for a_p are specific to the individual patient and the region examined. The act of counting requires that the reader determines how many grid counting points intersect the structure being measured. It amounts to a series of yes, no decisions. An example of the grid arrangement is shown in **Figure 1**, and a schematic for the counting procedure is shown in **Figure 2**. The CE for the measurements was calculated as described below using methodology based on previously described techniques (17).

2.5. Measurement Reliability

2.5.1. Interrater Agreement

A second evaluator (PH) was enlisted for determining interrater agreement for volume estimates. The training session for this individual comprised instruction in identifying brain structures, measuring cranial length and width, and performing the counting procedure. Ten random image sets were used for training. This same individual then performed the measurements in 9 other dogs from the study population that were also chosen randomly for the inter–rater analyses. These values were then compared with those obtained in a repeat analysis in the same 9 individuals by the other evaluator (AP). Both evaluators were blinded to the results of previous measurements.

2.5.2. Intrarater Agreement

The same 9 dogs mentioned above for interrater analysis were also used for the intrarater reliability testing. The same individual (AP) performed repeated measurements at least 2 weeks after the initial measurements. This ensured that individual image stacks from the initial reading were not recalled during the second measurement session.

2.6. Data Analysis

CrI measurements for each dog were plotted against log-transformed C:V ratio. Correlation between CrI and the transformed C:V ratio was tested using Spearman's rank correlation coefficient (a non-Gaussian distribution was assumed). Linear regression was also used to test linearity of the relationship between the two variables.

Two possible confounding factors, age and weight, were tested against C:V ratio and CrI individually, to reveal possible associations, using the same methods as described above. For evaluation of interrater and intrarater agreement, Bland–Altman difference plots were used. All statistical data analysis was done using either the statistical software GraphPad Prism v.6 (GraphPad Software Inc., La Jolla, CA, USA) or R (version 3.3.1, R Foundation for Statistical Computing, Vienna, Austria) (21) according to availability. A p value <0.05 was considered statistically significant.

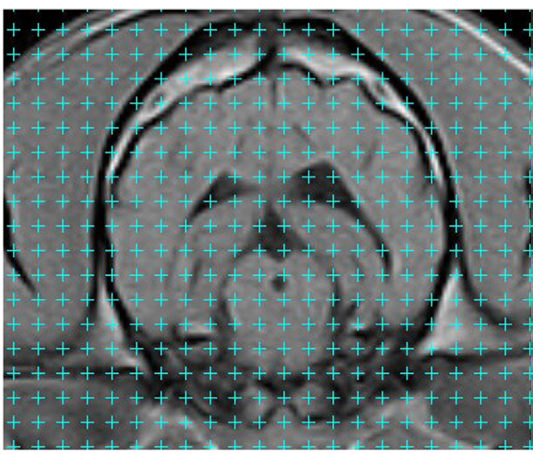

FIGURE 1 | Transverse T1-weighted magnetic resonance image of the cranial cavity taken at the level of the temporomandibular joints. A grid pattern has been applied. Volume measurement is achieved by counting the number of counting points superimposed on the structure to be measured. Counting points are located at the upper right corner of each of the crosses in the grid (i.e., for each cross, adjacent to the intersection of the two cross lines, at the pixel that is immediately right of the vertical line and immediately above the horizontal line of the cross). The counting process is a series of yes:no questions, most of which are readily answered.

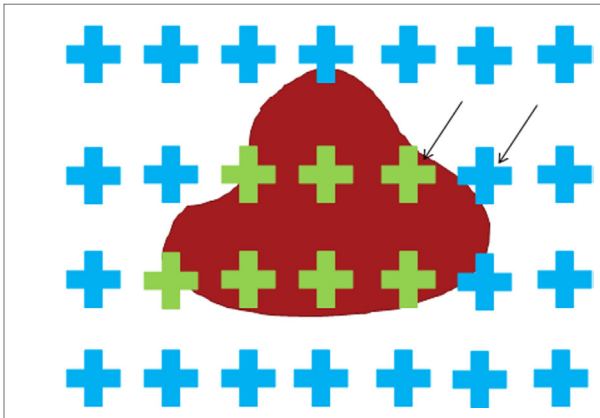

FIGURE 2 | Schematic of the point counting technique. The crosses serve to help the reader identify the counting points that are located at the upper right corner of each cross. The black arrows indicate two such points. The only decision to be made is whether the counting point is or is not on the object. In this illustration, the blue color indicates that the point associated with the cross does not intersect the object. The green color indicates that the point associated with the cross does intersect the object.

3. RESULTS

3.1. Study Population

Sixty–three dogs met the inclusion criteria. Scans were performed for a variety of reasons mainly for the investigation of epilepsy (47 dogs), seizures (6 dogs), and lesser numbers for investigation of other suspected diseases including middle ear disease. The mean age was 2.5 years (median, 2 years; SD, 1.6 years). Mean body weight was 20.8 kg (median, 18 kg; SD, 14.4 kg). A total of 40 dog breeds were included. Breeds encountered were retriever type dogs (n = 8), followed by Cavalier King Charles spaniels (n = 4) and lesser numbers of the other breeds.

3.2. Cortex: Ventricular Ratio (C:V Ratio) and Cranial Index (CrI) Estimates

Volume estimates of the cortex ranged from 21.8 to 77.8 cm^3, while those for the ventricle ranged from 0.2 to 4.6 cm^3. This resulted in a range in C:V ratio values from 7.5 to 408. Values of CrI ranged from 43 to 91%. There was a significant negative correlation between CrI and log_{10} C:V ratio (r = −0.44, $p = 0.0003$, 95%confidence interval = −0.62 to −0.21). A linear regression model for the association between CrI and log_{10} C:V ratio showed the relationship between the variables to be represented by the equation $CrI = 2.8 - 0.02\log_{10}(C{:}\ V\ ratio)$. This regression line is shown in **Figure 3** together with its 95% confidence interval.

3.3. Measurement Reliability

3.3.1. Interrater Agreement

The interrater agreement for C:V ratio was 82%. This result and other interrater agreement data are given in **Table 1**. The variability between readers was independent of the size of measurements concerned.

3.3.2. Intrarater Reliability

The intrarater agreement for C:V ratio was 94%. This result and other intrarater agreement data are also given in **Table 1**. The within-reader variability was independent of the size of measurements concerned.

3.4. Confounding Factors

No associations were found between weight, age, and C:V ratio nor between age and CrI. A negative linear correlation (r = 0.74, $p < 0.0001$) was seen between weight and CrI. These data, however, also showed a significant deviation from linearity ($p = 0.0035$). Thus, confirmation of an association between weight and CrI would require non-linear regression, which was beyond the scope of this study.

4. DISCUSSION

The results show a significant moderate negative correlation, r = −0.44 ($p = 0.0003$), between the log transform of the C:V ratio and CrI, the latter used as a measurement of skull type. The log transform of the volume measurements resulted in a correlation that was more readily observed and that could be represented by a simple linear model. The linear regression is shown in **Figure 3**.

TABLE 1 | Intrarater and interrater agreement for measurements made from 9 samples using Cavalieri's principle.

	Bias (agreement%)	95% limits of agreement
Intrarater agreement		
C:V ratio	6 (94)	−43 to 55
Cortical volume	3 (97)	−15 to 21
Ventricular volume	22.9 (77.1)	−48 to 41.7
CrI	0.1 (99.9)	−8 to 8
Interrater agreement		
C:V ratio	−18 (82)	−81 to 46
Cortical volume	−2 (98)	−23 to 18
Ventricular volume	15 (85)	−49 to 79
CrI	4 (96)	−48 to 79

Dimensions for bias are mm^3 for both cortical and ventricular volumes. Bias values for cortex to ventricular volume ratio (C:V ratio) and for cranial index (CrI) are dimensionless. Agreement is quoted as percent.

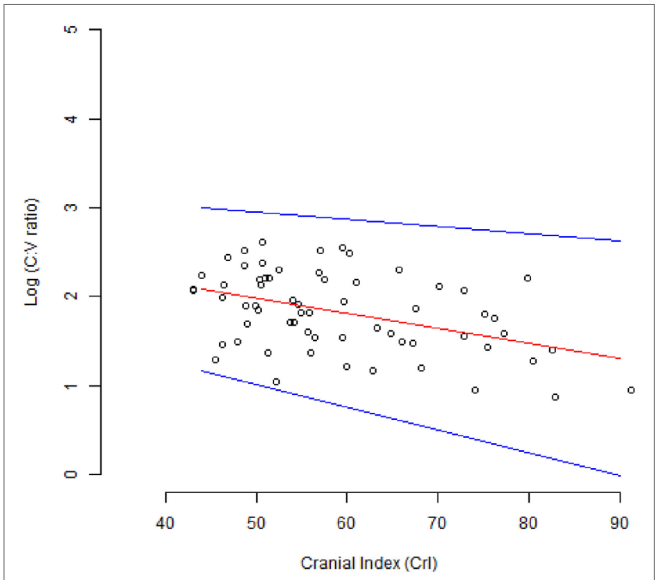

FIGURE 3 | Scatter plot of the relationship between the log_{10} *C: V ratio* and the cranial index (CrI). The red line shows the line of best fit for the linear regression model. The blue lines show the 95% confidence interval.

As the CrI of the dog skull increased, the C:V ratio decreased. This decrease in C:V ratio could be explained by a naturally larger ventricular volume, a smaller cortical volume, or a combination of the two. This is likely a physiological or breed-related phenomenon rather than CCD-associated cortical atrophy, since all of the dogs participating were ≤6 years of age and too young to show changes of CCD.

Breed-related differences in ventricle size would explain our findings and accord with findings from other studies. In one study, miniature and brachycephalic breeds in particular exhibited what was defined as ventriculomegaly (15). The same study showed no correlation between ventricular size and clinical signs of neurological disease. In another study, MRI images from Yorkshire Terriers were compared to images from German Shepherd dogs (14). A significant difference in the ratio of ventricular size to cortex between the two breeds was found, and again there were

no findings to indicate that the variations in ventricular size demonstrated were associated with neurological disease. These results indicate that there is a breed-related variation in ventricular size.

We chose to use a continuous variable, the CrI, as a descriptor of cranial shape. The alternative of dividing dogs into categories depending on skull type (brachycephalic, mesaticephalic, or dolichocephalic) is problematic (14). First, the division on the basis of breed is unreliable, as within-breed variation of skull type can be significant. In-breed variation in ventricle size has been demonstrated, and this could be linked to in-breed variation of skull type (22). Second, no clear and generally agreed criteria exist for placement of a breed in a particular category. There are differing criteria concerning methods of measurements and thresholds for the three categories mentioned above. The criteria chosen may vary between studies. In three separate studies, dogs of the boxer breed were assigned to the brachycephalic category in one study, mesaticephalic category in a second study, and the dolichocephalic category in third study (12, 23, 24). Finally, the three categories are arbitrary designations and are not based on clinical considerations. A continuous scale of measurement is more desirable, and thus, CrI was used in this study.

Analysis of possible confounding factors in this study found a negative correlation between CrI and body weight. This association could be explained by the fact that many dogs with high CrI were from the smaller breeds, which have been selected for a brachycephalic type head conformation.

The method of volume estimation utilizes Cavalieri's principle. This volumetric stereological measurement technique has been used for estimation of brain volume and recommended for clinical use in elderly people with dementia (25). The method has been used also in the evaluation of tumor volume from MRI images and again recommended for clinical use (26). The counting procedure lasted on average approximately 10 minutes per patient. An advantage of this technique is that the position of most counting points, cortical or ventricular, will be clear. Only a few will be on a border between the two regions and require effort for a decision. In contrast methods that require the operator to outline the limits of a structure by definition require the user to constantly work at the image area of maximum uncertainty; the border between two tissues. An additional benefit is that the coefficient of error (CE) for the method can be calculated. This gives a statistical estimate of the reliability of the measurements and depends in part on the relationship between the grid spacing and the object to be measured. The greater the number of grid point counts, the lower the CE. The CE is also dependent on the number of slices encompassing the object to be measured. This is a function of object size and slice thickness. It is accepted that while the ease with which measurements can be made and volumes calculated are merits of the technique; it is also true that the calculation of the coefficient of error is somewhat involved.

There are many alternative methods for evaluating the volume of body structures, and these include, but are not limited to, manual or automatic segmentation methods that require the creation of regions of interest. Region growing algorithms and other methods for determining volumes from image stacks are available in widely used software such as ImageJ (27) and Osirix (28). However, their use for this purpose is typically time consuming when evaluating structures that are irregular and complicated in shape and will result in volume estimates with uncertain error coefficients. Also, the structure to be measured must completely contrast with adjacent tissue, otherwise the region of interest will escape the structure to be measured. Methodologies such as measurement of interthalamic adhesion measurement are simple to perform but are oversimplistic in that it is difficult for a one-dimension spatial measurement to represent a geometrically irregular volume. In contrast, the methodology used in this article lacks the apparent sophistication of analysis software, is simple to perform, and yet provides a volume estimate, together with its coefficient of error. It is a methodology that is not widely used in the veterinary community but perhaps deserves more attention.

Our results show excellent interrater and intrarater agreement with the method. The low coefficient of error (3.4%) in cortical estimations and the high levels of intrarater and interrater agreement (97 and 98%, respectively) show that the method has high precision when used to estimate cortex volume in a dog brain. Measurements of the ventricles were less precise (coefficient of error 13%) due to their smaller volume. The higher coefficient of error values was obtained from scans in which the ventricles were visible on either 3 or on 4 slices only. Volume estimates from low numbers of slices will result in a high coefficient of error. The error in the method, however, is symmetrically distributed, so that one is as likely to overestimate a volume as to underestimate it. Therefore, we do not think that there is a bias in this regard. Compensating for low slice numbers by selecting a smaller point grid and thus more counts per slice will help reduce the coefficient of error, but only to a limited extent and at the cost of disproportionate increased effort in point counting. The method ideally requires that the object to be measured appears on 6–8 slices or more. Slice thickness should be chosen accordingly. An MRI scanner with a higher magnetic field strength would have allowed thinner and therefore more slices with superior contrast resolution than those available from the low-field magnet used in this study.

Notwithstanding these reservations, the C:V ratio appears to be a good candidate for assisting in the diagnosis of conditions such as CCD, where cortical and ventricular volumes are important. The results of this study suggest that a correction based on the CrI can be applied for comparisons between dogs of different breed. If such a correction step is not taken, a low C:V ratio in breeds with a high CrI may be misinterpreted. This study comprised 63 dogs. Future experience with a with a larger cohort of healthy young dogs would of course assist in validating and defining this negative correlation between C:V ratio and CrI. Ultimately volume measurements will have to prove their clinical relevance for diagnosis or prognosis. The effect of aging on these indices also requires evaluation since age-related change in the ventricular system in clinically healthy dogs has been described (4, 6), and this should be differentiated from changes potentially related to disease.

5. CONCLUSION

This study shows an association between the ratio of cortical to ventricular volume (C:V ratio) and skull type, represented by CrI. Breeds with a high CrI (large latero-lateral compared to

rostro-caudal cranial cavity dimension) have a smaller ratio of cortical to ventricular volume (low C:V ratio) in comparison to breeds with lower CrI skull types. The index, C:V ratio, is a good candidate for future evaluation of cortical atrophy and ventricular dilation in elderly dogs and in dogs with CCD. In addition, this application of Cavalieri's principle to canine brain measurements resulted in high intrarater and interrater agreement. The simplicity of the method and the lack of special software requirements make it attractive for both the clinical researcher and general practitioner.

6. EQUATIONS

Coefficient of Error Calculations

Let the series of measurements in n slices that intersect a structure be denoted by $P_1, P_2, \ldots, P_n$, so that the number of points intersecting the structure in the ith slice is P_i. If A, B, and C are defined such that

$$A = \sum_{i=1}^{n} P_i \cdot P_i B = \sum_{i=1}^{n-1} P_i \cdot P_{i+1} C = \sum_{i=1}^{n-2} P_i \cdot P_{i+2},$$

then the variance due to systematic sampling and measurement error, Var_{sys} is given by:

$$Var_{sys} = \frac{1}{240} \cdot (3 \cdot (A - Var_{noise}) - 4 \cdot B + C).$$

The variance due to noise, Var_{noise} is given by:

$$Var_{noise} = 0.0724 \cdot 8 \cdot \sqrt{\sum_{i=1}^{n} n \cdot P_i},$$

where the constant 0.0724 is derived from the Riemann zeta function and the constant 8 is the cube of a form factor of 2, which has been chosen based on experience with the technique in brain volume analysis.

The total coefficient of error CE for the volume measurement can be calculated:

$$CE = \frac{\sqrt{Var_{sys} + Var_{noise}}}{\sum_{i=1}^{n} P_i}.$$

ETHICS STATEMENT

This retrospective study used imaging data acquired from veterinary patients at the university teaching hospital. As such these were animals under veterinary care and were not designated "experimental animals."

AUTHOR CONTRIBUTIONS

AP, MB, PH, and FM made substantial contributions to the design of the study, data acquisition, analysis, and interpretation. AM made substantial contributions to the design of the study, analysis, and interpretation.

FUNDING

This project was self funded from clinical income at the Department of Veterinary Clinical and Animal Sciences, University of Copenhagen.

REFERENCES

1. Schutt T, Toft N, Berendt M. Cognitive function, progression of age-related behavioral changes, biomarkers, and survival in dogs more than 8 years old. *J Vet Intern Med* (2015) 29(6):1569–77. doi:10.1111/jvim.13633
2. Fast R, Schutt T, Toft N, Moller A, Berendt M. An observational study with long-term follow-up of canine cognitive dysfunction: clinical characteristics, survival, and risk factors. *J Vet Intern Med* (2013) 27(4):822–9. doi:10.1111/jvim.12109
3. Cummings BJ, Head E, Afagh AJ, Milgram NW, Cotman CW. Beta-amyloid accumulation correlates with cognitive dysfunction in the aged canine. *Neurobiol Learn Mem* (1996) 66(1):11–23. doi:10.1006/nlme.1996.0039
4. Gonzalez-Soriano J, Garcia PM, Contreras-Rodriguez J, Martinez-Sainz P, Rodriguez-Veiga E. Age-related changes in the ventricular system of the dog brain. *Ann Anat* (2001) 183(3):283–91. doi:10.1016/S0940-9602(01)80236-3
5. Hussein AK, Sullivan M, Penderis J. Effect of brachycephalic, mesaticephalic, and dolichocephalic head conformations on olfactory bulb angle and orientation in dogs as determined by use of in vivo magnetic resonance imaging. *Am J Vet Res* (2012) 73(7):946–51. doi:10.2460/ajvr.73.7.946
6. Kimotsuki T, Nagaoka T, Yasuda M, Tamahara S, Matsuki N, Ono K. Changes of magnetic resonance imaging on the brain in beagle dogs with aging. *J Vet Med Sci* (2005) 67(10):961–7. doi:10.1292/jvms.67.961
7. Pugliese M, Carrasco JL, Gomez-Anson B, Andrade C, Zamora A, Rodriguez MJ, et al. Magnetic resonance imaging of cerebral involutional changes in dogs as markers of aging: an innovative tool adapted from a human visual rating scale. *Vet J* (2010) 186(2):166–71. doi:10.1016/j.tvjl.2009.08.009
8. Rofina JE, van Ederen AM, Toussaint MJ, Secreve M, van der Spek A, van der Meer I, et al. Cognitive disturbances in old dogs suffering from the canine counterpart of Alzheimer's disease. *Brain Res* (2006) 1069(1):216–26. doi:10.1016/j.brainres.2005.11.021
9. Tapp PD, Siwak CT, Gao FQ, Chiou JY, Black SE, Head E, et al. Frontal lobe volume, function, and beta-amyloid pathology in a canine model of aging. *J Neurosci* (2004) 24(38):8205–13. doi:10.1523/JNEUROSCI.1339-04.2004
10. Schutt T, Helboe L, Pedersen LO, Waldemar G, Berendt M, Pedersen JT. Dogs with cognitive dysfunction as a spontaneous model for early Alzheimer's disease: a translational study of neuropathological and inflammatory markers. *J Alzheimers Dis* (2016) 52(2):433–49. doi:10.3233/JAD-151085
11. Fast R. *A Clinical and Neuroimaging Study of Canine Cognitive Dysfunction with Comparative Aspects to Alzheimer's Disease in Humans*. Ph.D. thesis. Copenhagen: University of Copenhagen (2013).
12. Evans HE, DeLahunta A. *Miller's Anatomy of the Dog*. St. Louis: Elsevier Saunders (2012).
13. Hasegawa D, Yayoshi N, Fujita Y, Fujita M, Orima H. Measurement of interthalamic adhesion thickness as a criteria for brain atrophy in dogs with and without cognitive dysfunction (dementia). *Vet Radiol Ultrasound* (2005) 46(6):452–7. doi:10.1111/j.1740-8261.2005.00083.x
14. Esteve-Ratsch B, Kneissl S, Gabler C. Comparative evaluation of the ventricles in the yorkshire terrier and the german shepherd dog using low-field MRI. *Vet Radiol Ultrasound* (2001) 42(5):410–3. doi:10.1111/j.1740-8261.2001.tb00960.x
15. Spaulding KA, Sharp NJH. Ultrasonographic imaging of the lateral cerebral ventricles in the dog. *Vet Radiol* (1990) 31(2):59–64. doi:10.1111/j.1740-8261.1990.tb00783.x

16. Eriksen N, Rostrup E, Andersen K, Lauritzen MJ, Fabricius M, Larsen VA, et al. Application of stereological estimates in patients with severe head injuries using CT and MR scanning images. *Br J Radiol* (2010) 83(988):307–17. doi:10.1259/bjr/18575224
17. Gundersen HJ, Jensen EB, Kieu K, Nielsen J. The efficiency of systematic sampling in stereology – reconsidered. *J Microsc* (1999) 193(Pt 3):199–211. doi:10.1046/j.1365-2818.1999.00457.x
18. Garcia-Finana M, Cruz-Orive LM, Mackay CE, Pakkenberg B, Roberts N. Comparison of MR imaging against physical sectioning to estimate the volume of human cerebral compartments. *Neuroimage* (2003) 18(2):505–16. doi:10.1016/S1053-8119(02)00021-6
19. Jelsing J, Rostrup E, Markenroth K, Paulson OB, Gundersen HJ, Hemmingsen R, et al. Assessment of in vivo MR imaging compared to physical sections in vitro – a quantitative study of brain volumes using stereology. *Neuroimage* (2005) 26(1):57–65. doi:10.1016/j.neuroimage.2005.01.005
20. Mayhew TM, Olsen DR. Magnetic resonance imaging (MRI) and model-free estimates of brain volume determined using the cavalieri principle. *J Anat* (1991) 178:133–44.
21. Core Team R. *R: A Language and Environment for Statistical Computing*. Vienna, Austria: R Foundation for Statistical Computing (2015).
22. Haan CED, Kraft SL, Gavin PR, Wendling LR, Griebenow ML. Normal variation in size of the lateral ventricles of the labrador retriever dog as assessed by magnetic resonance imaging. *Vet Radiol Ultrasound* (1994) 35(2):83–6. doi:10.1111/j.1740-8261.1994.tb00191.x
23. Alpak H, Mutus R, Onar V. Correlation analysis of the skull and long bone measurements of the dog. *Ann Anat* (2004) 186(4):323–30. doi:10.1016/S0940-9602(04)80050-5
24. Ellis JL, Thomason J, Kebreab E, Zubair K, France J. Cranial dimensions and forces of biting in the domestic dog. *J Anat* (2009) 214(3):362–73. doi:10.1111/j.1469-7580.2008.01042.x
25. Fernandez-Viadero C, Gonzalez-Mandly A, Verduga R, Crespo D, Cruz-Orive LM. Stereology as a tool to estimate brain volume and cortical atrophy in elders with dementia. *Rev Esp Geriatr Gerontol* (2008) 43(1):32–43.
26. Sonmez OF, Odaci E, Bas O, Colakoglu S, Sahin B, Bilgic S, et al. A stereological study of MRI and the cavalieri principle combined for diagnosis and monitoring of brain tumor volume. *J Clin Neurosci* (2010) 17(12):1499–502. doi:10.1016/j.jocn.2010.03.044
27. Schneider CA, Rasband WS, Eliceiri KW. NIH Image to ImageJ: 25 years of image analysis. *Nat Methods* (2012) 9(7):671–5. doi:10.1038/nmeth.2089
28. Rosset A, Spadola L, Ratib O. OsiriX: an open-source software for navigating in multidimensional DICOM images. *J Digit Imaging* (2004) 17(3):205–16. doi:10.1007/s10278-004-1014-6

Conflict of Interest Statement: The authors declare that the research was conducted in the absence of any commercial or financial relationships that could be construed as a potential conflict of interest.

frontiers in Veterinary Science

METHODS
published: 21 March 2017
doi: 10.3389/fvets.2017.00041

Dynamic Susceptibility Contrast Magnetic Resonance Imaging Protocol of the Normal Canine Brain

Krystina L. Stadler†, Anthony P. Pease and Elizabeth A. Ballegeer*

Department of Small Animal Clinical Sciences, Michigan State University College of Veterinary Medicine, East Lansing, MI, USA

OPEN ACCESS

Edited by:
Andrea Tipold,
University of Veterinary Medicine Hanover, Germany

Reviewed by:
Christopher R. Lamb,
Royal Veterinary College (RVC), UK
Elsa Beltran,
Royal Veterinary College (RVC), UK

***Correspondence:**
Krystina L. Stadler
krystina@vt.edu

Presented in abstract form at the American College of Veterinary Radiology Annual Conference, Minneapolis, MN, USA, 2015.

†Present address:
Krystina L. Stadler, Department of Small Animal Clinical Sciences, Virginia-Maryland College of Veterinary Medicine, Blacksburg, VA, USA

Specialty section:
This article was submitted to Veterinary Imaging, a section of the journal Frontiers in Veterinary Science

Received: *23 November 2016*
Accepted: *07 March 2017*
Published: *21 March 2017*

Citation:
Stadler KL, Pease AP and Ballegeer EA (2017) Dynamic Susceptibility Contrast Magnetic Resonance Imaging Protocol of the Normal Canine Brain. Front. Vet. Sci. 4:41. doi: 10.3389/fvets.2017.00041

Perfusion magnetic resonance imaging (MRI), specifically dynamic susceptibility MRI (DSC-MRI) is routinely performed as a supplement to conventional MRI in human medicine for patients with intracranial neoplasia and cerebrovascular events. There is minimal data on the use of DSC-MRI in veterinary patients and a DSC-MRI protocol in the veterinary patient has not been described. Sixteen normal dogs, 6 years or older were recruited for this study. The sample population included 11 large dogs (>11 kg) and 5 small dogs (<11 kg). DSC-MRI was performed on a 1.5-T MRI using an adjusted protocol inherent to the MRI. Contrast media was injected using an automatic power injector. Injections were made after five MR measurements were obtained. Following image acquisition, an arterial input function (AIF) graph mapping the transit time of contrast within the cerebral arteries was generated. The manually selected time points along this graph were used to compute perfusion maps. A dose and rate of 0.1 mmol/kg gadolinium-based contrast media at 3 ml/s followed by 10 ml saline flush at 3 ml/s was used in all dogs greater than 11 kg. In all dogs >11 kg, a useable AIF and perfusion map was generated. One dog less than 11 kg received the same contrast dose and rate. In this patient, the protocol did not generate a useable AIF. The remainder of the dogs less than 11 kg followed a protocol of 0.2 mmol/kg gadolinium-based contrast media at 1.5 ml/s with a 10 ml saline flush at 1.5 ml/s. A useable AIF and perfusion map was generated in the remaining dogs <11 kg using the higher contrast dose and slower rate protocol. This study establishes a contrast dose and administration rate for canine DSC-MRI imaging that is different in dogs greater than 11 kg compared to dogs less than 11 kg. These protocols may be used for future applications to evaluate hemodynamic disturbances in canine intracranial pathology.

Keywords: canine, perfusion, dynamic susceptibility contrast, magnetic resonance imaging, neuroimaging

Abbreviations: AIF, arterial input function; CBF, cerebral blood flow; CBV, cerebral blood volume; DCE-MRI, dynamic contrast-enhanced magnetic resonance imaging; DSC-MRI, dynamic susceptibility contrast magnetic resonance imaging; FLAIR, fluid attenuating inversion recovery; MRI, magnetic resonance imaging; MTT, mean transit time; ROI, region of interest; T1W, T1-weighted; T2(*)W, T2(*)-weighted.

INTRODUCTION

Perfusion magnetic resonance imaging (MRI) is an important non-invasive tool in human medicine for evaluating cerebral hemodynamics (1). Two contrast-based perfusion imaging sequences are described: dynamic susceptibility weighted dynamic susceptibility MRI (DSC-MRI) and dynamic contrast-enhanced MRI (DCE-MRI) (2). In human medicine, DSC-MRI is the most widely used method to measure brain perfusion due to the software availability and ease of use (2, 3).

Dynamic susceptibility MRI images the first pass of a bolus of gadolinium-based contrast through the brain by a series of T2*-weighted (T2*W) MRI images to generate a signal intensity to time curve, also known as an arterial input function (AIF). The susceptibility of the contrast causes a decrease in signal intensity, which leads to a signal loss in the AIF. From this curve, multiple hemodynamic parameters such as time to peak, mean transit time (MTT), cerebral blood flow (CBF), and cerebral blood volume (CBV) can be determined for each pixel and perfusion maps are generated (2, 4). A major assumption in DSC-MRI studies is that contrast remains within the blood vessels such that a susceptibility gradient can be induced between the intravascular and extravascular space, this assumption can lead to underestimation of perfusion, specifically in brain tumors (5, 6). DCE-MRI allows for better quantitative measurement of the blood–brain barrier, assessing the tissue permeability and the extracellular space, the values are sensitive to tumor growth and treatment response (7). DCE-MRI techniques involve serial T1-weighted (T1W) images before, during, and after gadolinium contrast administration (7). The reason DSC-MRI is used more often in the clinical setting is due to the complexity in image acquisition and post-processing of DCE-MRI data and the lack of widely available software (2). In contrast, most commercially available MRI scanners have inherent acquisition parameters and software for DSC-MRI. To the authors' knowledge, the only descriptive study in veterinary medicine using perfusion MRI is a quantitative perfusion study using DCE-MRI in dogs with intracranial neoplasia using 3-T MRI and manual contrast injection (8). Since both DSC-MRI and DCE-MRI involve dynamic imaging acquisitions, the use of an automated power injector is considered necessary to allow a fast injection needed for DSC-MRI and reproducible administration DCE-MRI perfusion (2). No studies using DSC-MRI in the normal canine brain have been described.

Extensive research and clinical applications of DSC-MRI are described in human patients with stroke (9, 10), neoplasia (11–13), dementia (14), anesthesia (15), epilepsy (16), and trauma (17, 18). Of the described clinical applications of DSC-MRI in human medicine, the use of DSC-MRI in intracranial neoplasia grading and therapeutic monitoring is the most clinically relevant to our canine patients and translational research (12, 19–24). Despite the amount of data available in human medicine, few reports in veterinary medicine have been published, with most available studies using animals as a model of disease. Examples include canine studies of ischemic stroke (25) and brain changes secondary to cardiac arrest (26). Within the veterinary literature, to the authors' knowledge, in addition to the previously mentioned DCE-MRI study, two descriptive reviews are available for vascular and perfusion imaging in the canine brain, with no protocol details (27, 28).

A protocol for DSC-MRI at 1.5 T in the normal canine brain with a power injector has not been described. The aim of this study was to determine a DSC-MRI protocol for the normal canine brain.

METHODS

The study protocol was designed in accordance with and approved by the Michigan State University animal care and use committee. The study was a prospective cohort study performed by recruiting client owned, consented healthy dogs, middle to senior in age (≥6 years).

All study dogs underwent a physical exam and bloodwork (complete blood count and serum chemistry) to ensure the animals were healthy and able to undergo anesthesia. All dogs were imaged under general anesthesia. All dogs received butorphanol (0.2 mg/kg, IV, or IM) as a premedication prior to induction. Varying by case, acepromazine (0.05 mg/kg, IV, or IM) was also administered as a premedication. General anesthesia was induced with propofol (4 mg/kg, IV, titrated to effect). The dogs were intubated and maintained on light anesthetic plane using sevofluorane gas anesthesia. Depending on patient size, an 18- or 20-gauge catheter was placed within the cephalic vein approximately 20 min after premedication administration and prior to anesthetic induction for anesthetic intravenous fluid delivery and contrast bolus administration.

Images were acquired using a 1.5-T Siemens Espree (Melvin, PA, USA) and an 8-channel coil head or knee coil. In general, large dogs were placed in the head coil due to its greater internal diameter and smaller dogs in the knee coil to minimize air gap between the coil and patient. All dogs had an abbreviated pre-contrast conventional brain MRI study including transverse T1W and fluid attenuating inversion recovery sequences.

Dynamic susceptibility MRI images were acquired using a first pass gadolinium contrast-enhanced T2*W echo-planar image sequence (Siemens, ep2d_perf) with 50 measurements. Each measurement ranged from 1.5 to 2 s long depending on number of slices. Continuous transverse slices throughout the brain were made with each measurement. The number of slices was dependent on patient size. The image acquisition parameters were as follows repetition time: average 2,008 ms (range: 1,690–2,250), echo time: 62.4 ms, flip angle: 90°, slice thickness: 4 mm, field of view: 140 or 150, number of excitations: 1, and matrix size of $64 \times 64 \times 16$. Paramagnetic contrast media, gadobenate dimeglumine (Multihance®), was injected into the cephalic vein catheter using an automatic power injector (Spectris Solaris®, Medrad) after five measurements. All dogs greater than 11 kg received a 0.1 mmol/kg contrast bolus at 3 ml/s followed by10 ml saline flush at 3 ml/s. One dog less than 11 kg received the same dose and rate. The remainder of dogs less than 11 kg followed a modified protocol of 0.2 mmol/kg contrast at 1.5 ml/s with a 10 ml saline flush at 1.5 ml/s. After perfusion data was obtained, all dogs underwent a post-contrast transverse T1W study.

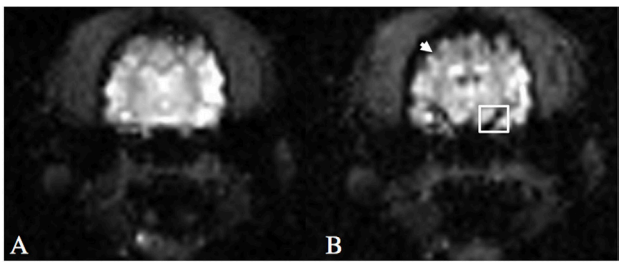

FIGURE 1 | T2*W echo-planar imaging sequence following gadolinium-based contrast injection at T = 0 (A) and time of peak arterial contrast susceptibility (B) at the level of the middle cerebral artery. Note the hypointense cortical arteries around the periphery of the cerebrum (arrow) and the middle cerebral artery (box) at peak contrast susceptibility.

Post-processing of DSC-MRI images was performed using the Siemens MRI analysis software (syngo.MR.NeuroPerfusion®) by one of the authors (Krystina L. Stadler). This commercially available software generates multiple AIF graphs based on a defined region of interest (ROI) centered over an area of high perfusion. For this study, the middle cerebral artery was used as the ROI (**Figure 1**). The AIF graphs T2*signal strength (*y*-axis) against time (*x*-axis). As the bolus arrives to the ROI, there is a drop-in signal strength (susceptibility on T2*W images), which remains until redistribution occurs (**Figure 2**). For further analysis, three of the AIF graphs were selected (**Figure 2A**). The selection of the three best AIF was subjective, defined by the AIF with the greatest defined peak and least amount of background noise. The graphs are then averaged by the software and used to generative a representative averaged AIF that is used to create cerebral perfusion maps (**Figure 2B**). From the generated average, AIF, the baseline

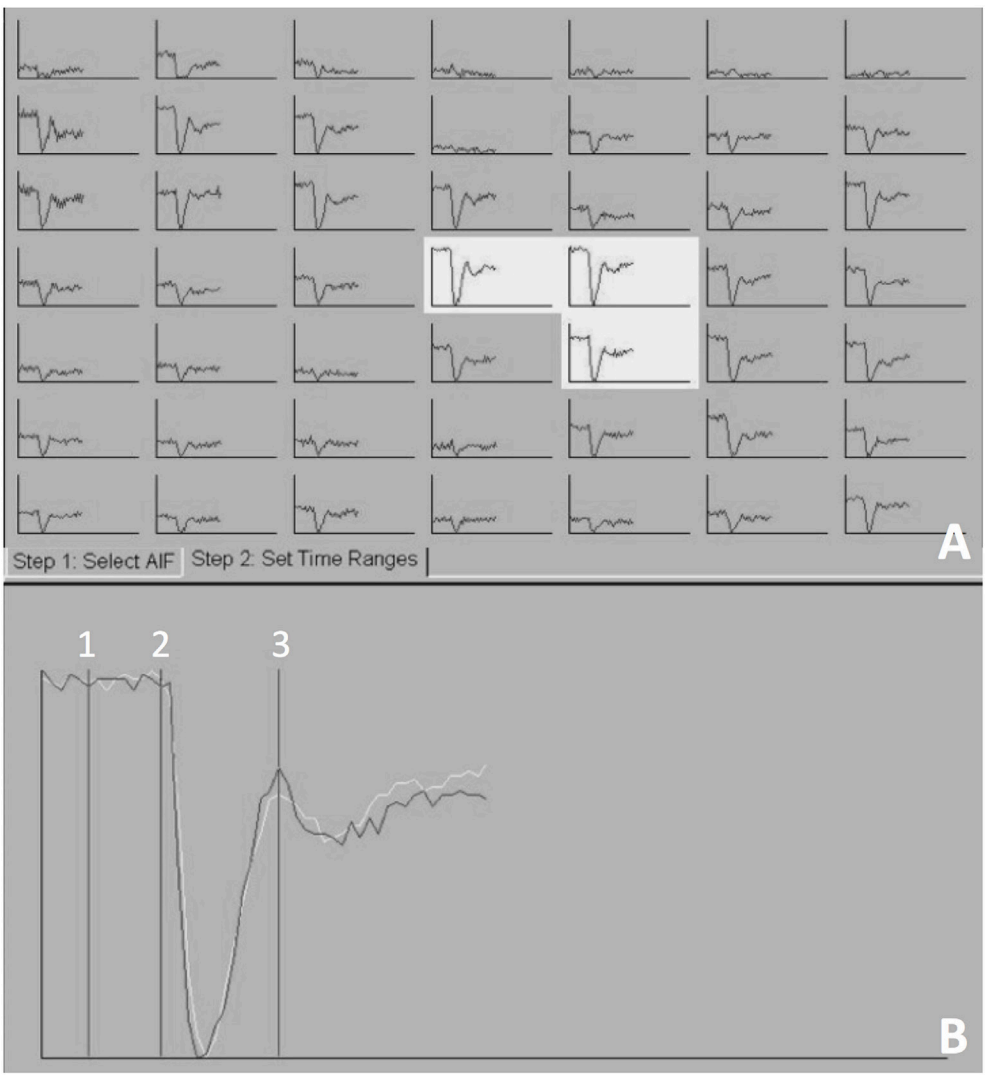

FIGURE 2 | The arterial input function (AIF) generated at the level of the middle cerebral artery, mapping T2*signal (*y*-axis) against time (*x*-axis). Three AIF graphs were selected **(A)** and a representative averaged AIF was generated **(B)**. Three points on the averaged AIF were selected 1—the baseline prior to the contrast arrival, 2—point on the graph immediately prior to signal loss peak, and 3—time immediately after return to baseline.

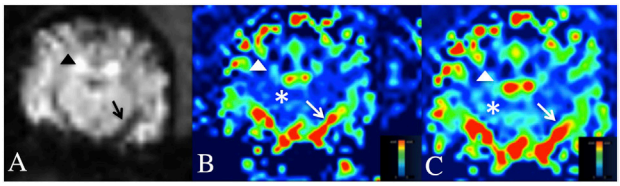

FIGURE 3 | Dynamic susceptibility MRI (DSC-MRI) in the normal canine brain. **(A)** DSC-MRI T2*W image at the level of the middle cerebral artery. Note the hypointensity of the cortical arteries (black arrow head) and middle cerebral artery (black arrow) during the arterial first pass of the gadolinium contrast bolus. **(B,C)** Cerebral blood volume **(B)** and cerebral blood flow **(C)** maps at the level of the middle cerebral artery. A blue-red scale is used on these maps, where red is high perfusion and blue is low perfusion. Note the red middle cerebral arteries and red–green cortical arteries (white arrow and arrow head) and the blue–green cerebral parenchyma (white asterisks).

prior to the contrast arrival, point on the graph immediately prior to signal loss peak, and time immediately after return to baseline were selected (**Figure 2B**). After these points are selected, the software generates relative color perfusion maps of the entire brain based on the perfusion imaging physics in which CBV is represented by the integrated area under the AIF curve, relative MTT is the width of the curve and CBF as the ratio between CBV and MTT. The software uses a blue–green–red color scheme for CBV and CBF maps with red being highly perfused, dark blue indicating extremely low perfusion, and green being intermediate perfusion (**Figure 3**).

RESULTS

Sixteen dogs met the inclusion criteria for this study. Multiple breeds were represented including: Staffordshire terrier ($n = 4$), mixed breed dogs (3), Laborador retriever (1 pure, one crossbreed), and one of each the following: Papillion, Beagle, Shiba Inu, Jack Russel Terrier, German Shepherd and Chihuahua. Nine dogs were spayed females, five were neutered males, and one was an intact male. The mean dog weight was 21.2 kg (range: 3.7–40.4 kg). Body condition score was not evaluated.

The injection protocol of 0.1 mmol/kg gadolinium followed by 10 ml saline flush at an injection rate of 3 ml/s generated a useable perfusion map in all dogs >11 kg ($n = 11$). In a small dog, weighing 10.5 kg, this protocol did not generate a useable map. This dog had evidence of contrast administration noted on the post-contrast T1W images. Following this dog, the protocol was augmented and a useable perfusion map was generated in the remaining dogs weighing less than 11 kg ($n = 4$) receiving the 0.2 mmol/kg of contrast medium and 10 ml saline flush at an injection rate of 1.5 ml/s protocol.

On the CBV and CBF maps, the large arterial structures (cerebral and cortical arteries) of the cerebrum were red on perfusion maps (high perfusion) with the smaller peripheral branches of these structures being green. The normal cerebral parenchyma was predominately royal blue (low perfusion) with small foci of light blue (low, but slightly higher perfusion). Areas of no perfusion, such as the lateral ventricles were dark blue.

DISCUSSION

The main clinical indications for perfusion imaging are neoplasia or a cerebrovascular event. Therefore, dogs 6 years or older were selected for this study to best match the age of dogs more commonly affected with intracranial diseases diagnosed by DSC-MRI. In human medicine, quantitative MRI CBF changes with age; however, in adults, qualitative maps are generated without changing protocol (29). This study did not validate this protocol in dogs younger than 6 years. The cause of the 0.1 mmol/kg at 3 ml/s protocol failure in one of the small dogs is unknown. This dog was the first small dog to be included in the study and was imaged after multiple successful DSC-MRI in dogs larger than this one. The augmentation of the protocol for smaller dogs was based on protocols successfully used in neonatal humans and piglets (1, 30, 31). Ideally, additional small dogs would have been tested at the protocol to see if the failure occurred repeatedly, however, given the funding available and limited availability of small dogs fitting our inclusion criteria, this was not possible and is a limitation to this study. The dog that failed to generate perfusion maps was 10.5 kg and thus the threshold weight limit between small and large dogs was placed at 11 kg. The closest large dog weight to the 11 kg cutoff was 15 kg; this dog generated a useable AIF with the lower contrast dose, higher rate protocol. The authors postulate that the small volume of contrast and/or the rate of contrast administration are a contributing factor of the lower contrast/higher rate DSC-MRI protocol not working in the small dogs. In the authors' clinical experience, the lower contrast dose/higher rate was not successful in additional small dogs; these dogs were not included in this study because they had a known intracranial disease, which may have resultant alterations in their cerebrovascular perfusion. Dosing by mmol/body weight (kg) is convention at our institution. Body condition score was not factored into contrast dosing. To the author's knowledge, the relationship between patient body condition and gadolinium-based contrast media dosage has not been described. It is unknown if altering the DSC-MRI protocol for ideal body condition weight in patients that are over or under conditioned into the small or large dog protocol would affect the AIF and is a limitation of this study.

In this study, the middle cerebral artery was chosen to generate the AIF because of its reproducible susceptibility that occurred on arterial first pass and for continuity in map generation. Although not assessed in this study, the placement of the ROI on any large artery, preferably in the same slice as your pathology is recommended in human medicine and should generate a similar perfusion map (32). This study's aim was to describe a contrast protocol that can be used in the canine patients for future studies evaluating cerebral perfusion. The testing of multiple different contrast doses and bolus rates were beyond the scope of this study. Additional studies with a large population of normal dogs may help to determine if any alterations to the recommended dose and rate could be implemented. Gadolinium is a considered a safe contrast medium; doubling

the dose is common in pediatric human medicine (1). Thus, the current recommended dose for small dogs should have minimal ill effect to the patient and provide consistent diagnostic DSC-MRI perfusion maps.

It is the authors' belief that the addition of perfusion maps to conventional MRI images in canine patients will optimize the diagnostic accuracy of intracranial lesions and aid in treatment and prognosis as it has in human medicine. This is the study in veterinary medicine to describe a protocol for the use of DSC-MRI in canine patients. This study used a 1.5-T MRI and a power injector to obtain repeatable, uniform perfusion maps. This study establishes a protocol for canine 1.5-T DSC-MRI imaging that is different in large and small dogs. These protocols may be used for future applications to evaluate hemodynamic disturbances in canine intracranial pathology.

AUTHOR CONTRIBUTIONS

KS: principal investigator and primary author of the manuscript. As PI, KS was responsible for research development and adjustment of the methods, grantsmanship, and authoring of the manuscript. This research was done as part of KS's radiology residency. AP and EB: both faculty resident and research mentors responsible for editing and approving methodology prior to initiation, editing, and co-PI on grants and IACUC, as well as internal editing of the manuscript.

FUNDING

This study was supported by Michigan State University College of Veterinary Medicine Endowed Research Grant.

REFERENCES

1. Huisman TA, Sorensen AG. Perfusion-weighted magnetic resonance imaging of the brain: techniques and application in children. *Eur Radiol* (2004) 14(1):59–72. doi:10.1007/s00330-003-1972-y
2. Essig M, Nguyen TB, Shiroishi MS, Saake M, Provenzale JM, Enterline DS, et al. Perfusion MRI: the five most frequently asked clinical questions. *AJR Am J Roentgenol* (2013) 201(3):W495–510. doi:10.2214/AJR.12.9544
3. Keston P, Murray AD, Jackson A. Cerebral perfusion imaging using contrast-enhanced MRI. *Clin Radiol* (2003) 58(7):505–13. doi:10.1016/S0009-9260(03)00130-2
4. Rosen BR, Belliveau JW, Aronen HJ, Kennedy D, Buchbinder BR, Fischman A, et al. Susceptibility contrast imaging of cerebral blood volume: human experience. *Magn Reson Med* (1991) 22(2):293–9; discussion 300–3. doi:10.1002/mrm.1910220227
5. Donahue KM, Krouwer HG, Rand SD, Pathak AP, Marszalkowski CS, Censky SC, et al. Utility of simultaneously acquired gradient-echo and spin-echo cerebral blood volume and morphology maps in brain tumor patients. *Magn Reson Med* (2000) 43(6):845–53. doi:10.1002/1522-2594(200006)43:6<845::AID-MRM10>3.0.CO;2-J
6. Quarles CC, Ward BD, Schmainda KM. Improving the reliability of obtaining tumor hemodynamic parameters in the presence of contrast agent extravasation. *Magn Reson Med* (2005) 53(6):1307–16. doi:10.1002/mrm.20497
7. Gossmann A, Helbich TH, Kuriyama N, Ostrowitzki S, Roberts TP, Shames DM, et al. Dynamic contrast-enhanced magnetic resonance imaging as a surrogate marker of tumor response to anti-angiogenic therapy in a xenograft model of glioblastoma multiforme. *J Magn Reson Imaging* (2002) 15(3):233–40. doi:10.1002/jmri.10072
8. Zhao Q, Lee S, Kent M, Schatzberg S, Platt S. Dynamic contrast-enhanced magnetic resonance imaging of canine brain tumors. *Vet Radiol Ultrasound* (2010) 51(2):122–9. doi:10.1111/j.1740-8261.2009.01635.x
9. Keir SL, Wardlaw JM. Systematic review of diffusion and perfusion imaging in acute ischemic stroke. *Stroke* (2000) 31(11):2723–31. doi:10.1161/01.STR.31.11.2723
10. Hoggard N, Wilkinson ID, Griffiths PD. The imaging of ischaemic stroke. *Clin Radiol* (2001) 56(3):171–83. doi:10.1053/crad.2000.0619
11. Knopp MV, Essig M, Hawighorst H, Wenz F, Brix G, Schad LR, et al. Functional neuroimaging in the assessment of CNS neoplasms. *Eur Radiol* (1997) 7(Suppl 5):209–15. doi:10.1007/PL00006894
12. Law M, Cha S, Knopp EA, Johnson G, Arnett J, Litt AW. High-grade gliomas and solitary metastases: differentiation by using perfusion and proton spectroscopic MR imaging. *Radiology* (2002) 222(3):715–21. doi:10.1148/radiol.2223010558
13. Cha S. Update on brain tumor imaging: from anatomy to physiology. *Am J Neuroradiol* (2006) 27(3):475–87.
14. Bozzao A, Floris R, Baviera ME, Apruzzese A, Simonetti G. Diffusion and perfusion MR imaging in cases of Alzheimer's disease: correlations with cortical atrophy and lesion load. *AJNR Am J Neuroradiol* (2001) 22(6):1030–6.
15. Lorenz IH, Kolbitsch C, Hormann C, Luger TJ, Schocke M, Eisner W, et al. The influence of nitrous oxide and remifentanil on cerebral hemodynamics in conscious human volunteers. *Neuroimage* (2002) 17(2):1056–64. doi:10.1006/nimg.2002.1228
16. O'Brien TJ, David EP, Kilpatrick CJ, Desmond P, Tress B. Contrast-enhanced perfusion and diffusion MRI accurately lateralize temporal lobe epilepsy: a pilot study. *J Clin Neurosci* (2007) 14(9):841–9. doi:10.1016/j.jocn.2006.07.003
17. Beaumont A, Fatouros P, Gennarelli T, Corwin F, Marmarou A. Bolus tracer delivery measured by MRI confirms edema without blood-brain barrier permeability in diffuse traumatic brain injury. *Acta Neurochir Suppl* (2006) 96:171–4. doi:10.1007/3-211-30714-1_38
18. Dagal A, Lam AM. Cerebral blood flow and the injured brain: how should we monitor and manipulate it? *Curr Opin Anaesthesiol* (2011) 24(2):131–7. doi:10.1097/ACO.0b013e3283445898
19. Law M, Yang S, Wang H, Babb JS, Johnson G, Cha S, et al. Glioma grading: sensitivity, specificity, and predictive values of perfusion MR imaging and proton MR spectroscopic imaging compared with conventional MR imaging. *AJNR Am J Neuroradiol* (2003) 24(10):1989–98.
20. Lev MH, Ozsunar Y, Henson JW, Rasheed AA, Barest GD, Harsh GRT, et al. Glial tumor grading and outcome prediction using dynamic spin-echo MR susceptibility mapping compared with conventional contrast-enhanced MR: confounding effect of elevated rCBV of oligodendrogliomas [corrected]. *AJNR Am J Neuroradiol* (2004) 25(2):214–21.
21. Law M, Oh S, Babb JS, Wang E, Inglese M, Zagzag D, et al. Low-grade gliomas: dynamic susceptibility-weighted contrast-enhanced perfusion MR imaging – prediction of patient clinical response. *Radiology* (2006) 238(2):658–67. doi:10.1148/radiol.2382042180
22. Law M, Young RJ, Babb JS, Peccerelli N, Chheang S, Gruber ML, et al. Gliomas: predicting time to progression or survival with cerebral blood volume measurements at dynamic susceptibility-weighted contrast-enhanced perfusion MR imaging. *Radiology* (2008) 247(2):490–8. doi:10.1148/radiol.2472070898
23. Server A, Kulle B, Gadmar OB, Josefsen R, Kumar T, Nakstad PH. Measurements of diagnostic examination performance using quantitative apparent diffusion coefficient and proton MR spectroscopic imaging in the preoperative evaluation of tumor grade in cerebral gliomas. *Eur J Radiol* (2011) 80(2):462–70. doi:10.1016/j.ejrad.2010.07.017
24. Hilario A, Ramos A, Perez-Nunez A, Salvador E, Millan JM, Lagares A, et al. The added value of apparent diffusion coefficient to cerebral blood volume in the preoperative grading of diffuse gliomas. *AJNR Am J Neuroradiol* (2012) 33(4):701–7. doi:10.3174/ajnr.A2846
25. Harris AD, Kosior JC, Ryder RC, Andersen LB, Hu WY, Hudon M, et al. MRI of ischemic stroke in canines: applications for monitoring intraarterial thrombolysis. *J Magn Reson Imaging* (2007) 26(6):1421–8. doi:10.1002/jmri.21189
26. Liu R, Li X, Hu CL, Jiang L, Dai G, Wu GF, et al. The changes of brain water diffusion and blood flow on diffusion-weighted and perfusion-weighted imaging in a canine model of cardiac arrest. *Resuscitation* (2012) 83(5):645–51. doi:10.1016/j.resuscitation.2011.10.017

27. Tidwell AS, Robertson ID. Magnetic resonance imaging of normal and abnormal brain perfusion. *Vet Radiol Ultrasound* (2011) 52(1 Suppl 1):S62–71. doi:10.1111/j.1740-8261.2010.01786.x
28. Dickinson PJ. Advances in diagnostic and treatment modalities for intracranial tumors. *J Vet Intern Med* (2014) 28(4):1165–85. doi:10.1111/jvim.12370
29. Chen JJ, Rosas HD, Salat DH. Age-associated reductions in cerebral blood flow are independent from regional atrophy. *Neuroimage* (2011) 55(2):468–78. doi:10.1016/j.neuroimage.2010.12.032
30. de Lange C, Brabrand K, Emblem KE, Bjornerud A, Loberg EM, Saugstad OD, et al. Cerebral perfusion in perinatal hypoxia and resuscitation assessed by transcranial contrast-enhanced ultrasound and 3 T MRI in newborn pigs. *Invest Radiol* (2011) 46(11):686–96. doi:10.1097/RLI.0b013e3182266431
31. Lobel U, Sedlacik J, Reddick WE, Kocak M, Ji Q, Broniscer A, et al. Quantitative diffusion-weighted and dynamic susceptibility-weighted contrast-enhanced perfusion MR imaging analysis of T2 hypointense lesion components in pediatric diffuse intrinsic pontine glioma. *AJNR Am J Neuroradiol* (2011) 32(2):315–22. doi:10.3174/ajnr.A2277
32. Cha S. Perfusion MR imaging of brain tumors. *Top Magn Reson Imaging* (2004) 15(5):279–89. doi:10.1097/00002142-200410000-00002

Conflict of Interest Statement: The authors declare that the research was conducted in the absence of any commercial or financial relationships that could be construed as a potential conflict of interest.

Advantages of publishing in Frontiers

OPEN ACCESS
Articles are free to read for greatest visibility and readership

FAST PUBLICATION
Around 90 days from submission to decision

HIGH QUALITY PEER-REVIEW
Rigorous, collaborative, and constructive peer-review

TRANSPARENT PEER-REVIEW
Editors and reviewers acknowledged by name on published articles

Frontiers
Avenue du Tribunal-Fédéral 34
1005 Lausanne | Switzerland

Visit us: www.frontiersin.org
Contact us: info@frontiersin.org | +41 21 510 17 00

REPRODUCIBILITY OF RESEARCH
Support open data and methods to enhance research reproducibility

DIGITAL PUBLISHING
Articles designed for optimal readership across devices

FOLLOW US
@frontiersin

IMPACT METRICS
Advanced article metrics track visibility across digital media

EXTENSIVE PROMOTION
Marketing and promotion of impactful research

LOOP RESEARCH NETWORK
Our network increases your article's readership